Co-evolution of Life and Environment across Earth History: Empirical & Modeling Constraints on Nutrient Cycling, the Rise of Oxygen, and Eukaryotic Evolution

Michael Kipp

A dissertation
submitted in partial fulfillment of the
requirements for the degree of

Doctor of Philosophy

University of Washington

2019

Reading Committee:

Roger Buick, Chair

David Catling

Bruce Nelson

Program Authorized to Offer Degree:
Earth & Space Sciences

University of Washington

Abstract

Co-evolution of Life and Environment across Earth History:
Empirical & Modeling Constraints
on Nutrient Cycling, the Rise of Oxygen,
and Eukaryotic Evolution

Michael Kipp

Chair of the Supervisory Committee:
Prof. Roger Buick
Earth & Space Sciences

That life and its environment have co-evolved through Earth's history, and in doing so have maintained the conditions required for planetary habitability, is one of the great discoveries in the natural sciences during 20^{th} century. This dissertation joins a large body of work that has arisen since this discovery permeated the Earth sciences; the goal of the work now is not only to better understand the processes that enabled Earth to reach its present state, but also to use the Earth through time as an analog for better understanding the diversity of exoplanets that are rapidly being discovered around nearby stars. Specifcally, the work described here aims to place novel constraints on various aspects of Earth's evolution as a habitable planet. In Part I, the oxygenation history of Earth's surface is probed using a relatively new proxy - selenium geochemistry. These data reveal substantial atmospheric and marine oxygen accumulation during the Great Oxidation Event, and also implicate a close relationship between oxygenation and the cycling of major nutrients. Building off these findings, Part II aims to elucidate the response of the major nutrient cycles (nitrogen and phosphorus) to the oxygenation of Earth's surface environment. These chapters demonstrate that major shifts occurred in both the nitrogen and phosphorus cycles across the Great Oxidation Event, with implications for the early evolution of eukaryotes. In Part III, various

new tools and approaches for studying ancient life and environments are explored. This includes a review of C/N ratios in marine sediments and their possible relationship to oxygen availability, as well as a novel application of nitrogen isotope ratios to deduce nitrogen fixation in fossil plants. In total, the projects contained in this dissertation provide various pieces of information that deepen our understanding of Earth's evolution as a habitable planet. Ultimately these findings may serve to guide our interpretation of exoplanetary atmospheric compositions (and their biospheric implications), or even to help us grasp the magnitude of forthcoming environmental change as humans continue to act as a forceful environment-modifying agent.

TABLE OF CONTENTS

LIST OF FIGURES

LIST OF TABLES

ACKNOWLEDGMENTS

It is difficult to narrow down an appropriately short list of acknowledgements for such a lengthy and all-encompassing task as the completion of this thesis. Moving roughly chronologically, I first thank my undergrad mentors, Gary Belovsky, David Hernandez, Stuart Jones and Will West for motivating me - through advice and example - to pursue a career in science.

From UW, I first thank the Astrobiology Program for providing me with a vibrant community that added a fun dimension to my research from day one. Vikki Meadows in particular deserves a sincere thank you for always encouraging students to seek out unique learning experiences, and always somehow finding the funding to make those experiences a reality. I further thank all of my fellow AB students and postdocs from whom I learned a great deal in places ranging from Icelandic hot springs to Camp Muir to the College Inn.

I also owe much thanks to the Department of Earth & Space Sciences for serving as my home during my five years at UW. My work in the lab would have fallen off the rails many times if not for the savvy and generous advice constantly provided by Andy Schauer and Scott Kuehner. They deserve more credit than they ever get (or ask for).

My committee members each deserve a special thanks for contributing their time and expertise to the compilation of this thesis. Jodi Young very willingly provided an oceanographer's perspective on my ancient biogeochemical studies, and Alex Gagnon stepped in on short notice to provide more insights from the world of modern marine chemistry. Drew Gorman-Lewis was generous to host me in his lab as I experimented with geomicrobiology in my first years, and continued to provide thoughtful feedback on the remaining studies that I undertook. David Catling taught me a great deal about planetary atmospheres in the classroom, and also had a knack for asking good questions that forced me to re-frame

concepts in the simplest and clearest way possible. Bruce Nelson very kindly let me take over large swathes of his lab for selenium chemistry and analysis, and was always quick to chime in (along with Fangzhen Teng and Yan Hu) with good ideas about how to get the mass spec to behave - even all the way from his sabbatical in France.

Beyond my committee, the members of the Buick group were each instrumental and invaluable to the success of the projects I worked on. Eva Stüeken was an incredible resource throughout my PhD, particularly by getting me started in the lab and set up with tractable and exciting projects - it is hard to over-state the importance of that mentorship and my gratitude for it. Matt Koehler was a great companion to have throughout the bulk of our PhDs and was always ready to run with a new idea or provide critical feedback when needed. Jana Meixnerova bore with me as I learned to be a mentor, and her indomitable work ethic plus eager questioning made for an always exciting and enriching time working on projects together. Brett Smith, Hillary Smith, and Kailey Busch each endured my early attempt at advising and always managed impressively well; I hope that they learned as much as I did.

Overseeing and orchestrating all this work was Roger Buick, whose sharp wit and sardonic humor strike a harmonious balance with an insatiable appetite for intriguing and impactful science. I'm deeply indebted to Roger, not only because of the many grant dollars he gambled on my ideas, but more so because he instilled in me a thirst for doing science that is cool.

Lastly, I owe a huge thank you to those who kept me sane during my PhD. Many new friends in Seattle and old friends from afar provided much-needed outlets from the day-to-day grind of research. Nick, Ben, John, Alex, Sean & Maddie all shook me out of lab-induced stupor on countless occassions with tasty cooking, various board games and over-amped jam sessions. My parents, Mike & Kim, and siblings, Stephen, Matt, Joe & Mary all heard more than they ever wanted to about biogeochemistry, and took it with grace and admiration. Finally, Tina, for always inspiring me, taking care of me, and helping me see the forest through the trees: it will take me a lifetime to return the favor for your support.

DEDICATION

to Mary - a budding scientist

"The question of all questions for humanity, the problem which lies behind all others and is more interesting than any of them is that of the determination of man's place in Nature and his relation to the Cosmos."

T.H. Huxley

INTRODUCTION

In spite of increasing solar luminosity, bombardment by asteroids, and ecologically-devastating biological innovations, the Earth has remained not only a habitable planet, but an *inhabited* one, for well over 3 billion years. This fact is a testament to the resilience of biogeochemical feedbacks that actively maintain clement conditions on our planet's surface, buffering it against dramatic swings that might extinguish life as we know it.

A great deal of work has focused on reconstructing the narrative of Earth's long history as a living planet, and the storylines are always riveting as they tell us the tale of how we came to exist in this place and time on this particular piece of cosmic debris. However, the societal role of this work is currently shifting from that of reconstructing "origins stories" to a precise cataloguing of past planetary states (atmospheric, biological, geophysical, *etc.*) for one reason in particular: our species is within a few decades of measuring the atmospheric composition of reams of planets orbiting nearby stars. This could potentially acquaint us with many Earth-like worlds, but the question remains - *would we recognize the younger Earth if we saw it?*

This thesis is part of a larger body of research that is attempting to prepare us for that endeavor, so that we can reliably say that we would indeed recognize the different faces of our same inhabited planet at different points in its history. Specifically, the work in this thesis aims to more precisely reconcile our empirical records of environmental evolution with our current understanding of the timetable of biological evolution. This will allow us to say, for instance, that in Earth's past an abundance of atmospheric oxygen (a critical metabolic substrate for animals) *was* or *was not* always seen in conjunction with animal life. These types of constraints from our planet's own history will prove critical for robustly drawing biological inferences from exoplanetary atmospheric compositions. As large of a leap as that

may seem (from atmospheric composition to biological characterization), it is likely to be our only way to scientifically address the biotic activity (or lack thereof) of exoplanets in the near future. It therefore behooves us to be prepared for such interpretations.

In addition to working on questions that directly feed into that framework, some of the work included here involves expanding our geochemical toolkit for future studies of ancient Earth environments. In sum, the goal of the work is (a) to better understand the intricacies of the co-evolution of life and its environment across Earth's long history, and (b) improve our technical capabilities to advance that understanding.

In Part I of this thesis, selenium (Se) geochemistry is used as a proxy for changes in oxygen availability in seawater in deep time. As Se is prone to reductive immobilization at relatively high redox potentials, the movement of Se in the environment implies oxygen levels that are likely amenable to eukaryotes, or even simple animals. Chapter 1 specifically uses this proxy to determine whether the shallow ocean was sufficiently oxygenated during the Great Oxidation Event ($\sim$2.4 billion years ago, Ga) to support eukaryotic life. The data revealed that the shallow ocean was indeed hospitable to such organisms, despite their absence in the coeval fossil record, raising a mystery about their delayed emergence. Chapter 2 involves a more detailed stratigraphic utilization of the Se proxy in post-GOE shales from Russia, and the data reveal details of the relationship between redox conditions and nutrient cycling at that juncture in Earth's history. Chapter 3 dives into some of the weeds of the Se proxy and examines the role of basinal restriction in altering the enrichment and isotopic fractionation of Se in marine sediments.

In Part II, the focus is shifted from oxygen as a throttle on the biosphere to major nutrients: nitrogen (N) and phosphorus (P). Chapter 4 presents a new model for P limitation in the Precambrian ocean, which generates testable predictions and also implies new relationships between net primary productivity, oxidant availability and oxygen production in the prelude to the GOE. Chapter 5 presents new N isotope data from shales deposited during and after the GOE; the data reveal that surface waters were well-oxygenated and the nitrate was likely bioavailable for eukaryotic organisms at this time - further complicating

the mystery of eukaryotes' delayed appearance in the fossil record.

In Part III, geochemical proxies are developed and applied in novel ways, highlighting some of the directions that future work can take. Chapter 6 wrestles with the meaning of C/N ratios in ancient marine sedimentary rocks, and posits that there is some redox-sensitive information encoded in the C/N ratio of ancient organic matter preserved on geological timescales. Chapters 7 and 8 use the N isotope proxy in a somewhat novel fashion. In Chapter 7, N isotopes are measured in a range of cycads - ancient gymnosperms that feature N-fixing symbioses with cyanobacteria in all extant species. The data reveal that N isotopes consistently track the influence of this N-fixing symbiosis across variable environments. In Chapter 8, the N isotopic composition of fossilized cycads is used to track the presence or absence of N-fixing symbiosis going back $\sim$200 Myrs in the fossil record. The data reveal that the symbiosis was likely active by $\sim$50 Myrs ago, but perhaps not earlier.

In sum, this work contributes various tidbits to our larger understanding of how environmental conditions have permitted or resulted from biological innovations on the timescale of planetary evolution. Future work along each of these avenues (and in close collaboration with astronomers and planetary scientists) will hopefully bring us closer to the point where the characterization of another planet's atmospheric gases will be readily related to a plausible biospheric configuration. Such an undertaking is one of the grandest tasks faced by humanity this century, and has the potential to answer, in a way never conceivable before, the question of our "place in Nature and relation to the Cosmos."

Chapter 1

SELENIUM ISOTOPES RECORD EXTENSIVE MARINE SUBOXIA DURING THE GREAT OXIDATION EVENT

This manuscript is published as:
Kipp MA, Stüeken EE, Bekker A, Buick R. (2017). *Proceedings of the National Academy of Sciences*. 114(5): 875-880. https://doi.org/10.1073/pnas.1615867114

1.1 Abstract

It has been proposed that an "oxygen overshoot" occurred during the early Paleoproterozoic Great Oxidation Event (GOE) in association with the extreme positive carbon isotopic excursion known as the Lomagundi Event. Moreover, it has also been suggested that environmental oxygen levels then crashed to very low levels during the subsequent extremely negative Shunga-Francevillian carbon isotopic anomaly. These redox fluctuations could have profoundly influenced the course of eukaryotic evolution, as eukaryotes have several metabolic processes that are obligately aerobic. Here we investigate the magnitude of these proposed oxygen perturbations using selenium (Se) geochemistry, which is sensitive to redox transitions across suboxic conditions. We find that $\delta^{82/78}$Se values in offshore shales show a positive excursion from 2.32 Ga until 2.1 Ga (mean +1.03 ± 0.67‰). Selenium abundances and Se/TOC ratios similarly show a peak during this interval. Together these data suggest that during the GOE there was pervasive suboxia in near-shore environments, allowing non-quantitative Se reduction to drive the residual Se oxyanions isotopically heavy. This implies O_2 levels of >0.4 µM in these settings. Unlike in the late Neoproterozoic and Phanerozoic when negative $\delta^{82/78}$Se values are observed in offshore environments, only a single formation, evidently the shallowest, shows evidence of negative $\delta^{82/78}$Se. This suggests that there was

no upwelling of Se oxyanions from an oxic deep-ocean reservoir, which is consistent with previous estimates that the deep ocean remained anoxic throughout the GOE. The abrupt decline in $\delta^{82/78}$Se and Se/TOC values during the subsequent Shunga-Francevillian anomaly indicates a widespread decrease in surface oxygenation.

1.2 Introduction

The accumulation of molecular oxygen in Earth's atmosphere and ocean fundamentally restructured biogeochemical pathways, and ultimately allowed the evolution of aerobically-respiring eukaryotic life. Determining the tempo of the rise of oxygen to modern levels has thus been the focus of decades of research (Holland, 1984; Lyons et al., 2014). The beginning of the Paleoproterozoic Era (2.5-1.6 Ga) is of particular interest, since it was the first time in Earth's history when oxygen-rich conditions prevailed in surface environments for a prolonged interval (Bekker and Holland, 2012).

The first permanent step in the oxygenation of Earth's surface, the Great Oxidation Event (GOE), was originally identified by the disappearance of redox-sensitive detrital minerals (Schidlowski and Trurnit, 1966; Rasmussen and Buick, 1999) and the appearance of red beds (Cloud, 1968) around the Archean-Proterozoic boundary. More recently, the record of mass-independent fractionation of sulfur isotopes (MIF-S) in sedimentary sulfates and sulfides (Farquhar et al., 2000) revealed that atmospheric O_2 increased from negligible amounts to $>10^{-5}$ times present atmospheric levels (Pavlov and Kasting, 2002) between 2.45 and 2.32 Ga, which is now thought to mark the onset of the GOE (Bekker et al., 2004; Luo et al., 2016).

While its name may seem to imply a discrete upward step in the oxidation state of Earth's surface, a new view is emerging of the GOE as a dynamic interval of rising and then falling O_2 lasting until ca. 2.06 Ga (Bekker and Holland, 2012; Kump et al., 2011). The occurrence of the largest and longest-lived positive carbon isotope excursion in the geologic record – the Lomagundi Event (LE) (Bekker, 2014) – in the later stages of the GOE between 2.22 and 2.06 Ga, has been cited as evidence of enhanced organic carbon burial that may

have allowed even higher levels of free oxygen to temporarily accumulate at Earth's surface at this time (Karhu and Holland, 1996), *i.e.* an "oxygen overshoot".

Indeed, there is mounting evidence for expansion and contraction of the marine sulfate reservoir across the LE (Planavsky et al., 2012; Schröder et al., 2008; Scott et al., 2014), which is thought to reflect trends in oxidative sulfide weathering and oxygenation of the ocean as atmospheric oxygen levels rose and fell. Relative iodate abundances in carbonates also document an increase in shallow-water oxidation state near the onset of the GOE, peaking during the LE (Hardisty et al., 2014). Additionally, enrichments of molybdenum (Mo) and uranium (U) in organic-rich shales reflect vigorous oxidative weathering of the continents during the GOE (Partin et al., 2013; Scott et al., 2008). Thus, a fairly consistent picture is emerging of an O_2-rich world between ca. 2.3 and 2.1 Ga.

However, while the above proxies have indicated widespread oxygen availability in the early Paleoproterozoic, we still lack precise constraints on the extent of oxic, suboxic and anoxic (including euxinic) habitats in the oceans at this time. This is a matter of great evolutionary importance, since the spatial and temporal transience of oxic-to-suboxic environments may have been the dominant throttle on eukaryotic evolution prior to the late Neoproterozoic (0.8 - 0.54 Ga) (Reinhard et al., 2016). If oxygenated habitats were indeed abundant during the GOE, it could have constituted the first time in Earth's history that geographically extensive regions of the ocean were conducive to the evolution of complex life.

Accurately probing the redox landscape of the oceans during the GOE requires a suite of proxies that function at different spatial scales. Evidence for large marine sulfate, iodate, Mo and U reservoirs is suggestive of a global expansion of oxygenated water masses. However, these signals lack the resolution to assess basinal redox gradients that could be critical for eukaryote ecology. Conversely, Fe speciation is a well-developed local redox indicator, and has been used to identify euxinia in offshore environments during the GOE (Canfield et al., 2013; Scott et al., 2014). But because this signal records local conditions, with spatially limited data it lacks the ability to distinguish an oxygen-minimum zone in an otherwise globally oxic ocean from a globally anoxic deep ocean.

Selenium (Se) is well-suited for bridging the gaps between the aforementioned proxies, as its relatively short oceanic residence time ($\sim 10^3$ yrs) makes Se sensitive to basin-scale redox dynamics. Selenium is predominantly delivered to the oceans via oxidative weathering, making the marine Se reservoir scale with continental oxidative weathering rates. Additionally, Se isotopes can be fractionated by several permil during oxyanion (SeO_4^{2-}, SeO_3^{2-}, $HSeO^{3-}$) reduction to elemental Se and selenide in suboxic environments, such as modern oxygen-minimum zones and suboxic pore-waters. In these settings, if Se oxyanions are continuously supplied from oxygenated waters, reduction is non-quantitative and the resulting isotopic values of reduced Se compounds are typically negative (Mitchell et al., 2012; Stüeken et al., 2015b). Negative Se isotope ratios in sedimentary rocks can therefore be an indication that the sediments were deposited in an environment that was linked to a large oxic reservoir. Selenium isotopes have been used in this way to track the oxygenation of the deep ocean in the late Neoproterozoic, where fractionations down to -1.5‰ have been recorded in offshore shales that received upwelling Se oxyanions from oxic deep oceans (von Strandmann et al., 2015). In modern anoxic basins where Se oxyanions are not continuously re-supplied, Se is largely consumed by uptake into biomass without net fractionation and the reduction of Se oxyanions is quantitative (Cutter, 1982). Isotopic values in these settings are therefore typically heavy, approaching or exceeding the composition of seawater, which is $\sim$+0.3‰ today (Stüeken et al., 2015b).

We measured Se abundance and isotope ratios in organic-rich shales from 7 stratigraphic units deposited in offshore environments during and after the GOE. These lithologies capture the offshore Se reservoir, which records basin-scale redox structure. Viewed together, these snapshots of individual basins at different stages of the GOE offer a glimpse of secular changes in the redox structure of the global ocean. Our results thus provide a proxy record that can test the predictions made by other redox-sensitive indicators and help resolve the spatial and temporal distribution of oxic, suboxic and anoxic marine environments during the GOE. Specifically, these data allow us to test whether the Paleoproterozoic oxygen overshoot was at any time comparable in magnitude to the Neoproterozoic oxygenation event, and to assess

the implications for the early evolution of eukaryotic life.

1.3 Materials

We analyzed 75 samples from 7 shale units deposited between 2.2 and 1.85 Ga. These data were compared with 567 published Se measurements from samples with ages spanning 3.25 Ga to the present. Samples corresponding to the early stage of the GOE come from the Rooihoogte and Timeball Hill formations of the Pretoria Group (2.32 Ga), which were analyzed by Stüeken et al. (2015b), and are the oldest open-marine shales deposited without a MIF-S signature. In addition, we sampled the Wewe Slate (ca. 2.2-2.1 Ga) and Sengoma Argillite Formation (ca. 2.2-2.1 Ga), which were deposited in the middle of the GOE, during the Lomagundi carbon isotope excursion. Samples straddling the end of the GOE and Lomagundi carbon isotope excursion come from the Hautes Chutes Formation of the Labrador Trough (ca. 2.1 Ga), the Francevillian Series of Gabon (ca. 2.083 Ga), the Zaonega Formation of Karelia, Russia (ca. 2.11-2.06 Ga), and the Union Island Group of the Slave craton (ca. 2.1-2.0 Ga). In addition, organic-rich shales of the Menihek Formation from the Labrador Trough (1.85 Ga), post-dating the LE, were also analyzed. These samples span the latest stages of the GOE and the 200 Myr interval after its termination, and include the formations in which the Shunga-Francevillian negative carbon isotope anomaly was originally discovered (Kump et al., 2011).

1.4 Results

Shales deposited in offshore environments show a broad trend in Se concentrations across the GOE, with abundances increasing in the late Archean and subsequently falling through the Paleoproterozoic, with a peak between 2.32 Ga and 2.1 Ga (max. 27.97 ppm; Fig. 1.1). Mean Se abundance of shales deposited between 2.32 Ga and 2.1 Ga (6.79 ppm) is significantly higher than the mean Se abundance for shales older than 2.45 Ga (2.04 ppm; $p_{\text{one-tailed}} = 10^{-8}$) and with ages between 2.1 and 1.1 Ga (2.02 ppm; $p_{\text{one-tailed}} = 10^{-8}$). Se/TOC ratios similarly show a peak (max. 26.84 ppm/wt%) in the early stage of the GOE, but rapidly

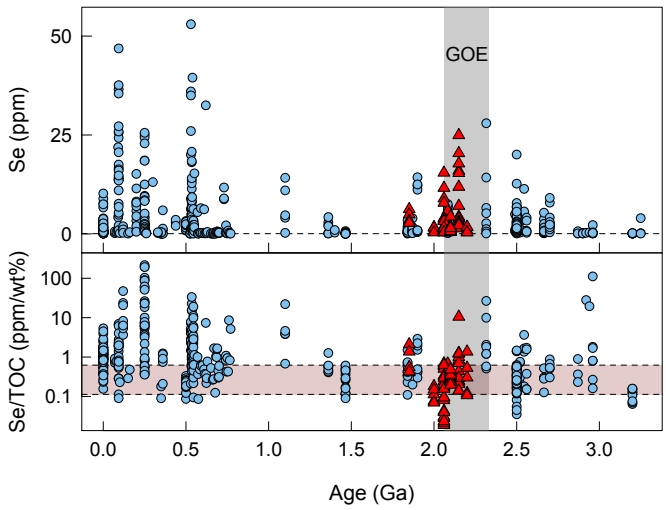

Figure 1.1: **Selenium (Se) abundance and Se/TOC (ppm/wt%) ratios in shales through geologic time (triangles – this study, circles – published data).** Dotted lines represent crustal Se abundance (top) and range of Se/TOC ratios in modern phytoplankton (Mitchell et al., 2012) (bottom).

decline between 2.1 Ga and 2.0 Ga to <<1 ppm/wt% (Figs. 1.1, 1.2). $\delta^{82/78}$Se values are consistently positive from 2.32 Ga until 2.1 Ga, and higher than in any other time in the geologic record (avg. +1.03 ± 0.67‰; Figs. 1.2, 1.3). The mean $\delta^{82/78}$Se value for samples older than 2.45 Ga is statistically indistinguishable from that for samples dating between 2.1 Ga and 1.1 Ga ($p_{\text{two-tailed}} = 0.11$), while samples with 2.32-2.1 Ga ages have significantly higher $\delta^{82/78}$Se values than both groups ($p_{\text{one-tailed}} = 10^{-10}$, 10^{-10}). Negative $\delta^{82/78}$Se values do not become prevalent until the late Neoproterozoic (von Strandmann et al., 2015), and persist throughout the Phanerozoic (Stüeken et al., 2015b) (Fig. 1.3).

1.5 Oxidative Weathering and the Marine Se Reservoir

In light of the mounting evidence for elevated atmospheric oxygen levels between 2.32 Ga and 2.06 Ga (Bekker and Holland, 2012; Hardisty et al., 2014; Partin et al., 2013; Planavsky et al., 2012; Scott et al., 2014, 2008), it is unsurprising that shales show an increase in Se

abundance at this time (Fig. 1.1). While Se can also be sourced to the marine environment by volcanism and hydrothermal activity, oxidative weathering is by far the dominant source on the modern Earth (∼90% of flux to oceans; volcanism ∼10%, hydrothermal input <<1%; (Stüeken, 2017). Furthermore, the parallel enrichment of U (Partin et al., 2013), Mo (Scott et al., 2008) and Se in samples from the Rooihoogte and Lower Timeball Hill formations and the Sengoma Argillite Formation is most parsimoniously explained by enhanced oxidative weathering. Unlike Se, U is exclusively delivered to the oceans via oxidative mobilization, and not by volcanic or hydrothermal inputs. Additionally, Mo is not volatile and thus cannot derive from volcanic sources. While it is not possible to definitively rule out a volcanic contribution to the sedimentary Se enrichment seen during the GOE, the vast majority of Se was likely delivered by oxidative continental weathering.

The trend in Se abundance does not correspond exactly with the inferred beginning and end of the GOE (Fig. 1.1). Se concentrations begin to increase in the late Archean (∼2.7 Ga), perhaps due to increasing rates of oxidative weathering in locally oxic environments on land (Stüeken et al., 2012). In the wake of the GOE, Se abundances remain higher than mid-Archean values until at least 1.9 Ga, and then return to low levels in the mid-Proterozoic. This trend could suggest that atmospheric oxygen levels (and thus oxidative weathering rates) did not experience a sharp fall at the end of the GOE. However, weathering of Se-rich sediments that were deposited during the GOE and subsequently uplifted on tectonic timescales of ∼100 Myr could have potentially contributed to the Se enrichment seen in shales deposited after ca. 2.06 Ga, leaving open the possibility that atmospheric oxygen levels did indeed decline abruptly, but Se flux decayed slowly. In either case, it would seem that the marine Se reservoir grew larger during the GOE than at any other time before the late Neoproterozoic.

Se/TOC ratios may be a more robust indicator of Se reservoir size than Se abundance, since they account for differences in primary productivity across depositional environments. Biological incorporation of Se and subsequent settling of organic material may be the dominant mechanism of Se transport to anoxic sediments; normalizing data to organic carbon

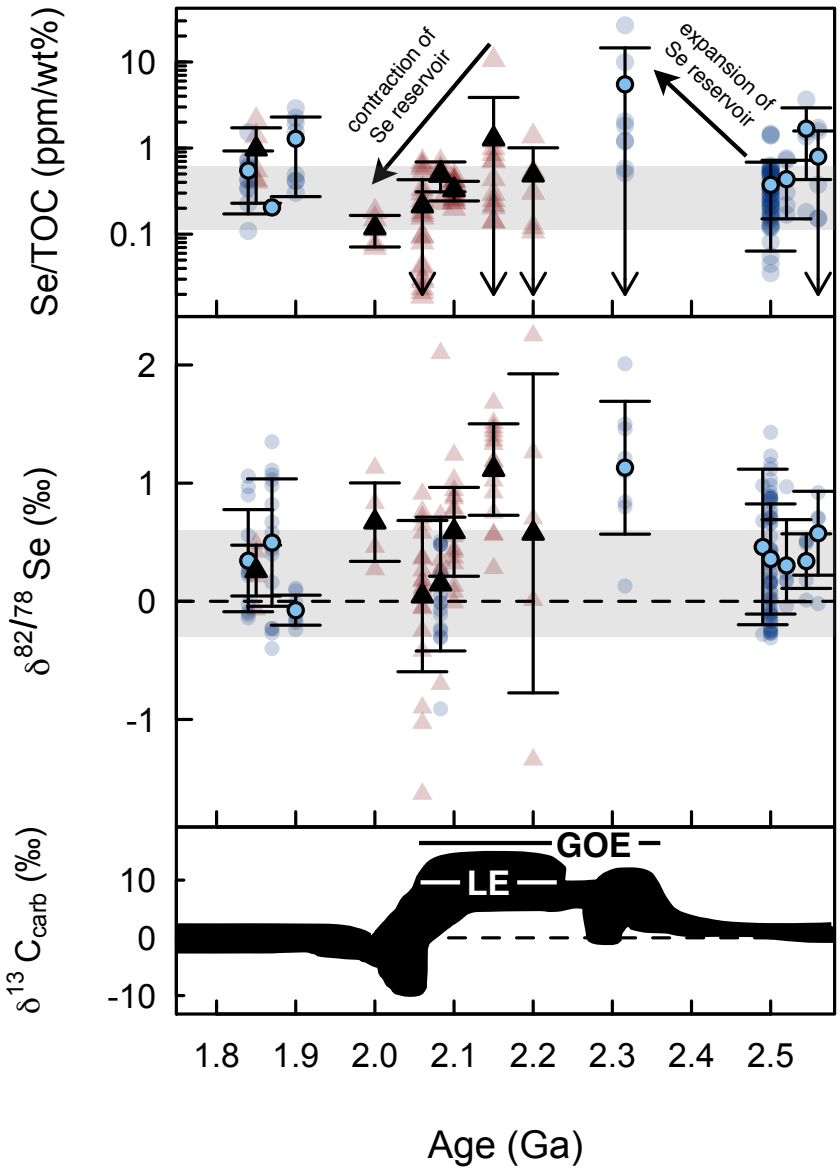

Figure 1.2: **Trends in Se/TOC, $\delta^{82/78}$Se and $\delta^{13}C_{carb}$ (triangles – this study, circles – published data).** Grey bands mark range of phytoplankton Se/TOC (top) and crustal $\delta^{82/78}$Se (middle). $\delta^{13}C_{carb}$ curve adapted from Lyons et al. (2014). Solid data points are average per formation, error bars are 1σ; shadowed data points are individual samples. Note log scale in top plot.

contents can thus gauge "Se excess" in the system. Like Se abundance, Se/TOC ratios steadily increase through the late Archean, and peak during the GOE at 2.32 Ga (max. 26.63 ppm/wt%). However, in contrast to the trend seen in Se abundance, Se/TOC ratios decline rapidly at the end of the GOE (Figs. 1.1, 1.2). This decline coincides with the falling limb of the Lomagundi carbon isotope excursion, which has been argued to record a time of rapid deoxygenation (Planavsky et al., 2012; Scott et al., 2014). The decreasing Se/TOC ratios therefore may suggest that the marine Se reservoir was in fact rapidly shrinking at the end of the GOE with the expansion of marine anoxia. Maximum enrichments greater than 10 ppm/wt% are not observed again for ∼1 Gyr after the termination of the GOE.

1.6 Ocean Redox Structure during the GOE

Shales deposited between 2.32 and 2.1 Ga show the largest and longest-lived positive Se isotope excursion seen in the geologic record (Fig. 1.3). Several processes other than oxyanion reduction are known to fractionate Se isotopes, but their fractionation factors are too small to explain the shift of $\delta^{82/78}$Se values to >+1‰ (max. +2.25‰) during the GOE. Oxidative weathering alone is unlikely to generate this magnitude of fractionation relative to crustal values since oxidation generally imparts a small (<0.5‰) fractionation (Johnson, 2004). Large fractionations associated with weathering have only been observed in unusually Se-rich soils (up to 2% Se content, Zhu et al., 2014), whereas Se-lean soils (<0.5 ppm) – more representative of average crust (<0.1 ppm) – show no significant fractionation (±0.25‰, Schilling et al., 2011). The absence of a significant fractionation during weathering is further supported by isotopic mass balance of marine sediments (Stüeken, 2017). Assimilation into biomass also causes only small fractionation (<+0.6‰, Clark and Johnson, 2010), so changes in biological utilization of Se cannot account for the large excursion. A shift in Se crustal sources cannot explain the heavy isotopic values seen between 2.32-2.1 Ga because there is little variability in the Se isotopic composition of different terrestrial reservoirs (crustal source rocks range from -0.3‰ to +0.6‰, Rouxel et al., 2002).

This leaves partial reduction of Se oxyanions as the most likely process to generate large

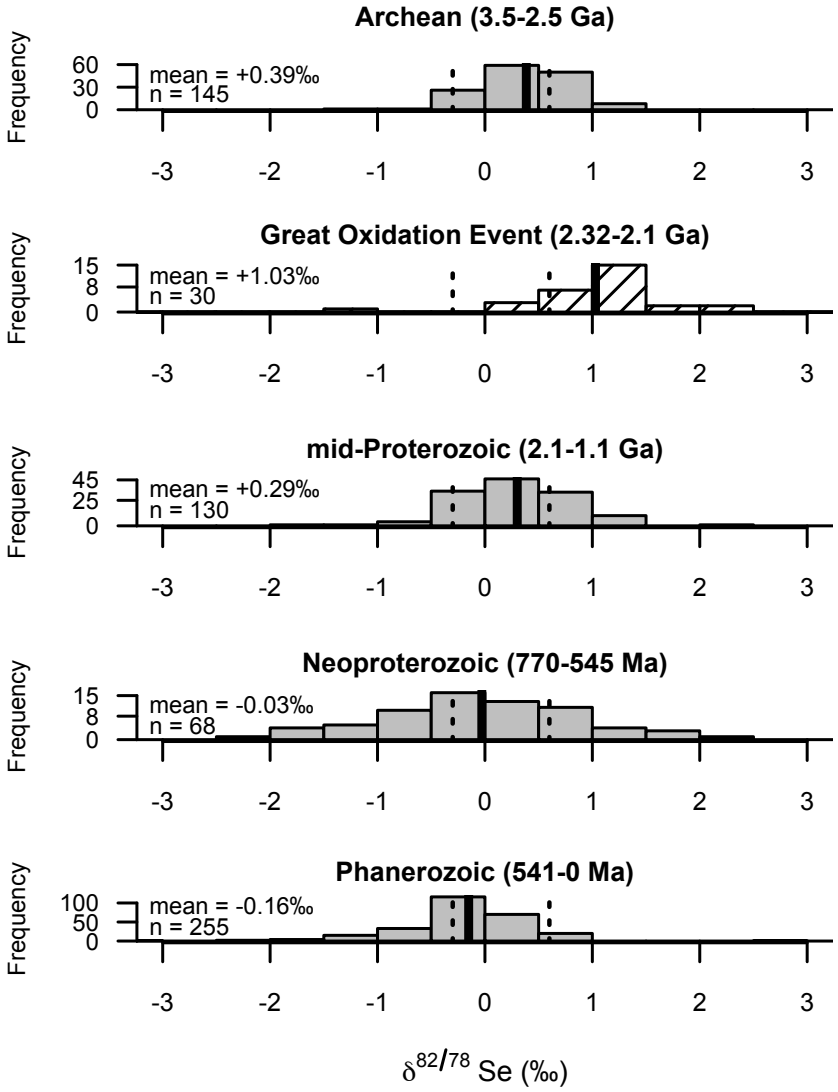

Figure 1.3: **Histogram of all published shale $\delta^{82/78}$Se values in different stages of geologic time.** Dotted lines indicate crustal $\delta^{82/78}$Se range. The interval from ca. 2.32 to 2.1 Ga marks the only time when offshore shales record persistently positive $\delta^{82/78}$Se values. Archean and mid-Proterozoic Se isotope ratios are near crustal values, while Neoproterozoic and Phanerozoic values are often negative.

(>1‰) fractionations that can be preserved in sedimentary rocks. In laboratory settings, both biotic and abiotic partial reduction generate isotopic fractionations of several permil, with lighter Se isotopes being preferentially enriched in reduced compounds (Johnson and Bullen, 2004). In bulk samples from natural settings, observed fractionations tend to be smaller (range from -2 to +2‰) perhaps because the isotopic signature of reduced Se gets diluted by co-deposition of biologically-assimilated Se in sediments (Mitchell et al., 2016). Still, dissimilatory reduction can alter the Se isotopic composition of residual oxyanions dissolved in seawater, and this has been documented in the Phanerozoic (Wen et al., 2014), Neoproterozoic (von Strandmann et al., 2015), and Archean (Stüeken et al., 2015a). In the 2.5 Ga Mt. McRae Shale, Se isotopes show a positive excursion parallel with a positive excursion in nitrogen isotopes and enrichments in redox-sensitive trace metals that have been interpreted as evidence for a transient pulse of oxygen that occurred before the onset of the GOE (Anbar et al., 2007; Garvin et al., 2009; Stüeken et al., 2015a). Stüeken et al. (Stüeken et al., 2015a) argued that this Se isotope excursion was generated in a redox-stratified water column where Se was partially reduced in shallow-marine, suboxic waters, driving the residual Se reservoir to more positive $\delta^{82/78}$Se values, which were then recorded in offshore shales. The positive $\delta^{82/78}$Se values seen during the GOE seem to indicate a similar scenario, although in this instance persisting in multiple basins on separate continents over a timescale of hundreds of millions of years.

The fact that most sedimentary Se isotope ratios in Archean and mid-Proterozoic shales do not significantly deviate from crustal values (Fig. 1.3) suggests that either Se influx was generally low or that Se oxyanions in the oceans during these intervals were quantitatively reduced and assimilated (Fig. 1.4a), allowing sediments to roughly record the isotopic composition of crustal source rocks. The observation of significantly positive $\delta^{82/78}$Se values in all analyzed offshore sediments dating within the GOE thus suggests an extreme isotopic distillation of an expanded marine Se reservoir at this time. In order to generate such a large isotopic excursion, there were likely extensive near-shore suboxic environments where Se oxyanions were constantly re-supplied, allowing substantial non-quantitative reduction to

occur in the water column. This would sequester isotopically light Se in near-shore sediments that were not sampled in this study, perhaps with the exception of the Wewe Slate (see below) (Fig. 1.4b). The residual Se reservoir would thus have been driven isotopically heavy. These heavy values could then have been recorded in the offshore environments sampled in this study either by quantitative or non-quantitative reduction and/or biological assimilation, depending on the extent of suboxia on the outer shelf.

This stands in contrast to the modern ocean, which receives a large flux of Se oxyanions but generates only small isotopic fractionations (Fig. 1.4c). Suboxic waters are scarce in the fully oxygenated modern oceans (<10% of ocean area; Paulmier and Ruiz-Pino, 2009) and diagenetic Se reduction in sediments seems to produce relatively small fractionations, perhaps because supply of Se oxyanions is diffusion-limited in pore waters. Thus, the magnitude of the positive $\delta^{82/78}$Se excursion seen in shales deposited during the GOE suggests that suboxia was a widespread and persistent feature along continental margins during this interval.

The lack of negative $\delta^{82/78}$Se values in offshore sediments deposited during the GOE also suggests that – unlike in the late Neoproterozoic and Phanerozoic – there was not any re-supply of Se oxyanions from an oxic deep-ocean reservoir. This is consistent with previous work that has suggested the deep ocean remained anoxic throughout the GOE (Bekker et al., 2008). So while the Se data alone remain somewhat ambiguous as to the precise redox state of the sampled offshore depositional environments, they can be used to confidently infer the persistence of widespread near-shore suboxia, and predominantly anoxic conditions in the deep ocean.

An isotopic record of Se in near-shore sediments that preserve the complementary negative $\delta^{82/78}$Se values and were deposited coevally with the shales bearing the positive $\delta^{82/78}$Se excursion would provide a test of this hypothesis. However, given current sensitivity limits for Se isotope analysis, this remains a challenging prospect. Se concentrations in carbonates, sandstones, and low-TOC shales associated with near-shore depositional environments are orders of magnitude less than in offshore organic-rich shales, requiring unfeasibly large sample sizes in order to obtain accurate measurements. Further methodological refinement

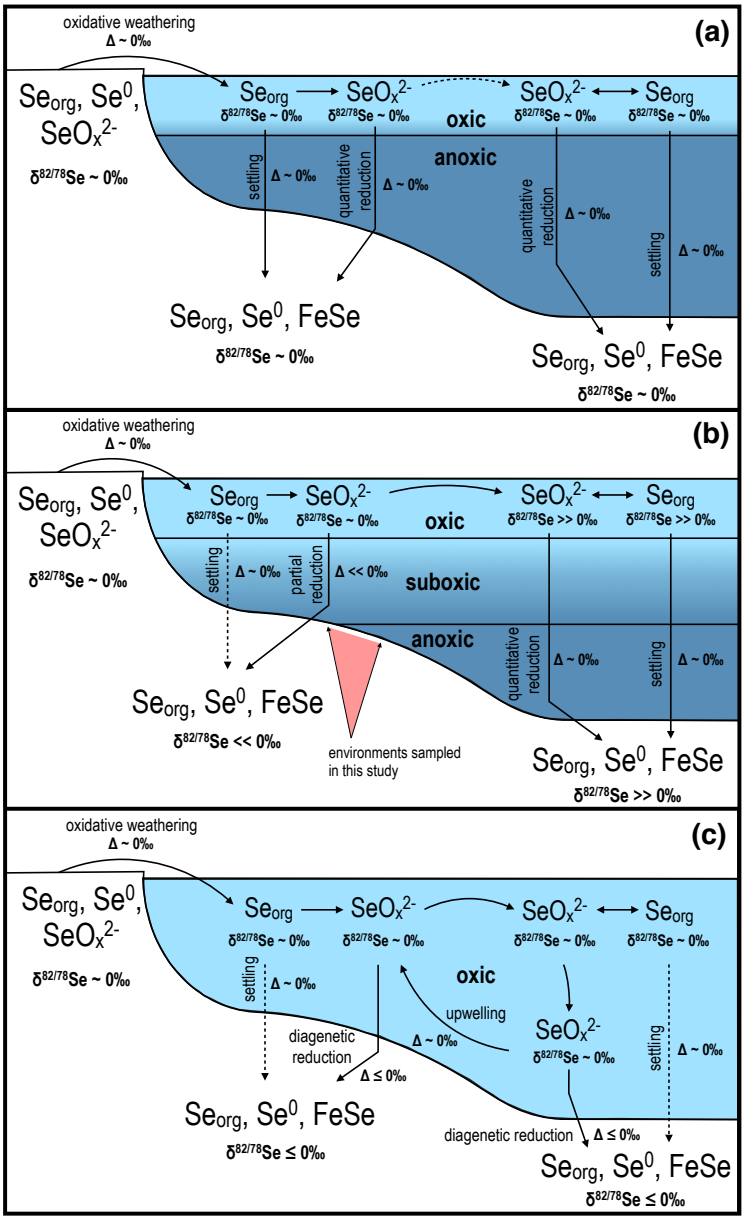

Figure 1.4: **Sketch of the selenium cycle during (a) the late Archean and mid-Proterozoic, (b) the Great Oxidation Event, and (c) the late Neoproterozoic and Phanerozoic.** "$\delta^{82/78}$Se" refers to the isotope ratio of a designated reservoir; "Δ" refers to the isotopic fractionation associated with a designated process. Dotted arrows for Se_{org} burial in oxic/suboxic environments signify that this process has minor significance, but in some cases may dilute sedimentary Se isotope signatures (Mitchell et al., 2016). See text for further discussion.

may eventually enable analysis of such materials.

Still, there is some evidence for a complementary light Se reservoir in shallow-water environments during the GOE. The Wewe Slate (ca. 2.2-2.1 Ga) displays by far the largest range of $\delta^{82/78}$Se values in our dataset (-1.34 to +2.25‰). We suspect that this is because this unit is capturing the seawater Se composition near the environmental gradient for Se reduction. The Wewe Slate is underlain by mature quartz sandstones and stromatolitic dolostones (Bekker et al., 2006) and has relatively low TSe and TOC contents (Fig. 1.1; Appendix A), all consistent with a near-shore depositional environment, in contrast to the TSe- and TOC-rich shales from other units included in this dataset. Since there is no noticeable stratigraphic trend in Se isotopes or abundance through the Wewe Slate (Appendix A), it is unlikely that the range of values reflects secular change in the depositional environment. We cannot rule out the possibility that the Wewe Slate is capturing transient deep-ocean oxygenation in the midst of the GOE, but the sedimentologic context is consistent with deposition of the Wewe Slate in a setting that straddled a chemocline with fluctuating depth, thus sampling both the shallow and deep Se reservoirs.

At the end of the GOE (2.1-2.0 Ga), $\delta^{82/78}$Se values sharply return to crustal values (Fig. 1.2), consistent with rapid deoxygenation of the ocean (Scott et al., 2014). The occurrence of some negative $\delta^{82/78}$Se values in the Zaonega and Francevillian formations may result from the weathering of isotopically light Se that was deposited in shallow settings during the GOE, and subsequently uplifted and eroded on tectonic timescales of ∼100 Myr. However, we cannot definitively rule out the possibility that these data represent a pulse of oxygenation at the culmination of the GOE (Kump et al., 2011). In either case, the longer-term trend reveals an ultimate return to widespread anoxia. Even if Se influx to the ocean decayed gradually as Se-rich sediments deposited during the GOE were weathered, a contraction of suboxic water masses and takeover by anoxic and strongly euxinic conditions could have rapidly pushed the system toward quantitative reduction of Se oxyanions, thus ending the Se isotopic excursion seen during the GOE. Contraction of the marine Se reservoir during deoxygenation would further accelerate the loss of isotopic fractionation, since a smaller Se

reservoir could be quantitatively reduced more easily.

1.7 How Oxic were Near-shore Environments during the GOE?

These data can be used to provide an approximate lower limit on shallow-marine oxygen levels across the GOE. Specifically, when used in conjunction with the iodine record, the Se data point to the presence of conditions that were at least suboxic. In the modern ocean, quantitative reduction of iodate (IO_3^-) to iodide (I^-) has been observed at dissolved O_2 concentrations less than ∼5 µM (Rue et al., 1997). In the same study, Se oxyanion reduction was non-quantitative at oxygen concentrations down to ∼1 µM O_2. Another investigation of Se speciation in the anoxic Saanich Inlet found that Se oxyanions became depleted to below the detection limit at <0.4 µM O_2 (Cutter, 1982). Within this framework, the occurrence of positive $\delta^{82/78}$Se values across the GOE implies a conservative lower limit for shallow-water oxygen concentrations of >0.4 µM O_2. In reality, it is likely that O_2 concentrations were higher in these settings, since reduction of Se oxyanions in near-shore environments was evidently far from being quantitative. High I/(Ca+Mg) ratios in LE-aged carbonates (Hardisty et al., 2014) may push the lower limit for surface ocean oxygen up to ∼5 µM O_2 for the later stage of the GOE. This would still only be a small fraction of the modern surface ocean oxygen concentration of ∼325 µM O_2, but it could have had important evolutionary implications.

1.8 Implications for Biological Evolution

Whether or not oxygen availability was the primary control on the evolution of deeply rooted eukaryotes remains a highly contentious issue. Recent evidence for extremely low mid-Proterozoic oxygen levels (Planavsky et al., 2014) has hinted that low oxygen indeed inhibited the diversification of multicellular, aerobically-respiring organisms until the late Neoproterozoic (see Zhang et al., (2016) for an alternative view). However, the recognition of oxygen-rich conditions in the early Paleoproterozoic opens up the possibility that there was a relatively long (∼200 Myr) interval that may have been favorable for the evolution of

complex life forms long before the fossil record indicates their rise to ecological importance (Knoll, 2011; Narbonne, 2005).

Convincing fossil evidence of multicellular eukaryotic life is hard to come by in the Proterozoic, but there are numerous reports of fossils with eukaryotic affinity that span nearly the entire temporal extent of the Proterozoic (Walter et al., 1976; Sharma and Shukla, 2009; Zhu et al., 2016). These include centimeter-scale structures in the ca. 2.1 Ga Francevillian Series of Gabon that have been interpreted as populations of multicellular organisms (El Albani et al., 2010). While such reports remain controversial, a better understanding of the redox architecture of the contemporary oceans would greatly aid our interpretation of the possible affinities of these ambiguous fossilized life forms.

The observed lower limit for survival of aerobically-respiring benthic animals is $\sim$0.88 µM O_2 (Levin et al., 2002; Breuer et al., 2009), and theoretical considerations suggest that the actual limit is even lower (Sperling et al., 2013). For steroid synthesis in unicellular eukaryotes, a lower limit of 7 nM O_2 has been inferred (Waldbauer et al., 2011) and aerobic respiration in bacteria continues down to 3 nM (Stolper et al., 2010). The lower limit proposed here of $>$0.4 µM O_2 in near-shore environments during the GOE therefore suggests that O_2 levels were high enough for the existence of eukaryotic organisms in multiple basins over a long period of time. However, these limits are very close to the metazoan O_2 threshold and so it is quite possible (and perhaps likely) that the evolution of motile, multicellular eukaryotes was hindered by redox instability at this time (Reinhard et al., 2016; Johnston et al., 2012). Nonetheless, the existing data allow the possibility that the early phases of unicellular eukaryotic evolution could have been underway in the early Paleoproterozoic. Subsequently lowered oxygen levels may have delayed the eukaryotic rise to ecological abundance for more than a billion years. Without a more complete fossil record it is all but impossible to test whether this was indeed the case. Nevertheless, during the GOE the redox restriction on microbial aerobic metabolism could have been lifted over wide areas of the continental shelves for the first time in Earth's history.

1.9 Conclusions

An increase in the abundance of Se in organic-rich shales deposited during the GOE is consistent with enhanced oxidative continental weathering at this time, and corroborates evidence from other redox-sensitive proxies (S, Mo, and U). A shift to the most positive offshore $\delta^{82/78}$Se values in geologic history suggests that extensive partial reduction of Se oxyanions in shallow, suboxic seawater drove the isotopic composition of residual oceanic Se heavier. Shallow-marine sediments thus acted as a sink for isotopically light Se, perhaps recorded by the negative $\delta^{82/78}$Se ratios found in the Wewe Slate. This state of enhanced oxidative continental weathering and extensive shallow-ocean suboxia appears to have prevailed until near the end of the GOE, when plummeting Se/TOC ratios and $\delta^{82/78}$Se values suggest that the marine Se reservoir rapidly diminished and suboxic water masses contracted at the expense of anoxic and, possibly, strongly euxinic waters. Thus, the period from ca. 2.32 to 2.1 Ga was the first interval in Earth's history when conditions that were at least suboxic persisted on continental margins on geological timescales, perhaps supporting the early evolution of aerobically-respiring life forms. The contraction of oxic and suboxic environments after the GOE may have limited the available habitats for the evolutionary radiation of eukaryotic life until the second rise of oxygen in the late Neoproterozoic.

1.10 Methods

Samples were prepared and analyzed following Stüeken et al. (2013). Rock powders were dissolved using HF, HNO_3 and $HClO_4$, and Se was isolated using thiol-cotton fiber columns. All analyses were conducted on a hydride-generator multi-collector inductively coupled plasma mass-spectrometer (Nu Instruments). Measurements were normalized using standard-sample bracketing. We note that both $\delta^{82/76}$Se and $\delta^{82/78}$Se notations are used in the literature; our data are expressed as $\delta^{82/78}$Se relative to National Institute of Standards and Technology (NIST, USA) reference SRM 3149 because, using our isotopic measurement method, mass 78 is much less affected by isobaric interferences than mass 76 (Stüeken et al. 2013). Average

precision (1σ) for samples was 0.07‰ for $\delta^{82/78}$Se values and 0.02 ppm for Se concentrations. $\delta^{82/78}$Se values for international reference material SGR-1 and in-house standard UW-McRae were $+0.12 \pm 0.18$‰ (1σ, $n = 5$) and $+0.85 \pm 0.18$‰ (1σ, $n = 27$), respectively, which agree well with published values (Mitchell et al., 2012; Stüeken et al., 2015b). TOC analysis followed Stüeken (2013). Carbonate was removed from rock powders via acidification with HCl. Decarbonated powders were analyzed on a Costech ECS 4010 Elemental Analyzer coupled to a continuous flow isotope-ratio mass-spectrometer (Finnigan MAT253) via a ThermoFinnigan Conflo III. Average precision for TOC measurements was 0.17% (1σ, $n = 49$).

1.11 References

Anbar, A.D., Duan, Y., Lyons, T.W., Arnold, G.L., Kendall, B., Creaser, R.A., Kaufman, A.J., Gordon, G.W., Scott, C., Garvin, J., Buick, R., 2007. A whiff of oxygen before the Great Oxidation Event? *Science* 317, 1903–1906.

Bekker, A., 2014. Lomagundi Carbon Isotope Excursion. *Encycl. Astrobiol.*

Bekker, A., Holland, H.D., 2012. Oxygen overshoot and recovery during the early Paleoproterozoic. *Earth Planet. Sci. Lett.* 317, 295–304.

Bekker, A., Holland, H.D., Wang, P.-L., Rumble, D., Stein, H.J., Hannah, J.L., Coetzee, L.L., Beukes, N.J., 2004. Dating the rise of atmospheric oxygen. *Nature* 427, 117–120.

Bekker, A., Holmden, C., Beukes, N.J., Kenig, F., Eglinton, B., Patterson, W.P., 2008. Fractionation between inorganic and organic carbon during the Lomagundi (2.22–2.1 Ga) carbon isotope excursion. *Earth Planet. Sci. Lett.* 271, 278–291.

Bekker, A., Karhu, J.A., Kaufman, A.J., 2006. Carbon isotope record for the onset of the Lomagundi carbon isotope excursion in the Great Lakes area, North America. *Precambrian Res.* 148, 145–180.

Breuer, E.R., Law, G.T., Woulds, C., Cowie, G.L., Shimmield, G.B., Peppe, O., Schwartz, M., McKinlay, S., 2009. Sedimentary oxygen consumption and microdistribution at sites across the Arabian Sea oxygen minimum zone (Pakistan margin). *Deep Sea Res. Part II Top. Stud. Oceanogr.* 56, 296–304.

Canfield, D.E., Ngombi-Pemba, L., Hammarlund, E.U., Bengtson, S., Chaussidon, M., Gauthier-Lafaye, F., Meunier, A., Riboulleau, A., Rollion-Bard, C., Rouxel, O., Asael, D., Pierson-Wickmann, A.-C., Albani, A.E., 2013. Oxygen dynamics in the aftermath of the Great Oxidation of Earth's atmosphere. *Proc. Natl. Acad. Sci.* 110, 16736–16741.

Clark, S.K., Johnson, T.M., 2010. Selenium stable isotope investigation into selenium biogeochemical cycling in a lacustrine environment: Sweitzer Lake, *Colorado. J. Environ. Qual.* 39, 2200–2210.

Cloud, P.E., 1968. Atmospheric and hydrospheric evolution on the primitive Earth. *Science* 160, 729–736.

Cutter, G.A., 1982. Selenium in reducing waters. *Science* 217, 829–831.

El Albani, A., Bengtson, S., Canfield, D.E., Bekker, A., Macchiarelli, R., Mazurier, A., Hammarlund, E.U., Boulvais, P., Dupuy, J.-J., Fontaine, C., Fürsich, F.T., Gauthier-Lafaye, F., Janvier, P., Javaux, E., Ossa, F.O., Pierson-Wickmann, A.-C., Riboulleau, A., Sardini, P., Vachard, D., Whitehouse, M., Meunier, A., 2010. Large colonial organisms with coordinated growth in oxygenated environments 2.1 Gyr ago. *Nature* 466, 100-104.

Farquhar, J., Bao, H.M., Thiemens, M., 2000. Atmospheric influence of Earth's earliest sulfur cycle. *Science* 289, 756–758.

Garvin, J., Buick, R., Anbar, A.D., Arnold, G.L., Kaufman, A.J., 2009. Isotopic evidence for an aerobic nitrogen cycle in the latest Archean. *Science* 323, 1045–1048.

Hardisty, D.S., Lu, Z., Planavsky, N.J., Bekker, A., Philippot, P., Zhou, X., Lyons, T.W., 2014. An iodine record of Paleoproterozoic surface ocean oxygenation. *Geology* 42, 619–622.

Holland, H.D., 1984. The chemical evolution of the atmosphere and oceans. Princeton University Press.

Johnson, T.M., 2004. A review of mass-dependent fractionation of selenium isotopes and implications for other heavy stable isotopes. *Chem. Geol.* 204, 201–214.

Johnson, T.M., Bullen, T.D., 2004. Mass-dependent fractionation of selenium and chromium isotopes in low-temperature environments. *Rev. Mineral. Geochem.* 55, 289–317.

Johnston, D.T., Poulton, S.W., Goldberg, T., Sergeev, V.N., Podkovyrov, V., Vorob'eva, N.G., Bekker, A., Knoll, A.H., 2012. Late Ediacaran redox stability and metazoan evolution. *Earth Planet. Sci. Lett.* 335, 25–35.

Karhu, J.A., Holland, H.D., 1996. Carbon isotopes and the rise of atmospheric oxygen. *Geology* 24, 867–870.

Knoll, A.H., 2011. The multiple origins of complex multicellularity. *Annu. Rev. Earth Planet. Sci.* 39, 217–239.

Kump, L.R., Junium, C., Arthur, M.A., Brasier, A., Fallick, A., Melezhik, V., Lepland, A., CČrne, A.E., Luo, G., 2011. Isotopic Evidence for Massive Oxidation of Organic Matter Following the Great Oxidation Event. *Science* 334, 1694–1696.

Levin, L., Gutiérrez, D., Rathburn, A., Neira, C., Sellanes, J., Munoz, P., Gallardo, V., Salamanca, M., 2002. Benthic processes on the Peru margin: a transect across the oxygen minimum zone during the 1997–98 El Niño. *Prog. Oceanogr.* 53, 1–27.

Luo, G., Ono, S., Beukes, N.J., Wang, D.T., Xie, S., Summons, R.E., 2016. Rapid oxygenation of Earth's atmosphere 2.33 billion years ago. *Sci. Adv.* 2, e1600134.

Lyons, T.W., Reinhard, C.T., Planavsky, N.J., 2014. The rise of oxygen in Earth's early ocean and atmosphere. *Nature* 506, 307–315.

Mitchell, K., Mansoor, S.Z., Mason, P.R.D., Johnson, T.M., Van Cappellen, P., 2016. Geological evolution of the marine selenium cycle: Insights from the bulk shale δ82/76Se record and isotope mass balance modeling. *Earth Planet. Sci. Lett.* 441, 178–187.

Mitchell, K., Mason, P.R., Van Cappellen, P., Johnson, T.M., Gill, B.C., Owens, J.D., Diaz, J., Ingall, E.D., Reichart, G.-J., Lyons, T.W., 2012. Selenium as paleo-oceanographic proxy: A first assessment. *Geochim. Cosmochim. Acta* 89, 302–317.

Narbonne, G.M., 2005. The ediacarabiota: Neoproterozoic origin of animals and their ecosystems. *Annu. Rev. Earth Planet. Sci.* 33, 421–442.

Partin, C.A., Bekker, A., Planavsky, N.J., Scott, C.T., Gill, B.C., Li, C., Podkovyrov, V., Maslov, A., Konhauser, K.O., Lalonde, S.V., Love, G.D., Poulton, S.W., Lyons, T.W., 2013. Large-scale fluctuations in Precambrian atmospheric and oceanic oxygen levels

from the record of U in shales. *Earth Planet. Sci. Lett.* 369, 284–293.

Paulmier, A., Ruiz-Pino, D., 2009. Oxygen minimum zones (OMZs) in the modern ocean. *Prog. Oceanogr.* 80, 113–128.

Pavlov, A.A., Kasting, J.F., 2002. Mass-independent fractionation of sulfur isotopes in Archean sediments: Strong evidence for an anoxic Archean atmosphere. *Astrobiology* 2, 27–41.

Planavsky, N.J., Bekker, A., Hofmann, A., Owens, J.D., Lyons, T.W., 2012. Sulfur record of rising and falling marine oxygen and sulfate levels during the Lomagundi event. *Proc. Natl. Acad. Sci.* 109, 18300–18305.

Planavsky, N.J., Reinhard, C.T., Wang, X., Thomson, D., McGoldrick, P., Rainbird, R.H., Johnson, T., Fischer, W.W., Lyons, T.W., 2014. Low Mid-Proterozoic atmospheric oxygen levels and the delayed rise of animals. *Science* 346, 635–638.

Rasmussen, B., Buick, R., 1999. Redox state of the Archean atmosphere: evidence from detrital heavy minerals in ca. 3250–2750 Ma sandstones from the Pilbara Craton, Australia. *Geology* 27, 115–118.

Reinhard, C.T., Planavsky, N.J., Olson, S.L., Lyons, T.W., Erwin, D.H., 2016. Earth's oxygen cycle and the evolution of animal life. *Proc. Natl. Acad. Sci.* 201521544.

Rouxel, O., Ludden, J., Carignan, J., Marin, L., Fouquet, Y., 2002. Natural variations of Se isotopic composition determined by hydride generation multiple collector inductively coupled plasma mass spectrometry. *Geochim. Cosmochim. Acta* 66, 3191–3199.

Rue, E.L., Smith, G.J., Cutter, G.A., Bruland, K.W., 1997. The response of trace element redox couples to suboxic conditions in the water column. *Deep Sea Res. Part Oceanogr. Res. Pap.* 44, 113–134.

Schidlowski, M., Trurnit, P., 1966. Drucklösungserscheinungen an Geröllpyriten aus den Witwatersrand-Konglomeraten. Ein Beitrag zur Frage des diagenetischen Verhaltens von Sulfiden. *Schweiz Miner. Petrog Mitt* 46, 332–342.

Schilling, K., Johnson, T.M., Wilcke, W., 2011. Selenium partitioning and stable isotope ratios in urban topsoils. *Soil Sci. Soc. Am. J.* 75, 1354–1364.

Schröder, S., Bekker, A., Beukes, N.J., Strauss, H., Van Niekerk, H.S., 2008. Rise in seawater sulphate concentration associated with the Paleoproterozoic positive carbon isotope excursion: evidence from sulphate evaporites in the 2.2–2.1 Gyr shallow-marine Lucknow Formation, South Africa. *Terra Nova* 20, 108–117.

Scott, C., Lyons, T.W., Bekker, A., Shen, Y., Poulton, S.W., Chu, X., Anbar, A.D., 2008. Tracing the stepwise oxygenation of the Proterozoic ocean. *Nature* 452, 456-U5.

Scott, C., Wing, B.A., Bekker, A., Planavsky, N.J., Medvedev, P., Bates, S.M., Yun, M., Lyons, T.W., 2014. Pyrite multiple-sulfur isotope evidence for rapid expansion and contraction of the early Paleoproterozoic seawater sulfate reservoir. *Earth Planet. Sci. Lett.* 389, 95–104.

Sharma, M., Shukla, Y., 2009. Taxonomy and affinity of Early Mesoproterozoic megascopic helically coiled and related fossils from the Rohtas Formation, the Vindhyan Supergroup, India. *Precambrian Res.* 173, 105–122.

Sperling, E.A., Halverson, G.P., Knoll, A.H., Macdonald, F.A., Johnston, D.T., 2013. A basin redox transect at the dawn of animal life. *Earth Planet. Sci. Lett.* 371, 143–155.

Stolper, D.A., Revsbech, N.P., Canfield, D.E., 2010. Aerobic growth at nanomolar oxygen concentrations. *Proc. Natl. Acad. Sci.* 107, 18755–18760.

Stüeken, E.E., 2013. A test of the nitrogen-limitation hypothesis for retarded eukaryote radiation: Nitrogen isotopes across a Mesoproterozoic basinal profile. *Geochim. Cosmochim. Acta* 120, 121–139.

Stüeken, E.E.,2017. Selenium isotopes as a biogeochemical proxy. *Rev. Mineral. Geochem.*

Stüeken, E.E., Buick, R., Anbar, A.D., 2015a. Selenium isotopes support free O_2 in the latest Archean. *Geology* 43, 259–262.

Stüeken, E.E., Buick, R., Bekker, A., Catling, D., Foriel, J., Guy, B.M., Kah, L.C., Machel, H.G., Montañez, I.P., Poulton, S.W., 2015b. The evolution of the global selenium cycle: Secular trends in Se isotopes and abundances. *Geochim. Cosmochim. Acta* 162, 109–125.

Stüeken, E.E., Catling, D.C., Buick, R., 2012. Contributions to late Archaean sulphur

cycling by life on land. *Nat. Geosci.* 5, 722–725.

Stüeken, E.E., Foriel, J., Nelson, B.K., Buick, R., Catling, D.C., 2013. Selenium isotope analysis of organic-rich shales: advances in sample preparation and isobaric interference correction. *J. Anal. At. Spectrom.* 28, 1734–1749.

von Strandmann, P.A.P., Stüeken, E.E., Elliott, T., Poulton, S.W., Dehler, C.M., Canfield, D.E., Catling, D.C., 2015. Selenium isotope evidence for progressive oxidation of the Neoproterozoic biosphere. *Nat. Commun.* 6.

Waldbauer, J.R., Newman, D.K., Summons, R.E., 2011. Microaerobic steroid biosynthesis and the molecular fossil record of Archean life. *Proc. Natl. Acad. Sci.* 108, 13409–13414.

Walter, M.R., Oehler, J.H., Oehler, D.Z., 1976. Megascopic algae 1300 million years old from the Belt Supergroup, Montana: a reinterpretation of Walcott's Helminthoidichnites. *J. Paleontol.* 872–881.

Wen, H., Carignan, J., Chu, X., Fan, H., Cloquet, C., Huang, J., Zhang, Y., Chang, H., 2014. Selenium isotopes trace anoxic and ferruginous seawater conditions in the Early Cambrian. *Chem. Geol.* 390, 164–172.

Zhang, S., Wang, X., Wang, H., Bjerrum, C.J., Hammarlund, E.U., Costa, M.M., Connelly, J.N., Zhang, B., Su, J., Canfield, D.E., 2016. Sufficient oxygen for animal respiration 1,400 million years ago. *Proc. Natl. Acad. Sci.* 201523449.

Zhu, J.-M., Johnson, T.M., Clark, S.K., Zhu, X.-K., Wang, X.-L., 2014. Selenium redox cycling during weathering of Se-rich shales: A selenium isotope study. *Geochim. Cosmochim. Acta* 126, 228–249.

Zhu, S., Zhu, M., Knoll, A.H., Yin, Z., Zhao, F., Sun, S., Qu, Y., Shi, M., Liu, H., 2016. Decimetre-scale multicellular eukaryotes from the 1.56-billion-year-old Gaoyuzhuang Formation in North China. *Nat. Commun.* 7.

Chapter 2

REDOX FLUCTUATIONS, TRACE METAL ENRICHMENT & PHOSPHOGENESIS IN THE ∼2.0 GA ZAONEGA FORMATION, RUSSIA

This manuscript is prepared for submission to *Precambrian Research*. Co-authors are Aivo Lepland and Roger Buick.

2.1 Abstract

The ∼2.0 Ga Zaonega Formation (ZF) holds one of the oldest phosphoritic shales in the geologic record, reaching >15% P_2O_5. Understanding the depositional conditions that enabled phosphorus enrichment in this unit will thus help us to interpret the significance of the temporal distribution of phosphorites in Earth's early history. Here we use an array of major and trace element data to constrain the redox conditions in the water column and extent of basinal restriction during deposition of the ZF. We also present new selenium (Se) abundance and isotopic data to provide firmer constraints on fluctuations across high redox potentials, which might be critical for phosphogenesis. We find that Se isotope ratios shift over a range of ∼3‰ in the ZF, with the earliest stratigraphically-resolved negative Se isotope excursion in the geologic record, implying at least temporarily suboxic waters in the basin. Furthermore, we find that extreme trace metal enrichments coincide with episodes of P enrichment, thereby implicating a common set of environmental controls on these processes. Together, our dataset implies deposition under a predominantly anoxic water column with periodic fluctuations to more oxidizing conditions via connection to a large oxic reservoir containing Se oxyanions (and other oxidized species), which was likely supplied from the open ocean. This is broadly consistent with the depositional setting of many modern and recent phos-

phorites, thereby tying these ancient deposits to a common depositional mechanism. Viewed through the lens of these data, the brief period of phosphogenesis in the Paleoproterozoic may therefore record a time when moderately oxic waters persisted on continental shelves, enabling phosphogenesis in basins with high rates of export production. This also suggests that the dominant control on the degree of P enrichment in marginal, marine siliciclastic sedimentary rocks is not dissolved P levels in the deep ocean, but rather redox conditions in the depositional environment.

2.2 Introduction

Phosphorus (P) is an essential macronutrient and its availability in seawater is thought to exert the dominant control on the rate of marine primary productivity over long (10^6-10^9 yr) timescales (Broecker and Peng, 1982; Tyrrell, 1999). Reconstructing marine P levels across Earth's history is thus a major focus of paleo-biogeochemical research, since it may enable an assessment of marine primary productivity in Earth's distant past. To date, several studies have analyzed the P content of ancient marine sedimentary rocks (Bjerrum and Canfield, 2002; Planavsky et al., 2010; Reinhard et al., 2017) and offered quantitative interpretations of the paleo-concentration of P in seawater (Bjerrum and Canfield, 2002; Jones et al., 2015; Konhauser et al., 2007). However, there remains some disagreement as to whether P was scarce or abundant in the Precambrian ocean (Poulton, 2017), and moreover it is even unclear what mechanism exerted the dominant control on marine P levels in Earth's early history (Kipp and Stüeken, 2017; Reinhard et al., 2017). One thing is clear, though: all of this work would benefit from an improved understanding of the mechanisms controlling P enrichment in ancient marine sedimentary rocks.

To understand ancient sedimentary P enrichment, we must first consider the P cycle in the modern ocean. As an essential and rate-limiting nutrient, P is efficiently scavenged in surface waters by phytoplankton (reviewed in Benitez-Nelson, 2000). While the dominant supply of P to the ocean is the riverine input of continentally-derived material (Meybeck, 1982), the recycling of P within the modern ocean proceeds 2-3 orders of magnitude more

rapidly (Schlesinger and Bernhardt, 2013), thereby extending the marine residence time of P and enabling high rates of primary productivity. The small proportion of P that escapes this recycling process (associated with organic matter exported from the photic zone) is transported to deep waters, and ultimately marine sediments.

Upon reaching marine sediments, P can be buried through multiple pathways. The first is that P can be retained in organic matter if the organic matter escapes remineralization. The second is that, if the organic-bound P is liberated during the oxidation of biomass, P can become sequestered in an inorganic mineral phase. One route for this mineral-trapping of P is the adsorption of P (as orthophosphate, PO_4^{3-}) onto iron (Fe) minerals (Berner, 1973). In the modern, oxygenated ocean, this is typically dominated by Fe-(oxyhydr)oxides (*e.g.*, ferrihydrite; Berner, 1973; Feely et al., 1998). However, reduced or mixed-valence Fe minerals can also bind anions (Zegeye et al., 2012), including phosphate (Hansen and Poulsen, 1999), and so it is thought that these phases could also have scavenged P in the anoxic Precambrian ocean (Derry, 2015; Halevy et al., 2017). Importantly, all these minerals can trap liberated P – either in the water column or sediment porewaters – and immobilize it in sediments. However, if porewater chemistry shifts toward a regime that favors the dissolution of these Fe minerals, P will be released back into porewaters. Thus, on diagenetic timescales, P in modern marine sediments typically undergoes a "sink switch" where liberated P precipitates as an authigenic apatite mineral phase (predominantly carbonate fluorapatite, CFA), with a smaller amount being incorporated in secondary Fe-(oxyhydr)oxide phases (Poulton and Canfield, 2006; Slomp et al., 1996). The supply of this liberated P in sediment porewaters derives from the remineralization of biomass as well as the dissolution of adsorbed P phases (Ruttenberg and Berner, 1993). So, in sum, phosphorus buried in ancient marine sedimentary rocks is predominantly found in the authigenic (apatite) phase, with lesser amounts bound to organic matter or diagenetically-stable Fe minerals (Ruttenberg, 2003).

Despite the many routes for P burial in marine environments, most modern marine sediments have fairly low (<0.3 wt. % P_2O_5) P contents (Ruttenberg, 2003). This is a testament to the low abundance of P relative to carbon in phytoplankton biomass (*i.e.*,

the Redfield ratio, 106 C: 1 P; Redfield, 1958) as well as the selective removal of P from biomass during remineralization (Clark et al., 1998). These processes thus conspire to make P enrichment a rarity in marine sediments. The few modern environments that do promote higher P concentrations (>1 wt. % P_2O_5) tend to favor authigenic precipitation of CFA through a combination of factors (reviewed in Filippelli, 2011; Föllmi, 1996; Ruttenberg, 2003), including (i) high rates of export production (*i.e.*, a large organic-bound P flux to sediments), (ii) high sedimentation rates, which can facilitate burial of organic matter and associated P (Föllmi, 1996; Ingall and Van Cappellen, 1990), and (iii) bottom-water redox conditions that are amenable to CFA precipitation (Jahnke, 1984). In the modern ocean, such conditions tend to be found under regions of nutrient upwelling and high productivity (*e.g.*, the Peru margin, Burnett, 1977; Namibian shelf, Price and Calvert, 1978).

Based on this understanding of P enrichment in modern marine sediments, an empirical record of P concentrations in ancient marine sediments spanning Earth's history should be able to inform the secular evolution of one or more of the processes controlling P enrichment. Specifically, by tracking the magnitude of P burial through time, we should be able to make inferences about the rate of P export to sediments and prevalence of authigenic P precipitation in ancient marine sediments. Such a record was recently compiled by Reinhard et al. (2017), who showed that the P content of marginal, marine siliciclastic sedimentary rocks was in fact lower in the Precambrian than in the Phanerozoic by a factor of ∼4. These authors surmised that the lower P concentrations (and higher C:P ratios) were a result of limited P export to sediments in a low-productivity ocean, which thereby muted the precipitation of authigenic apatite.

While this record clearly demonstrates a shift in the marine P cycle near the end of the Precambrian, some important questions remain. First, the compilation of Reinhard et al. (2017) was filtered to target "typical" marginal marine siliciclastic sedimentary rocks. In doing so, it leaves out "phosphorites," which are extremely P-enriched sedimentary rocks (*e.g.*, Sheldon, 1981). Phosphorites in fact show a small peak in temporal and spatial abundance during the Paleoproterozoic (Papineau, 2010), suggesting that there was a shift in marine P

burial at this time that was distinct from the Archean or mid-Proterozoic.

Also, while the record of P concentrations in marginal marine settings (Reinhard et al., 2017) clearly shows that the rate of P burial was muted in the Precambrian, there are multiple viable interpretations for the dominant mechanism controlling the rate of P burial. Reinhard et al. (2017), following previous workers (Bjerrum and Canfield, 2002; Derry, 2015; Laakso and Schrag, 2014), invoked scavenging of P by Fe-minerals as the main reason for low seawater P levels in the Precambrian. As a result, in their modeling scenarios net primary productivity is kept low due to P scarcity, thereby limiting export production and the flux of P to sediments (Reinhard et al., 2017). Another mechanism has recently been invoked for Precambrian P scarcity, which postulates that higher burial efficiency in the reducing Precambrian ocean would have limited the recycling of P, thereby promoting efficient P burial with organic matter and low steady-state P concentrations in seawater (Kipp and Stüeken, 2017; Laakso and Schrag, 2018). Lastly, it has also been argued that low P would be expected in Precambrian marine sediments simply due to the fact that P burial is ineffective in modern anoxic settings due to the dissolution of adsorbed P phases and inhibition of CFA precipitation (Ingall and Jahnke, 1994; Poulton, 2017; Van Cappellen and Ingall, 1996). Thus, some authors have cited this mechanism in support of a high-P Precambrian ocean with inefficient burial in sediments (Lenton et al., 2014; Poulton, 2017).

Each of these proposed scenarios has slightly different implications for the sedimentary geochemistry of P in the Precambrian. In the first scenario, P would be expected to co-vary with Fe in many marine sediments. In settings were phosphogenesis was favored (*i.e.*, in certain environments in the Paleoproterozoic), this relationship might break down, with more organic-bound P being sourced to sediments and authigenic phosphate precipitation becoming important. In the second model, P would be expected to occur in stoichiometric proportions with organic matter in most Precambrian marine sediments, with little or no relationship to Fe minerals sourced from the water column. In phosphogenic settings, this relationship would change as authigenic P burial became more important (thus lowering the sedimentary C:P ratio). In the third model, there would not necessarily be a clear preference

for P burial with Fe versus organic matter. However, there should be geochemical signatures of high export production in such a high-productivity world, even in non-phosphogenic settings.

Here, we aim to explore these possible controls on P burial in ancient marine sediments. We studied ∼2.0 Ga black shales of the Zaonega Formation (ZF) in the Karelia region of NW Russia (Fig. 2.1). This unit contains abundant organic-rich shales that are thought to have been deposited under predominantly anoxic waters, thus typifying Precambrian conditions. However, certain horizons of the ZF display large authigenic P enrichments, in places exceeding 15% P_2O_5 (Lepland et al., 2014), thus representing one of the earliest phosphorites in the geologic record. This stratigraphic variability makes the ZF a fitting place to examine the various controls on sedimentary P enrichment in the Precambrian. We present a suite of major and trace element data from the ZF in order to constrain the redox conditions and extent of basinal restriction during deposition. We also present new selenium (Se) abundance and isotopic data to more precisely identify fluctuations across high redox potentials, which could have been important for enabling phosphogenesis. Together, we use this dataset to assess the dominant controls on P burial in Precambrian marine sediments.

2.3 Materials

2.3.1 Geologic setting

The Onega Basin of Karelia, NW Russia hosts a large succession of volcanic and sedimentary rocks deposited atop granitic Archean basement in the early Paleoproterozoic (∼2.5-2.0 Ga; Melezhik et al., 2013) (Fig. 2.1). All units in the Onega Basin were deformed and regionally metamorphosed to greenschist facies during the 1.89-1.79 Ga Svecofennian orogeny (Melezhik and Hanski, 2013); since that time they have been relatively well-preserved on the Russian portion of the Karelian craton. The modern exposure of these units across NW Russia has made them a long-studied archive of Earth system evolution across the interval of rising atmospheric oxygen in the early Paleoproterozoic.

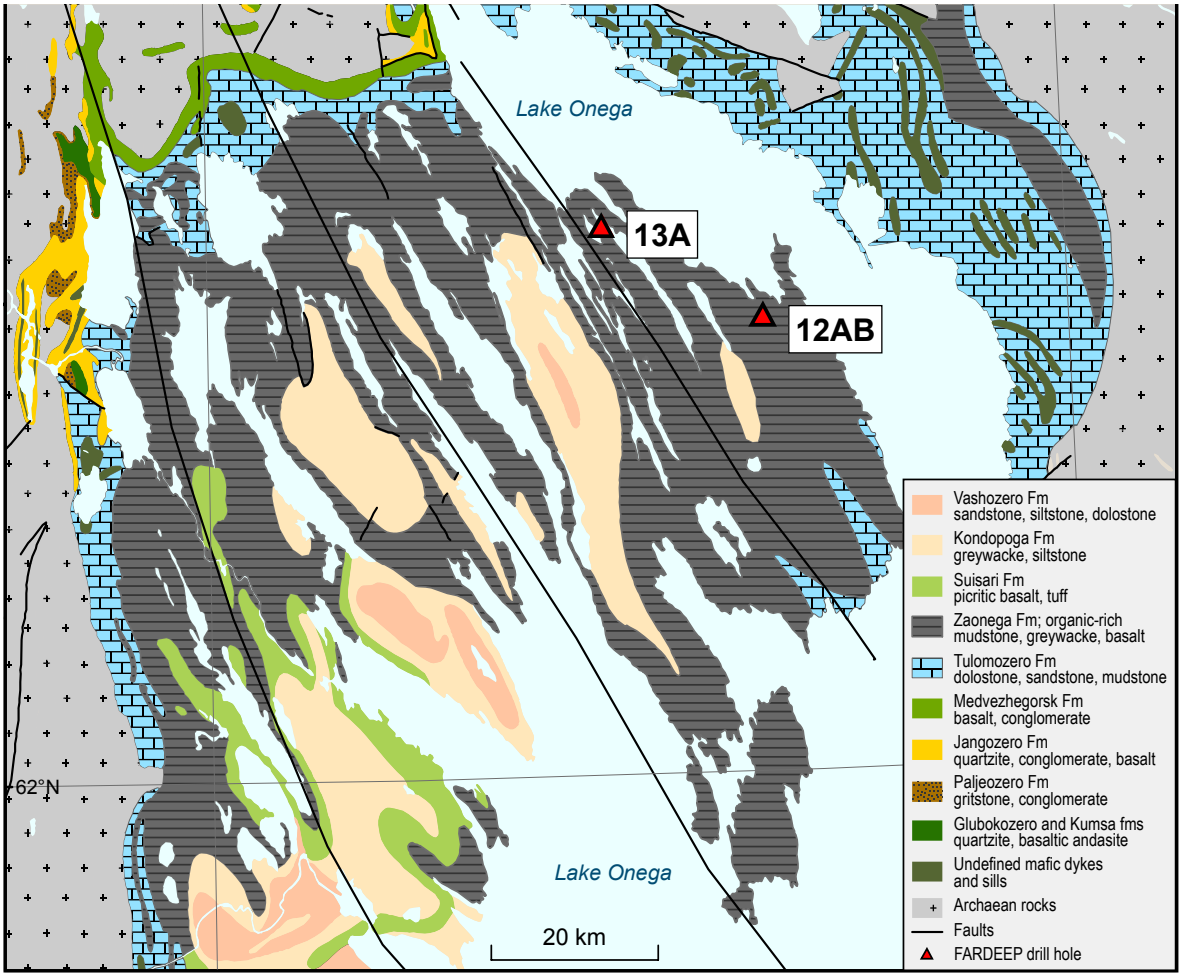

Figure 2.1: **Geological map of Paleoproterozoic successions in the Onega Basin.** Sites of cores 12AB and 13A are marked with red triangles. The Shunga outcrop is near the drilling site of core 12AB.

The Zaonega Formation (ZF) sits in the upper portion of the Onega succession and is comprised of ∼1500 m of organic-rich siliciclastic and carbonate sedimentary rocks as well as abundant magmatic deposits including mafic tuffs, lavas and dolerite sills (Melezhik et al., 2013). The early recognition of high $\delta^{13}C$ values in carbonates of the Tulomozero Formation, which conformably underlies the ZF, led to an association of these two units with the Lomagundi-Jatuli carbon isotope excursion (Karhu and Holland, 1996; Melezhik et al., 1999a). Specifically, the organic-rich ZF was considered a possible candidate for the elusive sedimentological counterpart to the carbon isotopic evidence for rampant organic carbon burial during the Lomagundi Event (Melezhik et al., 1999b). Since the original identification of these pivotal events recorded in the Onega Basin, successive geochronological work has aimed to place them in a firmer temporal context.

The maximum age for all deposition in the Onega Basin comes from a Pb-Pb ID-TIMS date of 2449 ± 1.1 Ma on the Burakovka Pluton (Amelin et al., 1995), which cross-cuts the granitic Archean basement. A lower bound on deposition of the Tulomozero and Zaonega Formations was originally provided by the overlying Suisari magmatic complex, which was dated at 1988 ± 34 via Sm-Nd whole rock + clinopyroxene dating (Puchtel et al., 1998) and 1969 ± 18 Ma via a Re-Os isochron (Puchtel et al., 1999). Carbonates of the Tulomozero Formation were later Pb-Pb dated at 2090 ± 70 Ma (Ovchinnikova et al., 2007), which is consistent with the canonical interpretation of the Lomagundi-Jatuli carbon isotope excursion as a global event lasting from 2220 to 2060 Ma (Karhu and Holland, 1996; Melezhik et al., 1999a). In this view, the organic-rich ZF was thus deposited either during or shortly after the Lomagundi-Jatuli event. This was further corroborated by Pb-Pb dating of zircons from dolerite sills intruding the ZF, which yielded ages of 1919 ± 18 Ma (Priyatkina et al., 2014) and 1956 ± 5 Ma (Stepanova et al., 2014). However, a recent study has challenged the prevailing interpretation.

Martin et al. (2015) obtained a U-Pb zircon and baddelyite age of 1975 ± 3 Ma from the upper Jangozero Formation. This unit was previously interpreted as a dolerite sill that intruded the Tulomozero Formation, and once yielded a 1976 ± 9 Ma Pb-Pb age on zircon

(Puchtel et al., 1998). In such a context this date would represent another lower limit on the age of deposition for the Tulomozero and Zaonega Formations, which is consistent with the timing of the Suisari magmatic activity and associated intrusions observed throughout the ZF. However, Martin et al. (2015) re-interpreted the upper Jangozero Formation as a volcanic deposit, which thereby implicates rapid deposition of the Tulomozero and Zaonega Formations in <10 Myrs. In addition to invoking extremely rapid sedimentation in the Onega Basin, this newly proposed geochronological framework suggests that the $\delta^{13}C$ excursion recorded in Tulomozero carbonates is in fact a later event than the canonical Lomagundi-Jatuli event, which is thought to have terminated at ∼2060 Ma (Karhu and Holland, 1996; Melezhik et al., 1999b).

While this is an intriguing possibility, this new geochronological framework for the Onega Basin has yet to be confirmed through analyses of other igneous units that should yield consistent ages (*e.g.*, the Medvezhegorsk Formation). For the purpose of this investigation, we adopt a ∼2.0 Ga age for the ZF, noting that its precise temporal relationship to events in Earth system evolution in the early Paleoproterozoic may be revised by future geochronological work. In any case, though, these rocks clearly post-date the permanent rise of atmospheric oxygen in the Great Oxidation Event, which occurred at ∼2.4 Ga (Gumsley et al., 2017) and is corroborated by an absence of substantial mass-independent sulfur isotope fractionation (Blättler et al., 2018; Paiste et al., 2018; Scott et al., 2014). Furthermore, they are deposited during an interval of the Paleoproterozoic that is characterized by an increase in phosphorite deposition worldwide (Papineau, 2010).

2.3.2 Paleo-environmental context

The abundance of magmatic rocks in the ZF indicates deposition in a tectonically-active setting. In addition to interbedded tuffs and late-stage dolerite intrusions, some mafic sills in the ZF display peperite contacts, indicating emplacement into soft sediment (Črne et al., 2013; Galdobina and Sokolov, 1987). Thus, the sedimentary facies of the ZF must be interpreted within the context of this dynamic environment.

As noted above, early work inferred that the extremely organic-rich deposits of the ZF (up to tens of percent organic carbon by weight) were indicative of a global organic carbon burial event (Karhu and Holland, 1996; Melezhik et al., 1999a,b). This view was refined by a study of organic carbon and nitrogen isotope ratios in which a step-wise decrease in $\delta^{13}C_{org}$ was interpreted as a sign of massive oxidation of sedimentary organic matter resulting from global atmospheric oxygenation (Kump et al., 2011). Since this early work considering the deposition of these organic-rich mudstones in the context of global redox evolution, more detailed regional studies have revealed that local factors likely also contributed to the unique geochemical signals observed in the ZF.

Qu et al. (2012) undertook a high-resolution study of organic carbon isotope ratios throughout the ZF and attributed the very negative $\delta^{13}C_{org}$ values to methanotrophy occurring via sulfate reduction in a methane-seep system. This inference is supported by the abundant evidence of syndepositional magmatism, which readily provides a mechanism for hydrocarbon generation and consumption that is analogous to modern systems (*e.g.*, Niemann et al., 2005; Orphan et al., 2002). One consequence of this vigorous methane oxidation could have been depletion of the basinal sulfate reservoir, which is indicated by $\delta^{34}S$ values in sedimentary sulfides that are typically positive (+15-25‰; Paiste et al., 2018; Scott et al., 2014). While depletion of seawater sulfate is difficult to achieve at modern concentrations (∼28 mM), this could have occurred in the Onega Basin either due to globally low sulfate levels (Scott et al., 2014) and/or because of restricted watermass exchange with the open ocean (thereby cutting off re-supply of sulfate). Transient excursions up to even more positive $\delta^{34}S$ values (up to +45‰) seem to support the latter scenario (Paiste et al., 2018), as does the occurrence of massive evaporite deposits in the Onega Basin (Blättler et al., 2018).

In the midst of variable basinal restriction and methane seepage, it is conceivable that the redox chemistry of the water column was also characterized by substantial temporal variability. Evidence for such redox fluctuations is indeed found in trace element geochemistry. Kipp et al. (2017) found small Se enrichments and negligible Se isotopic fractionation in organic-rich horizons of the ZF, implying local redox conditions that were strongly anoxic

and perhaps impacted by basinal restriction. In the same samples, Asael et al. (2013) found muted enrichment and isotopic fractionation of molybdenum (Mo) and uranium (U), consistent with the Se data. However, Lepland et al. (2014) and Mand et al. (in review) have reported extremely large Mo and U enrichments in the upper portion of the ZF. Such stark differences require a substantial change in local and/or global redox chemistry between the deposition of these different portions of the ZF. Joosu et al. (2015) documented negative cerium anomalies in diagenetic apatite from the upper, trace-metal-enriched portion of the ZF, suggesting that this enrichment in trace metals indeed corresponds to evidence for some amount of oxygenated seawater in the basin at that time. By analogy to modern settings, the evidence for organic matter accumulation and redox fluctuations in the Onega Basin suggest that this setting may have been ripe for phosphogenesis at times. Indeed, the fact that diagenetic apatite and trace metal enrichments broadly co-occur in the upper ZF (Lepland et al., 2014) seems to support the notion that there is a shared redox-dependence of these processes. However, previous studies have not undertaken a stratigraphically-resolved investigation of various proxies for redox chemistry and basinal restriction. In the present investigation, we aim to use a suite of proxies for paleo-redox conditions and watermass restriction in order to tease apart the various controls on phosphogenesis in the ZF.

2.3.3 Samples from FAR-DEEP

Samples utilized in this study come from cores that were drilled as part of the Fennoscandia Arctic Russia – Drilling Early Earth Project (FAR-DEEP). In total the FAR-DEEP cores recovered >3500 m of Paleoproterozoic volcanic and sedimentary rocks; two of the cores (12AB, 13A) intersect the ZF (Figs. 2.1, 2.2). Both cores 12AB and 13A are predominantly comprised of sedimentary rocks, with <30% of the stratigraphy consisting of tuff beds, mafic lava flows and dolerite sills.

The lower portion of core 12AB (>150 m depth) contains mostly greywackes, marls and mudstones, with minor dolostones and mafic intrusions. A massive organic-rich rock, sometimes referred to as “shungite” after the town of Shunga near the site of FAR-DEEP

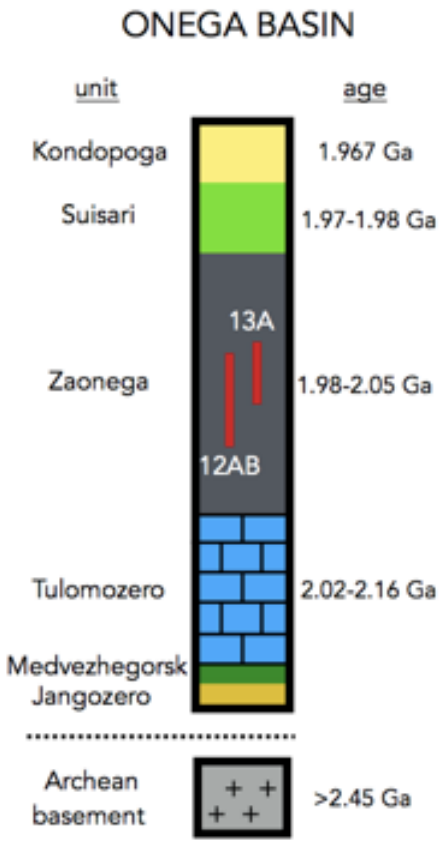

Figure 2.2: **Stratigraphic context of FAR-DEEP drill cores 12AB and 13A.** Ages adapted from Martin et al. (2015) and references therein. Colors and patterns for each unit follow those used in Figure 2.1

13A (Melezhik et al., 1999b), is present from 136 to 156 m and represents petrified oil. Atop this layer are mudstone-marls and dolerite sills until ∼50 m depth. The top ∼50 m of the core is comprised of organic-rich mudstones and dolostones.

The lowermost portion of core 13A (196 – 240 m) is comprised of mafic lavas and sills, followed by ∼70 m of moderately organic-rich (0 – 15% TOC) greywackes, marls and mudstones. Mafic lavas and sills comprise 86 to 129 m, with thin interbeds of siliciclastic sediments. The upper contact of these intrusive layers (86 – 91 m) displays a peperite texture indicative of emplacement into soft sediment (Črne et al., 2013). Atop the magmatic rocks is a ∼90 m succession of dolostones and organic-rich mudstones.

Additional samples were obtained from a ∼7 m outcrop section in an abandoned mining area near the Shunga village, close to the drill site of core 13A (Fig. 2.1). These samples were studied by Lepland et al. (2014) and are extremely enriched in organic matter (up to >50 wt. % TOC) and phosphorus (up to >15 wt. % P_2O_5). Stratigraphically, the outcrop roughly corresponds to the uppermost portion of core 12AB (<12 m) and the ∼35-50 m interval in core 13A (Lepland et al., 2014).

2.4 Methods

2.4.1 Major and trace element concentrations

The abundance of major and trace elements was determined by X-ray fluorescence (XRF) spectrometry at the Geological Survey of Norway using the Philips PW 1480 and PANanalytical Axios instruments. For major element analysis, pre-combusted (1000°C) sample powders were fused to a bead with lithium tetraborate. For trace element analysis, sample powders were mixed with Hoechst wax in a Spex Mixer and then pressed into a pellet. Detection limits were <0.01% for major element oxides (Al_2O_3, Fe_2O_3, P_2O_5 and TiO_2), <10 ppm for Mo and U, <4 ppm for Th, and <2 ppm for Ni and Cu. The XRF data were also used to constrain Se concentrations prior to analysis via HG-MC-ICP-MS; the detection limit for Se via XRF was <5 ppm.

Enrichment factors (EF) were calculated for P, Ni, Cu, Mo, U and Se following the approach described by Tribovillard et al. (2006) and Anbar et al. (2007). In all cases, the enrichment factor represents the abundance of the element of interest relative to a detrital tracer in the sample, normalized to the ratio of that element and its detrital tracer in the upper continental crust, such that

$$X(EF) = \frac{X_{sample}/Y_{sample}}{X_{crust}/Y_{crust}} \tag{2.1}$$

where X represents the element of interest and Y is its respective detrital tracer.

Following previous work (Anbar et al., 2007; Cole et al., 2017; Tribovillard et al., 2006), aluminum was used as the detrital tracer for Mo, Cu and Se, titanium (TiO_2) was used for P and Ni, and thorium (Th) was used for U. We used the upper crust composition estimate of Rudnick and Gao (2003) in all calculations except for two instances. For the crustal Mo/Al ratio, we followed Anbar et al. (2007) in using the estimate of 0.19 (ppm/wt. %) from Taylor and McLennan (1995) so that our results would be comparable to previously published data. Similarly, for the crustal Se/Al ratio we adopted a value of 0.017 (ppm/wt. %), following recent studies (Koehler et al., 2018; Stüeken et al., 2015a) that used data from Taylor and McLennan (1995) and Li and Schoonmaker (2003), in order for our data to be directly comparable with recent work on Se in Precambrian marine sedimentary rocks.

2.4.2 Total organic carbon and total sulfur concentrations

Total organic carbon (TOC) and total sulfur (TS) concentrations were measured at Acme Analytical Laboratories, Canada using a LECO carbon/sulfur analyzer. De-carbonated powders were used for TOC measurements; bulk rock powders were used for TS measurements. The detection limits were <0.02% for TOC and <0.01% for TS.

Additional total sulfur measurements on select samples were conducted in IsoLab at the Department of Earth & Space Sciences, University of Washington. Bulk sample powders were weighed into tin cups along with V_2O_5 as a combustion aid. Samples were analyzed on a Eurovector Elemental Analyzer coupled to a ThermoFinnigan MAT253 continuous flow

isotope ratio mass spectrometer. The average analytical precision, determined by replicate analyses of an in-house standard, was ±2% (relative error).

2.4.3 Selenium concentrations and isotope ratios

Bulk rock powders were prepared for measurement of Se stable isotope ratios following published protocols (Stüeken et al., 2013). Rock powders were digested in a combination of HF, $HClO_4$ and HNO_3. Thiol cotton fiber was used to isolate Se from the digests. Purified Se solutions were treated with aqua regia prior to evaporative concentration for analysis.

Selenium stable isotope ratios were measured using a Hydride Generator-Inductively Coupled Plasma-Mass Spectrometer (Nu Instruments) housed in the Isotope Geochemistry Laboratory at the Department of Earth & Space Sciences, University of Washington. The operating environment (torch position, carrier gas flow rate, lens voltage potentials) was tuned daily to optimize signal strength and stability. All Se isotope data are reported in delta notation as $\delta^{82/78}$Se values relative to NIST reference SRM 3149 (cf. Carignan and Wen, 2007), because under our analytical protocol masses 82 and 78 are least affected by isobaric interferences (Stüeken et al., 2013).

In-house standard UW-McRae (n = 22) and USGS standard SGR-1 (n = 10) were analyzed in all analytical sessions. The Se concentrations (3.1 ± 0.4 ppm, 3.3 ± 0.2 ppm) and $\delta^{82/78}$Se values (0.76 ± 0.20‰, -0.13 ± 0.26‰) obtained for these materials are in agreement with previous studies (Kipp et al., 2017; Kurzawa et al., 2017; Mitchell et al., 2012; Stüeken et al., 2013). The average analytical precision of all replicate samples was ±0.24‰ (1σ, n = 24).

2.5 Results

The P_2O_5 content of samples from cores 12AB and 13A ranges from 0.01% to 1.38% (Figs. 2.3, 2.4). Throughout most of the sedimentary portion of the core, P_2O_5 remains close to average Precambrian shale (∼0.1%; Reinhard et al., 2017). Horizons of higher P_2O_5 concentrations are observed in both cores (Figs. 2.3, 2.4) as well as in the correlative outcrop

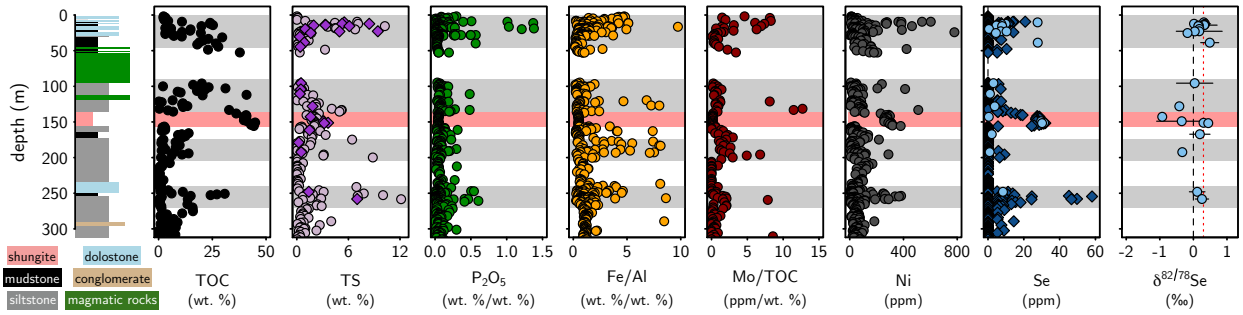

Figure 2.3: **Chemostratigraphy of FAR-DEEP core 12AB.** Grey shaded regions denote intervals of P enrichment. In $\delta^{82/78}$Se plot, dashed line denotes crustal composition, dotted red line denotes modern seawater composition, error bars are 1σ.

section (Fig. 2.5), where P_2O_5 exceeds 15% (Lepland et al., 2014).

A correlation is observed between P_2O_5 and TiO_2 in both cores (Fig. 6), though both cores contain a population of samples that plot at distinctly higher P_2O_5/TiO_2 ratios. When normalizing the stratigraphic P trends to TiO_2, the same pattern is observed (Figs. 2.7, 2.8).

The intervals of P enrichment (grey shaded regions in Figs. 2.3, 2.4, 2.7, 2.8), also feature higher TOC and TS (Figs. 2.3, 2.4) as well as increases in the enrichment of Fe, Mo, Ni and Se (Figs. 2.3, 2.4). In particular, large P enrichments are shown to begin around an Fe/Al ratio of ~0.6 in both cores (Fig. 2.9). Positive correlations are observed in both cores between P (EF) and Ni (EF) as well as P (EF) and Cu (EF) (Fig. 2.10).

The abundance of P_2O_5 is moderately correlated with Fe_2O_3 in non-P-enriched samples from both cores (Fig. 2.11A, C); however, the correlation is weaker or absent in P-enriched samples. In contrast, P_2O_5 does not strongly correlate with TOC in either core (Fig. 2.11B, D). The C_{org}:P ratios in both cores are typically greater than 1000, which is much higher than the modern Redfield ratio or the values observed in modern marine sediments (typical C_{org}:P of ~250; Ruttenberg, 2003).

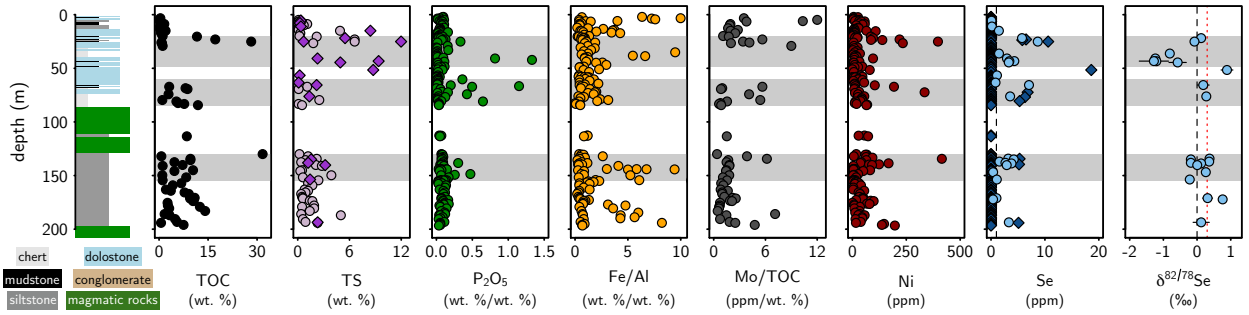

Figure 2.4: **Chemostratigraphy of FAR-DEEP core 13A.** Grey shaded regions denote intervals of P enrichment. Annotations as in Fig. 3.

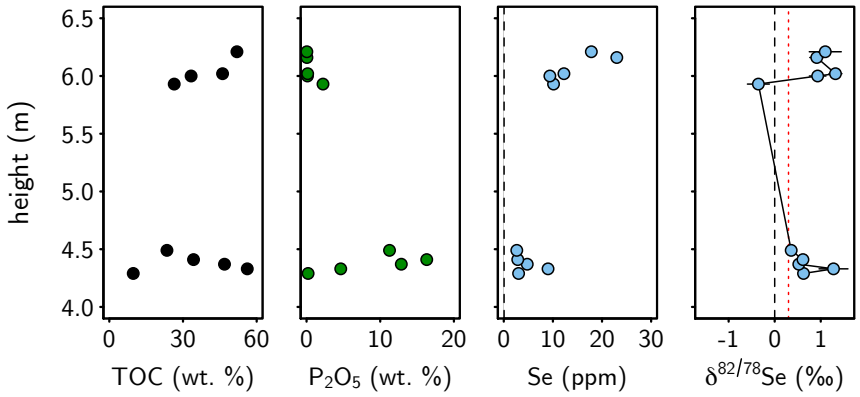

Figure 2.5: **Chemostratigraphy of outcrop near Shunga village.** Outcrop corresponds to <12m in core 12AB and 35-50m depth in core 13A. Annotations as in Figs. 3 and 4.

2.6 Discussion

2.6.1 Stratigraphic trends in phosphorus enrichment

Relative to P concentrations in roughly co-eval Precambrian marine sediments, the "background" conditions during deposition of the ZF are unremarkable. For instance, the intervals from 205 – 240 m and >270 m in core 12AB (Fig. 2.3), as well as the interval >150 m in core 13A (Fig. 2.4) have a mean P_2O_5 concentration of 0.07%, which is quite similar to the mean of all Precambrian marginal marine siliciclastic sediments observed in Reinhard et al. (2017). Thus, despite the unique tectonic setting of the ZF, in some respects background P burial appears normal.

However, notable exceptions occur in transient episodes of P-rich sedimentation (grey shaded regions in Figs. 2.3, 2.4). In these intervals, P_2O_5 reaches ∼0.5% and even exceeds 1% in some cases (Figs. 2.3, 2.4). In the outcrop near Shunga village, P_2O_5 reaches >15% (Fig. 2.5). In the case of the Shunga outcrop samples, the extremely high P levels and previously-described phosphatic nodules clearly demonstrate that this enrichment is due to diagenetic apatite precipitation (Lepland et al., 2014). For the smaller enrichments observed in the drill cores, we sought to confirm that these are indeed authigenic enrichments (and not artifacts of differential detrital P delivery) by normalizing the P data to titanium (as TiO_2), which can be used as a detrital tracer with similar geochemical behavior to P (*e.g.*, Filippelli et al., 2003; Latimer and Filippelli, 2001).

Across the entire dataset, P_2O_5 shows a correlation with TiO_2 in a sub-set of samples (Fig. 2.6), likely defining a trend of varying detrital input. Many samples in fact have lower P_2O_5/TiO_2 ratios than the upper continental crust (<0.23; Rudnick and Gao, 2003). This likely does not reflect a change in crustal composition, as estimates of Archean P_2O_5/TiO_2 ratios are not substantially different (∼0.18; Greber et al., 2017) and many samples in our dataset plot below that value as well (Fig. 2.6). Instead, the very low P levels in these sediments may derive from the fact that P burial is very inefficient in anoxic settings, with P tending to get recycled back into the water column instead of incorporated in authigenic

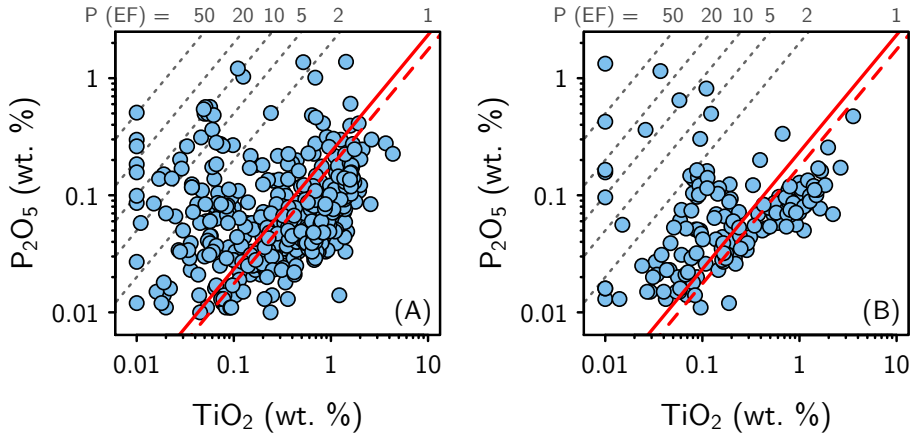

Figure 2.6: **P_2O_5 vs. TiO_2 in core 12AB (A) and core 13A (B).** Solid red line denotes P_2O_5/TiO_2 ratio of upper continental crust (Rudnick and Gao, 2003); dashed red line denotes estimated composition of Archean crust (Greber et al., 2017). Grey dotted lines denote contours of P (EF), with the most enriched samples plotted toward the top left of the plot.

phases (Ingall and Jahnke, 1994). Thus, these data may lend some support to the notion that limited P burial in the Precambrian ocean is in some way related to inefficient anoxic P burial (Poulton, 2017).

In contrast, many other samples in our dataset have P_2O_5/TiO_2 ratios that substantially exceed the crustal value. These samples are enriched in P relative to the upper continental crust by factors of $\sim$10 to $>$100, suggesting that P transport to the sediments and precipitation of diagenetic apatite were occurring at these times. This quantification of P enrichment relative to crustal values makes the P_2O_5/TiO_2 ratio useful for considering the environmental controls on P enrichment, which we will explore below.

Lastly, when the drillcore data are normalized for detrital inputs (P_2O_5/TiO_2), the stratigraphic trends resemble those of total P_2O_5 concentrations (Fig. 2.7). The most parsimonious explanation of this similarity is that both parameters are tracking authigenic P enrichment. We therefore consider the intervals of high P_2O_5 and high P_2O_5/TiO_2 to represent deviations from the "background" conditions, during which times the cycling of

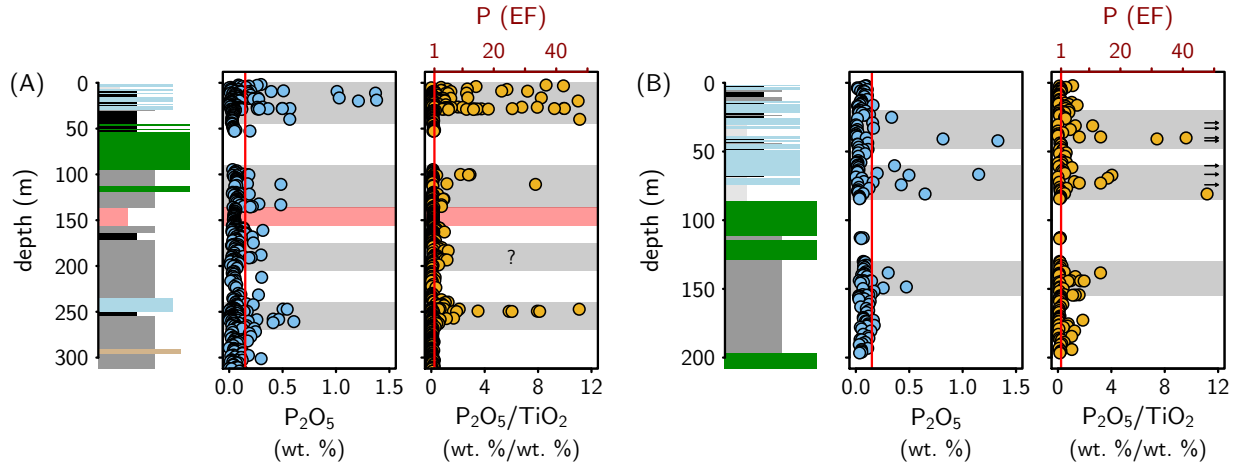

Figure 2.7: **P_2O_5 and P_2O_5/TiO_2 profiles in cores 12AB (A) and 13A (B).** Arrows denote points that plot off the axis toward higher values. Normalizing P_2O_5 to TiO_2 reveals the same intervals of P enrichment.

P changed such that sedimentary enrichment became feasible. In the rest of the paper, we consider what environmental factors could have enabled certain horizons of the ZF to become enriched in P while others did not.

2.6.2 Relationship between phosphorus enrichment and redox conditions

One possible explanation for transient episodes of sedimentary P enrichment is that redox conditions shifted in those times to a regime more favorable for phosphogenesis. It is known that in modern marine sediments, fluctuating redox conditions can favor phosphogenesis by promoting the activity of sulfur-oxidizing bacteria (*e.g.*, *Thiomargarita* and *Beggiatoa*). These bacteria accumulate phosphate within their cells and occasionally release it to porewaters in times of more reducing conditions, thereby stimulating diagenetic apatite precipitation (Schulz and Schulz, 2005). These bacteria require porewater sulfide, implicating sulfate reduction below a certain level in the sediments, as well as a supply of oxidants, requiring oxidant penetration to some depth in the sediments.

Such a scenario has previously been invoked to explain phosphogenesis in the ZF on

the basis of *Thiomargarita*-sized phosphate nodules as well as large trace metal enrichments suggestive of fluctuating redox conditions (Lepland et al., 2014). In this model, the background conditions in the basin are more strongly anoxic, with periods of redox fluctuations near "suboxic" conditions. Here we explore this hypothesis further using an array of major and trace element proxies with various redox sensitivities.

First we consider the iron to aluminum (Fe/Al) ratio. In the modern ocean, the Fe/Al ratio of siliciclastic sediments increases under reducing conditions, particularly in anoxic and sulfidic (*i.e.*, euxinic) settings, when Fe is efficiently scavenged during pyrite precipitation (Lyons and Severmann, 2006). In modern euxinic settings, such as the Black Sea, Fe/Al ratios range from 0.6 – 1.2 (Lyons and Severmann, 2006). Average shales, in contrast, have an Fe/Al ratio of ∼0.5, which is the Fe/Al ratio of the upper continental crust (Rudnick and Gao, 2003; Taylor and McLennan, 1995), reflecting a trend of detrital input. Thus, if episodes of P enrichment were associated with the proliferation of sulfur-oxidizing bacteria, which thrive in settings with sedimentary sulfate reduction, we might expect to see a positive correlation between P enrichment and Fe/Al ratios.

Across our dataset, large P enrichments seem to initiate around the modern euxinic Fe/Al values of 0.6 – 1.2 (Fig. 2.8). This is consistent with higher sulfate reduction rates during episodes of phosphogenesis in the ZF. The fact that some Fe/Al ratios are much higher than observed in modern sediments (>10) can in part be attributed to low detrital input, as the samples with the highest Fe/Al ratios tend to have very low Al_2O_3 concentrations. Additionally, it is possible that some of the Fe/Al ratios >> 1 in fact reflect progressively stronger euxinia. In that scenario, the fact that P enrichments peak at moderate Fe/Al ratios could reflect that fact that phosphogenesis benefits from fluctuating redox conditions with oxidants meeting hydrogen sulfide in sediment porewaters (Schulz and Schulz, 2005). Strongly euxinic deposition, on the other hand (*i.e.*, euxinic bottom waters), would tend to be unfavorable for the sulfur-oxidizing bacteria that are known to mediate phosphogenesis. In either case, the data from P-enriched samples seem to fit with the redox-fluctuation mechanism for phosphogenesis, at least when viewed through the lens of the Fe/Al proxy.

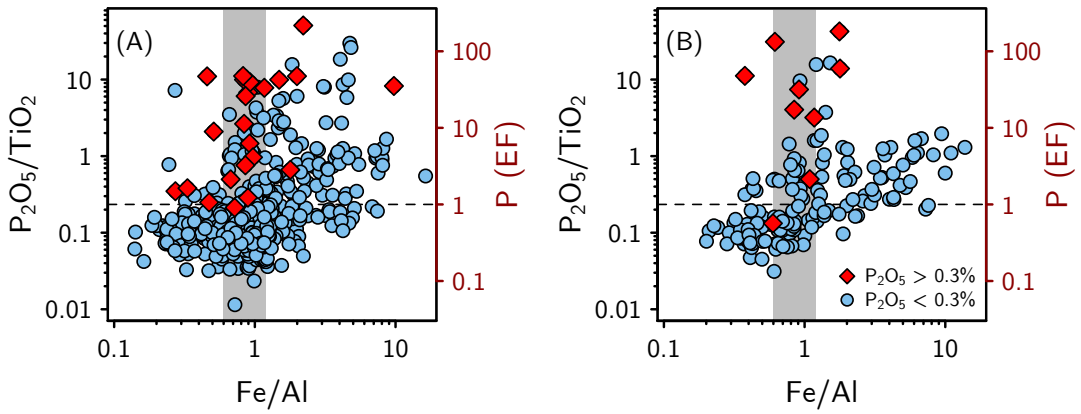

Figure 2.8: **Phosphorus enrichment vs. Fe/Al in core 12AB (A) and core 13A (B).** Grey shaded region denotes range of Fe/Al ratios observed in modern euxinic sediments (Lyons and Severmann, 2006). Dashed line denotes crustal P_2O_5/TiO_2 ratio (0.234; Rudnick and Gao, 2014), which corresponds to P (EF) = 1. Red diamonds denote samples with >0.3 wt. % P_2O_5; all other samples are shown as blue circles. An increase in P enrichment is seen at Fe/Al ratios similar to those of modern euxinic sediments.

Another implication of this mechanism – namely, that redox fluctuations supportive of sulfur-oxidizing bacteria were enabling phosphogenesis in the ZF – is that diagenetic sulfide minerals should also be more abundant in the P-rich horizons than in the background intervals. This is precisely the pattern that is observed in the drill cores (Figs. 2.3, 2.4). Importantly, it is known from sulfur isotope ratios ($\delta^{34}S$) in sedimentary sulfides of the ZF that the basin was sulfate-limited (Paiste et al., 2018; Scott et al., 2014). This means that the increases in the rate of sulfate reduction and diagenetic sulfide burial during these episodes were likely driven by growth of the basinal sulfate reservoir, instead of merely a shift in the redox state of deep waters.

An increase in the size of the basinal sulfate reservoir could have promoted phosphogenesis in multiple ways. First, as mentioned above, stimulation of sulfate reduction in sediment porewaters could have promoted the proliferation of sulfur-oxidizing bacteria, which are

known to directly mediate phosphogenesis through uptake and release of phosphate (Schulz and Schulz, 2005). Second, in addition to the direct bacterial role in phosphate supersaturation, sulfate reduction can also indirectly promote diagenetic apatite precipitation by increasing alkalinity in porewaters (Jahnke, 1984). Third, if P burial in the basin was limited due to high burial efficiency during "background" intervals because of a scarcity of oxidants (including sulfate, cf. Kipp and Stüeken, 2017), then an increase in sulfate levels (globally or locally) could have stimulated P recycling and productivity, thereby promoting phosphogenesis.

The latter scenario is consistent with observed co-incident increases in Ni and Cu in the P-rich horizons (Figs. 2.3, 2.4). Both Ni and Cu are predominantly sourced to sediments via organic matter and are efficiently scavenged under euxinic conditions, meaning that increases in Ni and Cu can reflect higher rates of organic matter export to sediments (Tribovillard et al., 2006). In both cores, P_2O_5/TiO_2 ratios are correlated with Ni (EF) and Cu (EF) (Fig. 2.9); albeit only weakly in core 12AB. This is consistent with greater organic matter export to sediments (and perhaps higher rates of primary productivity) during episodes of phosphogenesis; however, the fact that heightened euxinia can also influence Ni and Cu scavenging makes it difficult to disentangle the competing role of benthic redox on these enrichments. In both cases, however, the coincident enrichments of Ni and Cu in the P-rich horizons support the redox mechanism for phosphogenesis in the ZF.

In addition to Ni and Cu enrichments, molybdenum (Mo) is enriched in the P-rich horizons, as evidenced by large increases in the Mo/TOC ratio (Figs. 2.3, 2.4). In the modern ocean, Mo is efficiently scavenged under euxinic conditions (Helz et al., 1996). Across basins with similarly reducing bottoms waters, differences in sedimentary Mo/TOC ratios have been shown to correlate with aqueous Mo concentrations (Algeo and Lyons, 2006). The primary driver of differences in aqueous Mo concentrations is basinal restriction, where more restricted basins tend to progressively deplete their Mo reservoir, leading to a "reservoir effect" where sedimentary enrichments become smaller with time (Algeo and Lyons, 2006). Thus, Mo/TOC can trace either benthic redox and/or the size of the aqueous Mo reservoir.

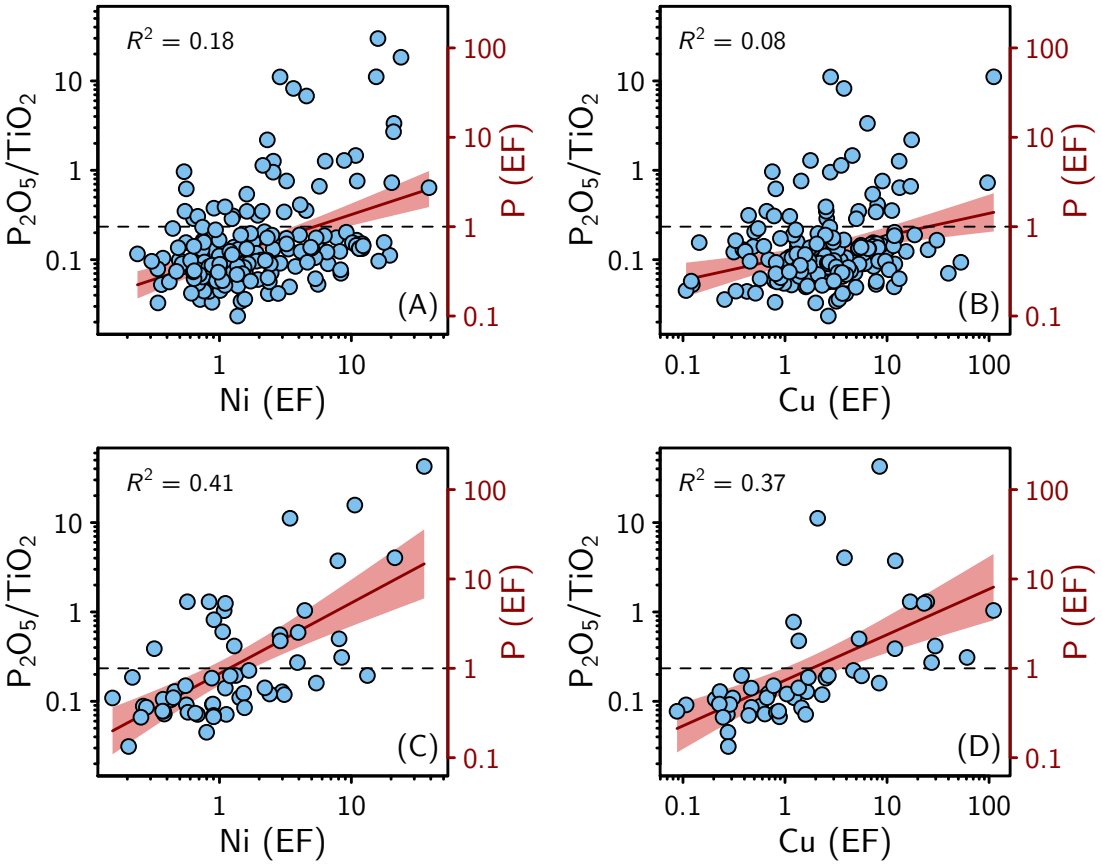

Figure 2.9: **P enrichment vs. Ni (A, C) and Cu (B, D) enrichment in core 12AB (A, B) and core 13A (C, D).** Dashed lines denote crustal P_2O_5/TiO_2 ratio, which corresponds to P (EF) = 1. Dark red lines denote linear regression, with 95% confidence intervals shaded in light red. The positive co-variation of P_2O_5/TiO_2 with Ni (EF) and Cu (EF) is consistent with higher export production during phosphogenic intervals, as well as perhaps stronger euxinia.

The higher Mo/TOC ratios in times of P-rich deposition have two possible explanations. First, it is possible that a shift from anoxic to euxinic deposition promoted more efficient Mo scavenging to sediments. Second, it is possible that the aqueous Mo reservoir grew due to influx of waters from the open ocean. These two scenarios are not mutually exclusive. As mentioned above, the fact that the basin was sulfate-limited implies that episodes of greater sulfate reduction would likely have been stimulated by an influx of sulfate. It is therefore conceivable that influx of seawater to the basin would have also brought a renewed supply of Mo. On top of this mechanism, though, it is quite likely that the expansion of euxinia promoted more efficient Mo scavenging. Thus, we take the Mo/TOC trends to be suggestive of both seawater influx and increasing benthic sulfate reduction rates.

Lastly, we use the Se data to disambiguate between some of the potential interpretations presented above. First, we find that Se is also enriched in the intervals of P enrichment (Figs. 2.3, 2.4). As with Mo, this could either derive from an increase in scavenging efficiency and/or an increase in the aqueous Se concentration. However, as Se is efficiently scavenged under anoxic (and not just euxinic) conditions (*e.g.*, Cutter, 1982; Rue et al., 1997), and the background deposition of the ZF is thought to have been anoxic (Asael et al., 2013; Scott et al., 2014), it is unlikely that merely a shift in redox conditions explains the observed Se enrichment trend. Thus, we take the Se enrichments as further support for influx of seawater to the basin during episodes of P enrichment.

Second, we note that Se isotopes are not largely fractionated within most of the P-rich horizons (Figs. 2.3, 2.4). For the most part, $\delta^{82/78}$Se values across both cores fall close to the crustal value (0‰; Stüeken, 2017) and modern seawater composition (+0.3‰; Chang et al., 2017; Stüeken et al., 2015b; Stüeken, 2017). This implies that sequestration of Se in sediments was proceeding efficiently, without a kinetic isotopic preference. Such a scenario is consistent with quantitative oxyanion reduction, which is thought to occur in restricted, anoxic basins in the modern ocean (Stüeken et al., 2015b; Stüeken, 2017) and recent geological past (Kipp et al., submitted). This would thus seem to be further support for the inference of basinal restriction, though we note that with a small global Se reservoir

at this time, in the aftermath of the GOE (Kipp et al., 2017), it is perhaps likely that quantitative Se oxyanion reduction would have been more feasible in open marine settings as well.

There are two notable instances where $\delta^{82/78}$Se values do markedly shift. The first is around ∼150m in core 12AB (red shaded region in Fig. 2.3). This is an anomalous horizon, since the material in this portion of the core is a massive, organo-siliceous rock thought to derive from migrated pyrobitumen (*i.e.*, "fossilized oil"). This interval has been interpreted as an asphalt spill onto the seafloor (Qu et al., 2012), which is further evidence for the seep-affected environment and active tectonic setting. Interpretation of $\delta^{82/78}$Se values in this horizon is thus difficult, as it is unclear what proportion of the Se was sourced from export production (as typically occurs during marine Se burial) and what proportion derives from the hydrocarbons, which were subject to extensive diagenetic and catagenic re-working that could have altered Se isotope signatures. We therefore do not attempt to interpret this isotopic excursion in the context of water column paleo-redox.

In contrast, another negative $\delta^{82/78}$Se excursion occurs near ∼40m in core 13A (Fig. 2.4). In this case, the sedimentological context (organic-rich dolostone and siltstone) does seem to suggest that the isotopic shift is recording paleo-redox conditions. The fact that $\delta^{82/78}$Se is depleted relative to crustal values suggests non-quantitative oxyanion reduction. In the modern ocean, this primarily occurs in open-marine settings where porewater Se reduction is coupled to a large Se supply from oxic ocean water (Mitchell et al., 2012; Stüeken et al., 2015b). Thus, the transition toward lighter Se isotope ratios might reflect a larger aqueous Se reservoir that was not being quantitatively consumed. It could also reflect less-reducing conditions, leading to less efficient Se reduction, which is also consistent with the smaller Se enrichments during the negative isotopic excursion. It is difficult to parse out which of these mechanisms was the dominant control on Se behavior, but it is possible that both were occurring to some extent.

To summarize, a variety of paleo-redox indicators provide suggestive evidence that conditions shifted from anoxic (but not euxinic) during background intervals to more variable

during times of P-enrichment, with higher rates of sulfate reduction and perhaps also periodic supply of oxidants to sediments. These inferences are consistent with previous hypotheses about redox conditions during phosphogenic episodes in the ZF (Joosu et al., 2015; Lepland et al., 2014), but now this array of stratigraphically-constrained geochemical data can be leveraged to address the underlying drivers of redox variability across the ZF. Below we explore one such mechanism.

2.6.3 Relationship between phosphorus enrichment and basinal restriction

As noted above, the trends in a number of the paleo-redox indicators could potentially be explained by prevailing basinal restriction punctuated by intervals of greater seawater influx to the basin. Higher Fe/Al and TS in P-rich horizons imply that sulfate reduction was somehow stimulated in these intervals. Given the sulfate-limited nature of the basin, this was likely stimulated by growth of the basinal sulfate reservoir. While such transient pulses could potentially be attributed to global waxing and waning of the sulfate reservoir (*e.g.*, Scott et al., 2014), recent work has established that the global marine sulfate reservoir approached its modern size during deposition in the Onega Basin (>10 mM; Blättler et al., 2018). Such a large reservoir would be well-buffered against rapid, large-magnitude fluctuations in sulfate concentrations, as evidenced by the 10^7-10^8 yr periodicity in reconstructions of large-magnitude oscillations in the Phanerozoic sulfate reservoir (Algeo et al., 2015; Berner, 2004; Halevy et al., 2012), consistent with an inferred ∼20 Myr marine residence time of sulfate (Claypool et al., 1980; Holland, 1973). Thus, we favor an alternative interpretation: that intervals of enhanced communication between the basin and open ocean brought a re-supply of sulfate from the global marine reservoir, thereby stimulating sulfate reduction and the observed transient episodes of redox-sensitive trace metal enrichment and P burial.

Along with sulfate, an influx of seawater would likely have also replenished the supply of macronutrients (*i.e.*, N and P). The existing $\delta^{15}N$ data from the ZF show only slight changes across the core (Kump et al., 2011), implying consistent aerobic nitrogen cycling in surface waters of the basin – similar to other roughly coeval organic-rich shales that were deposited

in open marine settings (Kipp et al., 2018). To a first-order, this suggests that surface waters remained oxygenated and amenable to nitrate accumulation even in the "more restricted" intervals. This is unlike the modern Black Sea, for instance, which has depleted its nitrate reservoir and is dominated by a $\delta^{15}N$ signature of nitrogen-fixation in its sediments (*e.g.*, Fulton et al., 2012), and perhaps provides some constraint as to the severity of the basinal restriction.

Although the $\delta^{15}N$ data do not clearly point to a change in the macronutrient balance of the basin during phosphogenic episodes, the enrichment of Ni and Cu in these intervals may suggest that rates of export production (and thus rates of primary production in surface waters) were indeed higher at these times. This is further supported by the breakdown of the P_2O_5 vs. TiO_2 correlation in P-rich samples (Fig. 2.6), which implies that another source of P exceeded the detrital input of P to sediments (which could very likely have been organic matter exported from the photic zone). Thus, it is possible that in influx of nutrients stimulated productivity (more likely via P than N) at these times.

Additionally, as noted above, the Mo/TOC and Se data are best explained by growth of the basinal Mo and Se reservoirs during phosphogenic episodes. This is particularly clear for Se, which would have been effectively scavenged during the background anoxic deposition, and so likely requires an additional input to explain the large enrichments during phosphogenic episodes. One possible explanation for such an increase in aqueous Mo and Se reservoirs is an increase in the intensity of oxidative continental weathering. Such a mechanism could perhaps explain the increase in sulfate as well. However, as mentioned before regarding the size of the marine sulfate reservoir – this mechanism would be invoking much larger magnitude global changes, which implies substantial changes in the global balance of the sulfur and oxygen cycles. We thus posit that the trends observed in these major and trace element proxies are best explained by changes in basinal hydrography, where more open-marine-influenced conditions were co-incident with the episodes of sedimentary P enrichment.

We further explore this hypothesis using molybdenum-uranium (Mo-U) co-variation,

following Algeo and Tribovillard (2009) who pioneered the technique using Paleozoic black shales. The logic of this comparison is that the relative enrichment pattern of these elements can be informative of the redox and hydrographic conditions, since each element has distinct processes controlling transport to sediments and also a different abundance in seawater. Specifically, Mo can be transported to sediments via a Mn-oxide "particulate shuttle" when surface waters are oxic, unlike U (Algeo and Tribovillard, 2009; Crusius et al., 1996; Morford and Emerson, 1999; Murray, 1975). In weakly restricted basins that deplete some of their trace metal inventory, Mo can thus become more enriched than U due to continued scavenging via Mn-oxides at the chemocline. If such settings become strongly restricted, a trend toward higher U (EF) but constant Mo (EF) is observed, reflecting depletion of the Mo reservoir under restricted conditions and euxinic bottom waters. In contrast to restricted basins, open marine settings follow a different trajectory with x-intercepts $>$ 1 U (EF). This is due to the fact that U can be scavenged under suboxic conditions, whereas Mo is only efficiently sequestered in the presence of sulfide (Morford and Emerson, 1999; Tribovillard et al., 2006). As open marine settings transition from suboxic toward anoxic and euxinic conditions, they follow a trajectory toward equal Mo and U enrichment factors.

While this technique was developed using sediments deposited after oxygenation of the deep ocean (Algeo and Tribovillard, 2009), and thus has been calibrated to different trace metal inventories than are likely to have persisted in the Paleoproterozoic, the relative pattern of Mo-U enrichment is still likely to hold due to the same removal processes dictating their behavior (*i.e.*, the same redox thresholds).

We find that samples from intervals of background anoxic deposition plot along the "particulate shuttle, weakly restricted basin" trajectory (Fig. 2.10). This is consistent with our inference above that the basin had limited exchange with the open ocean during much of its depositional timeframe. Additionally, the lack of evidence for strong restriction is consistent with the positive $\delta^{15}N$ values, as mentioned above. In contrast, the few data from P-enriched samples perhaps show a different trend that is shifted toward the "open ocean, redox variation" trajectory (Fig. 2.10). This would be expected if the episodes of

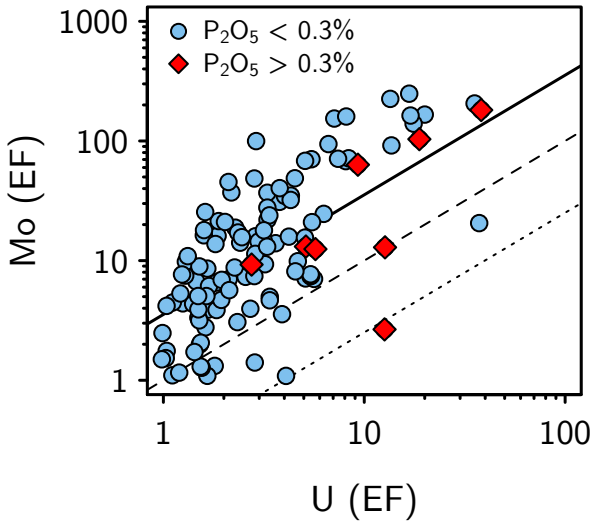

Figure 2.10: **Mo (EF) vs. U (EF) in core 12AB.** Red diamonds denote samples with >0.3% P_2O_5; all other data shown in blue circles. Solid line denotes the Mo/U ratio of modern seawater; dashed and dotted lines denote 0.3x and 0.1x the seawater ratio, respectively. The trajectory of non-P-enriched samples follows that expected for a particulate shuttle operating in a weakly restricted basin. In contrast, P-enriched samples seem to plot closer to the open-marine trajectory. Plot modified after Algeo and Tribovillard (2009).

P enrichment indeed occurred during times of greater communication of the basin with the open ocean, and perhaps also featured variable benthic redox conditions. While the inference from the P-rich samples is limited by the small number of samples, the more general trend reflecting a weakly restricted basin is consistent with our inferred role of basinal hydrography in explaining the geochemical trends observed across the ZF.

To summarize: while no single proxy serves as a "smoking gun" for stark changes in basinal circulation between phosphogenic and background conditions, the aggregation of evidence from a diverse array of proxies is readily explained by such a mechanism. We thus take this to be the most parsimonious provisional explanation for the control of P enrichment in the ZF.

2.6.4 Dominant controls on P enrichment: Fe-scavenging, high burial efficiency, or muted anoxic burial?

Finally, we consider whether the observed trends in P enrichment can tell us anything about the dominant mechanism causing limited background P burial at this time in the Precambrian. Precambrian shales average <0.1 wt. % P_2O_5 (Reinhard et al., 2017), in contrast to what is observed in these transient phosphogenic episodes of the ZF, where P becomes enriched by up to two orders of magnitude. The fact that redox fluctuations and incursions of open marine waters may have stimulated P enrichment in the ZF can perhaps shed light on what was limiting P burial more broadly in the Precambrian ocean.

At first glance, the role of basinal restriction provides a ready explanation. Since the geologic record is biased toward continental sediments (Husson and Peters, 2018), including restricted epicontinental seaways, it is at least plausible that the limited P burial observed in the Precambrian is influenced by a lack of data from truly open marine settings. However, while likely important on some level, this explanation does not provide an answer for why P burial increased suddenly in the late Neoproterozoic (Reinhard et al., 2017), or why all sedimentary archives from the Precambrian are characterized by low P, when some are fairly certainly interpreted as open marine deposits. So we regard this explanation as insufficient, while perhaps playing some role in the observed secular trends.

The mechanism for Precambrian P limitation that has been favored by most workers on this topic to-date is that P was scavenged by Fe minerals in the anoxic Precambrian ocean. Both Fe-oxides (Berner, 1973; Feely et al., 1998) and reduced/mixed-valence Fe minerals (Hansen and Poulsen, 1999; Zegeye et al., 2012) can scavenge dissolved P from seawater, and could conceivably have choked-out the P supply to the biosphere in the photic zone by efficiently transporting Fe-bound P to sediments, namely in the deep ocean. While pelagic settings are not preserved in the rock record, we still might expect to see some signature of Fe-scavenging in marginal marine sediments. We searched for such a signature by comparing P and Fe concentrations in these samples (Fig. 2.11A, C). We found that in background

intervals, the P/Fe ratio is similar to that of the continental crust (which is consistent with both the P_2O_5/TiO_2 and Fe/Al ratios being similar to their crustal compositions), suggesting that this is a result of detrital dominance of both the P and Fe contents of these samples. In contrast, the most P-enriched samples (here defined as having P_2O_5/TiO_2 ratios at least 10 times higher than the upper crust) contain substantially greater P relative to Fe (Fig. 2.11A, C). This implies that another source, besides detrital material, was contributing P to these sediments. The weak positive P vs. Fe correlation in the P-rich samples of core 12AB (Fig. 2.11A) allows for the possibility that Fe played some role in P transport to sediments at these times, but no such correlation is seen in core 13A (Fig. 2.11C). Thus, in sum, despite observing correlations between P_2O_5 and Fe_2O_3, we find no compelling evidence for strong scavenging of P from the water column via Fe minerals. In the phosphogenic intervals, in particular, another source must have been transporting P to sediments.

The other viable route of P transport to sediments is with organic matter. It has been proposed that high burial efficiency of organic carbon (and associated P) could have been the dominant throttle on low Precambrian P levels (Kipp and Stüeken, 2017; Laakso and Schrag, 2018), rather than Fe-scavenging. In such a model, P would be expected to occur in stoichiometric proportions with organic matter. While the molar C:P ratio of primary producers in the Precambrian is highly uncertain (Planavsky, 2014), we can consider a range of values that spans the modern (C:P = 106) to extremely high (C:P = 1000) to get a sense of the plausibility of this mechanism. In both cores, there is no significant correlation between P_2O_5 and TOC (Fig. 2.11B, D). To a first order, this would seem to suggest that organic matter was not the dominant P source to sediments, in background intervals or in times of phosphogenesis. However, there are multiple complicating factors precluding this simple interpretation.

First, the remineralization of organic matter can variably increase the C:P ratio (Clark et al., 1998; Ruttenberg, 2003), thus obfuscating the stoichiometric relationship between TOC and P_2O_5 in sediments. Tracers for original organic matter content, such as Ni and Cu, should allow stronger inferences about the relationship between P levels and exported

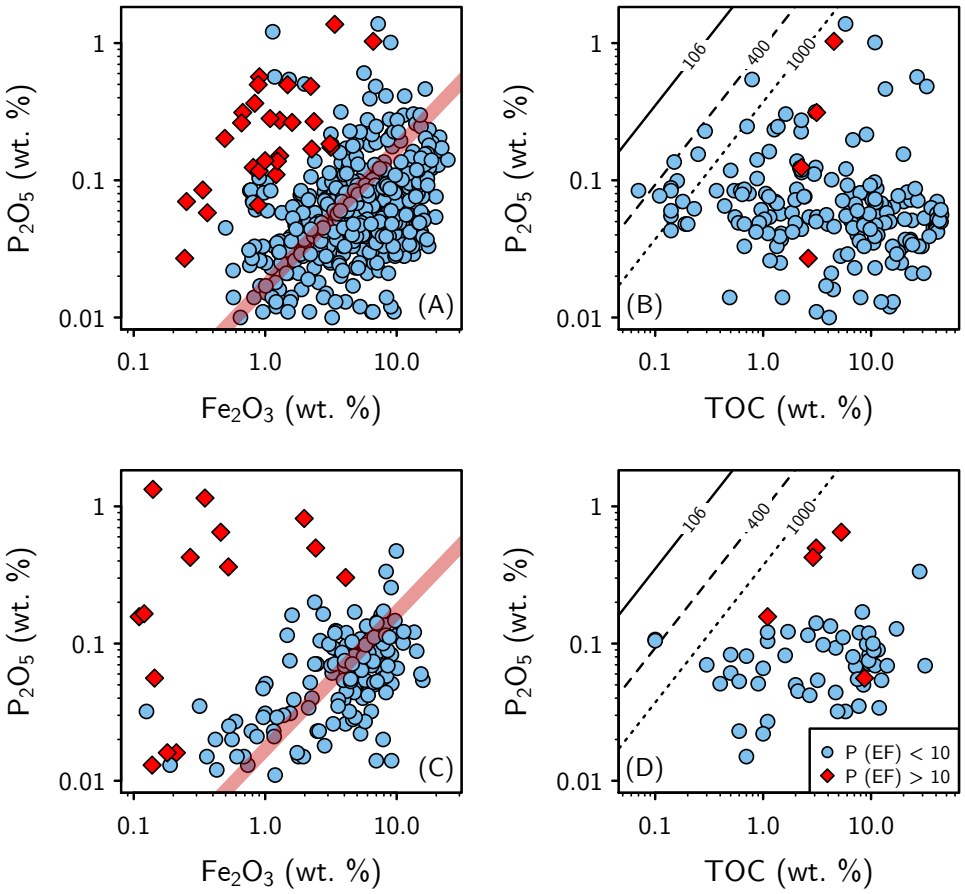

Figure 2.11: **P_2O_5 vs. Fe_2O_3 (A, C) and P_2O_5 vs. TOC (B, D) in core 12AB (A, B) and core 13A (C, D).** Red band in panels A and C denotes crustal P_2O_5/Fe_2O_3 ratio (0.167; Rudnick and Gao, 2014). Contours in panels B and D denote molar C:P ratios of 106, 400 and 1000. Red diamonds denote samples with P_2O_5/TiO_2 ratios that are 10x or more enriched relative to the crustal ratio (0.234; Rudnick and Gao, 2014); blue circles denote all other samples. Non-P-enriched samples tend to have P_2O_5/Fe_2O_3 ratios near the crustal value, while P-enriched samples have more P relative to Fe. The C/P ratios of all samples are much higher than observed in typical modern marine sediments or biomass, suggesting either extensive remineralization of organic-bound P or dilution via addition of migrated bitumen.

organic matter. As shown above, the correlation of P enrichment with both Ni and Cu is suggestive of such a mechanism (Fig. 2.10). However, this alone is not conclusive of organic matter dominating the P flux to sediments. In phosphogenic episodes, it is likely that greater organic matter export brought more P to sediments; however, in background intervals, detrital P seems to dominate the signal. Second, the migration of hydrocarbons during and after deposition of the ZF likely played a role in elevating the TOC content of these rocks. Thus, it is unclear to what extent the sedimentary C_{org}:P ratios reflect processes akin to what is observed in typical modern settings.

While observed co-variation (or lack thereof) of P_2O_5 with Fe_2O_3 and TOC does not clearly implicate either the Fe-scavenging or limited recycling mechanism for low Precambrian P levels, this dataset can perhaps be used to assess the third model: inefficient anoxic P burial (Ingall and Jahnke, 1994) leading to high marine P levels and high Precambrian productivity (Lenton et al., 2014). The fact that Ni and Cu pulses are stratigraphically-constrained to the same horizons that feature P enrichment (Figs. 2.3, 2.4) is suggestive of an increase in export production at these times. If productivity were in fact high even during background intervals, we might expect to see greater enrichments of Ni and Cu in those intervals than are observed. This doesn't mean that anoxia does not play a role in setting the efficiency of P burial – if anything, the fact that many P_2O_5/TiO_2 ratios plot below the crustal ratio could be suggesting that background P burial is indeed plagued by recycling of P out of sediments (cf. Ingall and Jahnke, 1994). Rather, our interpretation is that such a mechanism must be co-occurring with one or both of the other mechanisms described above, such that episodes of sedimentary P enrichment are the result of both heightened export production and permissive benthic redox conditions.

2.7 Conclusion

We have shown that sedimentary P enrichment in the ∼2.0 Ga Zaonega Formation was influenced by variable redox conditions as well as basinal restriction. One the one hand, this finding suggests that the low P levels observed in Precambrian shales could in some

instances be an artifact of deposition in a restricted basin. On the other hand, the fact that communication with the open ocean stimulated phosphogenesis seems at odds with the generally low P concentrations in shales of this age. One explanation for this discrepancy is that transient, global pulses of oxygenation spurred sporadic phosphogenesis throughout the Paleoproterozoic. Another, perhaps more parsimonious, interpretation is that semi-restricted basins are in some ways favorable for phosphogenesis, which is supported by the occurrence of other phosphorites in epicontinental seaways (Sheldon, 1981). Overall, this work suggests that the record of low P concentrations in marginal marine siliciclastic sedimentary rocks misses some of the dynamic behavior of the P cycle that was occurring during the Precambrian. Importantly, the fact that a global episode of phosphogenesis is restricted to the early-to-mid Paleoproterozoic likely tells us something about a change in sedimentary P burial at this time. Future work can help to disentangle whether the Paleoproterozoic phosphogenic episode was a result of a global increase in oxygenated seawater, a larger seawater sulfate reservoir, favorable tectonic conditions for deposition in epicontinental sea, or any combination of these and other effects.

2.8 References

Algeo, T.J., Luo, G.M., Song, H.Y., Lyons, T.W., Canfield, D.E., 2015. Reconstruction of secular variation in seawater sulfate concentrations. *Biogeosciences* 12, 2131–2151.

Algeo, T.J., Lyons, T.W., 2006. Mo–total organic carbon covariation in modern anoxic marine environments: Implications for analysis of paleoredox and paleohydrographic conditions. *Paleoceanography* 21.

Algeo, T.J., Tribovillard, N., 2009. Environmental analysis of paleoceanographic systems based on molybdenum–uranium covariation. *Chemical Geology* 268, 211–225.

Amelin, Y.V., Heaman, L.M., Semenov, V.S., 1995. U-Pb geochronology of layered mafic intrusions in the eastern Baltic Shield: implications for the timing and duration of Paleoproterozoic continental rifting. *Precambrian Research* 75, 31–46.

Anbar, A.D., Duan, Y., Lyons, T.W., Arnold, G.L., Kendall, B., Creaser, R.A., Kaufman,

A.J., Gordon, G.W., Scott, C., Garvin, J., Buick, R., 2007. A whiff of oxygen before the Great Oxidation Event? *Science* 317, 1903–1906.

Asael, D., Tissot, F.L., Reinhard, C.T., Rouxel, O., Dauphas, N., Lyons, T.W., Ponzevera, E., Liorzou, C., Chéron, S., 2013. Coupled molybdenum, iron and uranium stable isotopes as oceanic paleoredox proxies during the Paleoproterozoic Shunga Event. *Chemical Geology* 362, 193–210.

Benitez-Nelson, C.R., 2000. The biogeochemical cycling of phosphorus in marine systems. *Earth-Science Reviews* 51, 109–135.

Berner, R.A., 2004. A model for calcium, magnesium and sulfate in seawater over Phanerozoic time. *American Journal of Science* 304, 438–453.

Berner, R.A., 1973. Phosphate removal from sea water by adsorption on volcanogenic ferric oxides. *Earth and Planetary Science Letters* 18, 77–86.

Bjerrum, C.J., Canfield, D.E., 2002. Ocean productivity before about 1.9 Gyr ago limited by phosphorus adsorption onto iron oxides. *Nature* 417, 159–162.

Blättler, C.L., Claire, M.W., Prave, A.R., Kirsimäe, K., Higgins, J.A., Medvedev, P.V., Romashkin, A.E., Rychanchik, D.V., Zerkle, A.L., Paiste, K., 2018. Two-billion-year-old evaporites capture Earth's great oxidation. *Science* 360, 320–323.

Broecker, W.S., Peng, T.-H., 1982. Tracers in the Sea. Lamont-Doherty Geological Observatory, Columbia University.

Burnett, W.C., 1977. Geochemistry and origin of phosphorite deposits from off Peru and Chile. *Geological Society of America Bulletin* 88, 813–823.

Carignan, J., Wen, H., 2007. Scaling NIST SRM 3149 for Se isotope analysis and isotopic variations of natural samples. *Chemical Geology* 242, 347–350.

Chang, Y., Zhang, J., Qu, J.-Q., Xue, Y., 2017. Precise selenium isotope measurement in seawater by carbon-containing hydride generation-Desolvation-MC-ICP-MS after thiol resin preconcentration. *Chemical Geology* 471, 65–73.

Clark, L.L., Ingall, E.D., Benner, R., 1998. Marine phosphorus is selectively remineralized. *Nature* 393, 426–426.

Claypool, G.E., Holser, W.T., Kaplan, I.R., Sakai, H., Zak, I., 1980. The age curves of sulfur and oxygen isotopes in marine sulfate and their mutual interpretation. *Chemical Geology* 28, 199–260.

Cole, D.B., Zhang, S., Planavsky, N.J., 2017. A new estimate of detrital redox-sensitive metal concentrations and variability in fluxes to marine sediments. *Geochimica et Cosmochimica Acta* 215, 337–353.

Črne, A.E., Melezhik, V.A., Prave, A.R., Lepland, A., Romashkin, A.E., Rychanchik, D.V., Hanski, E.J., Luo, Z.-Y., 2013. Zaonega formation: FAR-DEEP hole 13A. *Frontiers in Earth Sciences* 7, 1008–1046.

Crusius, J., Calvert, S., Pedersen, T., Sage, D., 1996. Rhenium and molybdenum enrichments in sediments as indicators of oxic, suboxic and sulfidic conditions of deposition. *Earth and Planetary Science Letters* 145, 65–78.

Cutter, G.A., 1982. Selenium in reducing waters. *Science* 217, 829–831.

Derry, L.A., 2015. Causes and consequences of mid-Proterozoic anoxia. *Geophysical Research Letters* 42, 8538–8546.

Feely, R.A., Trefry, J.H., Lebon, G.T., German, C.R., 1998. The relationship between P/Fe and V/Fe ratios in hydrothermal precipitates and dissolved phosphate in seawater. *Geophysical Research Letters* 25, 2253–2256.

Filippelli, G.M., 2011. Phosphate rock formation and marine phosphorus geochemistry: The deep time perspective. *Chemosphere* 84, 759–766.

Filippelli, G.M., Sierro, F.J., Flores, J.A., Vázquez, A., Utrilla, R., Pérez-Folgado, M., Latimer, J.C., 2003. A sediment–nutrient–oxygen feedback responsible for productivity variations in Late Miocene sapropel sequences of the western Mediterranean. *Palaeogeography, Palaeoclimatology, Palaeoecology* 190, 335–348.

Föllmi, K.B., 1996. The phosphorus cycle, phosphogenesis and marine phosphate-rich deposits. *Earth-Science Reviews* 40, 55–124.

Fulton, J.M., Arthur, M.A., Freeman, K.H., 2012. Black Sea nitrogen cycling and the preservation of phytoplankton $\delta^{15}N$ signals during the Holocene. *Global Biogeochemical*

Cycles 26.

Galdobina, L.P., Sokolov, V.A., 1987. The Ludicovian super-horizon. Geology of Karelia. Nauka (Science), Leningrad 59–67.

Greber, N.D., Dauphas, N., Bekker, A., Ptáček, M.P., Bindeman, I.N., Hofmann, A., 2017. Titanium isotopic evidence for felsic crust and plate tectonics 3.5 billion years ago. *Science* 357, 1271–1274.

Gumsley, A.P., Chamberlain, K.R., Bleeker, W., Söderlund, U., Kock, M.O. de, Larsson, E.R., Bekker, A., 2017. Timing and tempo of the Great Oxidation Event. *Proceedings of the National Academy of Sciences* 114, 1811–1816.

Halevy, I., Alesker, M., Schuster, E.M., Popovitz-Biro, R., Feldman, Y., 2017. A key role for green rust in the Precambrian oceans and the genesis of iron formations. *Nature Geoscience* 10, 135–139.

Halevy, I., Peters, S.E., Fischer, W.W., 2012. Sulfate burial constraints on the Phanerozoic sulfur cycle. *Science* 337, 331–334.

Hansen, H.C.B., Poulsen, I.F., 1999. Interaction of synthetic sulphate "green rust" with phosphate and the crystallization of vivianite. *Clays and Clay Minerals* 47, 312–318.

Helz, G.R., Miller, C.V., Charnock, J.M., Mosselmans, J.F.W., Pattrick, R.A.D., Garner, C.D., Vaughan, D.J., 1996. Mechanism of molybdenum removal from the sea and its concentration in black shales: EXAFS evidence. *Geochimica et Cosmochimica Acta* 60, 3631–3642.

Holland, H.D., 1973. Systematics of the isotopic composition of sulfur in the oceans during the Phanerozoic and its implications for atmospheric oxygen. *Geochimica et Cosmochimica Acta* 37, 2605–2616.

Husson, J.M., Peters, S.E., 2018. Nature of the sedimentary rock record and its implications for Earth system evolution. *Emerging Topics in Life Sciences* 2, 125–136.

Ingall, E., Jahnke, R., 1994. Evidence for enhanced phosphorus regeneration from marine sediments overlain by oxygen depleted waters. *Geochimica et Cosmochimica Acta* 58, 2571–2575.

Ingall, E.D., Van Cappellen, P., 1990. Relation between sedimentation rate and burial of organic phosphorus and organic carbon in marine sediments. *Geochimica et Cosmochimica Acta* 54, 373–386.

Jahnke, R.A., 1984. The synthesis and solubility of carbonate fluorapatite. *American Journal of Science* 284, 58–78.

Jones, C., Nomosatryo, S., Crowe, S.A., Bjerrum, C.J., Canfield, D.E., 2015. Iron oxides, divalent cations, silica, and the early Earth phosphorus crisis. *Geology* 43, 135–138.

Joosu, L., Lepland, A., Kirsimäe, K., Romashkin, A.E., Roberts, N.M., Martin, A.P., Črne, A.E., 2015. The REE-composition and petrography of apatite in 2Ga Zaonega Formation, Russia: The environmental setting for phosphogenesis. *Chemical Geology* 395, 88–107.

Karhu, J.A., Holland, H.D., 1996. Carbon isotopes and the rise of atmospheric oxygen. *Geology* 24, 867–870.

Kipp, M.A., Algeo, T.J., Buick, R., submitted. Basinal hydrographic and redox controls on selenium enrichment and isotopic fractionation in Paleozoic black shales. *Geochimica et Cosmochimica Acta*.

Kipp, M.A., Stüeken, E.E., 2017. Biomass recycling and Earth's early phosphorus cycle. *Science Advances* 3, eaao4795.

Kipp, M.A., Stüeken, E.E., Bekker, A., Buick, R., 2017. Selenium isotopes record extensive marine suboxia during the Great Oxidation Event. *Proceedings of the National Academy of Sciences* 114, 875–880.

Kipp, M.A., Stüeken, E.E., Yun, M., Bekker, A., Buick, R., 2018. Pervasive aerobic nitrogen cycling in the surface ocean across the Paleoproterozoic Era. *Earth and Planetary Science Letters* 500, 117–126.

Koehler, M.C., Buick, R., Kipp, M.A., Stüeken, E.E., Zaloumis, J., 2018. Transient surface ocean oxygenation recorded in the ∼2.66 Ga Jeerinah Formation, Australia. *Proceedings of the National Academy of Sciences* 115, 7711–7716.

Konhauser, K.O., Lalonde, S.V., Amskold, L., Holland, H.D., 2007. Was there really an

Archean phosphate crisis? *Science* 315, 1234–1234.

Kump, L.R., Junium, C., Arthur, M.A., Brasier, A., Fallick, A., Melezhik, V., Lepland, A., CČrne, A.E., Luo, G., 2011. Isotopic Evidence for Massive Oxidation of Organic Matter Following the Great Oxidation Event. *Science* 334, 1694–1696.

Kurzawa, T., König, S., Labidi, J., Yierpan, A., Schoenberg, R., 2017. A method for Se isotope analysis of low ng-level geological samples via double spike and hydride generation MC-ICP-MS. *Chemical Geology* 466, 219–228.

Laakso, T.A., Schrag, D.P., 2018. Limitations on limitation. *Global Biogeochemical Cycles* 32, 486–496.

Laakso, T.A., Schrag, D.P., 2014. Regulation of atmospheric oxygen during the Proterozoic. *Earth and Planetary Science Letters* 388, 81–91.

Latimer, J.C., Filippelli, G.M., 2001. Terrigenous input and paleoproductivity in the Southern Ocean. *Paleoceanography* 16, 627–643.

Lenton, T.M., Boyle, R.A., Poulton, S.W., Shields-Zhou, G.A., Butterfield, N.J., 2014. Co-evolution of eukaryotes and ocean oxygenation in the Neoproterozoic era. *Nature Geoscience* 7, 257–265.

Lepland, A., Joosu, L., Kirsimäe, K., Prave, A.R., Romashkin, A.E., Crne, A.E., Martin, A.P., Fallick, A.E., Somelar, P., Üpraus, K., others, 2014. Potential influence of sulphur bacteria on Palaeoproterozoic phosphogenesis. *Nature Geoscience* 7, 20.

Li, Y.H., Schoonmaker, J.E., 2003. Chemical composition and mineralogy of marine sediments, in: Treatise on Geochemistry.

Lyons, T.W., Severmann, S., 2006. A critical look at iron paleoredox proxies: New insights from modern euxinic marine basins. *Geochimica et Cosmochimica Acta* 70, 5698–5722.

Martin, A.P., Prave, A.R., Condon, D.J., Lepland, A., Fallick, A.E., Romashkin, A.E., Medvedev, P.V., Rychanchik, D.V., 2015. Multiple Palaeoproterozoic carbon burial episodes and excursions. *Earth and Planetary Science Letters* 424, 226–236.

Melezhik, V.A., Fallick, A.E., Filippov, M.M., Larsen, O., 1999a. Karelian shungite—an indication of 2.0-Ga-old metamorphosed oil-shale and generation of petroleum: Geology,

lithology and geochemistry. *Earth-Science Reviews* 47, 1–40.

Melezhik, V.A., Fallick, A.E., Medvedev, P.V., Makarikhin, V.V., 1999b. Extreme $^{13}C_{carb}$ enrichment in ca. 2.0 Ga magnesite–stromatolite–dolomite–red beds' association in a global context: a case for the world-wide signal enhanced by a local environment. *Earth-Science Reviews* 48, 71–120.

Melezhik, V.A., Hanski, E.J., 2013. Palaeotectonic and palaeogeographic evolution of Fennoscandia in the Early Palaeoproterozoic, in: Reading the Archive of Earth's Oxygenation. Springer, pp. 111–178.

Melezhik, V.A., Medvedev, P.V., Svetov, S.A., 2013. The Onega Basin, in: Reading the Archive of Earth's Oxygenation. Springer, pp. 387–490.

Meybeck, M., 1982. Carbon, nitrogen, and phosphorus transport by world rivers. *American Journal of Science* 282, 401–450.

Mitchell, K., Mason, P.R., Van Cappellen, P., Johnson, T.M., Gill, B.C., Owens, J.D., Diaz, J., Ingall, E.D., Reichart, G.-J., Lyons, T.W., 2012. Selenium as paleo-oceanographic proxy: A first assessment. *Geochimica et Cosmochimica Acta* 89, 302–317.

Morford, J.L., Emerson, S., 1999. The geochemistry of redox sensitive trace metals in sediments. *Geochimica et Cosmochimica Acta* 63, 1735–1750.

Murray, J.W., 1975. The interaction of metal ions at the manganese dioxide-solution interface. *Geochimica et Cosmochimica Acta* 39, 505–519.

Niemann, H., Elvert, M., Hovland, M., Orcutt, B., Judd, A., Suck, I., Gutt, J., Joye, S., Damm, E., Finster, K., 2005. Methane emission and consumption at a North Sea gas seep (Tommeliten area). *Biogeosciences Discussions* 2, 1197–1241.

Orphan, V.J., House, C.H., Hinrichs, K.-U., McKeegan, K.D., DeLong, E.F., 2002. Multiple archaeal groups mediate methane oxidation in anoxic cold seep sediments. *Proceedings of the National Academy of Sciences* 99, 7663–7668.

Ovchinnikova, G.V., Kuznetsov, A.B., Melezhik, V.A., Gorokhov, I.M., Vasil'eva, I.M., Gorokhovskii, B.M., 2007. Pb-Pb age of Jatulian carbonate rocks: the Tulomozero Formation of southeast Karelia. *Stratigraphy and Geological Correlation* 15, 359–372.

Paiste, K., Lepland, A., Zerkle, A.L., Kirsimäe, K., Izon, G., Patel, N.K., McLean, F., Kreitsmann, T., Mänd, K., Bui, T.H., 2018. Multiple sulphur isotope records tracking basinal and global processes in the 1.98 Ga Zaonega Formation, NW Russia. *Chemical Geology* 499, 151–164.

Papineau, D., 2010. Global biogeochemical changes at both ends of the Proterozoic: insights from phosphorites. *Astrobiology* 10, 165–181.

Planavsky, N.J., 2014. The elements of marine life. *Nature Geoscience* 7, 855–856.

Planavsky, N.J., Rouxel, O.J., Bekker, A., Lalonde, S.V., Konhauser, K.O., Reinhard, C.T., Lyons, T.W., 2010. The evolution of the marine phosphate reservoir. *Nature* 467, 1088–1090.

Poulton, S.W., 2017. Biogeochemistry: Early phosphorus redigested. *Nature Geoscience* 10, 75–76.

Poulton, S.W., Canfield, D.E., 2006. Co-diagenesis of iron and phosphorus in hydrothermal sediments from the southern East Pacific Rise: Implications for the evaluation of paleoseawater phosphate concentrations. *Geochimica et Cosmochimica Acta*, 70, 5883–5898.

Price, N.B., Calvert, S.E., 1978. The geochemistry of phosphorites from the Namibian shelf. *Chemical Geology* 23, 151–170.

Priyatkina, N., Khudoley, A.K., Ustinov, V.N., Kullerud, K. are, 2014. 1.92 Ga kimberlitic rocks from Kimozero, NW Russia: Their geochemistry, tectonic setting and unusual field occurrence. *Precambrian Research* 249, 162–179.

Puchtel, I.S., Arndt, N.T., Hofmann, A.W., Haase, K.M., Kröner, A., Kulikov, V.S., Kulikova, V.V., Garbe-Schönberg, C.-D., Nemchin, A.A., 1998. Petrology of mafic lavas within the Onega plateau, central Karelia: Evidence for 2.0 Ga plume-related continental crustal growth in the Baltic Shield. *Contributions to Mineralogy and Petrology* 130, 134–153.

Puchtel, I.S., Brügmann, G.E., Hofmann, A.W., 1999. Precise Re–Os mineral isochron and Pb–Nd–Os isotope systematics of a mafic–ultramafic sill in the 2.0 Ga Onega plateau (Baltic Shield). *Earth and Planetary Science Letters* 170, 447–461.

Qu, Y., Črne, A.E., Lepland, A., Zuilen, M.A., 2012. Methanotrophy in a paleoproterozoic oil field ecosystem, Zaonega Formation, Karelia, Russia. *Geobiology* 10, 467–478.

Redfield, A.C., 1958. The biological control of chemical factors in the environment. *American Scientist* 46, 230A–221.

Reinhard, C.T., Planavsky, N.J., Gill, B.C., Ozaki, K., Robbins, L.J., Lyons, T.W., Fischer, W.W., Wang, C., Cole, D.B., Konhauser, K.O., 2017. Evolution of the global phosphorus cycle. *Nature* 541, 386–389.

Rudnick, R.L., Gao, S., 2003. Composition of the continental crust, in: Treatise on Feochemistry 3, 659.

Rue, E.L., Smith, G.J., Cutter, G.A., Bruland, K.W., 1997. The response of trace element redox couples to suboxic conditions in the water column. *Deep Sea Research Part I: Oceanographic Research Papers* 44, 113–134.

Ruttenberg, K.C., 2003. The global phosphorus cycle, in: Treatise on Feochemistry 8, 682.

Ruttenberg, K.C., Berner, R.A., 1993. Authigenic apatite formation and burial in sediments from non-upwelling, continental margin environments. *Geochimica et Cosmochimica Acta* 57, 991–1007.

Schlesinger, W.H., Bernhardt, E.S., 2013. Biogeochemistry: An Analysis of Global Change, 3rd ed. Academic Press.

Schulz, H.N., Schulz, H.D., 2005. Large sulfur bacteria and the formation of phosphorite. *Science* 307, 416–418.

Scott, C., Wing, B.A., Bekker, A., Planavsky, N.J., Medvedev, P., Bates, S.M., Yun, M., Lyons, T.W., 2014. Pyrite multiple-sulfur isotope evidence for rapid expansion and contraction of the early Paleoproterozoic seawater sulfate reservoir. *Earth and Planetary Science Letters* 389, 95–104.

Sheldon, R.P., 1981. Ancient marine phosphorites. *Annual Review of Earth and Planetary Sciences* 9, 251–284.

Slomp, C.P., Epping, E.H., Helder, W., Raaphorst, W.V., 1996. A key role for iron-bound phosphorus in authigenic apatite formation in North Atlantic continental platform sed-

iments. *Journal of Marine Research* 54, 1179–1205.

Stepanova, A.V., Samsonov, A.V., Larionov, A.N., 2014. The final episode of the Mid-Paleoproterozoic magmatism in the Onega Basin: data on dolerites in Zaonezhski peninsula. *Pros. Karel. Res. Centre RAS* 1, 3–16.

Stüeken, E.E., 2017. Selenium isotopes as a biogeochemical proxy in deep time. *Reviews in Mineralogy and Geochemistry* 82, 657–682.

Stüeken, E.E., Buick, R., Anbar, A.D., 2015a. Selenium isotopes support free O_2 in the latest Archean. *Geology* 43, 259–262.

Stüeken, E.E., Buick, R., Bekker, A., Catling, D., Foriel, J., Guy, B.M., Kah, L.C., Machel, H.G., Montañez, I.P., Poulton, S.W., 2015b. The evolution of the global selenium cycle: Secular trends in Se isotopes and abundances. *Geochimica et Cosmochimica Acta* 162, 109–125.

Stüeken, E.E., Foriel, J., Nelson, B.K., Buick, R., Catling, D.C., 2013. Selenium isotope analysis of organic-rich shales: advances in sample preparation and isobaric interference correction. *Journal of Analytical Atomic Spectrometry*28, 1734–1749.

Taylor, S.R., McLennan, S.M., 1995. The geochemical evolution of the continental crust. *Reviews of Feophysics* 33, 241–265.

Tribovillard, N., Algeo, T.J., Lyons, T., Riboulleau, A., 2006. Trace metals as paleoredox and paleoproductivity proxies: An update. *Chemical Geology* 232, 12–32.

Tyrrell, T., 1999. The relative influences of nitrogen and phosphorus on oceanic primary production. *Nature* 400, 525–531.

Van Cappellen, P., Ingall, E.D., 1996. Redox stabilization of the atmosphere and oceans by phosphorus-limited marine productivity. *Science* 271, 493–496.

Zegeye, A., Bonneville, S., Benning, L.G., Sturm, A., Fowle, D.A., Jones, C., Canfield, D.E., Ruby, C., MacLean, L.C., Nomosatryo, S., 2012. Green rust formation controls nutrient availability in a ferruginous water column. *Geology* 40, 599–602.

Chapter 3

BASINAL HYDROGRAPHIC AND REDOX CONTROLS ON SELENIUM ENRICHMENT AND ISOTOPIC COMPOSITION IN PALEOZOIC BLACK SHALES

This manuscript has been submitted to *Geochimica et Cosmochimica Acta*. Co-authors are Thomas Algeo and Roger Buick.

3.1 Abstract

Mass-dependent variations in selenium stable isotope ratios have recently been developed as a paleo-redox proxy. Since the reduction of selenium oxyanions occurs at a relatively high redox potential, this system holds promise for probing conditions relevant to the evolution and diversification of eukaryotic and animal life, which required substantial dissolved oxygen levels. Although several studies have identified selenium isotopic variability during oxygenation events in Earth's distant past, we still have only a coarse understanding of the mechanisms controlling this isotopic variability. This currently limits the robust interpretation of selenium isotope variability to first-order mechanisms driving large-magnitude changes. Here, we explore selenium isotope variability within and among Paleozoic black shales deposited on the North American continent that have been well-studied using a variety of other paleoenvironmental proxies. Using this combined dataset, we attempt to unravel the controls on selenium enrichments and isotope ratios in organic-rich ancient marine sedimentary rocks. We find that in the Late Pennsylvanian units, an estuarine nutrient trap on the Midcontinent Shelf enabled vigorous selenium recycling, leading to very high concentrations in sediments and progressive isotopic enrichment of the aqueous selenium reservoir. In contrast, we find that among the Late Devonian units, differences in local basinal hydrography led to a gra-

dient in selenium enrichment and isotopic fractionation, with the more restricted basins depleting their selenium reservoirs and causing isotopic enrichment. In both of these case studies, the additional context provided by complementary paleo-environmental proxies was critical for distinguishing between possible drivers of selenium isotopic variability. Extending these findings more broadly to other paleo-environmental settings, we suggest that the continued use of complementary datasets will enable the most robust use of the selenium paleo-redox proxy. Furthermore, the continued development of techniques for high-precision and phase-specific selenium isotope measurement will greatly improve the ability to deduce subtle redox fluctuations with this proxy.

3.2 Introduction

Evaluating the redox state of ancient seawater is a key aspect of studying Earth's environmental evolution. This task is critical to the study of rising oxygen levels throughout geologic history, environmental triggers of early animal evolution, kill mechanisms of mass extinction events, and even oceanographic mechanisms of carbon storage on glacial-interglacial timescales. As such, the paleoceanographic toolkit is always being refined to include novel paleo-redox proxies with ever-more precise informative power.

Over the last two decades there has been a surge of interest in trace-element proxies for paleo-redox conditions (Tribovillard et al., 2006; Anbar and Gordon, 2008; Algeo et al., 2012; Little et al., 2015). Studies of redox-sensitive trace-metal enrichment have proven greatly informative of first-order secular trends in Earth's stepwise oxygenation (Scott et al., 2008; Partin et al., 2013) and transient anoxic events in the more recent past (Brumsack, 2006). Taking this a step further, the field of "non-traditional" stable isotope geochemistry has recently grown into a discipline of its own (*e.g.*, Teng et al., 2017), creating a potentially richer source of information about oxidation-reduction reactions in a variety of paleo-environmental settings.

Some redox-sensitive trace-element isotopic systems have already yielded a wealth of information about modern and ancient redox processes in seawater. For instance, molybdenum

(Mo) isotopes in sulfidic black shales have become a well-established proxy for the global extent of anoxic and sulfidic seawater (Kendall et al., 2017) and have allowed inferences about the secular oxygenation of the Earth's ocean over billion-year timescales (Arnold et al., 2004; Dahl et al., 2010; Kendall et al., 2011; Chen et al., 2015; Kendall et al., 2015). Uranium (U) isotopes in carbonates have recently joined Mo as a quantitatively powerful global-ocean redox proxy, with sensitivity to the areal extent of anoxic sediments (cf. Tissot and Dauphas, 2015), and they have been used to study a wide range of events in deep time (Lau et al., 2016; Lau et al., 2017; Clarkson et al., 2018; Zhang et al., 2018; Tostevin et al., 2019). In addition to inferences about redox conditions in the global ocean, more localized redox assessments have been enabled by proxies such as the iodine content of carbonates (Lu et al., 2010; Lu et al., 2018). As iodate (IO_3^-) is quickly reduced to iodide (I^-) in sub-oxic water (*e.g.*, Rue et al., 1997), iodate incorporation in carbonates is only possible under fairly well-oxygenated waters. This high redox potential of the iodine system allows interrogation of redox fluctuations close to thresholds that are relevant to eukaryotic – including animal – life. However, without multiple stable isotopes the iodine system is less amenable to quantitative flux reconstructions than its aforementioned counterparts.

Although the above proxies all have demonstrable power in evaluating redox conditions in ancient seawater, there are gaps in their spatial, temporal and redox sensitivities that might be filled by other trace-element systems. The selenium (Se) system is particularly promising in this respect, since the high redox potential of Se oxyanion reduction is similar to that of iodate and nitrate (*e.g.*, Rue et al., 1997; Fig. 3.1). Furthermore, the marine residence time of Se (10^3-10^4 yr) is of a similar order of magnitude to the ocean mixing time (Broecker and Peng, 1982), meaning that it should yield more localized redox information than the Mo and U systems and respond to global perturbations on shorter timescales. With six stable isotopes, and an ability to shift between the -II, 0, +IV and +VI oxidation states in seawater, the Se system could conceivably encode a wealth of information about redox reactions in the marine environment. Despite this potential, Se isotopes remain much less studied than the aforementioned proxies.

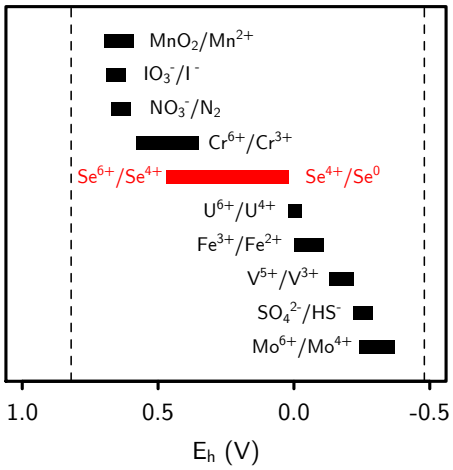

Figure 3.1: **Redox potentials of redox couplets commonly utilized in paleo-redox studies.** Data generated for a pH range of 7-8. Dashed lines denote stability field of liquid water. Reduction of selenium oxyanions begins at relatively high redox potentials, similar to the range for iodate and nitrate reduction (Rue et al., 1997).

There are several factors that conspire to make Se a difficult system to investigate. First, the measurement of Se isotope ratios is analytically and chemically challenging. Se volatilization during wet chemical sample preparation can alter Se concentrations and isotopic compositions, requiring vigilance during digestion and evaporation. Furthermore, the high ionization energy of Se requires sample introduction to the MC-ICP-MS via a hydride generator (HG-MC-ICP-MS), which can be a source of signal instability. Even following successful introduction to the plasma stream, Se measurement is complicated by substantial isobaric interferences from germanium, arsenic, krypton and – most insidiously – argon (Ar), which confounds analysis of the most abundant Se isotope (^{80}Se) through interference with Ar dimers. Beyond these analytical challenges, Se is generally present at very low abundance in geological materials, requiring digestion of large amounts of sample to obtain sufficient Se for precise analysis. Despite all of these complications, however, recent methodological developments in both the chemical preparation and analytical environment of Se isotope

analysis have successively pushed this isotopic system toward the realm of routine analysis (*e.g.*, Stüeken et al., 2013; von Strandmann et al., 2014; Kurzawa et al., 2017), opening up the possibility that Se isotope geochemistry can soon enter the standard toolkit of chemical oceanographers and paleoceanographers.

Although these advances have enabled the study of Se isotopic variability in a wide range of modern and ancient marine sediments, large gaps remain in our understanding of the behavior of Se and its isotopes across redox gradients in the modern ocean and during (de-)oxygenation events in Earth's past. Here, we attempt to leverage a wealth of data from other redox-sensitive elements to better evaluate the similarities and differences between the Se system and other proxies. Specifically, we focus on two sample sets of well-characterized black shales deposited on the North American continent during the late Paleozoic Era in two intervals: (a) the Late Pennsylvanian and (b) the Late Devonian. We measured Se concentrations and isotopic ratios in 65 samples from these units and compared the data to a variety of paleo-environmental indicators. In particular, we sought to determine the effects of watermass restriction and local redox conditions on Se enrichment and isotopic fractionation in these two settings. In doing so, we aimed to elucidate the mechanisms responsible for the observed variability in Se isotope ratios and enrichment factors among the study units, with broader implications for the further development of Se as a paleoceanographic proxy.

3.3 Selenium geochemistry

3.3.1 The selenium cycle

Selenium is a trace constituent of the upper continental crust, with a mean concentration of 60 ppb (Stüeken, 2017). Crustal Se is predominantly found in sulfide minerals, with Se substituting for sulfur. The Se isotopic composition (here and throughout the text reported in delta notation as $\delta^{82/78}$Se relative to Se NIST SRM 3149; Carignan and Wen, 2007) of the upper continental crust is estimated to be $\sim$0.0 $\pm$ 0.5‰ (Stüeken, 2017). The range of $\delta^{82/78}$Se values observed in bulk marine sediments deposited across all of Earth's history is

approximately –3‰ to +3‰ (Stüeken et al., 2015b; Mitchell et al., 2016), indicating that substantial isotopic fractionation of Se occurs during biogeochemical cycling.

The dominant input of Se to the modern ocean is oxidative continental weathering, whereby Se-II in crustal sulfides is oxidized to Se^{IV} or Se^{VI}, which form highly soluble oxyanions. The process of oxidative weathering typically induces rather small isotopic fractionations (<0.5‰; Johnson et al., 1999; Schilling et al., 2011). Weathering of exceptionally Se-rich shales (up ∼2 wt. % Se) has been shown to enable larger fractionations (Zhu et al., 2014), though this is neither thought to be representative of most weathering environments nor of net global inputs. Given generally small fractionations during weathering and transport, the riverine supply of Se to the ocean is thought to have an isotopic composition similar to the upper continental crust (∼0‰). Additional Se input from volcanic gases (which can contain H_2Se) plays a minor role in the global Se budget today (Stüeken, 2017), but could conceivably have been more important early in Earth's history prior to the onset of significant oxidative continental weathering in the late Archean (Stüeken et al., 2012). The isotopic composition of volcanic Se has not been directly constrained, and so it is assumed that this flux generally matches the isotopic composition of the upper crust and does not substantially alter the marine Se isotope mass balance.

Upon reaching the marine environment, Se is scavenged in the photic zone as an essential micronutrient, yielding nutrient-type vertical profiles in the ocean (Measures et al., 1980; Measures and Burton, 1980). The biological pump is the dominant vector of Se transport from surface waters to the deep ocean and marine sediments. Se has a short residence time (∼2-3 yr) as Se oxyanions in surface waters (Cutter and Bruland, 1984) and an intermediate residence time (10^3-10^4 yr, similar to oceanic mixing times) as regenerated Se oxyanions in the deep ocean (Broecker and Peng, 1982; Cutter and Bruland, 1984). The bioassimilation of Se by phytoplankton generally imparts a small isotopic fractionation (<0.6‰; Clark and Johnson, 2010), which may be negligible in natural systems if uptake is quantitative. The isotopic composition of Se in planktonic biomass should therefore approximate the isotopic composition of dissolved Se in seawater.

Owing to its low concentration (∼1-2 nM), there are very few direct measurements of Se isotope ratios in seawater. A recently developed method for determining the concentration and isotopic composition of Se in seawater yielded $\delta^{82/78}$Se values (scaled from $\delta^{82/76}$Se assuming mass-dependent fractionation) of +0.27‰ for deep waters of the NW Pacific Ocean (Chang et al., 2017). This closely agrees (within a 1σ analytical precision of +0.1-0.2‰; cf. Mitchell et al., 2012; Stüeken et al., 2015b, 2015c; this study) with a single measurement of phytoplankton biomass (+0.27‰; Mitchell et al., 2012), a single measurement of a deep-sea Fe-Mn nodule (+0.32‰; Rouxel et al., 2004), and mass balance calculations estimating the Se-isotopic composition of seawater as ∼+0.3‰ (Stüeken, 2017).

Marine sediments are commonly enriched in Se. Sediments deposited in oxic, open-ocean settings over the last ∼500 kyr have an average (geometric mean) Se concentration of 0.68 ppm (95% confidence interval of 0.55 to 0.83, $n = 100$), whereas sediments deposited in restricted, anoxic settings have systematically higher Se concentrations (geom. mean = 2.18 ppm; 95% confidence interval of 1.46 to 3.27 ppm, $n = 38$) (data compiled in Stüeken et al., 2015b). For this reason, the study of Se isotopes as a paleo-redox proxy has thus far focused predominantly on marine sediments with moderate to high Se concentrations. Our understanding of the processes controlling Se enrichment and isotopic fractionation in these settings is reviewed below.

3.3.2 The selenium isotope paleo-redox proxy

Removal of Se to marine sediments and fractionation of Se isotopes occur in conjunction with various biogeochemical processes. Remineralization of organic matter in sediments results in the release of some bio-assimilated Se, the fate of which is redox dependent. In oxic facies, adsorption of selenite onto Fe-Mn-oxides can be significant (cf. Balistrieri and Chao, 1990; Rovira et al., 2008). In reducing facies (*i.e.*, the targets of the present study), seawater Se removal follows two main pathways: (a) the burial of biologically-assimilated Se in organic matter, and (b) the sequestration of Se as reduced oxyanions. The relative importance of these two burial pathways is poorly constrained, though limited phase-specific

Se measurements in modern settings suggest that the resulting Se pools can comprise roughly similar proportions of total sedimentary Se (Velinsky and Cutter, 1990).

The first route is likely dominated by organic matter exported from the photic zone, where primary productivity is highest and phytoplankton have a nutritional demand for Se. The second route chiefly involves reductive immobilization of Se oxyanions liberated from biomass in deep waters or sediment porewaters. At reduction potentials similar to that of nitrate reduction (Fig. 1), Se oxyanions are reduced first to Se^0 and then potentially further to Se^{-II} (Oremland et al., 1989). Fully reduced Se^{-II} can substitute for sulfur in diagenetic sulfide minerals (*e.g.*, pyrite), which provide a stable host phase for Se on geological timescales due to the stoichiometric incorporation of Se in the mineral structure (Large et al., 2014, and references therein). Processes surrounding the burial of Se^0 are less well constrained. Reduction to Se^0 generates nanoparticles that can sink out of the water column and accumulate in sediments (Oremland et al., 1989; Velinsky and Cutter, 1990). It is unclear to what extent these particles withstand diagenetic and metamorphic conditions, but some amount of elemental Se appears to be recoverable from ancient marine sedimentary rocks (Kulp and Pratt, 2004). It is likely, though, that subsequent reduction to Se^{-II} on diagenetic timescales enables a considerable degree of Se incorporation into sulfides, as the Se content of pyrite in ancient marine sedimentary rocks (Kulp and Pratt, 2004) far exceeds the amounts detected in modern sediments (Velinsky and Cutter, 1990).

The bulk Se isotopic composition of reducing marine sediments is a function of both the biogenic (*i.e.*, organic-bound) fraction and the reductively immobilized (i.e., elemental and sulfide-bound) fraction. Due to the generally small isotopic fractionations associated with biological uptake and remineralization, the Se isotopic composition of biomass in marine sediments is thought to fairly closely match that of dissolved Se in the surface ocean ($\sim$+0.3‰; Mitchell et al., 2012; Stüeken et al., 2015b). In contrast, Se sequestered through oxyanion reduction can become substantially isotopically lighter than seawater if the process is non-quantitative, as Se reduction exerts a large kinetic isotopic preference for lighter isotopes (as much as –11‰; Johnson and Bullen, 2004). Non-quantitative reduction is thought

to be prevalent in sediments with suboxic porewaters or bottom waters that are connected to a large, oxic reservoir of Se oxyanions, thereby allowing renewed Se supply and precluding complete consumption of the dissolved Se pool.

Modern environments that likely harbor non-quantitative Se reduction include open-marine settings such as the mid-Atlantic (Johnson and Bullen, 2004), the Bermuda Rise (Shore, 2011), and the Arabian Sea (Mitchell et al., 2012). Bulk marine sediments from these open-marine settings over the last ∼500 kyr are slightly isotopically depleted relative to seawater ($\delta^{82/78}$Se = –0.10 ± 0.21‰, n = 100; data compiled in Stüeken et al., 2015b), likely reflecting a small degree of kinetic isotopic fractionation during non-quantitative reduction. The fact that only slight isotopic depletion is observed in these bulk marine sediments – in contrast to the large isotopic effects (up to several per mille) seen in laboratory settings (Johnson and Bullen, 2004) – may partly derive from dilution of the isotopically depleted signal (which is likely retained in the elemental and/or sulfide phase) by unfractionated Se in the organic phase (Stüeken et al., 2015b; Mitchell et al., 2016). Phase-specific Se recovery has been explored in a number of studies (Martens and Suarez, 1997; Kulp and Pratt, 2004; Clark and Johnson, 2010; Fan et al., 2011; Schilling et al., 2011; Schilling et al., 2014; Stüeken et al., 2015c), but isotopic data on specific phases in marine sedimentary rocks are limited to a single sample from a study of end-Permian shales (Stüeken et al., 2015c) and three measurements of a weathered outcrop of the Cretaceous Mancos Shale (Clark and Johnson, 2010). These data show that elemental and sulfide-hosted Se are indeed typically isotopically depleted relative to bulk-rock values, and that Se associated with recalcitrant organic matter comprises the dominant host-phase, with an isotopic composition similar to that of the bulk-rock (Clark and Johnson, 2010; Stüeken et al., 2015c). Other phase-specific concentration measurements (Kulp and Pratt, 2004) also show that organic matter is typically the dominant Se host phase in ancient marine sediments, which suggests that it could conceivably dilute larger isotopic fractionations that are preserved in the elemental and pyrite phases.

In contrast to settings with non-quantitative reduction, strongly anoxic and/or restricted

basins with complete reduction of dissolved Se oxyanions will not fractionate Se isotopes during burial. This causes the underlying bulk marine sediments to approximately record the isotopic composition of aqueous Se in that basin, allowing black shales deposited in these settings to be used to infer the Se isotopic composition of overlying waters. This is conceptually analogous to the use of strongly euxinic facies characterized by quantitative Mo scavenging for the purpose of estimating the Mo-isotopic composition of contemporaneous seawater. However, in the case of Se, (a) quantitative reduction is thought to be possible under anoxic – and not strictly euxinic – conditions (Oremland et al., 1989; Rue et al., 1997), and (b) the recorded isotopic ratio may not be representative of the global ocean due to the shorter marine residence time of Se (10^3-10^4 yr) than Mo ($>10^5$ yr; Morford and Emerson, 1999). Black Sea sediments yielded a $\delta^{82/78}$Se composition (avg. $+0.2 \pm 0.1‰$, $n = 12$; Mitchell et al., 2012) that is thought to record quantitative scavenging of aqueous Se from the overlying watermass, whose $\delta^{82/78}$Se composition is therefore not substantially offset from that of the open ocean. However, the effects of basinal restriction and hydrography on Se isotope signatures remain unexplored in ancient settings. In the present study, we evaluate these effects using proxies for watermass exchange with the open ocean.

3.3.3 Evolution of the global selenium cycle

Although modern marine Se cycling involves a large, oxic reservoir of Se oxyanions with reductive immobilization limited to porewaters or volumetrically-limited anoxic water columns, this does not describe the operation of the Se cycle in deep time prior to the oxygenation of the atmosphere and ocean. In Archean sediments deposited prior to the Great Oxidation Event (GOE), Se enrichments and isotopic fractionation are typically small – likely owing to limited oxidative weathering and efficient, quantitative oxyanion reduction in strongly anoxic oceans (Stüeken et al., 2015b). Notable exceptions occur during transient pulses of oceanic and atmospheric oxygenation wherein Se was evidently mobilized at higher rates and accumulated to higher concentrations in mildly oxic surface waters (Stüeken et al., 2015a; Koehler et al., 2018). The Se cycle was substantially perturbed by the GOE, with a sig-

nificant increase in Se enrichment in marine sediments and marked isotopic fractionation suggesting non-quantitative reduction in suboxic shallow waters (Kipp et al., 2017). The hypothesized mid-Proterozoic interval of reduced atmospheric pO_2 is marked by muted Se enrichment and isotopic variability (Stüeken et al., 2015b), followed by large isotopic excursions associated with the Neoproterozoic "Snowball Earth" glaciations that are thought to indicate progressive ocean oxygenation (von Strandmann et al., 2015). Following their first appearance in the Neoproterozoic, isotopically depleted marine sediments became more common in the Phanerozoic as well-oxygenated oceans with a large Se oxyanion reservoir and non-quantitative reduction became established (Stüeken et al., 2015b).

The units considered in the present study were deposited after deep-ocean oxygenation is thought to have occurred (Dahl et al., 2010; Chen et al., 2015; see review in Qie et al., 2019). This implies that a sizable Se oxyanion reservoir would have been available in open-marine settings, with any deviations from this signal likely attributable to local basinal restriction and redox chemistry rather than global secular changes in the marine oxygen inventory. We used a variety of major and trace elemental proxies to account for these potential local effects on Se enrichment and isotopic fractionation in a range of black shales deposited in the late Paleozoic.

3.4 Materials

3.4.1 Late Pennsylvanian: North American Midcontinent Sea

Paleogeoraphic context

The samples utilized in this study come from two intervals of deposition on the North American continent in the late Paleozoic Era. The first interval is the Late Pennsylvanian, during which time the North American Midcontinent Sea (NAMS) spread across the Laurentian Craton (Fig. 3.2A) at times of glacioeustatic highstand (Heckel, 1977, 1994; Algeo and Heckel, 2008). Marine waters were supplied at depth to the NAMS from oxygen-depleted intermediate depths of the eastern tropical Panthalassic Ocean (ETPO) (Algeo et al., 2008a,

2008b), which, in combination with terrestrial freshwater influx from surrounding mountains (indicated by depletion in carbonate $\delta^{18}O$ values; Joachimski and Lambert, 2015; Roark et al., 2017; Jimenez et al., 2019), led to a "superestuarine" circulation pattern in which oxygen-depleted marine waters underlay a reduced-salinity (probably brackish) surface layer (Algeo et al., 2008a, 2008b; Turner et al., 2019). Thick and laterally extensive organic-rich shales were deposited beneath these anoxic deep waters and are preserved across much of the midcontinent United States (Heckel, 1977, 1994; Algeo and Heckel, 2008).

The NAMS was separated into distinct basins by submarine structural highs, which prevented exchange of bottom waters (Heckel, 1977). The largest of these was the Mississippi River Arch, which divided the Midcontinent Shelf from the Illinois Basin (Fig. 3.2A) (Algeo and Herrmann, 2018). Spatial variation in sediment geochemistry across the NAMS has been used to identify lateral gradients in watermass chemistry (Herrmann et al., 2015, 2019) and sources of detrital siliciclastic material from the Laurentian Craton, Alleghenian Mountains, and Ouachita Mountains (Turner et al., 2019). The influx of terrigenous material and freshwater from these regions led to a counter-clockwise gyral surface circulation pattern (Turner et al., 2019), moving surface waters toward the Panhandle Strait, *i.e.*, the narrow corridor that connected the southwestern corner of the NAMS to the Midland Basin and Hovey Channel and thence to the ETPO (Algeo et al., 2008a, 2008b; Fig. 3.2A).

Stratigraphic context of drillcores

In this study, we utilized four organic-rich black shale units from three drillcores from the NAMS (Fig. 3.2A; Table 3.1). The Tacket Shale (lateral equivalent of the Hushpuckney Shale; cf. Algeo and Maynard, 2004; Cruse and Lyons, 2004) was investigated in drillcore C-TW-1 from the Oklahoma Geological Survey (cf. Cruse and Lyons, 2004; Algeo and Herrmann, 2018). The Stark and Muncie Creek shales of the Kansas City Group were investigated in the Edmonds #1A core from the Kansas Geological Survey (cf. Algeo and Maynard, 2004, 2008). The Teutopolis Shale of the Mattoon Formation (lateral equivalent of the Heebner Shale; cf. Turner et al., 2019) was investigated in the Englebart core from

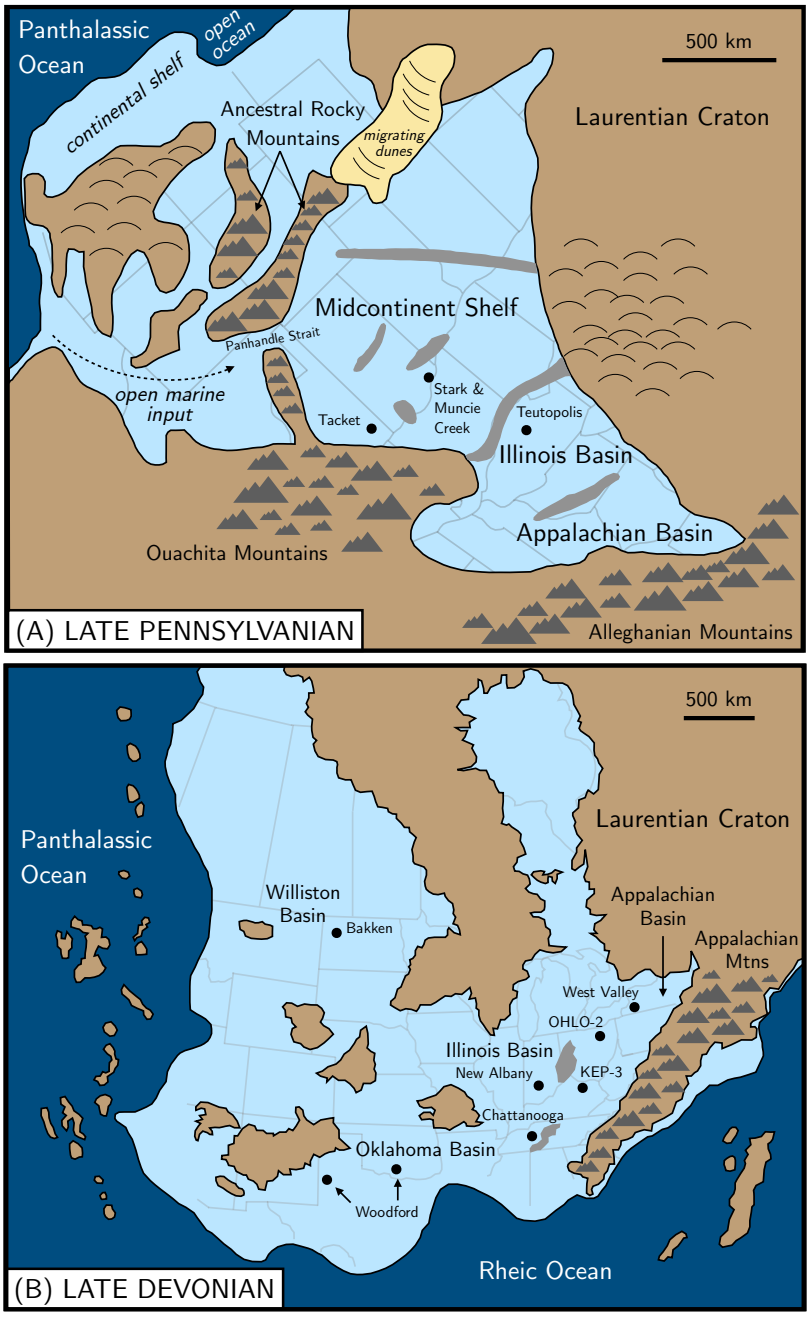

Figure 3.2: **Paleogeographic reconstruction of North America in the (A) Late Pennsylvanian and (B) Late Devonian.** All sample sites are denoted with labeled points. Grey bands denote submarine topographic highs separating basins. Maps were modified from Turner et al. (2019) and Algeo et al. (2007), respectively.

the Illinois Geological Survey. The Tacket, Stark, and Muncie Creek shales belong to the Missourian Stage, and the Teutopolis Shale to the Virgilian Stage of the North American Upper Pennsylvanian.

The three study sites represent a gradient in their proximity to marine source waters. The Tacket Shale was deposited nearest to the influx of marine waters through the Panhandle Strait, whereas the Stark and Muncie Creek shales were deposited toward the center of the Midcontinent Shelf (see Algeo et al., 2008a, their figure 5). The Teutopolis Shale was deposited in the Illinois Basin and so is likely to have experienced different bottom-water conditions due to lack of deep-water communication between the Illinois Basin and Midcontinent Shelf (Algeo and Herrmann, 2018). This hydrographic separation figures into our interpretation of controls on Se enrichment and isotopic variability between these units.

3.4.2 Late Devonian: North American Seaway

Paleogeographic context

The second interval considered in this study is the Late Devonian (and earliest Carboniferous at one locality; see below), when organic-rich black shales were widely deposited in multiple basins across the North American continent (Fig. 3.2B) in what is referred to as the North American Seaway (NAS) (Algeo et al., 2007). The basins within the NAS were typically silled and thus had limited bottom-water exchange with adjacent basins or the open ocean, although the degree of restriction was variable from basin to basin (Algeo et al., 2007). This variation in watermass restriction provides a basis for interpretation of variability in Se enrichment levels and isotopic compositions in the study units.

The easternmost of the black shale successions is from the Appalachian Basin. The oldest strata are found in the northern part of the basin, dating to the Middle Devonian with deposition of the Esopus and Needmore shales, followed by the Marcellus Group, Hamilton Group, and Geneseo through Dunkirk shales of early Late Devonian age (Werne et al., 2002; Sageman et al., 2003; Lash, 2017). The central and southern portions of the Appalachian

Basin host younger black shale successions, with deposition commencing in the Late Devonian, including the Ohio and Sunbury shales in the central Appalachian Basin and the Chattanooga Shale further south (Algeo et al., 2007). To the west, the Illinois Basin hosts Middle and Upper Devonian shales broadly assigned to the New Albany Shale (or New Albany Group) (e.g., Lineback, 1970). There, deposition commenced in the Middle Devonian with the Portwood and lower Blocher members, followed by the upper Blocher, Selmier, Morgan Trail, Camp Run and Clegg Creek members in the Late Devonian (Algeo et al., 2007). Still further west, widespread black shales across the central to southern Midcontinent region are assigned to the Woodford Formation (Over, 1992, 2002), which is up to ∼200 m thick in places and of Late Devonian age. To the north, uppermost Devonian and lowermost Carboniferous black shales of the Bakken Formation were deposited in the Williston Basin of North Dakota, Montana, and southern Alberta, and its lateral equivalent, the Exshaw Formation, was deposited in the Elk Point Basin of central and northern Alberta.

Stratigraphic context of drillcores

In this study, we analyzed black shale samples from eight sites representing multiple formations in several basins of the NAS (Table 3.1). This approach allowed us to evaluate Se concentrations and isotopic compositions in basins showing varying degrees of watermass restriction, from relatively weaker restriction along the southern margin of the NAS (*e.g.*, Oklahoma Basin) to relatively stronger restriction in craton-interior areas (*e.g.*, Illinois and Williston basins). The large Appalachian Basin, which extended from its silled southern margin in Tennessee >1000 km northward to the Catskill Delta complex in New York, is known to have exhibited internal lateral gradients in sediment chemistry and watermass properties (Algeo et al., 2007; Algeo and Tribovillard, 2009). These environmental conditions contributed to development of pervasive fine-scale (dm-thick) compositional cyclicity throughout this black shale succession (Liu et al., 2019).

In the northern Appalachian Basin, we analyzed the black shale succession of the Hanover and Dunkirk Formations in the West Valley core from western New York state

(cf. Sageman et al., 2003; Ver Straeten et al., 2011). In the central Appalachian Basin, we analyzed the Cleveland Member of the Ohio Shale in the OHLO-2 core from northern Ohio and the KEP-3 core from northern Kentucky (cf. Jaminski, 1997; Jaminski et al., 1998). In the southern Appalachian Basin, we sampled the Chattanooga Shale in the Dupont HGS drillcore from northern Tennessee (cf. Over et al., 2019; Song et al., 2019). In the Oklahoma Basin, we analyzed the Woodford Formation at three sites: the Ryan Shale Pit (RSP) and Classen Lake area YMCA (CLY) outcrops in south-central Oklahoma (cf. Over, 1992, 2002) and the Amoco A.J. Davis #9 (AJD) drillcore from Yoakum County, Texas. In the Williston Basin, we sampled the Upper Bakken Shale in the Texaco Thompson #5-1 core from Billings County, North Dakota (cf. Hartwell, 1998). We additionally compiled published Se concentration and isotopic data from the Camp Run member of the New Albany Shale (Mitchell et al., 2012). All of the sampled units listed above date to the Late Devonian (Frasnian-Famennian stages), with the exception of the Upper Bakken Shale, which was deposited in the earliest Mississippian.

3.5 Methods

3.5.1 Selenium measurements

Samples were prepared for Se isotope analysis following published protocols (Stüeken et al., 2013). Homogenized rock powders were dissolved in a mixture of concentrated HF, concentrated $HClO_4$, and 8 M HNO_3 at 130°C. Digests were then evaporated to incipient dryness and additional $HClO_4$ was added to ensure complete oxidation of recalcitrant organic matter. The final digests were evaporated to incipient dryness, 6 M HCl was added, and beakers were placed in a boiling water bath for at least 30 minutes in order to reduce all Se^{VI} to Se^{IV}. Solutions were then diluted to 0.6 M HCl and run through thiol cotton fiber (TCF) columns for isolation of Se. Following column chemistry, Se was liberated from the TCF by adding concentrated HNO_3 to the resin in test tubes, which were then placed in a boiling water bath for 20 minutes. Selenium was recovered from the solution in weak HNO_3 via

Table 3.1: **Location information for the 10 study sections.**

Section	Unit	Location	Curation
C-TW-1	Tacket	Tulsa Co., OK: T22N, R13E, Sec. 6 SE-NE-NE-SW-SE; 36.416°N, 95.957°W	Oklahoma GS
KGS Edmonds #1A (ED)	Stark	Leavenworth Co., KS: T9S, R22E, Sec. 35 SE-SE-NW-SW; 39.220°N, 94.933°W	Kansas GS
KGS Edmonds #1A (ED)	Muncie Creek	Leavenworth Co., KS: T9S, R22E, Sec. 35 SE-SE-NW-SW; 39.220°N, 94.933°W	Kansas GS
ISGS #1 Englebart (EB)	Teutopolis	Jasper Co., IL: 40' FSL, 340' FEL, Sec. 9, T8N, R8E; 39.146°N, 88.318°W; elev. 575'	Illinois GS
Western New York Nuclear Fuel Service #1 [NX-1], also "West Valley core" (WVC)	Hanover-Dunkirk	Cattaraugus County, NY (42.4457°N, 78.6344°W)	New York GS
OHLO-2	Cleveland Member, Ohio Shale	Loraine County, OH (41.4001°N, 82.2438°W, elev. 683 ft)	Ohio GS
KEP-3	Cleveland Member, Ohio Shale	Lewis County, KY (38.409°N, 83.437°W)	Kentucky GS
Dupont HGS (DHGS)	Chattanooga	Humphreys County, TN (36.075°N, 87.495°W)	Tennessee GS
Ryan Shale Pit (RSP)	Woodford	Pontotoc County, OK (34.674°N, 96.641°W)	outcrop
Classen Lake YMCA (CLY)	Woodford	Murray County, OK (34.46°N, 97.15°W)	outcrop
Amoco A.J. Davis #9 (AJD)	Woodford	Yoakum County, TX (33.14°N, 102.89°W) Block D, Sec. 514, 2173 FSL, 1430 FEL; elev. 3710'; J.H. Gibson survey	Texas BEG
Thompson	Upper Bakken	Billings County, ND (47.229 °N, 103.263 °W)	North Dakota GS

centrifugation. The weak HNO_3 solution was evaporated down to 0.5 mL at 55°C, at which point aqua regia (3:1 HCl:HNO_3) was added to the sample to remove germanium (Stüeken et al., 2013). The aqua regia solution was also evaporated down to 0.5 mL, at which point the sample was brought up in 6 M HCl and boiled in a water bath for 30 minutes to ensure quantitative reduction to Se^{IV}. The final sample solution was diluted to 0.6 M HCl for analysis.

The measurement of Se concentrations and isotope ratios was conducted on a Nu Plasma Multicollector Inductively Coupled Plasma Mass Spectrometer (MC-ICP-MS) in the Isotope Geochemistry Laboratory at University of Washington following analytical protocols described by Stüeken et al. (2013). Sample solutions were introduced to the MC-ICP-MS via a hydride generator (HG). Sample solutions were mixed in the HG with a $NaBH_4$ solution to catalyze the reduction of Se^{IV} to Se^{-II} (in the form of H_2Se), which was then carried across a teflon membrane and into the MC-ICP-MS via argon (Ar) carrier gas.

Lens voltage potentials, position of the plasma torch, and carrier gas flow rate were tuned daily to optimize signal strength and stability. Measurements were normalized using standard-sample bracketing with the Se NIST SRM 3149 solution (cf. Carignan and Wen, 2007) as the bracketing standard. Isobaric interferences deriving from Ar species were corrected following the method of Stüeken et al. (2013); other isobaric interferences were negligible within analytical precision and so were not corrected. All isotopic data are reported in delta notation relative to NIST reference SRM 3149. We report isotopic data as $\delta^{82/78}$Se values because this isotopic pair is the least affected by isobaric interferences under our analytical protocol.

Samples were analyzed in replicate whenever possible; the average analytical precision for all samples (1σ) was ±0.22‰ for $\delta^{82/78}$Se and ±7% for Se concentrations (relative error). Isotopic data obtained for in-house standard UW-McRae and USGS standard SGR-1 were +0.91 ± 0.18‰ (n = 11, separate digests) and –0.14 ± 0.28‰ (n = 4, separate digests), respectively, which are in agreement with previous studies (Mitchell et al., 2012; Stüeken et al., 2013, 2015b; Kurzawa et al., 2017; Kipp et al., 2017).

3.5.2 Published data compilation

Additional major and trace element data were compiled from published studies to supplement the Se data generated in this study. Where additional data had not been published, we made measurements following the protocols described below. All data that form the basis of conclusions drawn in this paper are reported in Tables 3.2-4 with corresponding references to original studies in the cases of compiled data.

3.5.3 Organic carbon and nitrogen measurements

The concentration and isotopic composition of total nitrogen and organic carbon were measured on de-carbonated powders following published protocols (Kipp et al., 2018). Bulk rock powders were treated with two overnight iterations of 6 M HCl to dissolve all carbonate phases. De-carbonated powders were then rinsed with 18 MΩ DI-H2O and dried in an oven at 60°C. The dried powders were weighed into tin cups for analysis. Total nitrogen (TN), total organic carbon (TOC), and the isotopic composition of bulk nitrogen ($\delta^{15}N$) and organic carbon ($\delta^{13}C$) were measured on single aliquots of decarbonated powder on a Costech ECS 4010 Elemental Analyzer coupled to a ThermoFinnigan MAT253 continuous flow isotope ratio mass spectrometer housed in IsoLab at the Department of Earth and Space Sciences, University of Washington. Combustion was carried out at 1000°C. The sample gases were carried through a reduced copper column to reduce NO_x species to N_2 and scrub excess O_2 from the gas stream. A magnesium perchlorate trap was then used to remove water from the gas stream. Raw data were corrected using a two-point calibration (Coplen et al., 2006) with three in-house standards: two glutamic acids (GA1, TOC = 40.8%, TN = 9.5%, $\delta^{13}C$ = -28.3‰, $\delta^{15}N$ = -4.6‰; GA2, TOC = 40.8%, TN = 9.5%, $\delta^{13}C$ = -13.7‰, $\delta^{15}N$ = -5.7‰) and dried salmon (SA, TOC = 45.7%, TN = 11.8%, $\delta^{13}C$ = -21.3‰, $\delta^{15}N$ = +11.3‰), which are calibrated to international reference materials USGS-40 and USGS-41 and were analyzed four times each per analytical session. Isotopic data are reported in delta notation relative to air for nitrogen and Vienna Pee Dee Belemnite (VPDB) for carbon. Analytical

blanks resulting from combustion were measured and subtracted from nitrogen data; analytical blanks were below detection limits for carbon. The average analytical precision (1σ) of isotopic measurements across all runs, as determined by replicate analyses of in-house standard UW-McRae ($\delta^{15}N$ = +5.6‰, $\delta^{13}C_{org}$ = -37.4‰), was ±0.3‰ for $\delta^{15}N$ and ±0.1‰ for $\delta^{13}C$. Average precision (relative error) of concentration measurements was ±2% for TN and ±0.5% for TOC.

3.5.4 Total sulfur measurements

For total sulfur (TS) analysis, bulk rock powders were weighed into tin cups along with V_2O_5 as a combustion aid. Measurements were conducted using a Eurovector Elemental Analyzer coupled to a ThermoFinnigan MAT253 continuous flow isotope ratio mass spectrometer housed in IsoLab at the Department of Earth and Space Sciences, University of Washington. Combustion was carried out at 1050°C. The combustion products were carried through a magnesium perchlorate trap to remove oxygen from the gas stream, followed by an 850°C quartz chip column to allow complete equilibration of oxygen isotopes in the resulting SO_2 with oxygen in the quartz chips (Fry et al., 2002). Raw data were corrected using a two-point calibration with three in-house standards: zinc sulfide (ZnS, TS = 32.9%) silver sulfide (Ag_2S, TS = 12.9%) and barium sulfate ($BaSO_4$, TS = 13.7%), which are calibrated to international reference material IAEA-S-1 and were analyzed three times each per analytical session. The average precision of TS measurements, as determined by replicate analyses of in-house standard $BaSO_4$, was ±2% (relative error).

3.6 Results

All new and compiled data for the Upper Pennsylvanian black shales of the NAMS are presented in Table 3.2. Selenium isotope ratios in this dataset range from –1.15‰ to +0.77‰, with unit averages showing >1‰ variation, *i.e.*, Muncie Creek = +0.50 ± 0.23‰ (n = 5), Tacket = –0.01 ± 0.37‰ (n = 7), Stark = –0.13 ± 0.47‰ (n = 6), and Teutopolis = –0.55 ± 0.32‰ (n = 7). Selenium concentrations range from 0.3 to 135.5 ppm. Selenium enrichment

factors (EF), calculated following the approach of Tribovillard et al. (2006), and with the same crustal Se/Al ratio (Se/Al = 1.74 x 10^{-5} g/g) that has been used in recent deep-time Se studies (Stüeken et al., 2015a; Koehler et al., 2018), range from 1.7 to 1465. Across all NAMS samples, $\delta^{82/78}$Se values positively correlate with TOC/TS (wt. %/wt. %) ($p < 0.01$; $R^2 = 0.58$, logarithmic regression) as well as Se (EF) ($p < 0.01$; $R^2 = 0.41$, linear regression) (Fig. 3.3).

No statistically significant correlations are observed between unit-average $\delta^{82/78}$Se values and proxies for redox or hydrographic conditions for the four Upper Pennsylvanian study units (Fig. 3.3). Nitrogen isotope ratios are nearly invariant (unit means range from +5.5‰ to +7.2‰) and do not correlate with $\delta^{82/78}$Se values ($p = 0.89$). Fe/Al ratios do not correlate with $\delta^{82/78}$Se values ($p = 0.89$) and are similar in all units except the Tacket Shale, which is relatively more Fe-rich. Similarly, DOP_T (the degree of pyritization as estimated from total S and Fe contents; Algeo et al., 2008b) is highest in the Tacket Shale, and across all units DOP_T is not correlated with $\delta^{82/78}$Se values ($p = 0.78$). Moderate differences are observed in unit-average Mo/TOC ratios (ppm/wt. %), which range from ∼3 to 10, but this variability is not correlated with $\delta^{82/78}$Se values ($p = 0.55$). Mean Sr/Ba (ppm/ppm) ratios of individual units range from 0.5 to 1.0 and do not correlate with $\delta^{82/78}$Se values ($p = 0.88$).

In contrast to the lack of relationships with unit-average values, individual data points within certain units show significant correlations between Se concentrations (ppm) and enrichment factors (EF) and other geochemical proxies. For example, Mo/TOC correlates positively with Se concentrations ($p < 0.01$, $R^2 = 0.31$, logarithmic regression) and Se (EF) ($p = 0.02$, $R^2 = 0.24$, logarithmic regression) for the units deposited on the Midcontinent Shelf (Tacket, Stark, Muncie Creek). Within these units, $\delta^{82/78}$Se values are also strongly correlated with Se (ppm) ($p < 0.01$, $R^2 = 0.48$). Note that this excludes the Teutopolis Shale, which was deposited in the Illinois Basin (Fig. 3.4) and thus was isolated from bottom-water exchange with the Midcontinent Shelf (Algeo and Herrmann, 2018).

All new and compiled data from the eight study units of the Late Devonian NAS are presented in Table 3. Compiled unit-average Mo/TOC and Sr/Ba ratios are presented in

Table 3.4. Selenium isotope ratios in these units range from –1.0‰ to +1.55‰, with unit averages showing ∼1.4‰ variation: Bakken = –0.31 ± 0.50‰ (n = 4), Woodford = –0.27 ± 0.56‰ (n = 9), Hanover-Dunkirk = –0.16 ± 0.28‰ (n = 4), Ohio Shale (KEP-3 core) = –0.16 ± 0.56‰ (n = 6), Chattanooga = +0.29 ± 0.83‰ (n = 6), New Albany (oxic) = +0.45 ± 0.16‰ (n = 5), Ohio Shale (OHLO-2 core) = +0.72 ± 0.33‰ (n = 7), and New Albany (anoxic) = +1.14 ± 0.25‰ (n = 5) (Fig. 5). Se concentrations range from 0.3 to 37.0 ppm (Fig. 3.5). Unlike in the NAMS shales, $\delta^{82/78}$Se values are only weakly correlated with TOC/TS (p ¡ 0.01, R2 = 0.17, logarithmic regression; Fig. 3.6A). Also unlike the NAMS shales, $\delta^{82/78}$Se values in the NAS samples are negatively correlated with δ^{15}N values ($p < 0.01$, $R^2 = 0.30$, linear regression; Fig. 3.6B). Se concentrations are also correlated with δ^{15}N values in the NAS samples ($p < 0.01$, $R^2 = 0.47$, logarithmic regression; Fig. 6C). Unit-average $\delta^{82/78}$Se values show a significant negative correlation with Mo/TOC ($p = 0.01$, $R^2 = 0.77$, logarithmic regression) (Fig. 3.7) for the NAS samples.

Across both datasets as a whole, Se concentrations are significantly higher in the Upper Pennsylvanian NAMS black shales than those from the Upper Devonian NAS (p ¡ 0.01; Fig. 8). The NAMS shales also have higher Sr/Ba ratios (p ¡ 0.01) and δ^{15}N values (p ¡ 0.01) than those from the NAS, but there is no significant difference in TOC ($p = 0.18$) or TS ($p = 0.48$) between the two datasets (Fig. 3.8).

3.7 Discussion

3.7.1 Late Pennsylvanian: Potential causes of isotopic variability among units

The large range of $\delta^{82/78}$Se values (Fig. 3.3A) observed in black shales of the NAMS (–1.15‰ to +0.77‰) spans much of the range of known Se isotopic variability from the geologic record. Furthermore, Se enrichment factors in the same samples span nearly 3 orders of magnitude (Fig. 3.3B). Together these data suggest a diversity of Se cycling regimes across these sites. The most positive $\delta^{82/78}$Se values co-occur with the largest Se enrichments (Fig. 3.3A, B), suggesting that a similar set of mechanisms controlled this covariation.

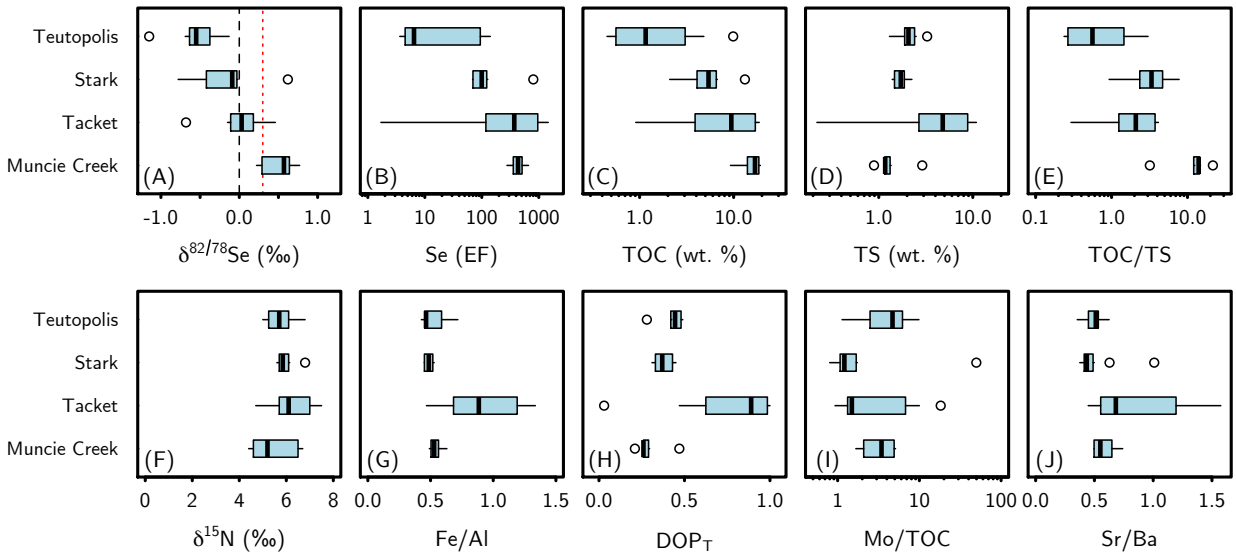

Figure 3.3: **Boxplot of (A) $\delta^{82/78}$Se, (B) Se (EF), (C) TOC (wt. %), (D) TS. (wt. %), (E) TOC/TS (wt. %/wt. %), (F) δ^{15}N, (G) Fe/Al (ppm/wt. %), (H) degree of pyritization (DOP_T), (I) Mo/TOC (ppm/wt. %), and (J) Sr/Ba (ppm/ppm) for Late Pennsylvanian units.** In panel A, upper crust composition is denoted with black dashed line; modern seawater composition is noted with red dotted line. The Sr/Ba values for Stark shale were calculated from 11 samples sitting 0-40 cm above the samples measured for Se isotopes. In this and subsequent boxplots, boxes are drawn as the limits of the first and third quartiles, whiskers comprise the 95% confidence interval, and black lines denote the median.

This wide range of Se enrichments and isotopic ratios conceivably could have arisen from variable redox conditions between the study sites. Specifically, sites with the most reducing bottom waters might be expected to have scavenged Se most efficiently, thereby leading to large Se enrichments and positive $\delta^{82/78}$Se values due to quantitative oxyanion reduction. In contrast, sites with bottomwaters that were suboxic or only transiently anoxic might have experienced non-quantitative Se reduction, thus yielding smaller Se enrichments and more negative $\delta^{82/78}$Se values. However, we do not see compelling evidence for such redox differences between sites.

Bulk-sediment δ^{15}N values are nearly constant across the study sites (Fig. 3.3F), suggesting that photic zone redox conditions were roughly similar in the different settings. The fact that δ^{15}N values are somewhat positive (+4 to +7‰; similar to modern marine sediments, cf. Tesdal et al., 2013) suggests that aerobic nitrogen cycling was occurring and a surface-water nitrate reservoir was present. As nitrate is reduced to N_2 via denitrification at a redox potential similar to that of Se oxyanion reduction (Fig. 3.1), this would seem to suggest that the upper water column was similarly favorable for Se oxyanion accumulation at each site. We therefore cannot invoke different surface-water redox conditions as a means to explain the variable Se enrichment and isotopic fractionation across the NAMS.

Bottom-water redox conditions also can be evaluated using Fe geochemistry. The similarities in Fe/Al (Fig. 3.3G) and DOP_T (Fig. 3.3H) across study sites – with the exception of the Tacket Shale, which has elevated values likely due to local euxinia (Cruse and Lyons, 2004; Algeo and Herrmann, 2018) – suggest that variable bottom-water redox conditions were not responsible for the observed variations in $\delta^{82/78}$Se or Se (EF). All Fe/Al and DOP_T values are consistent with anoxic deposition across the NAMS, as inferred in earlier studies (Algeo and Maynard, 2004; Algeo and Heckel, 2008).

If redox was not the dominant control on Se enrichment and isotopic fractionation across the NAMS, another possible mechanism for generating the observed variability in Se cycling is that basinal restriction influenced the size and isotopic composition of the aqueous Se reservoir. In modern anoxic, silled basins, rapid removal of redox-sensitive elements to the

sediment without sufficient resupply is known to diminish aqueous Mo concentrations (Algeo and Lyons, 2006), leading to lower sediment Mo/TOC ratios in more strongly restricted settings. We do observe some variability in Mo/TOC ratios across our dataset (Fig. 3.3I), but not in a fashion that clearly explains the Se trends observed in the NAMS samples. We also compiled Sr/Ba ratios from these samples, as this has recently been proposed as a paleosalinity proxy in shales (Wei et al., 2018; Wei and Algeo, 2019, this issue). Higher Sr/Ba ratios imply greater seawater influence (due to greater Sr concentrations relative to Ba, the latter being effectively scavenged in estuarine settings), but we do not observe much variability in Sr/Ba across the study sites. This suggests that variable seawater/freshwater mixing cannot account for the observed changes in Se cycling.

The lack of strong redox and salinity gradients across the NAMS is consistent with the recent findings of Algeo and Herrmann (2018). Notably, that study identified a large gradient in redox-sensitive trace metal enrichment across the NAMS, with strong enrichments of Mo, U and Zn limited to the most proximal areas of the Midcontinent Shelf. They inferred that this pattern was the result of a nutrient trap akin to that observed in modern estuaries (Shiller, 1996; Audry et al., 2006). In these settings, nutrients and trace metals are scavenged by organic matter and Fe-Mn-oxides and sink into bottom waters, where they are released through reductive dissolution of the host phases. Because bottom waters flow in the landward direction in estuarine circulation systems, this mechanism leads to a progressive concentration of nutrients and trace metals across the most proximal part of the deep watermass, *i.e.*, the "salt wedge" (Algeo and Herrmann, 2018). This process can lead to extreme local enrichments of nutrients and trace metals in sediments. In the case of the NAMS, a sharp drop in trace-metal enrichments between the Midcontinent Shelf and the Illinois Basin to its east was interpreted to represent a lack of deep-water exchange between those areas owing to the physical barrier of the Mississippi River Arch (Algeo and Herrmann, 2018).

Our Se data also seem to be best explained by the nutrient-trap mechanism. Se concentrations in Midcontinent Shelf samples correlate with Mo/TOC ratios (Fig. 3.4A), suggesting

a shared control on the enrichment of these elements. The Teutopolis Shale samples from the Illinois Basin also show a different trajectory with smaller Se enrichments (Fig. 3.4A), consistent with the isolation of deep waters of the Illinois Basin from the Midcontinent Shelf. The nutrient-trap mechanism also seems to account for the observed gradient in $\delta^{82/78}$Se values, with more positive $\delta^{82/78}$Se values occurring in the most trace-metal-enriched samples (Fig. 3.4A). One possible explanation for this trend is that non-quantitative Se sequestration in distal areas of the Midcontinent Shelf preferentially drew lighter Se isotopes into the sediments, enriching the residual aqueous Se in heavier isotopes, which were then captured via quantitative reduction in the more proximal shelf areas where nutrient trapping was operative. The lighter $\delta^{82/78}$Se values in the Teutopolis Shale are indicative of a separate deepwater Se reservoir that was not affected by the enrichment process operating in deep waters of the Midcontinent Shelf.

In this scenario of a nutrient-trap control on Se cycling on the Midcontinent Shelf, organic matter was likely the dominant shuttle for transfer of Se to deep waters. This is indicated by the similar trajectories of Se (EF) and TOC between study units (Fig. 3.3B, C). In contrast, Se enrichments do not correlate with TS (Fig. 3.3D), suggesting that Se transfer to the sediment was not controlled by rates of microbial sulfate reduction or pyrite formation. These observations are notable for two reasons. First, it may help to explain why Se is more strongly enriched than Mo in the Midcontinent Shelf samples (Fig. 3.4B). If substantial organic matter recycling was occurring in the NAMS water column, then Se may have been regenerated more efficiently than Mo, which was likely being recycled via Mn-oxide dissolution in sediment porewaters (and thus was prone to some degree of sequestration via co-precipitation with sulfide minerals). Second, dominance of total Se by the organic-bound fraction has important implications for bulk-rock Se isotopic compositions. As described above, enrichment of proximal bottom waters of the Midcontinent Shelf in heavy Se isotopes could explain the observed trend in $\delta^{82/78}$Se values.

An alternative possibility is that Se-isotopic variability reflects two-component mixing, in which organic Se and sulfide Se fractions have different $\delta^{82/78}$Se compositions. The limited

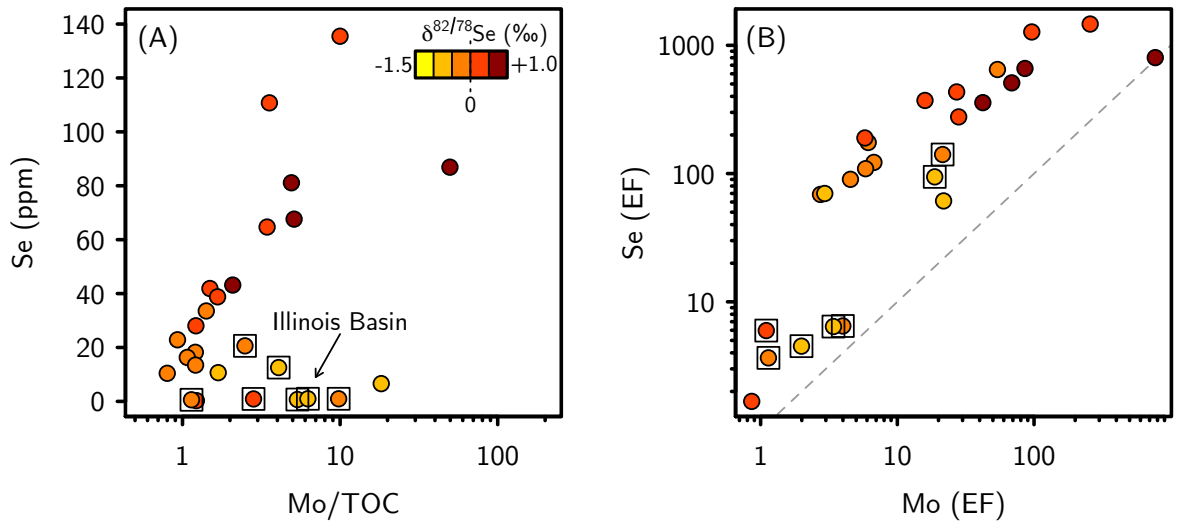

Figure 3.4: **Relationship between Se and Mo in Late Pennsylvanian units.** (A) Se (ppm) vs. Mo/TOC and (B) Se (EF) vs. Mo (EF). Coloration of data points denotes $\delta^{82/78}$Se values, with darker shading indicative of higher values. The positive correlation between Se enrichment and Mo/TOC in units within the Midcontinent Shelf environment suggests that the same mechanism was concentrating both trace metals. This is consistent with the nutrient-trap mechanism proposed by Algeo and Herrmann (2018). Furthermore, Se was being enriched relative to Mo by the nutrient trap, as evidenced by higher enrichment factors (EF) across the Midcontinent Shelf. The bottom waters that overlay the Teutopolis Shale in the Illinois Basin were isolated from exchange with the Midcontinent Shelf, thus giving distinct Se (ppm) vs. Mo/TOC and Se (EF) vs. Mo (EF) trends with smaller Se enrichments.

phase-specific data available suggest that Se can be present in subequal quantities in organic matter and sulfide minerals (Stüeken et al., 2015c), and this is also supported by Se data from phytoplankton biomass (Mitchell et al., 2012) and sedimentary pyrite (Large et al., 2014). Given plausible isotopic compositions for the organic and sulfidic components (*e.g.*, $\delta^{82/78}Se_{organic} = +0.3‰$ to $+1.0‰$, and $\delta^{82/78}Se_{sulfide} = -2.0‰$ to $-1.0‰$), it would be possible to generate the range of observed bulk-rock $\delta^{82/78}Se$ compositions in the NAMS black shales. In this case, as TOC levels increase, the organic Se fraction would become dominant over the sulfide fraction, leading to higher bulk-rock $\delta^{82/78}Se$ values (*i.e.*, approaching that of the organic-bound Se). We cannot disprove this possibility, but we regard it as secondary to the nutrient-trapping mechanism. The relationship of Se isotopes (Fig. 3A) to TOC (Fig. 3.3C) is strong, but not to TOC/TS (Fig. 3.3E). These observations suggest that the organic Se fraction exerts the dominant influence on the bulk-rock $\delta^{82/78}Se$ composition, which is consistent with the nutrient-trap hypothesis and a progressive isotopic enrichment of aqueous Se in the salt wedge toward the landward portion of the basin.

3.7.2 Late Devonian: Effect of watermass restriction on Se isotope ratios

The deposition of black shales in the Late Devonian NAS provides another case study of Se burial and isotopic fractionation in basins with variable redox and hydrographic conditions (Algeo et al., 2007). As in the Late Pennsylvanian NAMS, considerable Se isotopic variability is observed between units (Fig. 3.5), with $\delta^{82/78}Se$ values spanning much of the range observed in the geologic record. As in the NAMS dataset, the $\delta^{82/78}Se$ of NAS black shales correlates only weakly with TOC/TS ratios (Fig. 3.6A), suggesting that variable mixing of organic- and sulfide-bound Se fractions is not the dominant control on bulk-rock $\delta^{82/78}Se$ compositions.

For the NAS dataset, $\delta^{82/78}Se$ shows significant negative covariation with $\delta^{15}N$ (Fig. 3.6B). One possible explanation for this relationship is that watermasses with near-zero $\delta^{15}N$ values – which reflect systems scarce in nitrate and dominated by nitrogen fixation (Ader et al., 2016; Stüeken et al., 2016) – are also depleted in Se oxyanions, since Se reduction is initiated at redox potentials similar to denitrification (Fig. 3.1). This may be typical of more

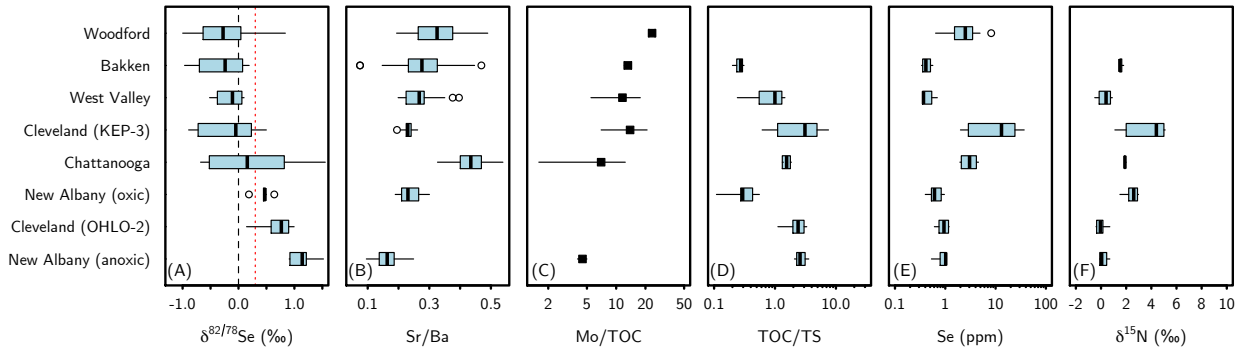

Figure 3.5: **Boxplot of (A) $\delta^{82/78}$Se values, (B) Sr/Ba, (C) unit-averaged Mo/TOC, (D) TOC/TS (wt. %/wt. %), (E) Se (ppm) and (F) δ^{15}N in Late Devonian units.** In panel A, upper crust composition is denoted with black dashed line; modern seawater composition is noted with red dotted line. Unlike in the NAMS black shales, $\delta^{82/78}$Se values do not closely correlate with TOC/TS. On the contrary, Mo/TOC and δ^{15}N show similar trajectories to the $\delta^{82/78}$Se values.

restricted settings in which nitrate is not readily replenished from a seawater source. Over time, such basins would tend to deplete their nitrate reservoirs, leading to strong nitrogen fixation as observed in the modern Black Sea (Fulton et al., 2012). A concurrent depletion of the Se oxyanion reservoir would result in progressive Se-isotopic enrichment. This inference is supported by the positive correlation between Se concentrations and δ^{15}N values in the NAS black shales (Fig. 3.6C). Units with near-zero δ^{15}N values indicative of a limited aqueous nitrate reservoir also tend to have low Se contents ($\sim$1 ppm or less). The only samples with Se concentrations >10 ppm also have δ^{15}N close to that of modern seawater nitrate ($\sim$+5‰), which is consistent with a close linkage between N and Se cycling. As redox conditions were more-or-less uniformly anoxic across all of the NAS basins (Algeo et al., 2007), we infer that differences in $\delta^{82/78}$Se between study units in different basins were due to variable degrees of basinal restriction and seawater renewal times.

Another way to test this hypothesis is to look for evidence of basinal restriction in other geochemical proxies. Basinal restriction commonly results in development of non-marine salinities, and paleosalinity variation in shale facies can be inferred from Sr/Ba ratios (Wei

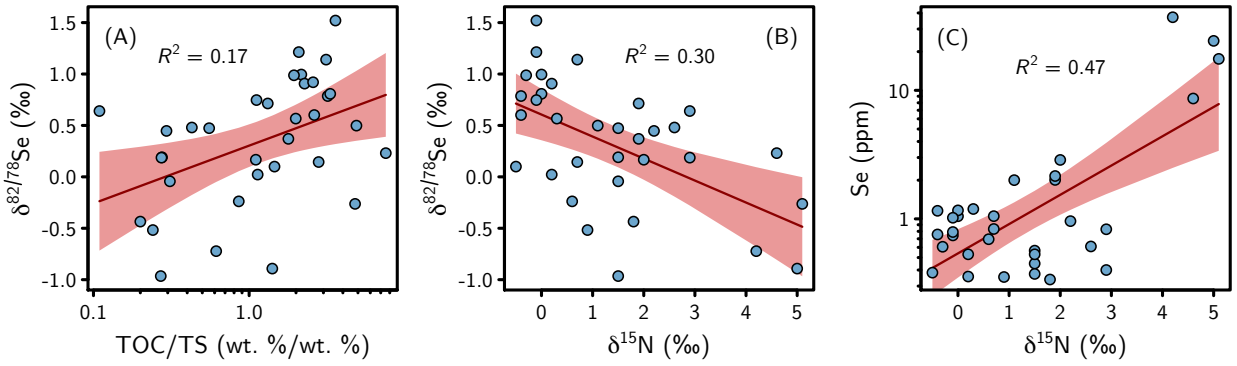

Figure 3.6: **Correlation between (A) $\delta^{82/78}$Se and TOC/TS, (B) $\delta^{82/78}$Se and δ^{15}N, and (C) Se (ppm) and δ^{15}N in Late Devonian units.** The relatively weak correlation between $\delta^{82/78}$Se and TOC/TS suggests that other factors altered the isotopic composition of the organic- and/or sulfide-bound Se fractions. The moderate negative correlation between $\delta^{82/78}$Se and δ^{15}N suggests that some portion of the Se oxyanion pool was being removed at high redox potentials similar to that of nitrate reduction. The muted Se concentrations in settings with near-zero δ^{15}N values suggest that depletion of the nitrate and Se oxyanion reservoirs was indeed concurrent. In contrast, the higher Se concentrations are found in samples with more positive δ^{15}N values, consistent with the presence of nitrate (and Se oxyanions) in the water column.

et al., 2018; Wei and Algeo, 2019, this issue). Across the NAS units sampled here, average Sr/Ba ratios range from 0.16 to 0.45 (Fig. 3.5; Table 3.4), which is consistent with mostly brackish (0.2-0.5) rather than marine salinity conditions (>0.5, as defined by Wei and Algeo, 2019, this issue). Thus, all of the interior NAS basins show a degree of watermass restriction, promoting mixing of seawater with freshwater runoff from the Laurentian Craton (cf. Liu et al., 2019; Song et al., 2019). However, unit-average Sr/Ba does not correlate strongly with $\delta^{82/78}$Se ($R^2 = 0.07$), perhaps because salinity and seawater renewal times are not strongly coupled in restricted-basinal settings (cf. Algeo and Lyons, 2006). Mo/TOC ratios can also reflect the degree of basinal restriction if bottom-water redox conditions are uniform (Algeo and Lyons, 2006), which is approximately true of NAS black shales (Algeo et al., 2007; note that the bioturbated gray shale horizons of the New Albany Shale were excluded from this analysis). In contrast to Sr/Ba, unit-average Mo/TOC exhibits a strong negative correlation with $\delta^{82/78}$Se (Fig. 3.7), which may indicate a hydrographic control on $\delta^{82/78}$Se in the NAS. Specifically, more restricted basins in which aqueous Mo is strongly depleted also tend to become more enriched in heavy Se isotopes as their Se reservoir is drawn down. We note that the $\delta^{82/78}$Se vs. Mo/TOC relationship is based on relatively few data (6 units), but it is supported by the Se-δ^{15}N relationships discussed above and by Sr/Ba evidence of generally brackish conditions, all of which are consistent with basinal restriction imparting a strong influence on Se isotopic compositions in the Late Devonian NAS.

The implication for controls on $\delta^{82/78}$Se compositions is that deepwater renewal in less restricted basins can replenish Se oxyanions, providing a larger Se reservoir that is less prone to quantitative reduction. This process can account for lower $\delta^{82/78}$Se in the Woodford Shale of the relatively open Oklahoma Basin relative to the more-restricted Appalachian and Illinois basin black shales. These data demonstrate the influence of basin hydrography on $\delta^{82/78}$Se values in reducing marine sediments, as previously inferred based on more limited evidence (Stüeken et al., 2015b). The implication for the use of $\delta^{82/78}$Se values as a paleo-redox proxy is that strongly restricted basins may not record signals that are representative of Se cycling in the open ocean. The marked Se-isotopic enrichment in anoxic

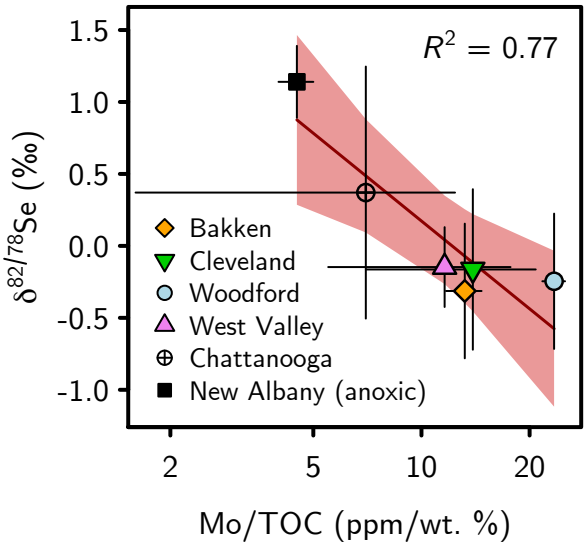

Figure 3.7: **Negative correlation between unit-averaged $\delta^{82/78}$Se and Mo/TOC in Late Devonian units.** More negative $\delta^{82/78}$Se values are found in units with higher Mo/TOC ratios, suggesting faster seawater replenishment, which may have enabled non-quantitative Se oxyanion reduction.

horizons of the New Albany Shale provides no evidence of non-quantitative oxyanion reduction, which could be interpreted as evidence of anoxic deep oceans. However, the Woodford Shale, which was accumulating at the same time and in closer proximity to the open ocean, recorded modern-seawater-like $\delta^{82/78}$Se values, which may be more representative of global Se cycling during the late Devonian. We therefore recommend that, when employing the Se isotope proxy in deep time, complementary datasets such as δ^{15}N, Sr/Ba and Mo/TOC be generated and evaluated across differing formations of similar age and setting. Although each paleoenvironmental proxy faces its own limitations, a combined approach allows the strongest possible inferences about ancient watermass chemistry. This will be particularly important for application of Se isotopes in the Precambrian, where comparatively little is known about the paleogeographic context of black shale basins.

3.7.3 Comparing controls on Se in Upper Pennsylvanian and Upper Devonian black shales

We close by comparing and contrasting the dominant controls on Se enrichment and isotopic fractionation between shales deposited in the Late Pennsylvanian NAMS and the Late Devonian NAS. The most pronounced difference between these two ancient seaways is that Se concentrations reach far higher levels in the NAMS (particularly on the Midcontinent Shelf) than in any of the Late Devonian NAS basins (Fig. 3.8). Several factors are likely to have contributed to this difference.

First, as noted in Section 3.7.2, the Late Devonian NAS basins appear to have been more restricted (as evidenced by lower Sr/Ba ratios; Fig. 3.8) than the Midcontinent Shelf and Illinois Basin in the Late Pennsylvanian. Due to slower seawater renewal times, the waters overlying the NAS shales became depleted in nitrate (as evidenced by lower δ^{15}N values) and likely also Se oxyanions (as evidenced by lower Se enrichment; Fig. 3.8). Importantly, these differences do not correspond to variations in TOC or TS content (Fig. 3.8), suggesting that the capacity for Se enrichment was limited in the NAS basins despite similarly anoxic bottom water conditions and a similar capacity for shuttling trace metals to deep waters. These considerations highlight the importance of basinal hydrography in controlling the

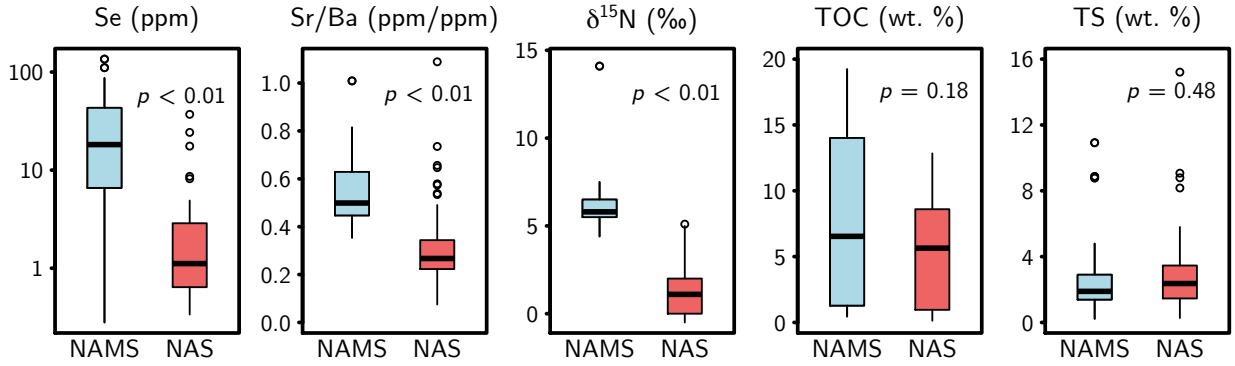

Figure 3.8: **Differences in redox, hydrography and Se cycling between the Late Pennsylvanian NAMS and the Late Devonian NAS.** Low Se concentrations in the NAS are likely the result of basinal restriction (evidenced by low Sr/Ba ratios) and Se oxyanion depletion (suggested by low $\delta^{15}N$ values, which imply nitrate depletion). The difference in Se concentrations between the NAMS and NAS is not due to differing TOC or TS contents, suggesting that the controls have to do with watermass circulation and seawater renewal instead of local bottom-water redox conditions.

degree of Se enrichment in restricted marine basins.

Second, the processes by which Se became enriched in the sediment differed between the Late Pennsylvanian and Late Devonian seaways. As described in Section 3.7.1, Se enrichment on the Midcontinent Shelf of the NAMS was likely due to a nutrient-trapping mechanism linked to its quasi-estuarine circulation pattern (Algeo et al., 2008a, 2008b; Algeo and Herrmann, 2018). These conditions not only promoted strong Se uptake by the sediment but led to significantly greater Se enrichment relative to other redox-sensitive trace metals, including Mo, U and V (Fig. 3.9). This pattern was probably due to Se being shuttled to deep waters mainly via sinking organic matter, which was more efficiently recycled in the water column than the Fe-Mn-oxides that transported trace metals such as Mo to the sediment-water interface. In contrast, the Late Devonian NAS basins, which were not characterized by the same sort of nutrient trap, show Se enrichments that are on par with other redox-sensitive trace metals such as U and V (Fig. 3.9B, C), and Mo is actually more enriched than Se in some Upper Devonian shales (Fig. 3.9A). As noted in Section 3.7.2, depletion of the Se oxyanion

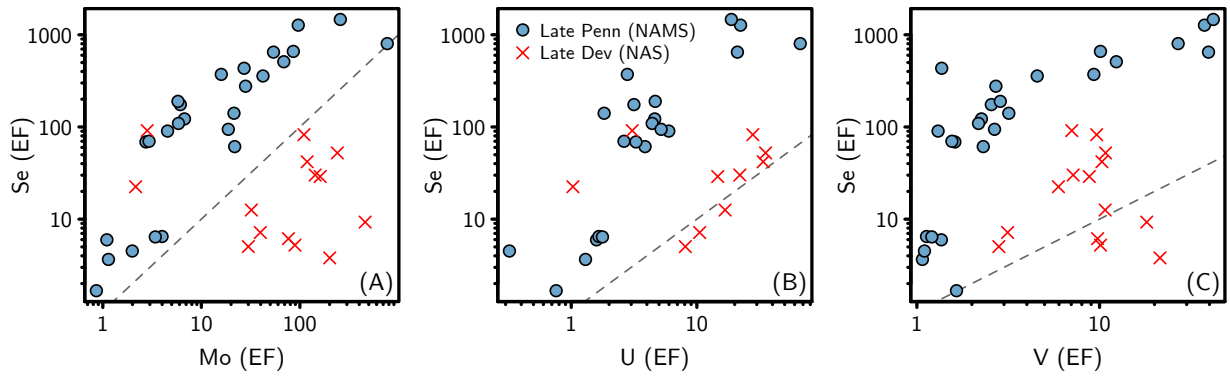

Figure 3.9: **Selenium enrichment factors relative to molybdenum (A), uranium (B) and vanadium (C).** The greater enrichment of Se relative to other redox-sensitive trace metals in the NAMS shales suggests that Se was more effectively recycled by the estuarine nutrient trap. In contrast, Se is not preferentially enriched relative to U and V in the NAS black shales, which did not feature a nutrient trap. The higher Mo enrichment relative to Se in the NAS samples may reflect depletion of the aqueous Se reservoir faster than the Mo reservoir at redox potentials higher than that required for Mo scavenging (*i.e.*, euxinic conditions).

reservoirs in the more restricted NAS basins occurred alongside nitrate depletion, but to a lesser degree than Mo depletion. This suggests that Se was being reductively immobilized at relatively high redox potentials, similar to nitrate reduction but above the redox potential at which Mo is efficiently scavenged (cf. Helz et al., 1996), impeding quantitative removal of aqueous Mo to the sediment. Thus, including Se in paleo-redox studies can provide additional insights into water column redox thresholds by adding a high-redox-potential species to the arsenal of trace-metal-enrichment proxies (cf. Tribovillard et al., 2006).

An important implication of both datasets is that bulk-rock $\delta^{82/78}$Se values in restricted basins can substantially diverge from open-ocean signatures. For deep-time applications of the $\delta^{82/78}$Se proxy, it is therefore imperative to constrain the degree of open-ocean exchange when interpreting $\delta^{82/78}$Se data in the context of global redox evolution. In the present study, we found that combining $\delta^{82/78}$Se data with proxies for basinal restriction (Sr/Ba,

Mo/TOC) and redox chemistry ($\delta^{15}N$, Fe/Al, DOP) provided a useful context for evaluating the significance of Se isotopic variations. Such an integrated approach will be critical in order to make the most effective use of $\delta^{82/78}Se$ as a proxy for Earth's secular oxygenation history.

3.8 Conclusion

We have analyzed Se concentrations and isotope ratios in a range of black shales deposited in epicontinental seas in the late Paleozoic. When viewed within the context provided by other major and trace elemental data, the Se data seem to reflect differences in both local redox conditions and basinal hydrography. On the Midcontinent Shelf of the Late Pennsylvanian NAMS, a quasi-estuarine nutrient trap concentrated Se and other trace metals in saline deep waters that became progressively isotopically enriched through successive recycling of organic-bound Se. In contrast, isotopic variability among basins in the Late Devonian NAS appears to have been controlled by differing hydrographic conditions, where more restricted settings featured Se oxyanion reduction alongside nitrate reduction with limited re-supply from the open marine reservoir. This caused the more restricted basins to record smaller Se enrichments and greater isotopic enrichment, in contrast to settings that received greater seawater influx. In both the NAMS and NAS datasets, the additional context provided by TOC, TS, Mo/TOC, Sr/Ba, Fe/Al, DOP, and $\delta^{15}N$ greatly helped in resolving the environmental drivers of variability in Se enrichment and isotopic composition. Extending these findings to other paleo-environmental settings, our results suggest that restricted basins are prone to record Se isotopic enrichment if not regularly replenished with a seawater source of Se oxyanions, which can make these settings unsuitable for assessing global redox conditions. The future utilization of Se isotopes as a paleo-redox proxy will greatly benefit from a concerted effort to make high-precision, phase-specific measurements, as well as from the use of complementary datasets to resolve aspects of basinal redox and hydrography that can provide critical context for Se isotopic interpretations.

Table 3.2: **Geochemical data from Late Pennsylvanian shales.**

unit	sample	Se (ppm)	$\delta^{82/78}$Se (‰)	1σ	TOC (%)	TS (%)	δ^{15}N (‰)	Al (%)	Fe (%)	Mo (ppm)	DOP_T
Muncie Creek	EDM 27-9	67.6	0.77	0.27	14.01	1.16	6.7	7.62	3.84	71.56	0.26
Muncie Creek	DMB-10	81.1	0.64	0.08	16.87	1.17	6.5	7.06	3.98	82.85	0.26
Muncie Creek	DMB-50	43.2	0.57	0.20	19.23	0.89	5.2	6.94	3.67	40.06	0.21
Muncie Creek	DMB-60 38.8	0.22	0.26	18.54	1.32	4.4	8.05	3.95	30.96	0.29	
Muncie Creek	DMB-73	64.7	0.29	0.04	9.26	2.90	4.6	8.58	5.41	31.87	0.47
Stark	S-ED-X4	86.9	0.62	0.30	13.18	1.70	6.8	6.22	3.29	655.71	0.45
Stark	S-ED-X26	18.2	-0.11	0.31	6.54	1.39	5.6	8.56	3.86	7.89	0.31
Stark	S-ED-X28	16.3	-0.03	0.07	6.41	1.47	6.0	8.58	3.86	6.87	0.33
Stark	S-ED-X31	13.5	-0.07	0.21	4.40	1.87	5.7	8.58	4.37	5.33	0.37
Stark	S-ED-X32	10.4	-0.42	0.32	4.08	1.73	5.7	8.70	4.03	3.26	0.37
Stark	S-ED-X33	10.7	-0.78	0.20	2.09	2.25	6.1	8.76	4.54	3.53	0.43
Tacket	275.2	0.3	0.03		0.91	0.22	4.7	9.48	6.99	1.12	0.03
Tacket	216-222	41.9	0.03	0.18	9.45	8.78	6.1	6.47	6.77	14.10	0.97
Tacket	202.5-205.0	33.6	-0.15	0.10	15.51	10.92	5.6	2.97	7.33	21.96	1.00
Tacket	174.0-176.3	110.8	0.33	0.20	18.51	8.87	5.8	5.00	6.68	65.89	1.00
Tacket	132.0-134.5	135.5	0.46	0.17	18.71	4.79	14.1	5.31	4.70	186.89	0.89
Tacket	84.5-87.5	6.6	-0.68	0.07	1.01	3.46	7.5	6.18	3.89	18.42	0.78
Tacket	57	22.9	-0.07	0.09	6.77	1.89	6.5	7.51	3.51	6.29	0.47
Teutopolis	5	0.6	-0.46	0.20	1.28	1.30	5.0	9.32	3.98	1.45	0.28
Teutopolis	15	0.7	-0.55		0.45	1.90	5.0	8.78	3.98	2.39	0.42
Teutopolis	35	1.0	-0.13	0.21	0.47	1.87	5.5	8.50	3.91	4.64	0.42
Teutopolis	45	1.0	-0.69	0.12	0.65	2.31	5.7	8.66	4.06	4.04	049
Teutopolis	55	2.2	-1.15	0.12	1.16	2.07	6.0				
Teutopolis	75	20.6	-0.29	0.22	9.89	3.27	6.8	8.40	6.03	24.64	0.47
Teutopolis	91	12.6	-0.58	0.16	4.82	2.50	6.2	7.65	4.5	19.64	0.48

Table 3.3: **Geochemical data from Late Devonian shales.**

unit	sample	Se (ppm)	$\delta^{82/78}$Se (‰)	1σ	TOC (%)	TS (%)	δ^{15}N (‰)
Dunkirk	WVC754-14	0.7	-0.24	0.54	1.89	2.20	0.6
Dunkirk	WVC754-2-5	0.4	-0.52		0.65	2.69	0.9
Hanover	WVC785-13	0.4	0.02		2.26	2.00	0.2
Hanover	WVC785-8	0.4	0.10		2.64	1.82	-0.5
Woodford	RSP-22	2.6	-0.30	0.25		0.44	
Woodford	RSP-40	8.2	-0.87	0.62		0.79	
Woodford	AJD-507	0.6	-0.36			0.52	
Woodford	AJD-513	1.1	-0.14			0.65	
Woodford	CLY-12	1.5	-1.00	1.05		0.27	
Woodford	CLY-24	4.9	0.24	0.43		2.22	
Woodford	CLY-26	3.2	0.84	0.16		15.21	
Woodford	CLY-30	1.9	-0.25			1.53	
Woodford	CLY-33	2.4	-0.63	0.05		1.92	
Ohio Shale	OHLO-2 540'0"	1.1	1.00		7.94	3.67	0.0
Ohio Shale	OHLO-2 530'0"	0.8	0.60		7.02	2.68	-0.4
Ohio Shale	OHLO-2 519'9"	1.2	0.81	0.13	7.00	2.11	0.0
Ohio Shale	OHLO-2 510'0"	1.2	0.57	0.13	5.24	2.63	0.3
Ohio Shale	OHLO-2 469'7"	0.6	0.99		7.20	3.71	-0.3
Ohio Shale	OHLO-2 460'0"	0.7	0.75		5.72	5.13	-0.1
Ohio Shale	OHLO-2 309'3"	0.8	0.14		4.92	1.76	0.7
Chattanooga	Dup-75	2.2	0.37	0.59	10.36	5.80	1.9
Chattanooga	Dup-64	4.6	-0.38	0.12			
Chattanooga	Dup-54	2.7	1.55				
Chattanooga	Dup-60	2.0	0.93	0.15			
Chattanooga	Dup-33	3.8	-0.66	0.01			
Chattanooga	Dup-15	4.5	-0.06	0.33			
Ohio Shale	K3-17-9/2	2.9	0.17	0.18	2.66	2.41	2.0
Ohio Shale	K3-17-9/10	2.0	0.50	0.21	6.60	1.35	1.1
Ohio Shale	K3-12-8/9	24.3	-0.89	0.15	12.38	8.79	5.0
Ohio Shale	K3-12-8/4	37.0	-0.72	0.15	5.57	9.07	4.2
Ohio Shale	K3-12-8/3	8.6	0.23	0.10	11.55	1.53	4.6
Ohio Shale	K3-12-8/10	17.6	-0.26	0.01	12.84	2.68	5.1
Bakken	T2-6	0.5	-0.04		0.96	3.10	1.5
Bakken	T2-2	0.4	-0.96		0.92	3.40	1.5
Bakken	T2-15	0.3	-0.44		0.60	3.00	1.8
Bakken	T1-7	0.6	0.19		1.24	4.50	1.5
New Albany (anoxic)		0.5	0.91		8.60	3.79	0.2
New Albany (anoxic)		1.1	0.92		8.96	3.48	
New Albany (anoxic)		0.8	1.20		7.17	3.44	-0.1
New Albany (anoxic)		1.1	1.14		7.24	2.32	0.7
New Albany (anoxic)		1.0	1.52		11.83	3.30	-0.1
New Albany (oxic)		0.5	0.47		0.31	0.56	1.5
New Albany (oxic)		1.0	0.45		0.48	1.63	2.2
New Albany (oxic)		0.8	0.64		0.13	1.19	2.9
New Albany (oxic)		0.6	0.48		0.18	0.42	2.6
New Albany (oxic)		0.4	0.19		0.38	1.39	2.9

Table 3.4: **Unit-average Mo/TOC and Sr/Ba data for Late Devonian units.**

section	formation	Mo/TOC (ppm/wt. %)	Sr/Ba (ppm/ppm)
RSP, CLY, AJD	Woodford	23.4 ± 1.7	0.34 ± 0.14
Thompson	Upper Bakken	13.2 ± 1.5	0.29 ± 0.08
WVC	Hanover-Dunkirk	11.6 ± 6.1	0.26 ± 0.05
KEP-3	Cleveland Member, Ohio Shale	13.9 ± 6.9	0.23 ± 0.02
DHGS	Chattanooga	7.0 ± 5.4	0.45 ± 0.09
INJK-13	Camp Run Member, New Albany Shale (oxic)	N/A	0.24 ± 0.06
INJK-13	Camp Run Member, New Albany Shale (anoxic)	4.5 ± 0.5	0.16 ± 0.04

3.9 References

Ader M., Thomazo C., Sansjofre P., Busigny V., Papineau D., Laffont R., Cartigny P. and Halverson G. P. (2016) Interpretation of the nitrogen isotopic composition of Precambrian sedimentary rocks: Assumptions and perspectives. *Chem. Geol.* 429, 93–110.

Algeo T. J. and Heckel P. H. (2008) The Late Pennsylvanian midcontinent sea of North America: A review. *Palaeogeogr. Palaeoclimatol. Palaeoecol.* 268, 205–221.

Algeo T. J. and Herrmann A. D. (2018) An ancient estuarine-circulation nutrient trap: The Late Pennsylvanian Midcontinent Sea of North America. *Geology* 46, 143–146.

Algeo T. J. and Lyons T. W. (2006) Mo–total organic carbon covariation in modern anoxic marine environments: Implications for analysis of paleoredox and paleohydrographic conditions. *Paleoceanography* 21.

Algeo T. J. and Maynard J. B. (2004) Trace-element behavior and redox facies in core shales of Upper Pennsylvanian Kansas-type cyclothems. *Chem. Geol.* 206, 289–318.

Algeo T. J. and Maynard J. B. (2008) Trace-metal covariation as a guide to water-mass conditions in ancient anoxic marine environments. *Geosphere* 4, 872–887.

Algeo T. J. and Tribovillard N. (2009) Environmental analysis of paleoceanographic systems based on molybdenum–uranium covariation. *Chem. Geol.* 268, 211–225.

Algeo T. J., Lyons T. W., Blakey R. C. and Over D. J. (2007) Hydrographic conditions of the Devono–Carboniferous North American Seaway inferred from sedimentary Mo–TOC

relationships. *Palaeogeogr. Palaeoclimatol. Palaeoecol.* 256, 204–230.

Algeo T. J., Heckel P. H., Maynard J. B., Blakey R., Rowe H., Pratt B. R. and Holmden C. (2008a) Modern and ancient epeiric seas and the super-estuarine circulation model of marine anoxia. Dyn. Epeiric Seas Sedimentol. Paleontol. Geochem. Perspect. St Johns Can. Geol. Assoc. Can. Spec. Publ. 48, 7–38.

Algeo T. J., Rowe H., Hower J. C., Schwark L., Herrmann A. and Heckel P. H. (2008b) Oceanic denitrification during Late Carboniferous glacial-interglacial cycles. *Nat. Geosci.* 1, 709-714.

Algeo T. J., Morford J. and Cruse A. (2012) New applications of trace metals as proxies in marine paleoenvironments. *Chem. Geol.* 306-307, 160-164.

Anbar A. D. and Gordon G. W. (2008) Redox renaissance. *Geology* 36(3), 271–272.

Arnold G. L., Anbar A. D., Barling J. and Lyons T. W. (2004) Molybdenum isotope evidence for widespread anoxia in mid-proterozoic oceans. *Science* 304, 87–90.

Audry S., Blanc G., Schäfer J., Chaillou G. and Robert S. (2006) Early diagenesis of trace metals (Cd, Cu, Co, Ni, U, Mo, and V) in the freshwater reaches of a macrotidal estuary. *Geochim. Cosmochim. Acta* 70, 2264–2282.

Balistrieri L. S. and Chao T. T. (1990) Adsorption of selenium by amorphous iron oxyhydroxide and manganese dioxide. *Geochim. Cosmochim. Acta* 54, 739–751.

Broecker W. S. and Peng T.-H. (1982) Tracers in the Sea, Lamont-Doherty Geological Observatory, Columbia University.

Brumsack H.-J. (2006) The trace metal content of recent organic carbon-rich sediments: implications for Cretaceous black shale formation. *Palaeogeogr. Palaeoclimatol. Palaeoecol.* 232, 344–361.

Calvert S. E., Bustin R. M. and Ingall E. D. (1996) Influence of water column anoxia and sediment supply on the burial and preservation of organic carbon in marine shales. *Geochim. Cosmochim. Acta* 60, 1577–1593.

Carignan J. and Wen H. (2007) Scaling NIST SRM 3149 for Se isotope analysis and isotopic variations of natural samples. *Chem. Geol.* 242, 347–350.

Chang Y., Zhang J., Qu J.-Q. and Xue Y. (2017) Precise selenium isotope measurement in seawater by carbon-containing hydride generation-Desolvation-MC-ICP-MS after thiol resin preconcentration. *Chem. Geol.* 471, 65–73.

Chen X., Ling H.-F., Vance D., Shields-Zhou G. A., Zhu M., Poulton S. W., Och L. M., Jiang S.-Y., Li D. and Cremonese L. (2015) Rise to modern levels of ocean oxygenation coincided with the Cambrian radiation of animals. *Nat. Commun.* 6, 7142.

Clark S. K. and Johnson T. M. (2010) Selenium stable isotope investigation into selenium biogeochemical cycling in a lacustrine environment: Sweitzer Lake, Colorado. *J. Environ. Qual.* 39, 2200–2210.

Clarkson M. O., Stirling C. H., Jenkyns H. C., Dickson A. J., Porcelli D., Moy C. M., von Strandmann P. A. P., Cooke I. R. and Lenton T. M. (2018) Uranium isotope evidence for two episodes of deoxygenation during Oceanic Anoxic Event 2. *Proc. Natl. Acad. Sci. (U.S.A.)*, 201715278.

Coplen T. B., Brand W. A., Gehre M., Gröning M., Meijer H. A., Toman B. and Verkouteren R. M. (2006) New guidelines for δ13C measurements. *Anal. Chem.* 78, 2439–2441.

Cruse A. M. and Lyons T. W. (2004) Trace metal records of regional paleoenvironmental variability in Pennsylvanian (Upper Carboniferous) black shales. *Chem. Geol.* 206, 319–345.

Cutter G. A. and Bruland K. W. (1984) The marine biogeochemistry of selenium: A re-evaluation. *Limnol. Oceanogr.* 29, 1179–1192.

Dahl T. W., Hammarlund E. U., Anbar A. D., Bond D. P. G., Gill B. C., Gordon G. W., Knoll A. H., Nielsen A. T., Schovsbo N. H. and Canfield D. E. (2010) Devonian rise in atmospheric oxygen correlated to the radiations of terrestrial plants and large predatory fish. *Proc. Natl. Acad. Sci. (U.S.A.)*, 107, 17911–17915.

Fan H., Wen H., Hu R. and Zhao H. (2011) Selenium speciation in Lower Cambrian Se-enriched strata in South China and its geological implications. *Geochim. Cosmochim. Acta* 75, 7725–7740.

Fry B., Silva S. R., Kendall C. and Anderson R. K. (2002) Oxygen isotope corrections for

online $\delta^{34}S$ analysis. *Rapid Commun. Mass Spectrom.* 16, 854–858.

Fulton J. M., Arthur M. A. and Freeman K. H. (2012) Black Sea nitrogen cycling and the preservation of phytoplankton $\delta^{15}N$ signals during the Holocene. *Glob. Biogeochem. Cycles* 26.

Hartwell W. J. (1998) Geochemical and petrographic analysis of the Upper Devonian-Lower Mississippian Bakken black shales from the Williston Basin, North Dakota. Master's Thesis, University of Cincinnati, Cincinnati, Ohio.

Heckel P. H. (1977) Origin of phosphatic black shale facies in Pennsylvanian cyclothems of mid-continent North America. *AAPG Bull.* 61, 1045–1068.

Heckel P. H. (1994) Evaluation of evidence for glacio-eustatic control over marine Pennsylvanian cyclothems in North America and consideration of possible tectonic effects. In: Dennison, J.M., Ettensohn, F.R. (Eds.), Tectonic and Eustatic Controls on Sedimentary Cycles. SEPM, Concepts in Sedimentology and Paleontology 4, pp. 65-87.

Helz G.R., Miller C.V., Charnock J.M., Mosselmans J.L.W., Pattrick R.A.D., Garner C.D. and Vaughan D.J. (1996) Mechanisms of molybdenum removal from the sea and its concentration in black shales: EXAFS evidences. *Geochim. Cosmochim. Acta* 60, 3631-3642.

Herrmann A. D., Barrick J. E. and Algeo T. J. (2015) The relationship of conodont biofacies to spatially variable watermass properties in the Late Pennsylvanian Midcontinent Sea. *Paleoceanography* 30(3), 269-283.

Herrmann A. D., Barrick J. E., Algeo T. J. and Peng Y. B. (2019) Conodont biofacies and watermass structure of the Middle Pennsylvanian North American Midcontinent Sea. *Palaeogeogr. Palaeoclimatol. Palaeoecol.,* in press.

Ingall E. D., Bustin R. M. and Van Cappellen P. (1993) Influence of water column anoxia on the burial and preservation of carbon and phosphorus in marine shales. *Geochim. Cosmochim. Acta* 57, 303–316.

Jaminski J. (1997) Geochemical and petrographic patterns of cyclicity in the Devonian-Mississippian black shales of the Central Appalachian Basin. Ph. D. dissertation, Uni-

versity of Cincinnati, Cincinnati, Ohio.

Jaminski J., Algeo T. J., Maynard J. B. and Hower J. C. (1998) Climatic origin of dm-scale compositional cyclicity in the Cleveland Member of the Ohio Shale (Upper Devonian), Central Appalachian Basin, USA. In: Schieber J., Zimmerle W. and Sethi P. S., eds., Shales and Mudstones, v. 1: Stuttgart, Schweizerbart'sche, pp. 217-242.

Jimenez M. Y., Ivany L. C., Judd E. J. and Henkes G. (2019) Low and seasonally variable salinity in the Pennsylvanian equatorial Appalachian Basin. *Earth Planet. Sci. Lett.* 519, 182–191.

Joachimski M. M. and Lambert L. L. (2015) Salinity contrast in the US Midcontinent Sea during Pennsylvanian glacio-eustatic highstands: Evidence from conodont apatite $\delta^{18}O$. *Palaeogeogr. Palaeoclimatol. Palaeoecol.* 433, 71–80.

Johnson T. M. and Bullen T. D. (2004) Mass-dependent fractionation of selenium and chromium isotopes in low-temperature environments. *Rev. Mineral. Geochem.* 55, 289–317.

Johnson T. M., Herbel M. J., Bullen T. D. and Zawislanski P. T. (1999) Selenium isotope ratios as indicators of selenium sources and oxyanion reduction. *Geochim. Cosmochim. Acta* 63, 2775–2783.

Kendall B., Dahl T. W. and Anbar A. D. (2017) The stable isotope geochemistry of molybdenum. *Rev. Mineral. Geochem.* 82, 683–732.

Kendall B., Gordon G. W., Poulton S. W. and Anbar A. D. (2011) Molybdenum isotope constraints on the extent of late Paleoproterozoic ocean euxinia. *Earth Planet. Sci. Lett.* 307, 450–460.

Kendall B., Komiya T., Lyons T. W., Bates S. M., Gordon G. W., Romaniello S. J., Jiang G., Creaser R. A., Xiao S., McFadden K., Sawaki Y., Tahata M., Shu D., Han J., Li Y., Chu X. and Anbar A. D. (2015) Uranium and molybdenum isotope evidence for an episode of widespread ocean oxygenation during the late Ediacaran Period. *Geochim. Cosmochim. Acta* 156, 173–193.

Kipp M. A., Stüeken E. E., Bekker A. and Buick R. (2017) Selenium isotopes record extensive

marine suboxia during the Great Oxidation Event. *Proc. Natl. Acad. Sci. (U.S.A.)*, 114, 875–880.

Kipp M. A., Stüeken E. E., Yun M., Bekker A. and Buick R. (2018) Pervasive aerobic nitrogen cycling in the surface ocean across the Paleoproterozoic Era. *Earth Planet. Sci. Lett.* 500, 117–126.

Koehler M. C., Buick R., Kipp M. A., Stüeken E. E. and Zaloumis J. (2018) Transient surface ocean oxygenation recorded in the 2.66 Ga Jeerinah Formation, Australia. *Proc. Natl. Acad. Sci. (U.S.A.)*, 115, 7711–7716.

Kulp T. R. and Pratt L. M. (2004) Speciation and weathering of selenium in Upper Cretaceous chalk and shale from South Dakota and Wyoming, USA. *Geochim. Cosmochim. Acta* 68, 3687–3701.

Kurzawa T., König S., Labidi J., Yierpan A. and Schoenberg R. (2017) A method for Se isotope analysis of low ng-level geological samples via double spike and hydride generation MC-ICP-MS. *Chem. Geol.* 466, 219–228.

Large R. R., Halpin J. A., Danyushevsky L. V., Maslennikov V. V., Bull S. W., Long J. A., Gregory D. D., Lounejeva E., Lyons T. W. and Sack P. J. (2014) Trace element content of sedimentary pyrite as a new proxy for deep-time ocean–atmosphere evolution. *Earth Planet. Sci. Lett.* 389, 209–220.

Lash G. G. (2017) A multiproxy analysis of the Frasnian-Famennian transition in western New York State, U.S.A. *Palaeogeogr. Palaeoclimatol. Palaeoecol.* 473, 108-122.

Lau K. V., Macdonald F. A., Maher K. and Payne J. L. (2017) Uranium isotope evidence for temporary ocean oxygenation in the aftermath of the Sturtian Snowball Earth. *Earth Planet. Sci. Lett.* 458, 282–292.

Lau K. V., Maher K., Altiner D., Kelley B. M., Kump L. R., Lehrmann D. J., Silva-Tamayo J. C., Weaver K. L., Yu M. and Payne J. L. (2016) Marine anoxia and delayed Earth system recovery after the end-Permian extinction. *Proc. Natl. Acad. Sci. (U.S.A.)*, 113, 2360–2365.

Lineback J. A. (1970) Stratigraphy of the New Albany Shale in Indiana, State of Indiana,

Department of Natural Resources.

Little S. H., Vance D., Lyons T. W. and McManus J. (2015). Controls on trace metal authigenic enrichment in reducing sediments: Insights from modern oxygen-deficient settings. *Am. J. Sci.* 315, 77-119.

Liu J. S. and Algeo T. J. (2019) Beyond redox: control of trace-metal enrichment in anoxic marine facies by watermass chemsitry and sedimentation rate. *Geochim. Cosmochim. Acta*, this volume.

Liu J. S., Algeo T. J., Jaminski J., Kuhn T. and Joachimski M. M. (2019) Evaluation of high-frequency paleoenvironmental variation using an optimized cyclostratigraphic framework: Example for C-S-Fe analysis of Devonian-Mississippi¬an black shales (Central Appalachian Basin, U.S.A.). *Chem. Geol.*, in press.

Lu W., Ridgwell A., Thomas E., Hardisty D. S., Luo G., Algeo T. J., Saltzman M. R., Gill B. C., Shen Y., Ling H.-F., Edwards C. T., Whalen M. T., Zhou X., Gutchess K. M., Jin L., Rickaby R. E. M., Jenkyns H. C., Lyons T. W., Lenton T. M., Kump L. R., and Lu Z. (2018) Late inception of a resiliently oxygenated upper ocean. *Science* 361, 174-177.

Lu Z., Jenkyns H. C. and Rickaby R. E. M. (2010) Iodine to calcium ratios in marine carbonate as a paleo-redox proxy during oceanic anoxic events. *Geology* 38, 1107–1110.

Martens D. A. and Suarez D. L. (1997) Selenium speciation of marine shales, alluvial soils, and evaporation basin soils of California. *J. Environ. Qual.* 26, 424–432.

Measures C. I. and Burton J. D. (1980) The vertical distribution and oxidation states of dissolved selenium in the northeast Atlantic Ocean and their relationship to biological processes. *Earth Planet. Sci. Lett.* 46, 385–396.

Measures C. I., McDuff R. E. and Edmond J. M. (1980) Selenium redox chemistry at GEOSECS I re-occupation. *Earth Planet. Sci. Lett.* 49, 102–108.

Mitchell K., Mansoor S. Z., Mason P. R. D., Johnson T. M. and Van Cappellen P. (2016) Geological evolution of the marine selenium cycle: Insights from the bulk shale $\delta^{82/76}$Se record and isotope mass balance modeling. *Earth Planet. Sci. Lett.* 441, 178–187.

Mitchell K., Mason P. R., Van Cappellen P., Johnson T. M., Gill B. C., Owens J. D., Diaz J., Ingall E. D., Reichart G.-J. and Lyons T. W. (2012) Selenium as paleo-oceanographic proxy: A first assessment. *Geochim. Cosmochim. Acta* 89, 302–317.

Morford J. L. and Emerson S. (1999) The geochemistry of redox sensitive trace metals in sediments. *Geochim. Cosmochim. Acta* 63, 1735–1750.

Oremland R. S., Hollibaugh J. T., Maest A. S., Presser T. S., Miller L. G. and Culbertson C. W. (1989) Selenate reduction to elemental selenium by anaerobic bacteria in sediments and culture: biogeochemical significance of a novel, sulfate-independent respiration. *Appl Env. Microbiol.* 55, 2333–2343.

Over D. J. (1992) Conodonts and the Devonian–Carboniferous boundary in the upper Woodford Shale, Arbuckle Mountains, south-central Oklahoma. *J. Paleontol.* 66, 293–311.

Over D. J. (2002) The Frasnian/Famennian boundary in central and eastern United States. *Palaeogeogr. Palaeoclimatol. Palaeoecol.* 181, 153–169.

Partin C. A., Bekker A., Planavsky N. J., Scott C. T., Gill B. C., Li C., Podkovyrov V., Maslov A., Konhauser K. O., Lalonde S. V., Love G. D., Poulton S. W. and Lyons T. W. (2013) Large-scale fluctuations in Precambrian atmospheric and oceanic oxygen levels from the record of U in shales. *Earth Planet. Sci. Lett.* 369, 284–293.

Qie W. K., Algeo T. J., Luo G. M. and Herrmann A. D. (2019) Global events of the Early Devonian to Middle Permian: A review. *Palaeogeogr. Palaeoclimatol. Palaeoecol.*, in press.

Roark A., Flake R., Grossman E. L., Olszewski T., Lebold J., Thomas D., Marcantonio F., Miller B., Raymond A. and Yancey T. (2017) Brachiopod geochemical records from across the Carboniferous seas of North America: Evidence for salinity gradients, stratification, and circulation patterns. *Palaeogeogr. Palaeoclimatol. Palaeoecol.* 485, 136–153.

Rouxel O., Fouquet Y. and Ludden J. N. (2004) Subsurface processes at the Lucky Strike hydrothermal field, Mid-Atlantic Ridge: evidence from sulfur, selenium, and iron isotopes. *Geochim. Cosmochim. Acta* 68, 2295–2311.

Rovira M., Giménez J., Martínez M., Martínez-Lladó X., de Pablo J., Marti V. and Duro L.

(2008) Sorption of selenium (IV) and selenium (VI) onto natural iron oxides: goethite and hematite. *J. Hazard. Mater.* 150, 279–284.

Rue E. L., Smith G. J., Cutter G. A. and Bruland K. W. (1997) The response of trace element redox couples to suboxic conditions in the water column. *Deep Sea Res. Part Oceanogr. Res. Pap.* 44, 113–134.

Sageman B. B., Murphy A. E., Werne J. P., Ver Straeten C. A., Hollander D. J. and Lyons T. W. (2003) A tale of shales: the relative roles of production, decomposition, and dilution in the accumulation of organic-rich strata, Middle–Upper Devonian, Appalachian basin. *Chem. Geol.* 195, 229–273.

Schilling K., Johnson T. M. and Mason P. R. (2014) A sequential extraction technique for mass-balanced stable selenium isotope analysis of soil samples. *Chem. Geol.* 381, 125–130.

Schilling K., Johnson T. M. and Wilcke W. (2011) Selenium partitioning and stable isotope ratios in urban topsoils. *Soil Sci. Soc. Am. J.* 75, 1354–1364.

Scott C., Lyons T. W., Bekker A., Shen Y., Poulton S. W., Chu X. and Anbar A. D. (2008) Tracing the stepwise oxygenation of the Proterozoic ocean. *Nature* 452, 456-U5.

Shiller A. M. (1996) The effect of recycling traps and upwelling on estuarine chemical flux estimates. *Geochim. Cosmochim. Acta* 60, 3177–3185.

Shore A. J. T. (2011) Selenium geochemistry and isotopic composition of sediments from the Cariaco Basin and the Bermuda Rise: a comparison between a restricted basin and the open ocean over the last 500 ka. Ph.D. dissertation, University of Leicester, Leicester, UK.

Song Y., Gilleaudeau G., Algeo T. J., Over D. J., Anbar A. D. and Xie S. C. (2019) Biomarker evidence of algal-microbial community changes linked to redox conditions and enhanced weathering, Upper Devonian Chattanooga Shale. In review.

von Strandmann P. A. P., Coath C. D., Catling D. C., Poulton S. W. and Elliott T. (2014) Analysis of mass dependent and mass independent selenium isotope variability in black shales. *J. Anal. At. Spectrom.* 29, 1648–1659.

von Strandmann P. A. P., Stüeken E. E., Elliott T., Poulton S. W., Dehler C. M., Canfield D. E. and Catling D. C. (2015) Selenium isotope evidence for progressive oxidation of the Neoproterozoic biosphere. *Nat. Commun.* 6.

Stüeken E. E. (2017) Selenium isotopes as a biogeochemical proxy in deep time. *Rev. Mineral. Geochem.* 82, 657–682.

Stüeken E. E., Buick R. and Anbar A. D. (2015a) Selenium isotopes support free O_2 in the latest Archean. *Geology* 43, 259–262.

Stüeken E. E., Buick R., Bekker A., Catling D., Foriel J., Guy B. M., Kah L. C., Machel H. G., Montañez I. P. and Poulton S. W. (2015b) The evolution of the global selenium cycle: Secular trends in Se isotopes and abundances. *Geochim. Cosmochim. Acta* 162, 109–125.

Stüeken E. E., Catling D. C. and Buick R. (2012) Contributions to late Archaean sulphur cycling by life on land. *Nat. Geosci.* 5, 722–725.

Stüeken E. E., Foriel J., Buick R. and Schoepfer S. D. (2015c) Selenium isotope ratios, redox changes and biological productivity across the end-Permian mass extinction. *Chem. Geol.* 410, 28–39.

Stüeken E. E., Foriel J., Nelson B. K., Buick R. and Catling D. C. (2013) Selenium isotope analysis of organic-rich shales: advances in sample preparation and isobaric interference correction. *J. Anal. At. Spectrom.* 28, 1734–1749.

Stüeken E. E., Kipp M. A., Koehler M. C. and Buick R. (2016) The evolution of Earth's biogeochemical nitrogen cycle. *Earth-Sci. Rev.* 160, 220–239.

Teng F.-Z., Watkins J. M. and Dauphas N. (2017) Non-Traditional Stable Isotopes. *Rev Mineral. Geochem.* 82, 885p.

Tesdal J.-E., Galbraith E. D. and Kienast M. (2013) Nitrogen isotopes in bulk marine sediment: linking seafloor observations with subseafloor records. *Biogeosciences* 10, 101–118.

Tissot F. L. and Dauphas N. (2015) Uranium isotopic compositions of the crust and ocean: Age corrections, U budget and global extent of modern anoxia. *Geochim. Cosmochim.*

Acta 167, 113–143.

Tostevin R., Clarkson M. O., Gangl S., Shields G. A., Wood R. A., Bowyer F., Penny A. M. and Stirling C. H. (2019) Uranium isotope evidence for an expansion of anoxia in terminal Ediacaran oceans. *Earth Planet. Sci. Lett.* 506, 104–112.

Tribovillard N., Algeo T. J., Lyons T. and Riboulleau A. (2006) Trace metals as paleoredox and paleoproductivity proxies: An update. *Chem. Geol.* 232, 12–32.

Turner A. C. E., Algeo T. J., Peng Y. and Herrmann A. D. (2019) Circulation patterns in the Late Pennsylvanian North American Midcontinent Sea inferred from spatial gradients in sediment chemsitry and mineralogy. *Palaeogeogr. Palaeoclimatol. Palaeoecol.*, in press.

Velinsky D. J. and Cutter G. A. (1990) Determination of elemental selenium and pyrite-selenium in sediments. *Anal. Chim. Acta* 235, 419–425.

Ver Straeten C. A., Brett C. E. and Sageman B. B. (2011) Mudrock sequence stratigraphy: A multi-proxy (sedimentological, paleobiological and geochemical) approach, Devonian Appalachian Basin. *Palaeogeogr. Palaeoclimatol. Palaeoecol.* 304, 54–73.

Wei W. and Algeo T. J. (2019) Elemental proxies for paleosalinity analysis of ancient shales and mudrocks. *Geochim. Cosmochim. Acta*, in press.

Wei W., Algeo T. J., Lu Y., Lu Y., Liu H., Zhang S., Peng L., Zhang J. and Chen L. (2018) Identifying marine incursions into the Paleogene Bohai Bay Basin lake system in northeastern China. *Int. J. Coal Geol.* 200, 1–17.

Werne J. P., Sageman B. B., Lyons T. W. and Hollander D. J. (2002) An integrated assessment of a "type euxinic" deposit: evidence for multiple controls on black shale deposition in the Middle Devonian Oatka Creek Formation. *Am. J. Sci.* 302, 110–143.

Zhang F., Algeo T. J., Romaniello S. J., Cui Y., Zhao L., Chen Z.-Q. and Anbar A. D. (2018) Congruent Permian-Triassic δ238U records at Panthalassic and Tethyan sites: Confirmation of global-oceanic anoxia and validation of the U-isotope paleoredox proxy. *Geology* 46, 327–330.

Zhu J.-M., Johnson T. M., Clark S. K., Zhu X.-K. and Wang X.-L. (2014) Selenium redox cycling during weathering of Se-rich shales: A selenium isotope study. *Geochim.*

Cosmochim. Acta 126, 228–249.

Chapter 4

BIOMASS RECYCLING AND EARTH'S EARLY PHOSPHORUS CYCLE

This manuscript is published as:
Kipp MA and Stüeken EE. (2017). *Science Advances*. 3(11): eaao4795.
https://doi.org/10.1126/sciadv.aao4795

4.1 Abstract

Phosphorus sets the pace of marine biological productivity on geological timescales. Recent estimates of Precambrian phosphorus levels suggest a severe deficit of this macronutrient, with the depletion attributed to scavenging by iron minerals. Here we propose that the size of the marine phosphorus reservoir was instead constrained by muted liberation of phosphorus during the remineralization of biomass. While most biomass-bound phosphorus gets aerobically recycled in the modern ocean, a dearth of oxidizing power in Earth's early oceans would have limited the stoichiometric capacity for remineralization, particularly during the Archean. The resulting low phosphorus concentrations would have substantially hampered primary productivity, contributing to the delayed rise of atmospheric oxygen.

4.2 Introduction

Phosphorus (P) availability is thought to dictate the amount of primary productivity that can be sustained in the oceans on geologic timescales (Broecker and Peng, 1982; Tyrrell, 1999). Estimating P concentrations in the ocean across Earth's history is thus critical for understanding the growth of the biosphere and the evolution of major biogeochemical cycles – namely the rise of atmospheric oxygen, which requires substantial burial of organic carbon

generated via oxygenic photosynthesis. Multiple proxies have been used to reconstruct P levels, including the P content of iron (Fe)-oxide-rich sedimentary rocks (Bjerrum and Canfield, 2002; Planavsky et al., 2010; Jones et al., 2015) and marginal marine siliciclastic sedimentary rocks (Reinhard et al., 2016). While deriving quantitative assessments of P levels from these records has been notoriously difficult (Bjerrum and Canfield, 2002; Konhauser et al., 2007), recent work is beginning to converge on a low P ocean [<20% modern concentrations; modern ∼2 µM (Broecker and Peng, 1982; Tyrrell, 1999)] persisting in the Archean, and perhaps through the Proterozoic (Jones et al., 2015; Reinhard et al., 2016). The favored mechanism for P depletion in the Precambrian ocean is scavenging of P from the water column by incorporation into ferrous minerals or by adsorption onto Fe-oxides (Bjerrum and Canfield, 2002; Jones et al., 2015; Reinhard et al., 2016). However, these models have not accounted for potential "upstream" throttles that could have kept P concentrations low without any influence of Fe-scavenging. Here we propose a new mechanism for maintaining low P: limited recycling of P in an oxidant-poor ocean.

The bioavailable P supply of the ocean derives almost entirely from riverine inputs, making P a scarce nutrient relative to carbon and nitrogen, which can be fixed from atmospheric sources (Tyrrell, 1999). The modern riverine flux of bioavailable P is very small [$\sim 2 \times 10^{12}$ g/yr (Schlesinger and Bernhardt, 2013)] compared to the amount annually utilized by the marine biosphere [$\sim 1200 \times 10^{12}$ g/yr (Schlesinger and Bernhardt, 2013)]. This large discrepancy between supply and demand is sustained by the efficient recycling of P within the ocean. After the P in the surface ocean is exhausted during primary production, the remineralization of sinking biomass releases P back into the marine environment. This recycling increases the residence time of P in the ocean. As water masses mature in the deep ocean, they accumulate nutrients regenerated through biomass recycling and ultimately deliver these nutrients to the continental shelves via upwelling, enabling high rates of biological productivity. In the modern ocean, ∼80-90% of primary productivity gets remineralized in the photic zone (upper ∼200m; Fig. B.1), with most of the remainder being oxidized at depth or in marine sediments (Emerson and Hedges, 1988; Martin et al., 1987). Only a

very small percentage (<<1%) of net primary productivity (and its associated P) escapes remineralization and is ultimately buried in marine sediments. Thus the magnitude of the P recycling flux has probably always dwarfed riverine inputs, even if early Precambrian riverine fluxes were an order of magnitude higher than today (Hao et al., 2017).

A critical difference between Precambrian and modern oceans is the availability of electron acceptors needed for the oxidation of biomass. In the oxygenated modern ocean, most organic matter degradation occurs aerobically (Sarmiento et al., 1988). Even when localized water masses or sedimentary porewaters become anoxic, there is ample supply of anaerobic electron acceptors (*e.g.*, sulfate; SO_4^{2-}) to fuel biomass decomposition (Calvert and Pedersen, 1992). Prior to the establishment of oxidizing conditions at Earth's surface, it is conceivable that the recycling of organic matter was limited by a scarcity of electron acceptors. Inhibited organic remineralization would mean that a greater proportion of sinking organic matter was preserved in marine sediments (*i.e.*, higher burial efficiency). However, the limited regeneration of P in such a system might maintain low steady-state P concentrations in the deep ocean and upwelling waters, which would ultimately limit net primary productivity, total organic burial, and oxygenesis. We quantitatively explored this hypothesis by compiling estimates of the paleo-concentrations of the major electron acceptors in seawater (Fig. 4.1A) and stoichiometrically calculating the concentration of P that could have been maintained throughout Earth's history.

The rationale for this approach comes from the observation that in the modern ocean the concentrations of P and oxygen in surface (P_{s}, $O_{2\mathrm{s}}$) and deep (P_{d}, $O_{2\mathrm{d}}$) waters can be stoichiometrically equated using the chemical equation of aerobic decomposition and concomitant liberation of P (Sarmiento et al., 1988) (Fig. B.2). This is based on the premise that all P in deep waters (P_{d}) derives from either (i) the release of P during the oxidation of organic matter, or (ii) downwelling of nutrient-rich waters (P_{s}) from high latitudes that is driven by thermohaline circulation. Thus, P_{d} can be calculated as shown in Equation 4.1, where r_{O2} is the stoichiometric coefficient of the liberation of P from organic matter during

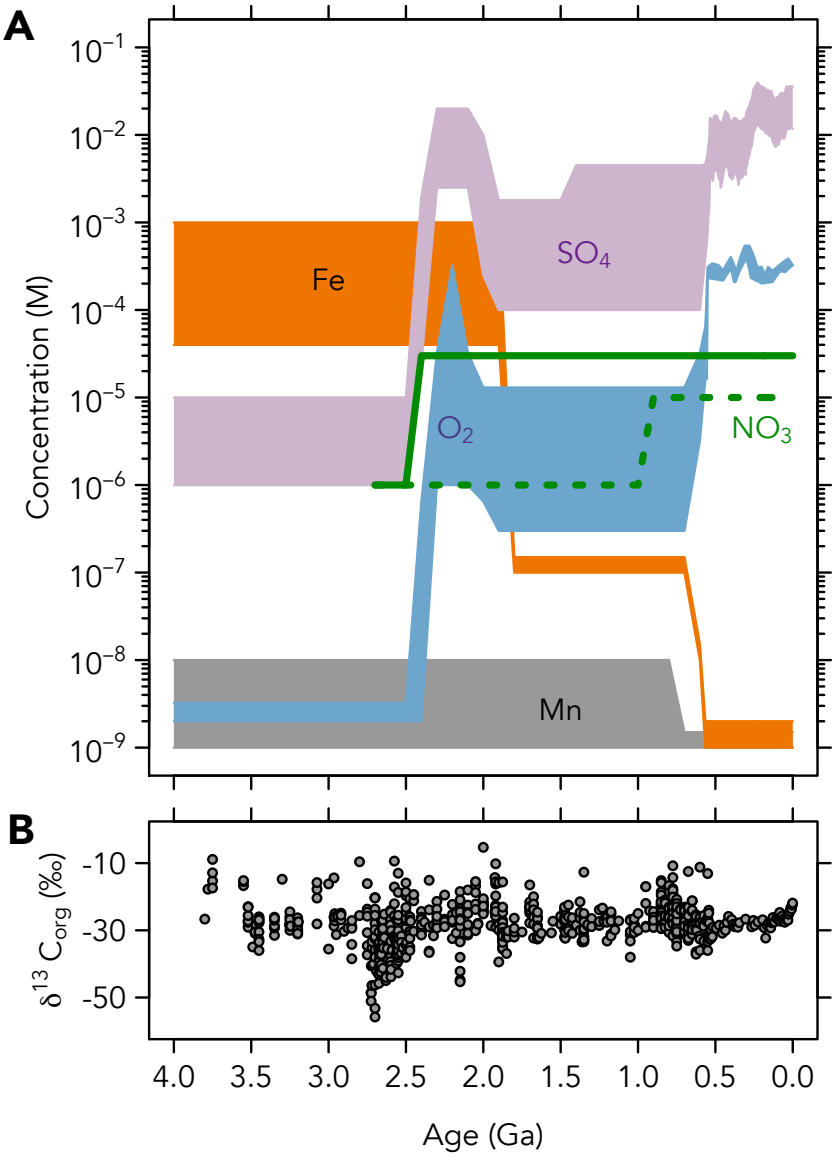

Figure 4.1: **Compilations of (A) electron acceptor availability in seawater and (B) sedimentary organic carbon isotope record.** The prevalence of extremely negative $\delta^{13}C$ values from ~2.8-2.5 Ga has been interpreted by some as a signal of widespread methanogenesis [(Krissansen-Totton et al., 2015) and refs. therein].

aerobic respiration [120-200, average 169 (Sarmiento et al., 1988; Canfield, 1998)]

$$P_d = P_s + \frac{O_{2s} - O_{2d}}{r_{O2}} \tag{4.1}$$

This equation has been validated for the modern ocean (Sarmiento et al., 1988) and has also been used to constrain Precambrian oxygen levels (Canfield, 1998). It is therefore a reasonable approach to track first-order trends in ocean chemistry.

We modified this equation in order to explore the possibility of limited P recycling in the Precambrian (extended methods are available as supplementary materials). First, we added the contribution of anaerobic respiration pathways, in descending order according to the thermodynamic favorability of the corresponding metabolic reaction (Froelich et al., 1979). Stoichiometric coefficients (r_{i}) were taken from Canfield et al. (1993). In order to assess the contribution of organic disproportionation reactions (*i.e.*, methanogenesis, fermentation), we derived an upper limit (P_{CH4}) using modeled methanogenesis rates for the Precambrian. Scaling the modern rate of methane production in marine sediments [20 Tmol/yr (Reeburgh, 2007)] to rates modeled for the late Archean [96 Tmol/yr (Izon et al., 2017)] – a time that may have had exceptionally vigorous methanogenesis (Fig. 4.1B) – suggests that disproportionation of organic matter likely never contributed more than 0.1 µM of additional P recycling (extended methods are available in Appendix B). We conservatively applied this value to all of our Precambrian calculations. The modified equation becomes

$$P_d = P_s + \frac{O_{2s} - O_{2d}}{r_{O2}} + \frac{NO_{3s} - NO_{3d}}{r_{NO3}} + \frac{MnO_{2s} - MnO_{2d}}{r_{MnO2}} + \frac{FeOOH_s - FeOOH_d}{r_{FeOOH}} + \frac{SO_{4s} - SO_{4d}}{r_{SO4}} + P_{CH4} \tag{4.2}$$

which can be simplified by combining the total contribution of P recycling into a single term (P_{r}), such that

$$P_d = P_s + P_r \tag{4.3}$$

We solved for P_{r} using published estimates for electron acceptor availability in the surface oceans (X_{s}; Fig. 4.1A), assuming that all electron acceptors were quantitatively consumed (*i.e.*, $X_{\mathrm{d}} = 0$). Our estimates are conservative and likely overestimate total P regeneration for several reasons. First, if SO_4^{2-} had been quantitatively consumed at all times, then net isotopic fractionations in $\delta^{34}S$ as recorded in marine sediments should be minimal as a result of quantitative mass transfer, counter to what is observed in the Proterozoic [though not Archean (Canfield, 1998)]. Second, we did not account for other reactions such as CH_4 or H_2 oxidation that can consume electron acceptors without liberating P. Lastly, unlike the other electron acceptors in this model, manganese (Mn) and Fe are insoluble in their oxidized states. Upon reaching the ocean, Mn and Fe oxides tend to settle out of the water column, restricting their P recycling contributions to localized sedimentary settings, where liberated P is often trapped by diagenetic P minerals such as carbonate-fluorapatite (CFA). Additionally, their oxidizing power is limited to particle surfaces, meaning that their true oxidative capacity is considerably lower than is suggested by simple bulk concentrations. For these reasons, we are likely over-estimating the contribution of Mn and Fe in these calculations. Fe^{3+} and SO_4^{2-} can be regenerated during biogeochemical cycling within the ocean, and thus can be used multiple times to recycle P; however, these re-oxidation pathways consume another oxidant that then becomes unavailable, hence there is no net change in P regeneration. Thus, we stress that these calculations are conservative, and, if they err, tend to over-estimate total P_{r}.

We also considered potential variability of the Redfield C:P ratio through time, since the stoichiometric coefficient (r_{i}) scales with the C:P ratio of the degraded biomass. While today there is a fairly conserved C:P ratio of $\sim$106 in marine phytoplankton (Redfield, 1963), it has been proposed that this ratio was substantially higher in the low-P Precambrian ocean (Reinhard et al., 2016). Laboratory cultures have demonstrated flexibility in cyanobacterial C:P ratios from $\sim$106 to $>$500 as a function of P availability (White et al., 2006). We therefore explored three cases of constant (106), moderately enriched (400) and highly enriched (1000)

C:P ratios in order to generate a comprehensive range of outputs.

To constrain P_s, we considered two endmember scenarios: (i) Through thermohaline circulation and upwelling, the maximum P content of the surface ocean (P_s) is equal to the P contained in deep waters that is initially set by biomass remineralization ($P_s = P_r$) (Sarmiento et al., 1988). (ii) Alternatively, thermohaline circulation may be suppressed, in particular during intervals in the Precambrian that lack geological evidence of glaciations. In this case, $P_s = 0$.

4.3 Results

Our calculations reveal a significant increase in the capacity for P recycling (P_r) as the Earth's surface environment evolved from a reduced to an oxidized state, in particular during the Great Oxidation Event (GOE) at ~2.4 Ga (Bekker et al., 2004), when marine sulfate levels increased markedly (Fig. 4.2). The modern ocean has a vast excess of oxidizing capacity that is not exhausted during the recycling of sinking biomass. In other words, the amount of organic matter remineralization that occurs in the modern ocean is not limited by the total abundance of electron acceptors, but rather by the kinetics of organic degradation, sorption of organics onto mineral surfaces, polymerization reactions leading to the formation of recalcitrant organic matter, and sedimentation rates (Emerson and Hedges, 1988; Calvert and Pedersen, 1992; Hedges and Keil, 1995). In contrast, our calculations suggest that the remineralization of organic matter could have been inhibited in the Archean simply due to the limited availability of electron acceptors (Fig. 4.2).

In the absence of appreciable dissolved oxygen, the recycling of biomass in the Archean would have relied heavily on respiration of Fe^{3+} and SO_4^{2-} (Fig. 4.1). Recent estimates (Crowe et al., 2014; Zhelezinskaia et al., 2014) place Archean [SO_4^{2-}] at <10 µM, meaning that sulfate reduction would have contributed no more than 0.2 µM to P_r (Fig. 4.3). Levels of dissolved Fe^{3+} may have been as high as 1 mM if Fe^{2+} levels were constrained by greenalite solubility (Tosca et al., 2016) and if all Fe^{2+} underwent oxidation to bioavailable Fe^{3+}. In this scenario, iron reduction could theoretically have contributed up to 1.5 µM to P_r (Fig.

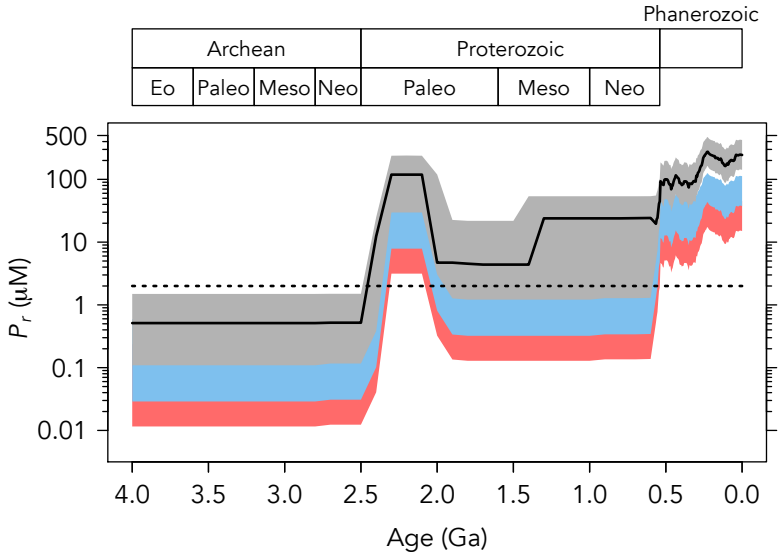

Figure 4.2: **Total possible phosphorus recycling through geologic time.** Black line indicates preferred values. Grey shaded area is uncertainty envelope for C:P ratios of 106:1. Blue shaded region is uncertainty envelope for C:P ratios of 400:1; red shaded region corresponds to C:P of 1000:1. Dotted line shows modern concentration of P in the deep ocean and upwelling water (∼2 µM).

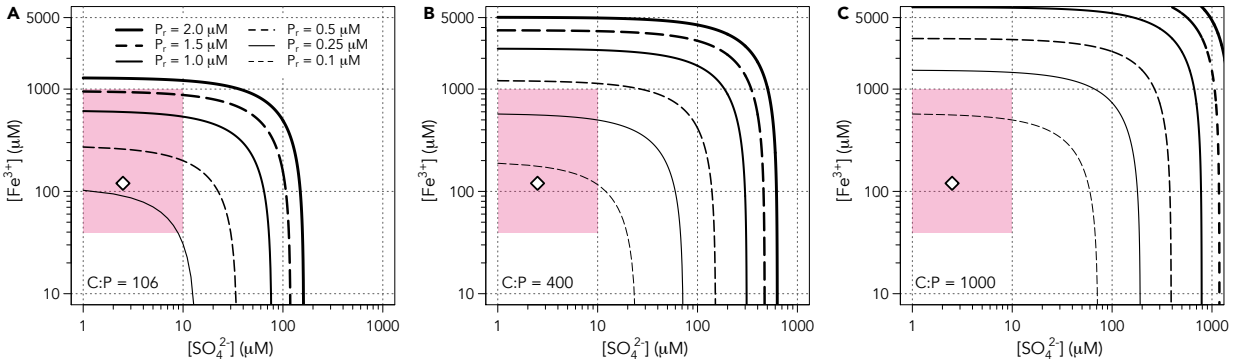

Figure 4.3: **Total possible Archean phosphorus recycling as a function of ferric iron and sulfate availability.** Calculations are presented for C:P ratios of 106 (A), 400 (B) and 1000 (C). Diamond shows preferred values; red shaded region shows published range of estimates for Archean seawater. Ferric iron reduction could have played a large role in phosphorus recycling if bioavailable Fe^{3+} levels were indeed ∼1 mM, but a scenario is very unlikely (discussed in text). Elevated C:P ratios in primary producers would have severely impeded P recycling in all scenarios.

4.3A). However, this upper limit is unlikely for several reasons. First, a large fraction of Fe^{3+} may have settled out of the water column as solid particles without being utilized for organic remineralization; second, siderite saturation may have kept Fe^{2+} levels below 120µM (Holland, 2003), which would push P_r to <0.4 µM; and lastly, if microbial C:P stoichiometry indeed shifted to higher levels under pervasive nutrient stress in the Precambrian (Reinhard et al., 2016), the effect of limited P recycling would become considerably more severe (Fig. 4.3B,C). Furthermore, episodes of high Fe input into the ocean could have exerted a negative feedback on P availability. When Fe input was high, it may have allowed for a high degree of P recycling by Fe^{3+} respiration, but at the same time, high levels of Fe^{2+} in the water column could subsequently have scavenged liberated P. The net burden for sustaining a large reservoir of dissolved P may thus have rested primarily on microbial sulfate reducers (max. $P_r < 0.2$ µM). As a conservative estimate, we proceed with a value of <0.4 µM for P_r to allow for some contribution of Fe^{3+} respiration (Fig. 4.3A).

If we now add our most conservative estimate of P dissolved in surface waters (P_s), our maximum calculated P_d value is <0.8 µM for the Archean. This is <40% of modern values, and is likely an over-estimate for the reasons outlined above. Actual concentrations could have been substantially lower, particularly if bacteria adjusted their C:P ratios to higher values (Fig. 4.3), or if thermohaline circulation was less effective than today. These upper limits agree well with recent estimates of Archean P concentrations [0.04-0.38 µM (Jones et al., 2015; Reinhard et al., 2016)].

However, our model allows for high P levels in the Proterozoic after growth of the seawater sulfate reservoir (Fig. 4.4) – counter to recent proxy evidence (Reinhard et al., 2016). There are a few possible solutions to this disagreement: (i) P recycling may have been operating more effectively in the Proterozoic, but Fe-scavenging depleted this recycled P and became the most significant sink for P, thus maintaining low P levels until the latest Proterozoic. (ii) Alternatively, P recycling may still have been inhibited if the marine sulfate reservoir was not quantitatively utilized, such that the full oxidation potential was not exploited. This would be consistent with an increase in the spread of $\delta^{34}S$ values of Proterozoic sedimentary sulfides, which indicate non-quantitative sulfate reduction in the marine environment (Canfield, 1998) (iii) Lastly, if C:P ratios were significantly elevated above modern values, even moderate P recycling could still have kept the P reservoir small in the Proterozoic (Fig. 4.4). It is therefore conceivable that electron acceptor limitation for P liberation extended into the Proterozoic eon.

4.4 Discussion

These results carry several important implications. First, oxidant-limited recycling of P rather than scavenging by Fe-minerals probably exerted the major control on P availability in the Archean, because secondary P-bearing minerals cannot form if P remains bound to organic matter. Fe-scavenging could, however, have become the major P sink in the Proterozoic if P recycling became more efficient (Figs. 4.2, 4.4). This would require that electron acceptors were nearly fully exploited, which is not the case today. Importantly, our model

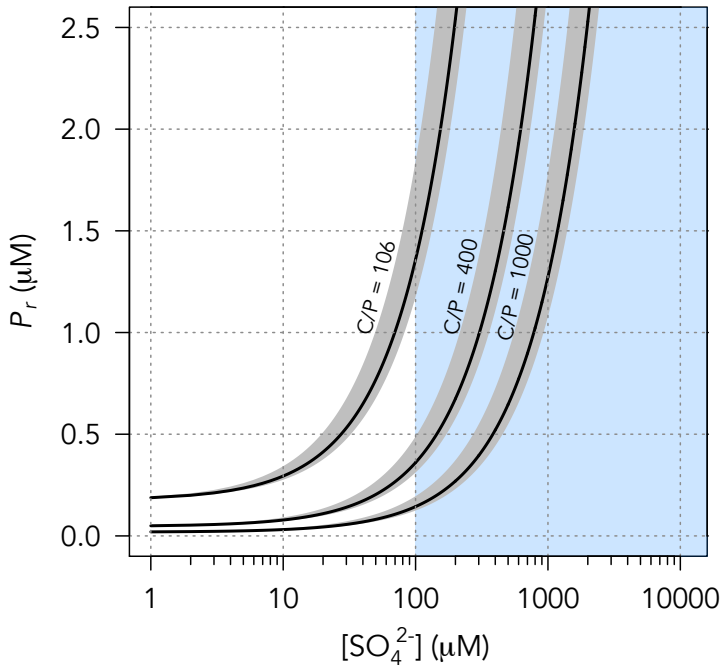

Figure 4.4: **Total possible Proterozoic phosphorus recycling as a function of sulfate availability.** Blue shaded region shows range of published estimates for Proterozoic sulfate concentrations. An increase in seawater sulfate levels after the GOE would have considerably increased the capacity for P recycling, though high C:P ratios could still have kept P levels low at the lower end of published estimates.

does not require higher-than-modern organic carbon concentrations in Archean sedimentary rocks but instead a relatively larger proportion of preservation of primary productivity, which would in turn have been suppressed with a lower P availability. The severity of this P scarcity imposed by limited biomass recycling increases substantially if bacterial C:P ratios were higher in the Precambrian (Figs. 4.3, 4.4). In such scenarios, the formation of authigenic P-bearing mineral phases (*e.g.*, CFA) may have been inhibited by the lower P input to marine sediments (Reinhard et al., 2016).

Secondly, our results suggest that in the Archean, microbial iron- and sulfate-reduction played an essential role in sustaining biological productivity by conducting the vast majority of P recycling within the ocean system (Fig. 4.3). The contributions of these two pathways may have been comparable despite a greater abundance of Fe^{3+} than SO_4^{2-} in Archean seawater, because sulfate reduction involves a transfer of eight electrons compared to one electron in iron reduction, meaning more P can be liberated per molecule. Prior to the onset of significant oxidative continental weathering (Stüeken et al., 2012) the major source of SO_4^{2-} to the ocean would have been photolysis of volcanic SO_2 (Farquhar et al., 2000). Our results thus highlight the potentially important role of volcanism in sustaining a significant biosphere on an anoxic planet by sourcing SO_4^{2-} to the ocean where it could contribute to biomass recycling. Additionally, the contribution of iron reduction to P recycling may have been sensitive to secular changes in heat flow and pulses in hydrothermal Fe inputs. These results thus illustrate another strong linkage between biological and planetary evolution.

Lastly, our proposed mechanism for low Archean P levels may help explain the delay between the earliest compelling evidence of oxygenic photosynthesis at ∼3.0 Ga (Planavsky et al., 2014) and the accumulation of atmospheric oxygen during the GOE (Bekker et al., 2004). It has long been recognized (Holland, 1984) that under near-modern rates of primary productivity, it is difficult to satisfy redox balance at Earth's surface while keeping atmospheric oxygen levels extremely low (Kasting, 2013). However, if suppressed recycling of biomass limited the P supply, then lower rates of primary productivity would alleviate the troubles with the Archean redox budget, due to diminished biospheric oxygen produc-

tion. This P-limited state could have been exited as incipient oxidation began on Earth's surface, delivering sulfate to the marine environment (Stüeken et al., 2012), thus increasing productivity and oxygenesis, culminating in the GOE.

4.5 Methods

We modified the box model approach used in (Sarmiento et al., 1988) in order to calculate dissolved P concentrations in the Precambrian oceans. This model relates deep ($O_{2\mathrm{d}}$) and surface ($O_{2\mathrm{s}}$) ocean oxygen concentrations by recognizing that their difference is equivalent to the amount of oxygen consumed during the oxidation of sinking organic matter, and that this can be stoichiometrically equated to the difference in surface and deep ocean P levels (P_{d} - P_{s}). This relationship can thus be expressed:

$$O_{2d} = O_{2s} - r(P_d - P_s) \tag{4.4}$$

where r is the stoichiometric coefficient of the liberation of P from biomass during aerobic remineralization (see model schematic, Fig. B.2). If P were not selectively remineralized during organic degradation, then r would approximately equal the Redfield C:P ratio of primary producers (*i.e.*, 106) due to the 1:1 O_2:C stoichiometry of aerobic respiration. However, it is known that P is in fact selectively released from organic matter during decomposition reactions (Clark et al., 1998), meaning that r is greater than the Redfield C:P ratio. The value of r has typically been estimated at 169 (Canfield, 1998; Sarmiento et al., 1988; Takahashi et al., 1985), although observations range from 120-200 in the modern ocean (Shaffer, 1996). We therefore used 169 as our preferred value, and explored the range from 120-200 to establish our confidence interval.

Equation 4.4 can then be used to predict deep-ocean oxygen concentrations if all other parameters are known. In order for this model to accurately capture the dynamics of the modern ocean, however, it is necessary to use $O_{2\mathrm{s}}$ and P_{s} values from high-latitude waters, since these water masses currently feed the deep ocean (Sarmiento et al., 1988). Failure to do so will generate very low (or negative) $O_{2\mathrm{d}}$ values, because some of the P in the deep

ocean today in fact derives from these downwelling nutrient-rich waters. Solving the equation with published P concentrations [P_{d} = 1.7-2.3 µM (Jones et al., 2015; Levitus et al., 1993; Sarmiento et al., 1988; Tyrrell, 1999); P_{s} = 0.7-1.24 µM (Levitus et al., 1993; Sarmiento et al., 1988)] and using an $O_{2\mathrm{s}}$ value of 325 µM – representative of high-latitude surface waters (Sarmiento et al., 1988) – yields an $O_{2\mathrm{d}}$ value of approximately 156 µM (confidence interval 110-185 µM) which is in good agreement with oceanographic observations (Baranova and others, 2005; Sarmiento et al., 1988).

In order to instead solve for deep ocean P concentrations, the equation can be rearranged:

$$P_d = P_s + \frac{O_{2s} - O_{2d}}{r_{O2}} \tag{4.5}$$

The amount of P in the deep ocean is thus shown to be equivalent to the amount sourced from nutrient-rich downwelling waters plus the amount liberated during biomass recycling.

We further modified the box model to include additional electron acceptors representing the most globally significant anaerobic metabolic pathways (Fig. B.2). While these pathways have a relatively minor role in phosphorus regeneration in the modern ocean, the reducing oceans of the Precambrian would have featured predominantly anaerobic microbial metabolisms (see main text for discussion).

4.6 References

Baranova, O., et al. 2005. World Ocean Atlas.

Bekker, A., Holland, H.D., Wang, P.-L., Rumble, D., Stein, H.J., Hannah, J.L., Coetzee, L.L., Beukes, N.J., 2004. Dating the rise of atmospheric oxygen. *Nature* 427, 117–120.

Bjerrum, C.J., Canfield, D.E., 2002. Ocean productivity before about 1.9 Gyr ago limited by phosphorus adsorption onto iron oxides. *Nature* 417, 159–162.

Broecker, W.S., Peng, T.-H., 1982. *Tracers in the Sea.* Lamont-Doherty Geological Observatory, Columbia University.

Calvert, S.E., Pedersen, T.F., 1992. Organic Carbon Accumulation and Preservation in Marine Sediments: How Important is Anoxia?, in: Whelan, J., Farrington, J.W. (Eds.),

Organic Matter: Productivity, Accumulation, and Preservation in Recent and Ancient Sediments. Columbia University Press, pp. 231–263.

Canfield, D.E., 1998. A new model for Proterozoic ocean chemistry. *Nature* 396, 450–453.

Canfield, D.E., Jørgensen, B.B., Fossing, H., Glud, R., Gundersen, J., Ramsing, N.B., Thamdrup, B., Hansen, J.W., Nielsen, L.P., Hall, P.O.J., 1993. Pathways of organic carbon oxidation in three continental margin sediments. *Mar. Geol.* 113, 27–40.

Clark, L.L., Ingall, E.D., Benner, R., 1998. Marine phosphorus is selectively remineralized. *Nature* 393, 426–426.

Crowe, S.A., Paris, G., Katsev, S., Jones, C., Kim, S.-T., Zerkle, A.L., Nomosatryo, S., Fowle, D.A., Adkins, J.F., Sessions, A.L., Farquhar, J., Canfield, D.E., 2014. Sulfate was a trace constituent of Archean seawater. *Science* 346, 735–739.

Emerson, S., Hedges, J.I., 1988. Processes controlling the organic carbon content of open ocean sediments. *Paleoceanography* 3, 621–634.

Farquhar, J., Bao, H.M., Thiemens, M., 2000. Atmospheric influence of Earth's earliest sulfur cycle. *Science* 289, 756–758.

Froelich, P., Klinkhammer, G.P., Bender, M. a al, Luedtke, N.A., Heath, G.R., Cullen, D., Dauphin, P., Hammond, D., Hartman, B., Maynard, V., 1979. Early oxidation of organic matter in pelagic sediments of the eastern equatorial Atlantic: suboxic diagenesis. *Geochim. Cosmochim. Acta* 43, 1075–1090.

Hao, J., Sverjensky, D.A., Hazen, R.M., 2017. A model for late Archean chemical weathering and world average river water. *Earth Planet. Sci. Lett.* 457, 191–203.

Hedges, J.I., Keil, R.G., 1995. Sedimentary organic matter preservation: An assessment and speculative synthesis. *Mar. Chem.* 49, 81–115.

Holland, H.D., 2003. The geologic history of seawater, in: *Treatise on Geochemistry.* pp. 583–625.

Holland, H.D., 1984. The chemical evolution of the atmosphere and oceans. Princeton University Press.

Izon, G., Zerkle, A.L., Williford, K.H., Farquhar, J., Poulton, S.W., Claire, M.W., 2017.

Biological regulation of atmospheric chemistry en route to planetary oxygenation. *Proc. Natl. Acad. Sci.* 114, E2571–E2579.

Jones, C., Nomosatryo, S., Crowe, S.A., Bjerrum, C.J., Canfield, D.E., 2015. Iron oxides, divalent cations, silica, and the early earth phosphorus crisis. *Geology* 43, 135–138.

Kasting, J.F., 2013. What caused the rise of atmospheric O_2? *Chem. Geol.* 362, 13–25.

Konhauser, K.O., Lalonde, S.V., Amskold, L., Holland, H.D., 2007. Was there really an Archean phosphate crisis? *Science* 315, 1234–1234.

Krissansen-Totton, J., Buick, R., Catling, D.C., 2015. A statistical analysis of the carbon isotope record from the Archean to Phanerozoic and implications for the rise of oxygen. *Am. J. Sci.* 315, 275–316.

Levitus, S., Conkright, M.E., Reid, J.L., Najjar, R.G., Mantyla, A., 1993. Distribution of nitrate, phosphate and silicate in the world oceans. *Prog. Oceanogr.* 31, 245–273.

Martin, J.H., Knauer, G.A., Karl, D.M., Broenkow, W.W., 1987. VERTEX: carbon cycling in the northeast Pacific. *Deep Sea Res. Part Oceanogr. Res. Pap.* 34, 267–285.

Planavsky, N.J., Asael, D., Hofmann, A., Reinhard, C.T., Lalonde, S.V., Knudsen, A., Wang, X., Ossa Ossa, F., Pecoits, E., Smith, A.J.B., Beukes, N.J., Bekker, A., Johnson, T.M., Konhauser, K.O., Lyons, T.W., Rouxel, O.J., 2014. Evidence for oxygenic photosynthesis half a billion years before the Great Oxidation Event. *Nat. Geosci.* 7, 283–286.

Planavsky, N.J., Rouxel, O.J., Bekker, A., Lalonde, S.V., Konhauser, K.O., Reinhard, C.T., Lyons, T.W., 2010. The evolution of the marine phosphate reservoir. *Nature* 467, 1088–1090.

Redfield, A.C., 1963. The influence of organisms on the composition of sea-water. *The Sea* 26–77.

Reeburgh, W.S., 2007. Oceanic methane biogeochemistry. *Chem. Rev.* 107, 486–513.

Reinhard, C.T., Planavsky, N.J., Gill, B.C., Ozaki, K., Robbins, L.J., Lyons, T.W., Fischer, W.W., Wang, C., Cole, D.B., Konhauser, K.O., 2016. Evolution of the global phosphorus cycle. *Nature* 541, 386–389.

Sarmiento, J.L., Herbert, T.D., Toggweiler, J.R., 1988. Causes of anoxia in the world ocean.

Glob. Biogeochem. Cycles 2, 115–128.

Schlesinger, W.H., Bernhardt, E.S., 2013. Biogeochemistry: An Analysis of Global Change, 3rd ed. Academic Press.

Shaffer, G., 1996. Biogeochemical cycling in the global ocean. 2. New production, Redfield ratios and remineralisation in the organic pump. *J Geophys Res* 101, C2.

Stüeken, E.E., Catling, D.C., Buick, R., 2012. Contributions to late Archaean sulphur cycling by life on land. *Nat. Geosci.* 5, 722–725.

Takahashi, T., Broecker, W.S., Langer, S., 1985. Redfield ratio based on chemical data from isopycnal surfaces. *J. Geophys. Res. Oceans* 90, 6907–6924.

Tosca, N.J., Guggenheim, S., Pufahl, P.K., 2016. An authigenic origin for Precambrian greenalite: Implications for iron formation and the chemistry of ancient seawater. *Geol. Soc. Am. Bull.* 128, 511–530.

Tyrrell, T., 1999. The relative influences of nitrogen and phosphorus on oceanic primary production. *Nature* 400, 525–531.

White, A.E., Spitz, Y.H., Karl, D.M., Letelier, R.M., 2006. Flexible elemental stoichiometry in *Trichodesmium* spp. and its ecological implications. *Limnol. Oceanogr.* 51, 1777–1790.

Zhelezinskaia, I., Kaufman, A.J., Farquhar, J., Cliff, J., 2014. Large sulfur isotope fractionations associated with Neoarchean microbial sulfate reduction. *Science* 346, 742–744.

Chapter 5

PERVASIVE AEROBIC NITROGEN CYCLING IN THE SURFACE OCEAN ACROSS THE PALEOPROTEROZOIC ERA

This manuscript is published as:

Kipp MA, Stueken EE, Yun M, Bekker A, Buick R. (2018). *Earth and Planetary Science Letters*. 500: 117-126. https://doi.org/10.1016/j.epsl.2018.08.007

5.1 Abstract

Nitrogen isotope ratios in marine sedimentary rocks have become a widely used biogeochemical proxy that records information about nutrient cycling and redox conditions in Earth's distant past. While the past two decades have seen considerable progress in our understanding of the Precambrian sedimentary nitrogen isotope record, it is still compromised by substantial temporal gaps. Furthermore, quantitative links between nitrogen isotope data, marine redox conditions, and nutrient availability are largely lacking in a Precambrian context. Here we present new nitrogen isotope data from a suite of marine sedimentary rocks with ca. 2.4 to 1.8 Ga ages, spanning the Great Oxidation Event in the Paleoproterozoic, to better constrain the response of the nitrogen cycle to the first major redox transition in Earth's history. We further construct a simple box model to describe the major pathways that influenced the nitrogen isotope mass balance of the Precambrian ocean and use this as a platform to evaluate the Precambrian nitrogen isotope record. Within this framework, we find that consistently positive nitrogen isotope values, ranging from +1.1 to +7.7‰, across the early Paleoproterozoic are strong evidence for an expansion of oxygenated surface waters. Since the isotopic signature of aerobic nitrogen cycling is recorded in the biomass of nitrate-assimilating organisms, this implicates widespread nitrate bioavailability in this time

interval. The decline in offshore nitrogen isotope ratios in the Mesoproterozoic is consistent with the contraction of oxic waters, which could have inhibited the expansion of nitrate-fueled ecosystems to pelagic waters until the widespread oxygenation of the ocean in the latest Neoproterozoic to early Phanerozoic.

5.2 Introduction

At the beginning of the Paleoproterozoic Era, Earth's atmosphere underwent a permanent shift from a reducing to an oxidizing state. This transition – termed the "Great Oxidation Event" (GOE) – began by ca. 2.43 Ga (Gumsley et al., 2017) and was characterized by oxygen-rich marine and terrestrial settings lasting until ca. 2.06 Ga (Bekker and Holland, 2012). In the aftermath of the GOE, atmospheric oxygen fell to an intermediate level that was substantially higher than in the Archean, but lower than Phanerozoic concentrations (Lyons et al., 2014). While the exact timing and mechanism of the GOE remain debated, the magnitude of its implications is clear: the biogeochemical pathways operating at Earth's surface were dramatically and permanently altered (Lyons et al., 2014), and the stage was set for the emergence of aerobically-respiring organisms, including the first eukaryotes (Javaux and Lepot, 2018).

Several paleo-redox proxies have been used to characterize the transition toward oxygenated surface environments in the Paleoproterozoic. Early evidence from oxidized paleosols documented the influence of atmospheric oxygen in weathering environments by ca. 2.2 Ga (*e.g.*, Beukes et al., 2002), and the recognition of a large perturbation in the global carbon cycle through carbon isotope systematics of carbonates has long been used to support a notion of extreme oxygen production during the GOE (*e.g.*, Karhu and Holland, 1996). More recently, the disappearance of mass-independent fractionation of sulfur isotopes (MIF-S) has been used to pinpoint the crossing of a threshold of 10^{-5} times the present atmospheric level of oxygen (PAL) between 2.46 and 2.32 Ga (Farquhar et al., 2000; Gumsley et al., 2017; Luo et al., 2016; Bekker et al., 2004), which has come to define the onset of the GOE proper.

The redox states of the atmosphere and ocean are coupled on geologic timescales, and so

the rise of atmospheric oxygen, the "oxygen overshoot," and the subsequent deoxygenation should have considerably affected marine redox chemistry. Indeed, enrichments of redox-sensitive trace elements in organic-rich shales implicate an expansion of oxygenated seawater during the GOE (Scott et al., 2008; Partin et al., 2013; Kipp et al., 2017), as do sulfur isotope ratios in marine sedimentary rocks, which suggest a waxing and waning seawater sulfate reservoir (Planavsky et al., 2012; Scott et al., 2014). Beyond these converging lines of evidence for widespread ocean oxygenation during the GOE, recent work has begun to decipher even regional redox gradients. Highly positive selenium isotope ratios in offshore marine sediments during the GOE imply oxygenated surface oceans, with anoxia prevailing at depth (Kipp et al., 2017). This finding is corroborated by the record of iodine enrichment in shallow-marine carbonates deposited at the same time, which requires at least mildly oxygenated surface waters (Hardisty et al., 2017).

Nitrogen isotope geochemistry can bring additional perspective to bear on the question of basinal redox structure, as nitrogen has a high redox potential – similar to that of selenium and iodine – and is sensitive to redox conditions in the photic zone, where primary productivity is highest. The nitrogen isotope composition of organic matter in offshore marine sediments can thus speak to redox chemistry in the photic zone overlying the outer shelf and open ocean. Furthermore, as nitrogen is an essential macronutrient, nitrogen isotopes in marine sediments also record the balance between nitrogen-fixing organisms (strictly prokaryotic) and nitrogen-assimilating organisms (which can be either prokaryotic or eukaryotic). Since nitrate (NO_3^-) is the preferred nitrogenous substrate for eukaryotes in the modern ocean (*e.g.*, Karl et al., 2001), tracing the prevalence of aerobic nitrogen cycling during the Paleoproterozoic can both constrain redox conditions and speak directly to the bioavailability of NO_3^- for eukaryotic organisms. Notably, despite the wealth of evidence from a variety of well-established paleo-redox proxies, the immediate response of the nitrogen cycle to the GOE has only been investigated in a few studies that focused specifically on the onset, culmination, or aftermath of the GOE (Kump et al., 2011; Luo et al., 2018; Papineau et al., 2009; Zerkle et al., 2017). While those studies have provided important evidence

for the presence of aerobic nitrogen cycling during the GOE, the sparse record through the Paleoproterozoic hinders reconstructions of global temporal and spatial patterns across the proposed "oxygen overshoot."

Here we present nitrogen isotope data from a suite of Paleoproterozoic marine sedimentary rocks that span the GOE in order to better characterize the response of the biogeochemical nitrogen cycle to the first permanent increase in atmospheric and marine oxygen levels. Taking this a step further, we then construct a simple steady-state isotope box model and use it as a platform for evaluating secular trends in the Precambrian nitrogen isotope record. To date, nitrogen isotopes in ancient marine sediments have been used at best as a semi-quantitative redox proxy. We find that even with this simple view of the nitrogen cycle, a robust correlation can be drawn between nitrogen isotope ratios in marine sediments and the extent of oxic surface waters. This new, quantitative framework for interpreting the nitrogen isotope record enables a direct comparison with results from other proxies, thereby refining our view of ocean oxygenation during and after the GOE.

5.3 Materials

We collected nitrogen and organic carbon isotopic data from a large sample set (n = 144) of marine, siliciclastic sedimentary rocks with ages spanning ca. 2.4 to 1.8 Ga. We targeted shales deposited in offshore depositional environments (below wave base) in basins that were open with respect to exchange with the global ocean. When viewed together, these lithologies capture a representative view of secular trends in global nitrogen cycling. None of the units studied here have experienced metamorphism beyond lower greenschist facies. Detailed descriptions of individual units can be found in the Supplementary Materials.

5.4 Methods

5.4.1 Sample preparation for bulk rock analyses

Sample preparation followed published methods (Stüeken, 2013; Koehler et al., 2017). Samples were crushed into centimeter-sized chips, and equipment was cleaned between samples with methanol and 18 MΩ DI-H_2O. Rock chips were sequentially cleaned with ethanol, 2N HCl, and DI-H_2O to remove modern contaminants, then dried in an oven at 60°C. Clean chips were pulverized using an aluminum oxide puck mill that was cleaned between samples using methanol, DI-H_2O, and pre-combusted (500°C) silica sand. Prior to analysis, powders were decarbonated using 6N HCl, then rinsed with DI-H_2O and dried in an oven at 60°C.

5.4.2 Kerogen extraction

Kerogen was extracted from bulk rock powders following published protocols (Stüeken et al., 2015). Rock powders were weighed out into teflon bottles and treated with a 50:50 mixture of DI-H2O and concentrated (29N) hydrofluoric acid (HF) in a shaking water bath at 55°C. Digests were then centrifuged and the supernatant was decanted. A BF_3 solution (62.5g H_3BO_3, 100 mL DI-H_2O, 100 mL 29N HF) was then added, and the samples were placed in a shaking water bath at 55°C to dissolve remaining fluoride minerals. Samples were then centrifuged, the supernatant was decanted, and the samples were washed with three iterations of DI-H_2O. The isolated kerogen was transferred to a combusted pyrex vial in DI-H_2O and freeze-dried to remove all moisture prior to analysis.

5.4.3 Isotopic analyses

The isotopic composition ($\delta^{15}N$ and $\delta^{13}C_{org}$) of decarbonated powders and kerogen isolates was measured on a CostechTM ECS 4010 Elemental Analyzer coupled to a Thermo Finnigan^{TM} MAT253 continuous flow isotope-ratio mass spectrometer housed in IsoLab at the Department of Earth & Space Sciences, University of Washington. Combustion was carried out with 20mL O_2 at 1000°C. A magnesium perchlorate trap was used to remove water

from the gas stream. Isotopic measurements were standardized against three in-house standards (two glutamic acids "GA1" and "GA2", and dried salmon "SA"), which are calibrated to international reference materials USGS40 and USGS41. An aliquot of the Neoarchean Mt. McRae Shale was analyzed as an in-house standard to test long-term precision. Isotopic data are reported in delta notation relative to air for nitrogen and Vienna PeeDee Belemnite (V-PDB) for carbon.

Analytical blanks resulting from combustion were monitored and subtracted from nitrogen data; blanks were negligible for carbon measurements. Average analytical accuracy of $\delta^{15}N$ among individual runs, based on in-house standard "GA1" was -0.03 ± 0.19‰ (1σ). Accuracy of $\delta^{13}C_{org}$ measurements based on in-house standard "SA" was -0.05 ± 0.07‰ (1σ). The average analytical precision among all runs based on in-house standard "UW-McRae" was 0.12‰ (1σ) for $\delta^{15}N$ and 0.04‰ (1σ) for $\delta^{13}C_{org}$. All samples were analyzed at least twice, with an average standard deviation between sample replicates of 0.25‰ for $\delta^{15}N$ and 0.17‰ for $\delta^{13}C_{org}$.

Samples from the Sengoma Argillite Formation were analyzed for bulk nitrogen content and $\delta^{15}N_{bulk}$ values (without decarbonation) following standard procedures in the Stable Isotopes for Innovative Research Laboratory at the Department of Geological Sciences, University of Manitoba (cf. Zerkle et al., 2017). Analyses were performed using a CostechTM 4010 Elemental Analyzer coupled to a Thermo FinniganTM Delta V Plus isotope-ratio mass spectrometer. A magnesium perchlorate-carbosorb trap was placed before ConFlo III to remove water and CO_2. Temperature in the oxidation column was raised to 1050°C for efficient sample combustion, and a 'macro' O_2 injection loop was utilized. CO_2 levels were monitored during analytical sessions. Sample normalization was performed using two-point calibration with two international standards (USGS40 and USGS41) at the beginning, middle, and end of each run. To monitor the quality of analytical performance, two certified standards were analyzed alongside with samples: B2153, soil, % TN = 0.13 ± 0.02%, $\delta^{15}N$ = +6.70 ± 0.15‰ (Elemental Microanalysis); and SDO-1, Devonian Ohio Shale, % TN = 0.36 ± 0.01%, $\delta^{15}N$ = -0.8 ± 0.3‰ (USGS). The data obtained were TN (wt. %) = 0.14 ± 0.00% and $\delta^{15}N$

values of +6.76 ± 0.02‰ (n=3) for B2153, and TN (wt. %) = 0.37 ± 0.00% and $\delta^{15}N$ values of -0.32 ± 0.02‰ (n=3) for SDO-1.

5.4.4 Isotope box model

We constructed a steady-state box model of the nitrogen cycle to track the salient processes affecting nitrogen isotope mass balance in the ocean system (Fig. 5.1). The major input of nitrogen to the ocean is biological N_2 fixation to NH_4^+, which is released during biomass degradation and oxidized rapidly to NO_3^- (nitrification). We assumed that nitrification occurs instantaneously as soon as NH_4^+ upwells to the surface ocean, because previous studies have shown that nitrification proceeds even at nanomolar levels of dissolved O_2 (*e.g.*, Kalvelage et al., 2011). The major output of nitrogen from the ocean is assumed to be denitrification (NO_3^- reduction to N_2), which occurs in suboxic-to-anoxic parts of the water column (here defined as <4.5 µM O_2; Keeling et al., 2009) and in anoxic sedimentary porewaters. We did not separately parameterize the anammox pathway (NH_4^+ oxidation to N_2 using NO_2^-) because the isotopic effect is similar to canonical denitrification and thus a changing balance between anammox and canonical denitrification is unlikely to affect the nitrogen isotope mass balance of the ocean (Devol, 2015).

We first calibrated our model to reproduce the isotopic mass balance of the modern ocean (Devol, 2015). Then we adjusted the balance of water column and sedimentary denitrification as a function of anoxia in the ocean. The isotopic composition of export production was calculated for two end-member scenarios: (i) a closed system where nitrate is irreversibly transformed into either N_2 (via denitrification) or biomass (via assimilation) (*i.e.*, resulting in progressive isotopic distillation of the residual pool at higher yields), and (ii) an open system at steady state (*i.e.*, resulting in isotopic offsets between products and reactants that are nearly identical to the fractionation factor) (cf. Hayes, 2004). Because the residence time of nitrogen in the modern ocean is ∼3 kyrs (Brandes and Devol, 2002), nitrogen is moderately well-mixed in the modern open ocean, and thus nitrogen isotope mass balance should generally follow open-system dynamics (as is assumed for carbon isotope mass balance; Hayes,

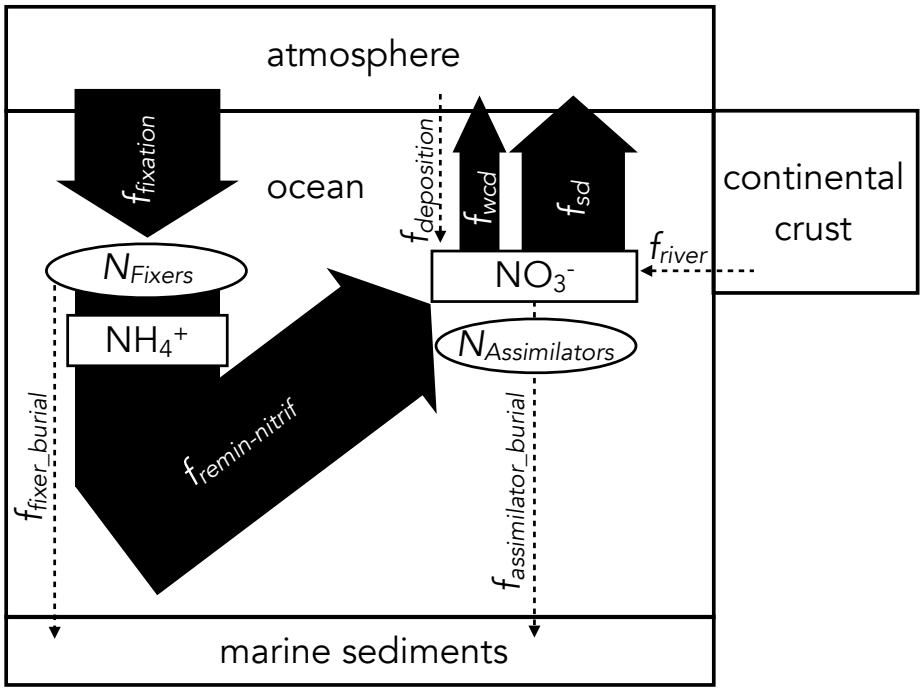

Figure 5.1: **Schematic of fluxes included in box model.** Nitrogen fixation ($f_{fixation}$) is the dominant input to the ocean system, with water column (f_{wcd}) and sediment (f_{sd}) denitrification constituting the major output fluxes. The dominant input (>99%) of nitrate is nitrification ($f_{remin\text{-}nitrif}$), with atmospheric deposition ($f_{deposition}$) and riverine (f_{river}) inputs comprising only minor contributions (<1%). Modern flux constants were used to calibrate the model, and then the balance of f_{wcd}, f_{sd}, and f_{burial} (including burial of both fixers and assimilators) was adjusted to simulate changes in ocean redox chemistry. Since remineralization of organic matter produces a small or negligible N isotope fractionation, ammonium burial with clay minerals is not treated separately in the model. A detailed description of model architecture can be found in Appendix C.

2004; Schidlowski, 2001). However, in modern basins with very high rates of water column denitrification, the isotopic distillation of residual NO_3^- can locally approach closed system dynamics, causing nitrogen isotope ratios in certain regions of the modern ocean to become substantially elevated above global mean values (Tesdal et al., 2013). In the low-oxygen Precambrian ocean, closed-system behavior of nitrogen isotopes may have been more prevalent, particularly prior to the GOE. Thus, we present both calculations, noting that the open-system scenario more accurately captures the global average value for marine sediments with predominantly oxic environments, while local environments can be susceptible to closed system dynamics. A full description of all parameterizations and equations can be found in the Supplementary Materials.

5.5 Results

5.5.1 Isotopic results

All of the studied units consistently show bulk-rock $\delta^{15}N$ values (Fig. 5.2; Table C.1) that are elevated above the range expected from nitrogen fixation alone (-2‰ to +1‰; Zhang et al., 2014). The mean $\delta^{15}N_{bulk}$ value of all units analyzed is +4.8 ± 1.4‰ (1σ), which closely resembles the nitrogen isotope composition of modern marine sediments (mode +4‰ to +6‰; Tesdal et al., 2013). Within individual units, $\delta^{15}N_{bulk}$ values are fairly consistent over several meters in stratigraphy, with an average per-unit standard deviation of 0.6‰ (ranging from 0.2‰ to 1.8‰). The full range of $\delta^{15}N_{bulk}$ values in the samples analyzed in this study is +1.1‰ to +7.7‰, which largely overlaps the range seen in modern marine sediments (Tesdal et al., 2013). Notably, we find no evidence of extremely enriched $\delta^{15}N_{bulk}$ values (>+10‰) in any of the units studied here (Fig. 5.2), which stands in contrast to the data from Paleoproterozoic shales of the Aravalli Supergroup in India (Papineau et al., 2009).

Kerogen isolates were isotopically lighter than their corresponding bulk-rock values by an average of -2.5‰ (Fig. 5.3; Table S1). The isotopic offset increased as a function of

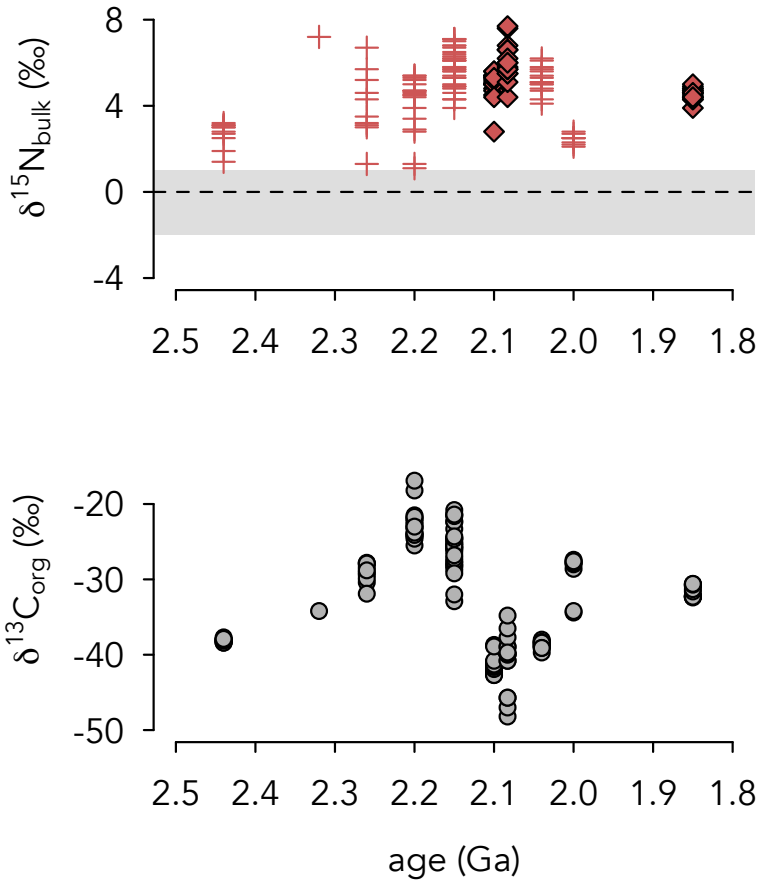

Figure 5.2: **Isotopic data generated in this study.** Crosses denote nitrogen isotope data from units that experienced lower greenschist facies metamorphism, diamonds denote data from units that remained below greenschist facies. All nitrogen isotope data are enriched above the range of values expected for nitrogen-fixation dominated systems (-2‰ to +1‰; grey shaded region). Most units contain carbon isotope ratios that are depleted below the normal range for marine phytoplankton (-26‰ ± 7‰; Schidlowski, 2001), perhaps reflecting heterotrophic degradation of sedimentary organic matter in anoxic seawater and sediments.

metamorphic grade, with unmetamorphosed samples showing a small positive offset (+0.6‰; $n = 4$), while samples that reached prehnite-pumpellyite facies (-2.4‰; $n = 6$) and lower greenschist facies (-3.2‰; $n = 20$) showed a moderate negative offset (Fig. 5.3).

A LOWESS (LOcally WEighted Scatterplot Smoothing) curve was used to describe variability in the nitrogen isotope record across the GOE (details can be found in Supplementary Materials). Bulk-rock nitrogen isotope data from Precambrian marine sedimentary rocks were compiled from the literature by updating a published database (Stüeken et al., 2016). All published data from units spanning 3.3 to 1.3 Ga were included in the LOWESS calculations. The mean $\delta^{15}N$ value of the LOWESS curve is +3.6 ± 1.2‰ (1σ). The curve shows a secular trend across the GOE, with $\delta^{15}N$ values rising in the late Archean, reaching a maximum just prior to the GOE, stabilizing across much of the Paleoproterozoic, and slightly decreasing in the Mesoproterozoic (Fig. 5.9).

The mean $\delta^{13}C_{org}$ value of all samples in our dataset is -32.5 ± 7.3‰ (1σ). As with $\delta^{15}N$, $\delta^{13}C_{org}$ values for individual units are fairly consistent, with an average per-unit standard deviation of 1.8‰ (ranging from 0.2‰ to 3.9‰). Most studied units contain samples with $\delta^{13}C_{org}$ values that are more negative than the range typically generated by marine phytoplankton (-26‰ ± 7‰; Schidlowski, 2001), which might reflect heterotrophic activity, including methanogenesis, occurring in predominantly anoxic sediments, and methanotrophy either at the sediment-water interface or throughout the overlying water column utilizing dissolved oxidants (e.g. Bekker et al., 2008; Luo et al., 2014). A notable exception is an increase in $\delta^{13}C_{org}$ values seen in units deposited during the ca. 2.22-2.06 Ga Lomagundi carbon isotope excursion (Fig. 5.2), with $\delta^{13}C_{org}$ values rising to -22.6 ± 2.2‰ (1σ) in the Wewe Slate and -25.7 ± 3.0‰ (1σ) in the Sengoma Argillite Formation (Bekker et al., 2008).

5.5.2 Model outputs

The box model-estimated mean $\delta^{15}N$ value for modern marine sediments (assuming open-system dynamics) is +4.5‰, with a confidence interval of +2.6‰ to +7.3‰ based on uncertainties in fractionation factors for nitrogen fixation and water column denitrification. The

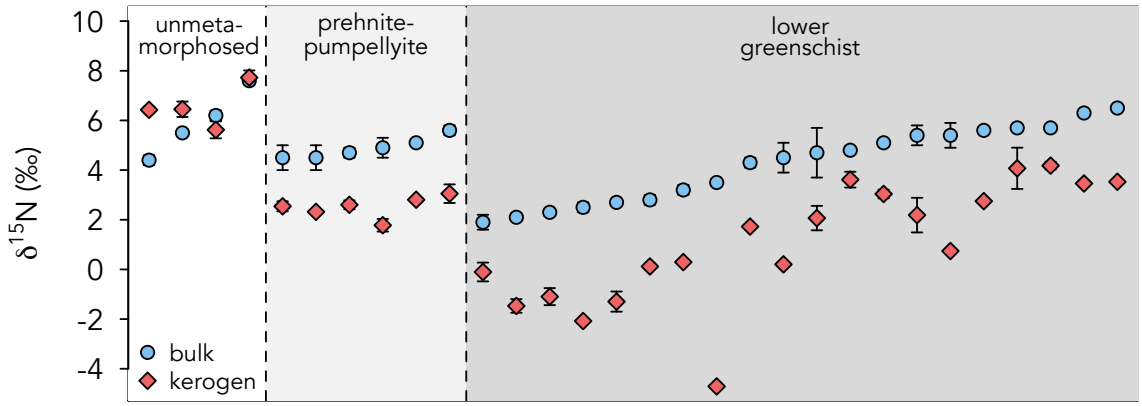

Figure 5.3: **Comparison of nitrogen isotope ratios in bulk rock samples versus kerogen extracts.** The $\delta^{15}N_{ker}$ values show a trend of being consistently isotopically lighter than their corresponding $\delta^{15}N_{bulk}$ values, which is consistent with a previous study (Stüeken et al., 2017). Furthermore, the isotopic offset tends to be larger at higher metamorphic grade, which corroborates the suggestion that isotopic re-equilibration occurs between nitrogen phases under progressive metamorphism. The isotopic offsets observed in the samples are consistent with the metamorphic grades that have been inferred from mineral assemblages.

closed system approach yields similar results (mean = +5.5‰, range of +3.5‰ to +8.5‰). Both approaches thus accurately capture the average composition of modern marine sediments (mode +4-6‰ ± 2.5‰; Tesdal et al., 2013).

As the relative proportion of suboxic-to-anoxic ocean water increases beyond modern values and approaches 100% (*i.e.*, $p_{\mathrm{an+sub}}$ approaches 100), sedimentary $\delta^{15}N$ values first increase due to enhanced water column denitrification, but ultimately decline toward the "N_2-fixation window" (-2‰ to +1‰) in strongly anoxic oceans (Fig. 5.8) because the rate of nitrogen removal is so rapid (and nearly quantitative) that nitrogen-fixing rather than nitrate-assimilating organisms dominate the nitrogen isotope mass-balance (cf. Fennel et al., 2005). In the closed system model, values do not return to the "N_2-fixation window" even in fully anoxic oceans ($p_{\mathrm{an+sub}} = 100$), because the extremely fractionated nitrate associated with a totally closed system would still drive sedimentary $\delta^{15}N$ values to become positive even with a minimal biomass contribution from nitrate-assimilating organisms. However, such extreme fractionations are unlikely to have occurred, since the ocean cannot be a totally closed system (*i.e.*, nitrogen is continually being fixed into biomass and made bioavailable through remineralization and nitrification). Reality for the full range of ocean redox states thus lies somewhere between the two endmembers captured by the separate calculations.

5.6 Discussion

5.6.1 Preservation of primary isotopic signals

Before using nitrogen isotopes in ancient marine sedimentary rocks to reconstruct paleoenvironmental conditions, it must be demonstrated on a case-by-case basis that the observed isotopic signatures indeed reflect the primary cycling of nitrogen in the ocean at the time of deposition (Ader et al., 2016). This screening draws first from consideration of nitrogen cycling in the modern ocean. The nitrogen isotopic composition of modern marine sediments faithfully records the $\delta^{15}N$ value of biomass exported from the photic zone (Altabet and Francois, 1994), which is an admixture of nitrogen-fixing and nitrogen-assimilating or-

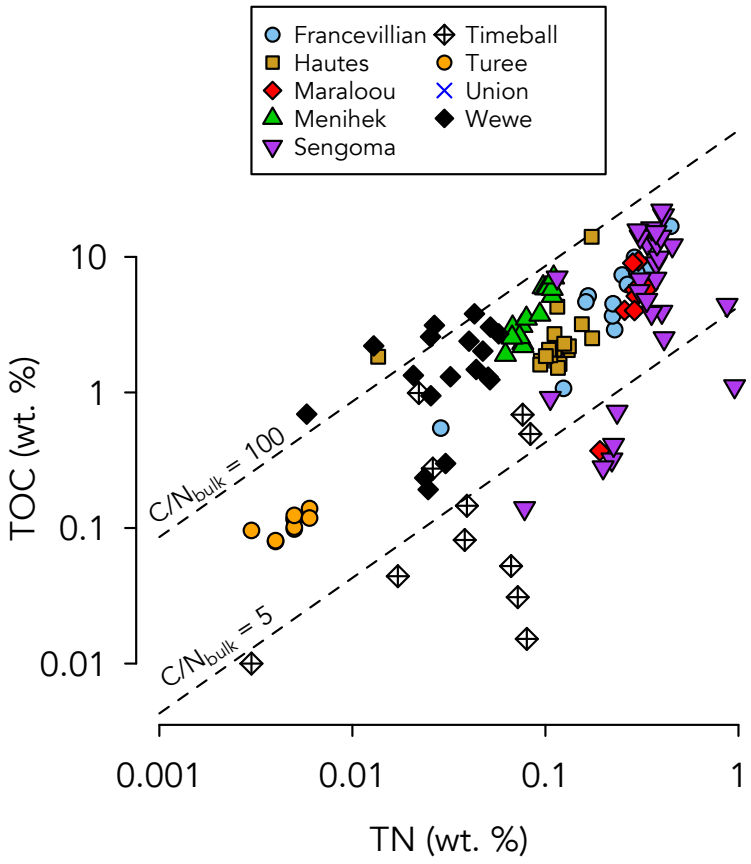

Figure 5.4: **Total organic carbon versus total nitrogen values for all bulk-rock measurements in this study.** Dotted lines show C/N ratios of 5 and 100, respectively. The average molar C/N ratio of planktonic biomass in the modern ocean is ~7 (Redfield, 1934). Water-column and sedimentary diagenesis can increase sedimentary C/N ratios, giving a spread in values similar to what is observed in most units in this study. Causes for low sedimentary C/N ratios are discussed in Section 5.5.1.

ganisms. Planktonic biomass in the modern ocean has an average molar C/N ratio of ∼7 (Redfield, 1934), and the remineralization of biomass in the water-column and sediments can increase the C/N values preserved in marine sediments. The C/N values of our samples predominantly fall between 5 and 100 (Fig. 5.4), which is consistent with moderate diagenetic reworking of primary biomass. The Timeball Hill Formation has several samples with C/N values <5 (Fig. 5.4), which suggests either (a) trapping of nitrogen in clay minerals during diagenesis, while carbon was oxidized and lost from the system, or (b) post-depositional introduction of non-primary nitrogen (perhaps via hydrothermal fluids). As discussed below, the fact that kerogen extracts from these samples show expected isotopic offsets is consistent with a primary biomass origin for the nitrogen in these samples, as was suggested by Luo et al. (2018).

Diagenesis can modify the $\delta^{15}N$ values of organic matter in marine sediments, but this effect is typically much smaller than the fractionations imparted during nitrogen cycling in the water column. In oxic sediments, the remineralization of organic-bound nitrogen can leave residual biomass isotopically heavier by 1.4-2.3‰ (Lehmann et al., 2002; Möbius, 2013). However, the effect is smaller under anoxic conditions (Lehmann et al., 2002), which likely prevailed in Precambrian marine sedimentary environments. Thus, while the precise contribution of diagenesis is difficult to assess, the isotopic effect of diagenesis on the $\delta^{15}N$ values was probably minor (<1‰) compared to the magnitude of the isotopic enrichment (>>1‰) seen in these samples.

After diagenesis, nitrogen isotope ratios can be further modified during metamorphism. This involves two types of isotopic effects: isotopic partitioning between kerogen- and mineral-bound nitrogen within the bulk rock (Stüeken et al., 2017) and loss of nitrogen out of the bulk rock (Bebout and Fogel, 1992; Haendel et al., 1986). While the isotopic partitioning between nitrogen phases within a bulk-rock sample can be significant (3-4‰) at low metamorphic grades (Stüeken et al., 2017), the effect of nitrogen loss on bulk-rock $\delta^{15}N$ values is typically small in units that have remained below greenschist-facies metamorphism (< 1‰) or even within greenschist facies (1-2‰; Rivera et al., 2015). The finding that $\delta^{15}N_{ker}$ values

are systematically depleted (on average by -2.5‰) relative to corresponding $\delta^{15}N_{bulk}$ values in this dataset is consistent with previous studies of metamorphic effects on nitrogen isotope partitioning (Stüeken et al., 2017). Furthermore, the increase in isotopic offset from near-zero in unmetamorphosed samples to ∼3‰ in lower greenschist facies samples (Fig. 5.3) is in good agreement with a systematic survey of metamorphic effects on sedimentary $\delta^{15}N$ values (Stüeken et al., 2017). Thus, we follow Stüeken et al. (2017) in taking $\delta^{15}N_{bulk}$ values as a more robust indicator of primary $\delta^{15}N$ values in these samples.

In cases where metamorphism has significantly altered bulk-rock nitrogen isotope ratios, it has been shown that progressive metamorphism causes preferential loss of nitrogen relative to carbon, and of ^{14}N relative to ^{15}N (Bebout and Fogel, 1992). Thus, a positive correlation between $\delta^{15}N_{bulk}$ and C/N ratios can be indicative of metamorphic alteration of bulk-rock nitrogen isotope ratios, and a positive correlation between $\delta^{15}N_{bulk}$ and $\delta^{13}C_{org}$ would suggest that both nitrogen and carbon isotopes were affected by metamorphism. There are no such positive correlations observed across our entire dataset (Fig. 5.5) or within individual units (Figs. C.1 and C.2), including those that reached greenschist facies metamorphism. The effect of metamorphism on the bulk-rock nitrogen and organic carbon isotope ratios in these samples was therefore probably minor, meaning that the trends in nitrogen and carbon isotopes seen across the GOE are primary isotopic signals indicative of environmental conditions at the time of deposition.

5.6.2 Interpretation of isotopic data

Mechanisms for generating positive $\delta^{15}N$ values

There are multiple ways to generate positive $\delta^{15}N$ values in ancient marine sedimentary rocks (see Ader et al., 2016; Stüeken et al., 2016). These mechanisms all pertain to the cycling of nitrogen after biological N_2 fixation, which imparts only a small fractionation under most conditions (-2‰ to +1‰; Zhang et al., 2014). Under conditions of replete dissolved Fe supply this fractionation can be slightly larger, generating biomass that is depleted by as

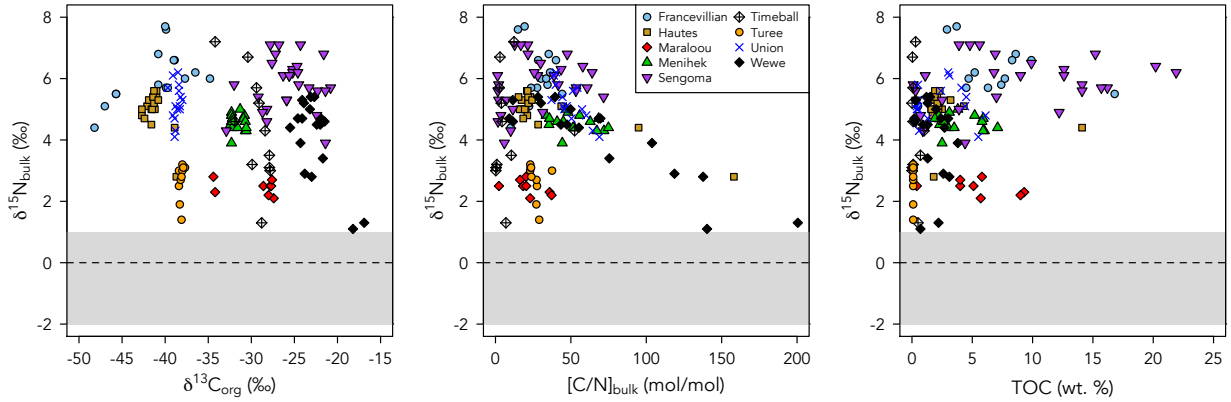

Figure 5.5: **Cross-plot assessment of the preservation of primary nitrogen isotope ratios.** Grey shaded region denotes $\delta^{15}N_{bulk}$ values associated with nitrogen fixation-dominated ecosystems. The lack of co-variation between $\delta^{15}N_{bulk}$ and $\delta^{13}C_{org}$, C/N, and TOC suggests that the $\delta^{15}N_{bulk}$ values were not strongly affected by diagenetic and metamorphic overprinting. See discussion for further details and Figs. C.1-C.3 for plots of individual units.

much as -4‰ relative to atmospheric nitrogen (Zerkle et al., 2008). However, the lack of fairly negative $\delta^{15}N$ values in the Precambrian rock record – even in environments that are thought to have been ferruginous and dominated by N_2 fixation – suggests that these extreme conditions were not representative of global nitrogen cycling (Koehler et al., 2017; Stüeken, 2013; Stüeken et al., 2015).

As discussed in Section 5.5.1, the release of nitrogen during remineralization of organic matter imparts a negligible fractionation, making it unlikely to explain an isotopic enrichment of several permil. However, the re-assimilation of ammonium (NH_4^+) generated during remineralization can impart a large isotopic fractionation (up to -27‰) if the process is non-quantitative, with biomass becoming isotopically light (Hoch et al., 1992). Such a mechanism has been proposed to explain the very large spread of $\delta^{15}N$ values seen in shales of the late Paleoproterozoic Aravalli Supergroup (Papineau et al., 2009). This mechanism would require that non-quantitative NH_4^+ assimilation created a pool of isotopically light biomass and drove the isotopic composition of residual NH_4^+ isotopically heavy. The transport of

the heavy nitrogen to another site and subsequent quantitative assimilation could plausibly generate elevated $\delta^{15}N$ values in marine sediments. However, the absence of isotopically light nitrogen in the nine units studied here makes this explanation seem unlikely. Furthermore, even in modern redox-stratified marine basins, such as the Black Sea, the accumulation of appreciable dissolved NH_4^+ does not correlate with isotopic evidence of partial assimilation (*e.g.*, Fulton et al., 2012). Sediments underlying these modern anoxic waters have $\delta^{15}N$ values near 0‰, suggestive of nitrogen fixation in the photic zone followed by quantitative uptake of liberated NH_4^+. This can be attributed to the fact that nitrogen is the limiting nutrient in the ocean on short, kyr-timescales (Tyrrell, 1999), and thus uptake of bioavailable nitrogen in the photic zone is typically quantitative.

While nitrogen uptake into biomass tends to have no net isotopic effect, partial removal of bioavailable nitrogen from the ocean through redox processes can result in significant isotopic fractionations. One such pathway is the nitrification of NH_4^+ into NO_3^-, which – if non-quantitative – can create a NO_3^- pool that is isotopically light and leave a residual, heavy pool of NH_4^+ (Casciotti et al., 2003). The resulting biomass could become isotopically heavy if organisms quantitatively assimilate the heavy NH_4^+, while the light NO_3^- is quantitatively removed via denitrification to the atmosphere (Thomazo et al., 2011). However, it is unlikely that this sort of system would have been stable on geological timescales. Today, partial nitrification is only observed in regions of the modern ocean where seasonal redox-stratification occurs (*e.g.*, Granger et al., 2011). This is because nitrification is rapid, and can even proceed at nanomolar levels of dissolved oxygen (*e.g.*, Kalvelage et al., 2011). Furthermore, the same conditions that would favor non-quantitative nitrification (seasonally variable redox-stratification) might be inimical to quantitative denitrification, as the latter process is not as rapid, and rarely goes to completion in the open ocean (Devol, 2015).

Another explanation for isotopic enrichment in marine settings is non-quantitative denitrification occurring in suboxic regions of the open ocean. This process imparts a large isotopic fractionation (-10 to -30‰; Devol, 2015; Kritee et al., 2012), causing residual dissolved NO_3^- to become isotopically heavy ($\delta^{15}N > 0$‰). Importantly, denitrification occur-

ring in sedimentary porewaters nearly goes to completion, resulting in a flux of isotopically heavy nitrogen from the ocean back into the atmosphere, counterbalancing the isotopically light flux from suboxic waters. The quantitative assimilation of the residual heavy NO_3^- then records the net isotopic distillation of the reservoir imparted by denitrification, which ultimately gets preserved in marine sediments. This mechanism is thought to control the isotopic mass balance of the modern ocean system (Devol, 2015), causing the $\delta^{15}N$ values of most modern marine sediments to fall between +4‰ and +6‰ (Tesdal et al., 2013).

Considering all possible mechanisms listed above, the positive $\delta^{15}N$ values seen in the Paleoproterozoic units studied here are most compellingly explained by similar processes to those operating in the modern ocean: rapid nitrification, non-quantitative denitrification in suboxic regions of the water column, and quantitative assimilation of residual NO_3^- in the photic zone. In other words, our nitrogen isotope data suggest that an aerobic nitrogen cycle persisted across continental shelves between about 2.44 and 1.85 Ga.

Aerobic nitrogen cycling in the early Paleoproterozoic

While transient excursions to elevated $\delta^{15}N$ values – indicative of local aerobic nitrogen cycling – have been observed in Neoarchean shales (Garvin et al., 2009; Koehler et al., 2018), it remains unclear to what extent these settings are representative of global redox conditions at that time. The large isotopic variability seen in some Neoarchean facies is consistent with a small NO_3^- reservoir (Garvin et al., 2009; Koehler et al., 2018), which could promote substantial inter-basinal variability and closed-system dynamics (discussed further in Section 5.5.3). In contrast, the more stable stratigraphic $\delta^{15}N$ profiles of the Paleoproterozoic (Fig. 5.5) may reflect growth of the NO_3^- reservoir, with the ocean residence time of NO_3^- becoming sufficiently long that relatively rapid and large-magnitude isotopic excursions are not seen within continuous lithostratigraphic units. This was first suggested by Zerkle et al. (2017), who found evidence of aerobic nitrogen cycling in the early stages of the GOE in the 2.32 Ga Lower Timeball Hill Formation of the Pretoria Group in South Africa, and further confirmed by the findings of another recent study of multiple drill cores in the Pretoria Group (Luo

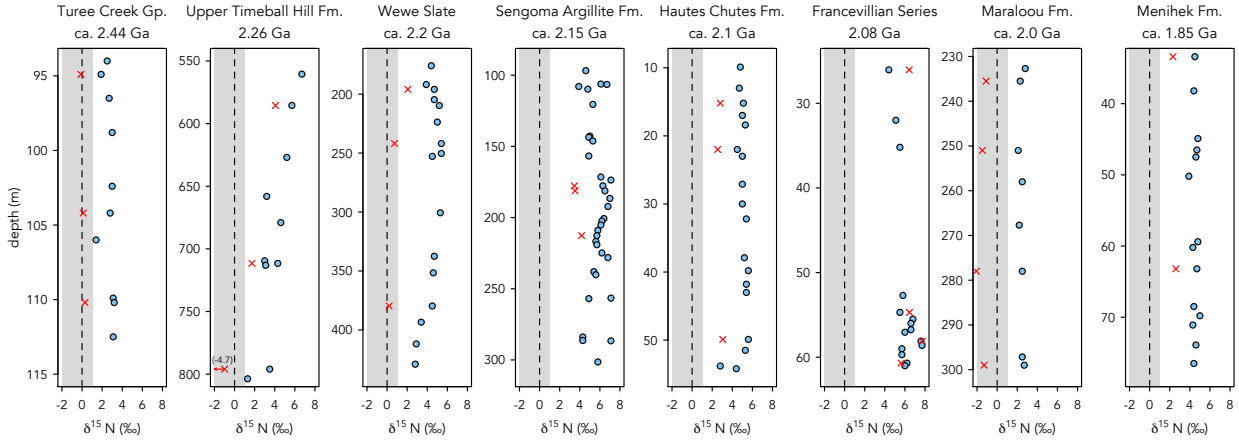

Figure 5.6: **Nitrogen isotope values plotted along stratigraphic profiles.** Circles show bulk-rock data, crosses denote kerogen isolates. All studied units show $\delta^{15}N_{bulk}$ values that are consistently above the values expected for a fully anaerobic, fixation-dominated ecosystem (grey shaded region). Outcrop samples from the Union Island Group are not plotted as they were collected from multiple outcrops.

et al., 2018). Our dataset corroborates those findings, showing instances of elevated $\delta^{15}N$ values in the Upper Timeball Hill Formation. Additionally, we find that shales of the ca. 2.44 Ga Turee Creek Group in Western Australia, which were deposited shortly before the onset of the GOE, have $\delta^{15}N$ values (ranging from +2‰ to +3‰) that are consistent with a minor, but persistent, contribution of aerobic nitrogen cycling to the isotopic composition of preserved biomass. However, because diagenetic and metamorphic overprinting could have potentially contributed a post-depositional enrichment of $\delta^{15}N_{bulk}$ values by ∼1-2‰, it is difficult to use the Turee Creek data to precisely gauge the extent of aerobic nitrogen cycling immediately prior to the GOE.

The state of the nitrogen cycle appears to have been fairly stable across the GOE and the proposed "oxygen overshoot" during the Lomagundi carbon isotope excursion (ca. 2.22-2.06 Ga; Bekker and Holland, 2012). Even in the aftermath of the GOE (*i.e.*, after ca. 2.06 Ga), when sulfur and selenium isotope records point to a contraction of oxygenated seawater

(Planavsky et al., 2012; Scott et al., 2014; Kipp et al., 2017), nitrogen isotopes continue to record aerobic nitrogen cycling in the surface ocean (Fig. 5.7). This is unlikely to be an artifact of poor age constraints and low sample density – many of the nitrogen isotope data are from the same units that were used to argue for waxing and waning marine oxygen levels across the GOE based on molybdenum (Scott et al., 2008) and uranium (Partin et al., 2013) enrichments, multiple sulfur isotopes (Scott et al., 2014), and selenium enrichments and isotope ratios (Kipp et al., 2017). Instead, the differential response of these redox proxies may be indicative of the mechanism by which the Earth transitioned from the "oxygen overshoot" interval to the apparently oxygen-limited mid-Proterozoic.

The record of sedimentary enrichments of redox-sensitive elements is influenced by both the rate of continental oxidative weathering, which supplies them to the ocean, and the areal extent of anoxic and euxinic marine sediments, which efficiently scavenge redox-sensitive elements from the water column. The sharp peak in redox-sensitive trace element enrichments between 2.32 Ga and 2.06 Ga is thus suggestive of both vigorous oxidative weathering and an expansion of at least mildly oxygenated waters at the expense of anoxic and euxinic settings (Partin et al., 2013; Kipp et al., 2017). The size of the marine sulfate reservoir is sensitive to the same conditions, and correspondingly shows a similar trend, as inferred from both carbonate-associated sulfate (Planavsky et al., 2012) and multiple sulfur isotope data from sedimentary sulfides (Scott et al., 2014). In contrast, sedimentary nitrogen isotope ratios reflect the balance between nitrogen fixation and assimilation of dissolved NO_3^- (the isotopic composition of the latter being predominantly set by rates of denitrification) in the part of the water column where primary productivity is the highest, i.e. the photic zone. Unlike sulfur and trace metals, NO_3^- is largely produced within the ocean via nitrification and thus to a first order is independent from oxidative weathering. The persistence of isotopic evidence for NO_3^- uptake after the proposed "oxygen overshoot" interval therefore suggests that the photic zone on continental shelves remained at least mildly oxygenated in the aftermath of the GOE, while the areal extent of anoxic marine sediments increased.

This aerobic state of the nitrogen cycle has not persisted uninterrupted since the GOE.

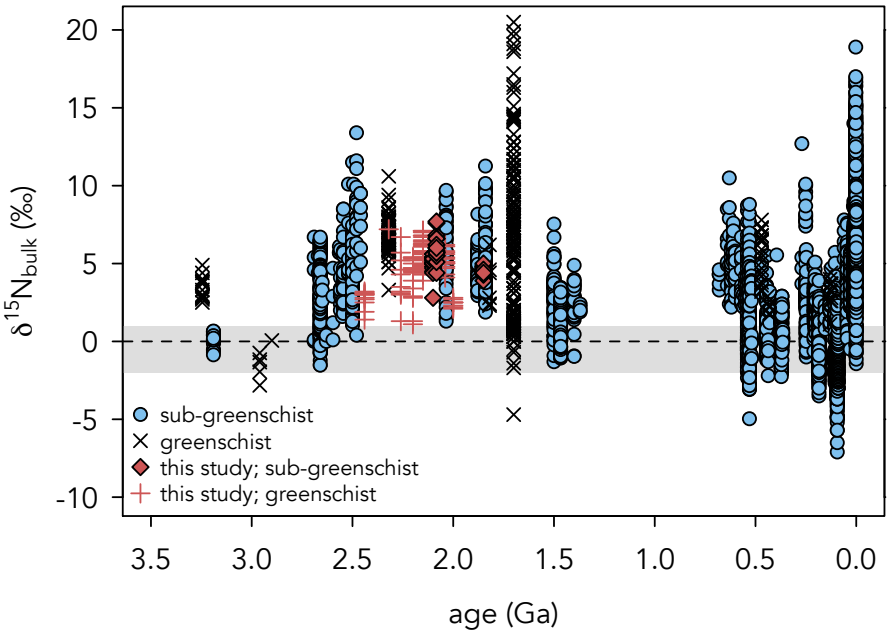

Figure 5.7: **Bulk-rock δ^{15}N values of marine sedimentary rocks through geologic time.** Consistently positive δ^{15}N values in Paleoproterozoic shales imply that oxic conditions were prevalent in surface waters for hundreds of millions of years after the onset of the Great Oxidation Event. Published data and references can be found in Appendix C.

In the Mesoproterozoic, basinal gradients in $\delta^{15}N$ values have been observed, with near-shore facies recording aerobic nitrogen cycling, while offshore facies reflect quantitative assimilation and nitrogen fixation (Stüeken, 2013; Koehler et al., 2017). Our dataset samples only relatively deep-water environments, so we cannot speak to basinal $\delta^{15}N$ gradients within any of the units studied here. However, the persistence of elevated $\delta^{15}N$ values in these settings during and after the GOE demonstrates that aerobic nitrogen cycling prevailed even on the outer shelf. With the available data we are unable to precisely constrain the time at which basinal gradients became representative of the global nitrogen cycle. However, some insight into this matter is offered by the youngest unit in our dataset, the ca. 1.85 Ga Menihek Formation of the Superior Craton in Canada. The positive $\delta^{15}N$ values (+3.9 to +5.0‰) and small isotopic variability ($1\sigma = 0.3$‰) in this unit are both consistent with a significant contribution of aerobic nitrogen cycling and a large bioavailable NO_3^- reservoir in offshore environments in this basin. Thus, this unit might provide a maximum age for the transition to the basinal stratification observed in the Mesoproterozoic nitrogen isotope record.

5.6.3 Quantifying the relationship between ocean oxygenation and nitrogen cycling

While a qualitative interpretation of this dataset yields a compelling story about the oxygenation of the surface ocean in the early Paleoproterozoic, more information can be gleaned by considering these data in a quantitative framework. Our model outputs (Fig. 5.8) show that under pervasive anoxia ($p_{\text{an-sub}}$ approaching 100), sedimentary $\delta^{15}N$ values approach the "N_2 fixation window" (-2‰ to +1‰), which indicates that assimilation of NO_3^- into biomass becomes negligible due to increasing denitrification rates. Under these conditions, the majority of marine biomass is comprised of either N_2-fixing organisms or NH_4^+ assimilating organisms (which were not explicitly tracked in the model). In either case, NO_3^-, which is the preferred nitrogenous compound utilized by eukaryotes in the modern ocean (Karl et al., 2001), is rapidly removed via water column denitrification in strongly anoxic oceans, preventing NO_3^- assimilators from contributing substantially to sedimentary export production (cf. Fennel et al., 2005).

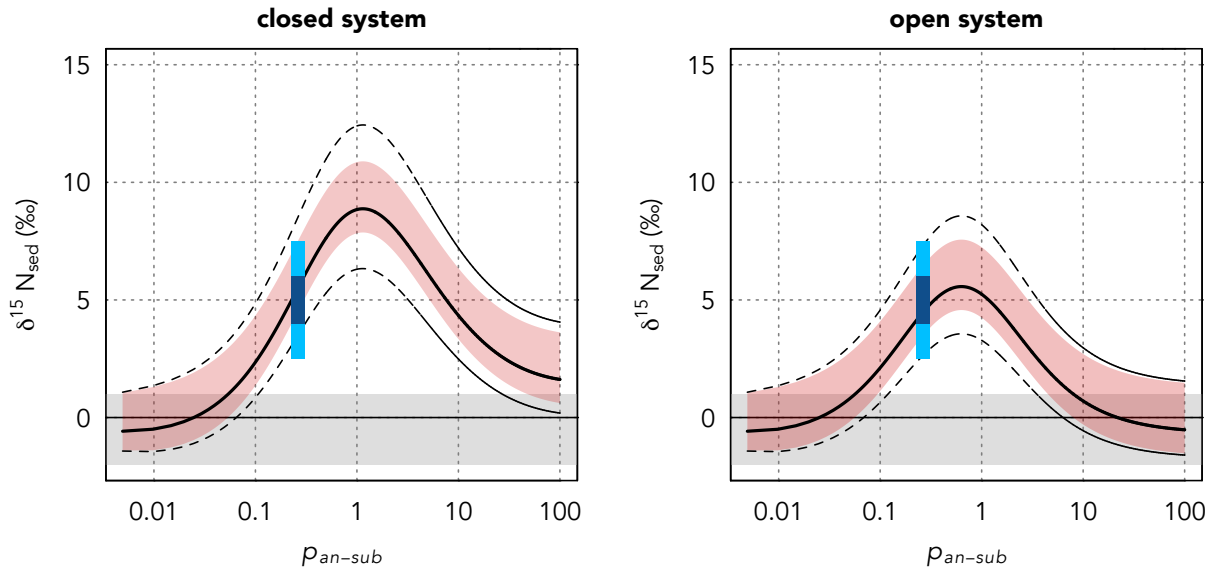

Figure 5.8: **Modeled bulk-rock sedimentary δ^{15}N values under closed (left) and open (right) system dynamics, as a function of anoxia-to-suboxia extent ($p_{an\text{-}sub}$) in the upper ocean.** Anoxia-to-suboxia is defined here as seawater with <4.5 µM of dissolved O_2 (see Appendix C for discussion), where $p_{an\text{-}sub} = 100$ corresponds to a globally anoxic ocean, and the modern ocean has a $p_{an\text{-}sub}$ value of ∼0.3. The mode in the δ^{15}N values of modern marine sediments is shown with a dark-blue bar (Tesdal et al., 2013); the lighter-blue bar corresponds to the 1σ range. Red-shaded region shows uncertainty interval derived from the range of isotopic fractionations associated with biological N_2-fixation. Black dashed lines show cumulative uncertainty interval including upper and lower limits on net isotopic effect of water column denitrification. Grey band denotes isotopic range of nitrogen fixation-dominated ecosystems.

These results suggest that the persistence of a stable, isotopically recordable NO_3^- reservoir requires perhaps as much as ~90% of the surface ocean to be at least mildly oxygenated (Fig. 8). Precisely what concentration of dissolved O_2 defines "mildly oxygenated" is unresolved by this model; for the purpose of this discussion, we are referring to the O_2 level at which nitrification outpaces denitrification, thereby allowing the accumulation of a bioavailable nitrate reservoir. In our model scenarios we dictated that the switch to denitrifying conditions occurs when dissolved O_2 falls below 4.5 µM (meaning that higher levels would constitute "mildly oxygenated" waters) because the majority of water column denitrification occurs in these settings in the modern ocean (Codispoti et al., 2001; Keeling et al., 2009; Paulmier and Ruiz-Pino, 2009). However, it is known that denitrification can occur at dissolved O_2 levels of >20 µM (Kalvelage et al., 2011) and previous modeling has suggested that denitrification outpaces nitrification until dissolved O_2 exceeds 11 µM (Fennel et al., 2005). Regardless of precisely where this threshold lies, the persistence of aerobic nitrogen cycling across much of the Paleoproterozoic suggests that the threshold was exceeded in the surface waters of most basins for a few hundred million years following the GOE.

This is a particularly important consideration when addressing the meaning of elevated $\delta^{15}N$ values in Neoarchean versus Paleoproterozoic marine sedimentary rocks. In studies of Neoarchean units, large deviations from the "N_2 fixation window" towards elevated values have been interpreted as indicating transient oxygenation in the water column prior to the GOE (Garvin et al., 2009; Koehler et al., 2018). The Neoarchean basins in which these trends were observed most likely conformed to closed system dynamics rather than the open-system dynamics that characterize nitrogen isotope mass balance in the modern ocean, because the NO_3^- was sourced locally in the upper water column and was unlikely to become well-mixed in such a strongly anoxic ocean. With this being the case, further studies that increase spatial resolution of the nitrogen isotope record in the potentially heterogeneous Neoarchean ocean could help determine whether the positive $\delta^{15}N$ values in those strata record local or global redox fluctuations.

5.6.4 Implications for primary productivity and the emergence of eukaryotic ecosystems

Before the GOE, it is thought that a scarcity of phosphorus restricted rates of primary productivity (Bekker and Holland, 2012; Kipp and Stüeken, 2017; Reinhard et al., 2016). The lack of sufficient oxidizing power may have inhibited the recycling of organic-bound phosphorus within the ocean until marine dissolved oxygen and sulfate levels rose in the Paleoproterozoic (Planavsky et al., 2012; Scott et al., 2014), implying that the total rate of carbon recycling and net primary productivity could have increased in tandem with the oxygenation of the Earth's surface environments (cf. Bekker and Holland, 2012). It is conceivable that an increase in phosphorus availability during the GOE (cf. Bekker and Holland, 2012) could have caused nitrogen to become the limiting nutrient in the marine environment. However, the data presented here, as well as those presented in previous studies of nitrogen isotopes in Paleoproterozoic marine sedimentary rocks (Godfrey et al., 2013; Kump et al., 2011; Luo et al., 2018; Papineau et al., 2009; Zerkle et al., 2017), show no evidence of persistent nitrogen limitation on geological timescales after the onset of the GOE. Quite to the contrary, the persistence of elevated nitrogen isotope ratios in Paleoproterozoic shales suggests that fixed nitrogen was sufficiently available to fuel primary production (discussed in Section 5.2.1). Still, while nitrogen was likely not limiting, it is not entirely clear whether it was phosphorus, trace metals, or some other factor that controlled the rate of primary productivity during the Lomagundi carbon isotope excursion and associated "oxygen overshoot" interval, which is thought to have been a time of extreme organic carbon burial (Bekker and Holland, 2012; Karhu and Holland, 1996).

A further question is whether these more productive, nitrate-fueled ecosystems contained eukaryotic organisms. Considerable controversy surrounds the oldest evidence of eukaryotes; it is generally accepted that the eukaryotic lineage had emerged by ca. 1.7 Ga (see Javaux and Lepot, 2018), though arguments for an earlier arrival of eukaryotes are not lacking (e.g. Bengtson et al., 2017; El Albani et al., 2010). Notably, a recent genomic effort to resolve the origin of sterol biosynthesis has suggested that this metabolic capacity – a hallmark

of eukaryotic organisms – evolved nearly contemporaneously with the onset of the GOE (Gold et al., 2017). However, the record of organic biomarkers in Proterozoic sedimentary successions implies that eukaryotes were not significant contributors to bulk organic matter until the late Neoproterozoic (Brocks et al., 2017). While efforts to confidently constrain when the eukaryotes first evolved and reached abundance in the sedimentary record will carry on, geochemical constraints will be critical to answering fundamental questions about the interplay between environmental changes and biological responses.

The data presented here have two implications for early eukaryotic evolution. First, the prevalence of elevated $\delta^{15}N$ values in the early Paleoproterozoic (Figs. 5.7, 5.9) is direct evidence of abundant nitrate-assimilating organisms. Whether a substantial portion of this biomass was comprised of eukaryotes is unclear from the nitrogen isotope data alone, but this trend in nitrogen isotopes confirms that NO_3^- was sufficiently bioavailable across continental shelves to alleviate any fixed-nitrogen limitation on eukaryotic proliferation at this time (Fig. 9). Second, the magnitude of nitrogen isotope enrichment and consistency of values, when viewed in the context of our model outputs, imply that much of the photic zone overlying continental shelves was at least mildly oxygenated for hundreds of millions of years in the Paleoproterozoic. Thus, if they had already evolved, eukaryotes with oxygen-requiring metabolic processes should have been able to persist in the upper part of the water column without severe oxygen-limitation. Still, it remains plausible that periodic incursions of anoxic waters and redox fluctuations at low dissolved O_2 levels could have restricted the proliferation and diversification of eukaryotes at this time (cf. Johnston et al., 2012). In any case, the data presented here allow for an earlier emergence of eukaryotes than is deemed likely under recent interpretations of the fossil and biomarker records (Fig. 5.9).

5.7 Conclusion

We have presented new nitrogen isotope data spanning the Paleoproterozoic Era that document persistent aerobic nitrogen cycling on continental shelves from ca. 2.44 to 1.85 Ga. The observation that nitrogen isotope ratios remain elevated when trace metal and sulfur-

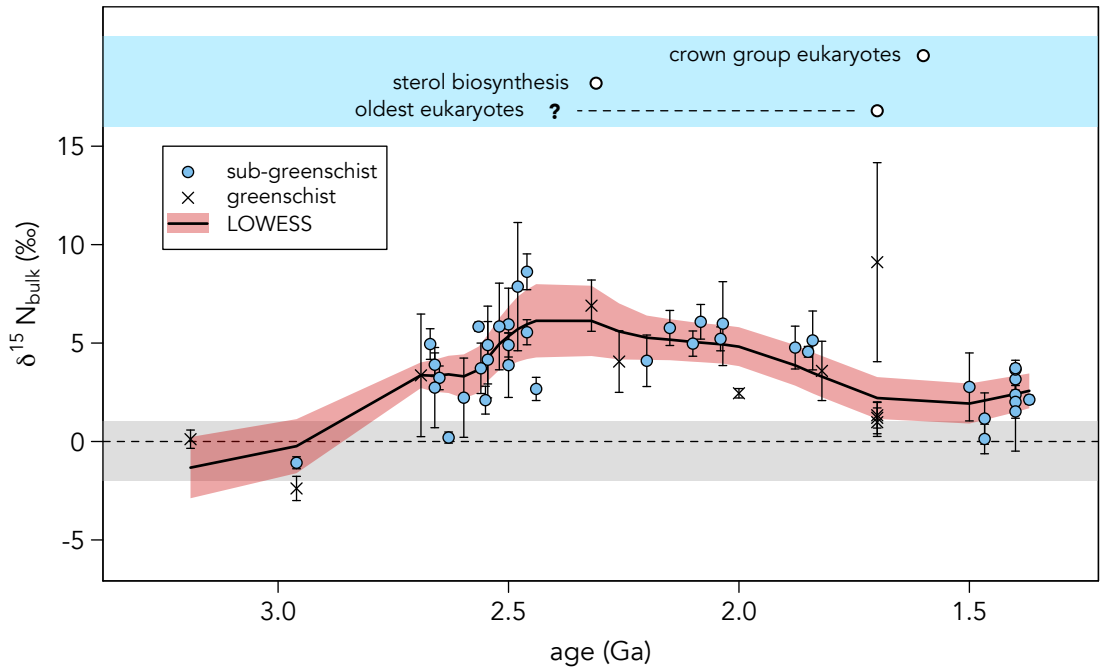

Figure 5.9: **Archean and Paleoproterozoic nitrogen isotope record and constraints on early eukaryotic evolution.** Points are mean δ^{15}N values for individual formations with 1σ error bars. Black line is LOWESS curve, with 1σ confidence interval shown in red shaded region. LOWESS calculations utilized a d value of 1 (local fits via linear regression) and an f value of 0.3 in order to investigate long-term ($\sim 10^8$ yr) trends. References for evolutionary events are discussed in Section 5.5.4.

based proxies point to a decrease in the extent of oxic settings following the ca. 2.32-2.06 Ga "oxygen overshoot" may derive from the fact that the latter proxies are sensitive to redox conditions at the sediment-water interface, while nitrogen isotope values record redox conditions in the photic zone. When viewed in light of our model outputs, these data implicate oxygenated surface seawater and substantial bioavailable NO_3^- lasting from the onset of the GOE until at least ca. 1.85 Ga. This may suggest that the upper ocean was already hospitable to eukaryotic organisms hundreds of millions of years before the fossil record firmly indicates their presence.

5.8 References

Ader, M., Thomazo, C., Sansjofre, P., Busigny, V., Papineau, D., Laffont, R., Cartigny, P., Halverson, G.P., 2016. Interpretation of the nitrogen isotopic composition of Precambrian sedimentary rocks: Assumptions and perspectives. *Chem. Geol.* 429, 93–110.

Altabet, M.A., Francois, R., 1994. Sedimentary nitrogen isotopic ratio as a recorder for surface ocean nitrate utilization. *Glob. Biogeochem. Cycles* 8, 103–116.

Bebout, G.E., Fogel, M.L., 1992. Nitrogen-isotope compositions of metasedimentary rocks in the Catalina Schist, California: implications for metamorphic devolatilization history. *Geochim. Cosmochim. Acta* 56, 2839–2849.

Bekker, A., Holland, H.D., 2012. Oxygen overshoot and recovery during the early Paleoproterozoic. *Earth Planet. Sci. Lett.* 317, 295–304.

Bekker, A., Holland, H.D., Wang, P.-L., Rumble, D., Stein, H.J., Hannah, J.L., Coetzee, L.L., Beukes, N.J., 2004. Dating the rise of atmospheric oxygen. *Nature* 427, 117–120.

Bekker, A., Holmden, C., Beukes, N.J., Kenig, F., Eglinton, B., Patterson, W.P., 2008. Fractionation between inorganic and organic carbon during the Lomagundi (2.22–2.1 Ga) carbon isotope excursion. *Earth Planet. Sci. Lett.* 271, 278–291.

Bengtson, S., Rasmussen, B., Ivarsson, M., Muhling, J., Broman, C., Marone, F., Stampanoni, M., Bekker, A., 2017. Fungus-like mycelial fossils in 2.4-billion-year-old vesicular basalt. *Nat. Ecol. Evol.* 1, 0141.

Beukes, N.J., Dorland, H., Gutzmer, J., Nedachi, M., Ohmoto, H., 2002. Tropical laterites, life on land, and the history of atmospheric oxygen in the Paleoproterozoic. *Geology* 30, 491–494.

Brandes, J.A., Devol, A.H., 2002. A global marine-fixed nitrogen isotopic budget: Implications for Holocene nitrogen cycling. *Glob. Biogeochem. Cycles* 16.

Brocks, J.J., Jarrett, A.J., Sirantoine, E., Hallmann, C., Hoshino, Y., Liyanage, T., 2017. The rise of algae in Cryogenian oceans and the emergence of animals. *Nature* 548, 578.

Casciotti, K.L., Sigman, D.M., Ward, B.B., 2003. Linking diversity and stable isotope fractionation in ammonia-oxidizing bacteria. *Geomicrobiol. J.* 20, 335–353.

Codispoti, L.A., Brandes, J.A., Christensen, J.P., Devol, A.H., Naqvi, S.W.A., Paerl, H.W., Yoshinari, T., 2001. The oceanic fixed nitrogen and nitrous oxide budgets: Moving targets as we enter the anthropocene? Sci. Mar. 65, 85–105.

Devol, A.H., 2015. Denitrification, anammox, and N_2 production in marine sediments. *Annu. Rev. Mar. Sci.* 7, 403–423.

El Albani, A., Bengtson, S., Canfield, D.E., Bekker, A., Macchiarelli, R., Mazurier, A., Hammarlund, E.U., Boulvais, P., Dupuy, J.-J., Fontaine, C., Fürsich, F.T., Gauthier-Lafaye, F., Janvier, P., Javaux, E., Ossa, F.O., Pierson-Wickmann, A.-C., Riboulleau, A., Sardini, P., Vachard, D., Whitehouse, M., Meunier, A., 2010. Large colonial organisms with coordinated growth in oxygenated environments 2.1Gyr ago. *Nature* 466, 100–104.

Farquhar, J., Bao, H.M., Thiemens, M., 2000. Atmospheric influence of Earth's earliest sulfur cycle. *Science* 289, 756–758.

Fennel, K., Follows, M., Falkowski, P.G., 2005. The co-evolution of the nitrogen, carbon and oxygen cycles in the Proterozoic ocean. *Am. J. Sci.* 305, 526–545.

Fulton, J.M., Arthur, M.A., Freeman, K.H., 2012. Black Sea nitrogen cycling and the preservation of phytoplankton $\delta^{15}N$ signals during the Holocene. *Glob. Biogeochem. Cycles* 26.

Garvin, J., Buick, R., Anbar, A.D., Arnold, G.L., Kaufman, A.J., 2009. Isotopic evidence for an aerobic nitrogen cycle in the latest Archean. *Science* 323, 1045–1048.

Godfrey, L.V., Poulton, S.W., Bebout, G.E., Fralick, P.W., 2013. Stability of the nitrogen cycle during development of sulfidic water in the redox-stratified late Paleoproterozoic Ocean. *Geology* 41, 655–658.

Gold, D.A., Caron, A., Fournier, G.P., Summons, R.E., 2017. Paleoproterozoic sterol biosynthesis and the rise of oxygen. *Nature* 543, 420–423.

Granger, J., Prokopenko, M.G., Sigman, D.M., Mordy, C.W., Morse, Z.M., Morales, L.V., Sambrotto, R.N., Plessen, B., 2011. Coupled nitrification-denitrification in sediment of the eastern Bering Sea shelf leads to ^{15}N enrichment of fixed N in shelf waters. *J. Geophys. Res. Oceans* 116.

Gumsley, A.P., Chamberlain, K.R., Bleeker, W., Söderlund, U., Kock, M.O. de, Larsson, E.R., Bekker, A., 2017. Timing and tempo of the Great Oxidation Event. *Proc. Natl. Acad. Sci.* 114, 1811–1816.

Haendel, D., Mühle, K., Nitzsche, H.-M., Stiehl, G., Wand, U., 1986. Isotopic variations of the fixed nitrogen in metamorphic rocks. *Geochim. Cosmochim. Acta* 50, 749–758.

Hardisty, D.S., Lu, Z., Bekker, A., Diamond, C.W., Gill, B.C., Jiang, G., Kah, L.C., Knoll, A.H., Loyd, S.J., Osburn, M.R., others, 2017. Perspectives on Proterozoic surface ocean redox from iodine contents in ancient and recent carbonate. *Earth Planet. Sci. Lett.* 463, 159–170.

Hayes, J.M., 2004. An introduction to isotopic calculations. Woods Hole Oceanogr. Inst. Woods Hole MA 2543.

Hoch, M.P., Fogel, M.L., Kirchman, D.L., 1992. Isotope fractionation associated with ammonium uptake by a marine bacterium. *Limnol. Oceanogr.* 37, 1447–1459.

Javaux, E., Lepot, K., 2018. The Paleoproterozoic fossil record: Implications for the evolution of the biosphere during Earth's middle-age. *Earth-Sci. Rev.* 176, 68–86.

Johnston, D.T., Poulton, S.W., Goldberg, T., Sergeev, V.N., Podkovyrov, V., Vorob'eva, N.G., Bekker, A., Knoll, A.H., 2012. Late Ediacaran redox stability and metazoan evolution. *Earth Planet. Sci. Lett.* 335, 25–35.

Kalvelage, T., Jensen, M.M., Contreras, S., Revsbech, N.P., Lam, P., Günter, M., LaRoche,

J., Lavik, G., Kuypers, M.M.M., 2011. Oxygen Sensitivity of Anammox and Coupled N-Cycle Processes in Oxygen Minimum Zones. *PLOS ONE* 6, e29299.

Karhu, J.A., Holland, H.D., 1996. Carbon isotopes and the rise of atmospheric oxygen. Geology 24, 867–870. Karl, D.M., Bidigare, R.R., Letelier, R.M., 2001. Long-term changes in plankton community structure and productivity in the North Pacific Subtropical Gyre: The domain shift hypothesis. *Deep Sea Res. Part II Top. Stud. Oceanogr.* 48, 1449–1470.

Keeling, R.F., Körtzinger, A., Gruber, N., 2009. Ocean deoxygenation in a warming world.

Kipp, M.A., Stüeken, E.E., 2017. Biomass recycling and Earth's early phosphorus cycle. *Sci. Adv.* 3, eaao4795.

Kipp, M.A., Stüeken, E.E., Bekker, A., Buick, R., 2017. Selenium isotopes record extensive marine suboxia during the Great Oxidation Event. *Proc. Natl. Acad. Sci.* 114, 875–880.

Koehler, M.C., Buick, R., Kipp, M.A., Stüeken, E.E., Zaloumis, J., 2018. Transient surface ocean oxygenation recorded in the ∼2.66-Ga Jeerinah Formation, Australia. *Proc. Natl. Acad. Sci.*

Koehler, M.C., Stüeken, E.E., Kipp, M.A., Buick, R., Knoll, A.H., 2017. Spatial and temporal trends in Precambrian nitrogen cycling: A Mesoproterozoic offshore nitrate minimum. *Geochim. Cosmochim. Acta* 198, 315–337.

Kritee, K., Sigman, D.M., Granger, J., Ward, B.B., Jayakumar, A., Deutsch, C., 2012. Reduced isotope fractionation by denitrification under conditions relevant to the ocean. *Geochim. Cosmochim. Acta* 92, 243–259.

Kump, L.R., Junium, C., Arthur, M.A., Brasier, A., Fallick, A., Melezhik, V., Lepland, A., CČrne, A.E., Luo, G., 2011. Isotopic Evidence for Massive Oxidation of Organic Matter Following the Great Oxidation Event. *Science* 334, 1694–1696.

Lehmann, M.F., Bernasconi, S.M., Barbieri, A., McKenzie, J.A., 2002. Preservation of organic matter and alteration of its carbon and nitrogen isotope composition during simulated and in situ early sedimentary diagenesis. *Geochim. Cosmochim. Acta* 66, 3573–3584.

Luo, G., Junium, C.K., Izon, G., Ono, S., Beukes, N.J., Algeo, T.J., Cui, Y., Xie, S., Summons, R.E., 2018. Nitrogen fixation sustained productivity in the wake of the Palaeoproterozoic Great Oxygenation Event. *Nat. Commun.* 9, 978.

Luo, G., Junium, C.K., Kump, L.R., Huang, J., Li, C., Feng, Q., Shi, X., Bai, X., Xie, S., 2014. Shallow stratification prevailed for 1700 to 1300 Ma ocean: Evidence from organic carbon isotopes in the North China Craton. *Earth Planet. Sci. Lett.* 400, 219–232.

Luo, G., Ono, S., Beukes, N.J., Wang, D.T., Xie, S., Summons, R.E., 2016. Rapid oxygenation of Earth's atmosphere 2.33 billion years ago. *Sci. Adv.* 2, e1600134.

Lyons, T.W., Reinhard, C.T., Planavsky, N.J., 2014. The rise of oxygen in Earth's early ocean and atmosphere. *Nature* 506, 307–315.

Möbius, J., 2013. Isotope fractionation during nitrogen remineralization (ammonification): Implications for nitrogen isotope biogeochemistry. *Geochim. Cosmochim. Acta* 105, 422–432.

Papineau, D., Purohit, R., Goldberg, T., Pi, D., Shields, G.A., Bhu, H., Steele, A., Fogel, M.L., 2009. High primary productivity and nitrogen cycling after the Paleoproterozoic phosphogenic event in the Aravalli Supergroup, India. *Precambrian Res.* 171, 37–56.

Partin, C.A., Bekker, A., Planavsky, N.J., Scott, C.T., Gill, B.C., Li, C., Podkovyrov, V., Maslov, A., Konhauser, K.O., Lalonde, S.V., Love, G.D., Poulton, S.W., Lyons, T.W., 2013. Large-scale fluctuations in Precambrian atmospheric and oceanic oxygen levels from the record of U in shales. *Earth Planet. Sci. Lett.* 369, 284–293.

Paulmier, A., Ruiz-Pino, D., 2009. Oxygen minimum zones (OMZs) in the modern ocean. *Prog. Oceanogr.* 80, 113–128.

Planavsky, N.J., Bekker, A., Hofmann, A., Owens, J.D., Lyons, T.W., 2012. Sulfur record of rising and falling marine oxygen and sulfate levels during the Lomagundi event. *Proc. Natl. Acad. Sci.* 109, 18300–18305.

Redfield, A.C., 1934. On the proportions of organic derivatives in sea water and their relation to the composition of plankton. *James Johnstone Meml. Vol.* 176–192.

Reinhard, C.T., Planavsky, N.J., Gill, B.C., Ozaki, K., Robbins, L.J., Lyons, T.W., Fis-

cher, W.W., Wang, C., Cole, D.B., Konhauser, K.O., 2016. Evolution of the global phosphorus cycle. *Nature* 541, 386–389.

Rivera, K.T., Puckette, J., Quan, T.M., 2015. Evaluation of redox versus thermal maturity controls on $\delta^{15}N$ in organic rich shales: a case study of the Woodford Shale, Anadarko Basin, Oklahoma, USA. *Org. Geochem.* 83, 127–139.

Schidlowski, M., 2001. Carbon isotopes as biogeochemical recorders of life over 3.8 Ga of Earth history: evolution of a concept. *Precambrian Res.* 106, 117–134.

Scott, C., Lyons, T.W., Bekker, A., Shen, Y., Poulton, S.W., Chu, X., Anbar, A.D., 2008. Tracing the stepwise oxygenation of the Proterozoic ocean. *Nature* 452, 456-U5.

Scott, C., Wing, B.A., Bekker, A., Planavsky, N.J., Medvedev, P., Bates, S.M., Yun, M., Lyons, T.W., 2014. Pyrite multiple-sulfur isotope evidence for rapid expansion and contraction of the early Paleoproterozoic seawater sulfate reservoir. *Earth Planet. Sci. Lett.* 389, 95–104.

Stüeken, E.E., 2013. A test of the nitrogen-limitation hypothesis for retarded eukaryote radiation: Nitrogen isotopes across a Mesoproterozoic basinal profile. *Geochim. Cosmochim. Acta* 120, 121–139.

Stüeken, E.E., Buick, R., Guy, B.M., Koehler, M.C., 2015. Isotopic evidence for biological nitrogen fixation by molybdenum-nitrogenase from 3.2 Gyr. *Nature* 520, 666–669.

Stüeken, E.E., Kipp, M.A., Koehler, M.C., Buick, R., 2016. The evolution of Earth's biogeochemical nitrogen cycle. *Earth-Sci. Rev.* 160, 220–239.

Stüeken, E.E., Zaloumis, J., Meixnerová, J., Buick, R., 2017. Differential metamorphic effects on nitrogen isotopes in kerogen extracts and bulk rocks. *Geochim. Cosmochim. Acta* 217, 80–94.

Tesdal, J.-E., Galbraith, E.D., Kienast, M., 2013. Nitrogen isotopes in bulk marine sediment: linking seafloor observations with subseafloor records. *Biogeosciences* 10, 101–118.

Thomazo, C., Ader, M., Philippot, P., 2011. Extreme ^{15}N-enrichments in 2.72-Gyr-old sediments: evidence for a turning point in the nitrogen cycle. *Geobiology* 9, 107–120.

Tyrrell, T., 1999. The relative influences of nitrogen and phosphorus on oceanic primary

production. *Nature* 400, 525–531.

Zerkle, A.L., Junium, C.K., Canfield, D.E., House, C.H., 2008. Production of ^{15}N-depleted biomass during cyanobacterial N_2-fixation at high Fe concentrations. *J. Geophys. Res. Biogeosciences* 113, G03014.

Zerkle, A.L., Poulton, S.W., Newton, R.J., Mettam, C., Claire, M.W., Bekker, A., Junium, C.K., 2017. Onset of the aerobic nitrogen cycle during the Great Oxidation Event. *Nature* 543, 465–467.

Zhang, X., Sigman, D.M., Morel, F.M., Kraepiel, A.M., 2014. Nitrogen isotope fractionation by alternative nitrogenases and past ocean anoxia. *Proc. Natl. Acad. Sci.* 111, 4782–4787.

Chapter 6

PROCESSES CONTROLLING THE C_{ORG}/N_{TOT} RATIO IN ANCIENT MARINE SEDIMENTARY ROCKS

This manuscript is being revised for re-submission to *Geochimica et Cosmochimica Acta*. Co-authors are Matthew Koehler, Andrey Bekker and Roger Buick.

6.1 Abstract

The carbon to nitrogen (C/N) ratio of marine phytoplankton has long been known to exert the dominant control on the major nutrient stoichiometry of the surface ocean. However, it is also known that the C/N ratio of planktonic biomass not always faithfully recorded in marine sediments. A number of processes can alter the bulk C/N ratio (C_{org}/N_{tot}) of ancient marine sediments and sedimentary rocks, including influx of terrestrial organic material (since the mid-Paleozoic), anaerobic remineralization of marine biomass, and thermal maturation of organic matter during diagenesis and metamorphism. Despite these complications, there remains some potential to use C_{org}/N_{tot} ratios in ancient marine sedimentary rocks to reconstruct paleo-environmental conditions. Here we present a synthesis and analysis of C_{org}/N_{tot} data from a large database of recent marine sediments and ancient marine sedimentary rocks, and consider the utility of C_{org}/N_{tot} as a paleo-environmental proxy. We find that (i) C_{org}/N_{tot} variations across a stratigraphic profile within a single unit can often be explained by a mixing relationship between kerogen- and silicate-bound nitrogen, (ii) thermal maturation can cause extreme enrichment in C_{org}/N_{tot} and $(C/N)_{kerogen}$ values starting in prehnite-pumpellyite facies metamorphism, and (iii) after screening for thermal maturity, early diagenetic redox effects on sedimentary $(C/N)_{kerogen}$ can be resolved, with high $(C/N)_{kerogen}$ ratios in immature marine sedimentary rocks apparently attributable to an

increased proportion of anaerobic remineralization. This demonstrates the potential utility of C/N ratios as a paleo-redox proxy, perhaps even with quantitative sensitivity to the extent of water-column anoxia, but warrants substantial caution and rigorous inter-comparison with other proxies before applying this tool to a wide range of settings in deep time.

6.2 Introduction

Phytoplankton have long been known to exert a strong control on the macronutrient stoichiometry (*e.g.*, C/N) of the surface ocean (Redfield, 1934; Redfield, 1958). The characteristic phytoplankton C/N ratio of 5-8 (here and throughout the paper expressed as a molar ratio) is distinct from terrestrial biomass (C/N > 15) due to the protein-rich nature of marine phytoplankton (Parsons et al., 1961; Fagerbakke et al., 1996; Geider and La Roche, 2002), which contain little structural material such as cellulose. With this as a constraint, many studies have used C_{org}/N_{tot} ratios in marine sediments to identify the input of terrestrial organic matter to marine settings (*e.g.*, Premuzic et al., 1982; Meyers, 1994). However, there are numerous occurrences of high C_{org}/N_{tot} ratios (>8) in marine sediments that show geochemical signatures inconsistent with terrestrial input (*e.g.*, high hydrogen content of organic matter; Meyers et al., 2006).

In these instances, it is clear that the primary C/N ratio of biomass has not been faithfully transmitted to marine sediments, but rather has been altered at some point during the deposition and early diagenesis of organic matter. One factor that can affect the C/N ratio of sinking and deposited organic matter is remineralization. While aerobic remineralization – which is the predominant pathway operating in the open ocean today – tends to uniformly degrade organic material without substantially altering C/N ratios (Anderson and Sarmiento, 1994), anaerobic remineralization has been shown to cause preferential degradation of nitrogen-rich components (*i.e.*, proteins and nucleic acids) relative to nitrogen-poor molecules (*i.e.*, lipids) (Van Mooy et al., 2002). As a result, the C/N ratio of residual biomass after anaerobic degradation can be substantially elevated relative to the original value (Van Mooy et al., 2002), causing marine sediments to have high C_{org}/N_{tot} ratios.

An additional complication is that the retention of nitrogen as ammonium (NH_4^+) in clay minerals (substituted for K^+) during progressive organic matter degradation during diagenesis can decrease the C_{org}/N_{tot} ratio of bulk marine sediments, potentially yielding ratios that are lower than the original C/N ratio of the sinking biomass. This is particularly prevalent in argillaceous sediments with low organic matter content (Müller, 1977; Meyers et al., 1996; Prahl et al., 2003), where remineralization of organic carbon is nearly complete but some nitrogen is retained in the mineral phase. Thus, for the reasons outlined above, C_{org}/N_{tot} ratios in marine sediments can vary widely relative to primary algal biomass, deviating toward both higher and lower values.

Despite these complications, sedimentary C_{org}/N_{tot} values have been shown to record coherent environmental signals in some marine settings. For instance, Twichell et al. (2002) showed that short-lived excursions to high C_{org}/N_{tot} ratios (up to ∼15) correlate with periods of greater export production under the Benguela Current upwelling system. Their interpretation was that the increased productivity caused oxygen consumption in the water column during remineralization, initiating anaerobic respiration (particularly denitrification), thereby causing an increase in the C/N ratios of residual sinking biomass (Twichell et al., 2002). A similar argument was put forward by Walsh et al. (1981) to explain the spatial C_{org}/N_{tot} variability in sediments on the Peru Margin, where values up to ∼10 were found under the most oxygen-depleted waters, while values close to ∼6 prevailed elsewhere. These findings suggest that C_{org}/N_{tot} ratios of marine sediments can potentially be used to assess the extent of aerobic versus anaerobic diagenesis, with higher values corresponding to a greater contribution of anaerobic pathways during organic remineralization.

This could make C_{org}/N_{tot} a particularly useful redox proxy to employ in studies of deep time, when marine oxygen levels are thought to have been substantially lower (Fig. 6.1a; Lyons et al., 2014). It has been proposed that the majority of organic matter remineralization occurred through anaerobic pathways in the Precambrian (*e.g.*, Bekker and Holland, 2012; Knoll et al., 2016; Kipp and Stüeken, 2017), but evaluating this hypothesis is difficult, with some organic geochemical proxies leading to inferences of aerobic remineralization in the

Proterozoic (Zhang et al., 2017; Wang et al., 2018), while other geochemical and geological proxies point to fluctuating diagenetic redox conditions in shallow marine environments (Joosu et al., 2015; Papineau et al., 2017). Importantly, most available proxies are unable to quantitatively assess the contribution of anaerobic versus aerobic remineralization; rather, each proxy can typically only qualitatively or semi-quantitatively identify the presence of a given pathway of organic remineralization, but not rule out the contribution of other pathways. For instance, sedimentary $\delta^{15}N$ values can indicate the occurrence of organic remineralization via nitrate reduction (*i.e.*, "canonical" denitrification) somewhere in the water column when values are elevated ($>+1‰$), but this is a qualitative to semi-quantitative proxy for denitrification (Ader et al., 2016; Stüeken et al., 2016). As such, the $\delta^{15}N$ proxy broadly tracks the secular oxygenation of Earth's surface environment (Fig. 6.1b), but lacks the resolution to distinguish between basins with subtle differences in redox profiles. The C_{org}/N_{tot} proxy may therefore be a useful tool for integrating the net effect of aerobic versus anaerobic metabolism in re-working organic matter as it sinks through the water column and gets buried in marine sediments, with implications for evaluating the redox structure of ancient marine water columns and corresponding implications for nutrient cycling.

However, an additional complication that must be considered when applying this proxy to deep-time settings is that the thermal maturation of organic matter during burial and metamorphism (and potentially hydrothermally-mediated metasomatism) can mimic the diagenetic increase in C/N ratios. It has been shown that as thermal maturation progresses, both nitrogen (as N_2 or NH_3) and carbon (as CO_2 or CH_4) are lost from sedimentary rocks, with nitrogen ultimately escaping faster than carbon, yielding elevated C/N ratios at high thermal maturity (Bebout and Fogel, 1992; Stüeken et al., 2017). This potential confounding effect therefore warrants further attention before extending the C_{org}/N_{tot} proxy to ancient marine sedimentary rocks.

Here we explore the potential utility of sedimentary C_{org}/N_{tot} ratios as a proxy for aerobic versus anaerobic remineralization in deep time. To do so, we assembled a large database of carbon and nitrogen concentrations in modern marine sediments and from marine sedimen-

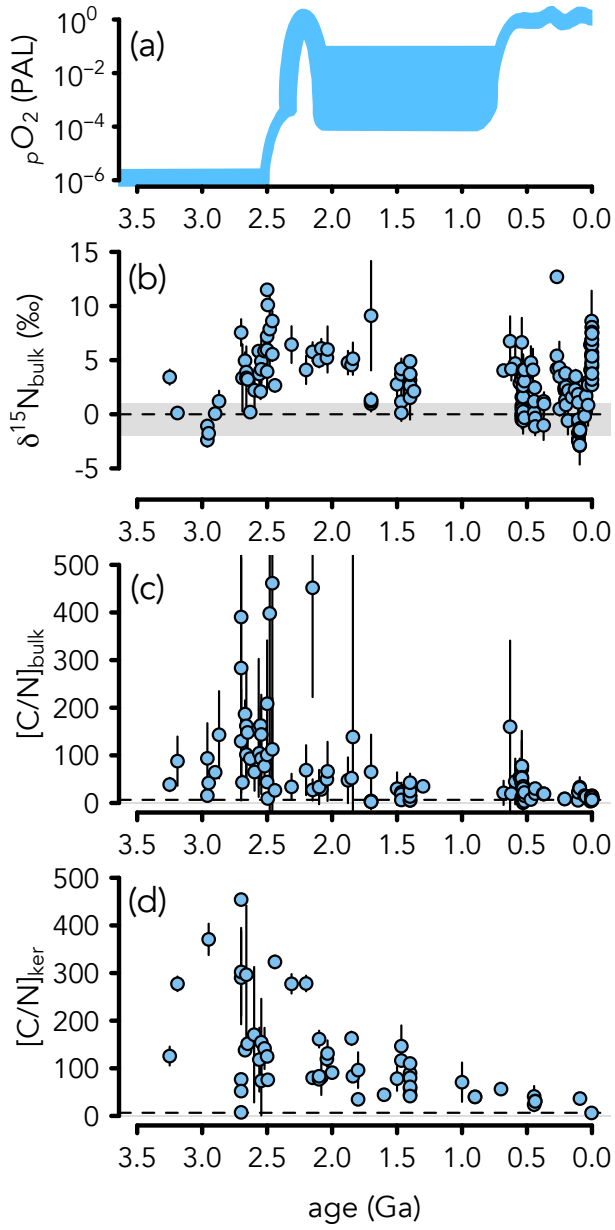

Figure 6.1: **Secular trends in (a) atmospheric oxygen, (b) δ^{15}N, (c) C_{org}/N_{tot}, and (d) $(C/N)_{kerogen}$ in marine sedimentary rocks.** Oxygen curve adapted from (Lyons et al., 2014); PAL = present atmospheric level. Data points represent per-unit averages (error bars = 1σ) for all units in the database. The δ^{15}N record roughly tracks the oxygenation of Earth's atmosphere and ocean. However, it is unclear to what degree C_{org}/N_{tot} and $(C/N)_{kerogen}$ record environmental or metamorphic signatures.

tary rocks spanning all of Earth's history. We additionally analyzed H/C ratios of extracted kerogen from a variety of units in order to assess the effect of thermal maturity on C/N ratios, and supplemented these measurements with published data from the literature. We then considered the relationship between C/N ratios and known modern and ancient water-column redox conditions to determine whether sedimentary C/N ratios retain information about water-column redox conditions in ancient marine sedimentary rocks.

6.3 Materials and Methods

6.3.1 Database compilation

A recently published database of organic carbon and nitrogen isotope data (Kipp et al., 2018) was updated to include recent publications as well as data from several studies that present organic carbon and nitrogen concentrations, but not isotopic ratios. We also assembled organic carbon and total nitrogen concentration data from recent marine sediments in the EarthChem database (https://www.earthchem.org). Both of these data files are available as part of the Supplementary Materials.

6.3.2 Sample selection

For H/C analysis, we targeted samples that had been analyzed in previous studies for organic carbon and nitrogen isotope ratios in both bulk-rock powders and kerogen extracts. We also sought out units that span a range of thermal maturities, depositional ages, and paleo-redox conditions.

The oldest of these units is the ~2.66 Ga Jeerinah Formation of Western Australia. The samples utilized in this study were obtained as part of the Agouron Institute Drilling Project (AIDP) in 2012. These samples have recently been shown to record evidence for transient surface ocean oxygenation prior to the Great Oxidation Event (GOE), and come from two drill cores (AIDP-2 and AIDP-3) that span a depth and redox gradient (Koehler et al., 2018). Detailed lithological descriptions of these samples can be found in French et

al. (2015) and Koehler et al. (2018).

The next oldest units span the Paleoproterozoic Era (2.5 – 1.6 Ga), and were described in Kipp et al. (2018). These comprise offshore siliciclastic marine sedimentary rocks with a range of thermal maturities from unmetamorphosed to greenschist facies metamorphism. Elevated $\delta^{15}N$ in these units were taken as evidence for pervasive aerobic nitrogen cycling in oxic-to-suboxic surface waters of the Paleoproterozoic ocean (Kipp et al., 2018).

The youngest samples analyzed for H/C ratios come from the mid-Permian Phosphoria Formation (∼260 Ma) of the western United States. These comprise both outcrop (Astoria Hot Springs; 43.301518°N, 110.780609°W) and drill core (Lakeridge Well No. 43-19-G; 42.48818°N, 110.46597°W; Sheldon, 1963; Perkins et al., 2003) samples. Analyses were focused on the organic-rich intervals of the Meade Peak Member.

6.3.3 Sample preparation

Prior to geochemical analysis, bulk rock samples from outcrops and drill cores were cut with a rock saw to remove weathered surfaces. Clean rock samples were crushed to cm-sized chips and successively rinsed with methanol, 2N HCl, and DI-H_2O to remove modern organic contaminants. Clean and dry rock chips were then pulverized in an aluminum oxide puck mill that was cleaned with methanol, DI-H_2O and pre-combusted silica sand between samples.

Inorganic carbon was removed from samples prior to analysis by treating powders with two overnight iterations of 6N HCl at 60°C, followed by rinsing with DI-H_2O and drying in an oven at 60°C. Acidified powders were weighed into tin cups for bulk-rock analysis.

Kerogen was extracted from bulk-rock powders as described in Koehler et al. (2018) and Kipp et al. (2018). Bulk-rock powders were weighed into Teflon bottles and treated with a 1:1 mixture of DI-H_2O and concentrated (29N) hydrofluoric acid (HF). Following digestion, solutions were centrifuged and the supernatant was decanted. A BF_3 solution (62.5g H_3BO_3, 100 mL DI-H_2O, 100 mL concentrated HF) was then added to dissolve residual fluoride minerals. After another round of centrifugation and decanting, samples were washed with three iterations of DI-H_2O. The rinsed, extracted kerogen was then desiccated in a freeze-

drier prior to analysis.

6.3.4 Analytical protocol

The carbon and nitrogen contents of bulk rocks and kerogen extracts were analyzed on a Costech ECS 4010 Elemental Analyzer coupled to a Thermo Finnigan MAT253 continuous flow isotope-ratio mass spectrometer housed in IsoLab at the Department of Earth & Space Sciences, University of Washington. Combustion was carried out with 20 mL O_2 at 1000°C. A magnesium perchlorate trap was used to remove water from the gas stream. An aliquot of the Neoarchean Mt. McRae Shale was analyzed as an in-house standard to test long-term precision. Analytical blanks were measured and subtracted from nitrogen data; blanks were negligible for carbon measurements.

The fraction of bulk-rock nitrogen (N_{tot}) residing in kerogen ($f_{kerogen}$) was calculated according to mass balance, following the approach of Stüeken et al. (2017), using the equation

$$f_{kerogen} = \frac{\frac{C_{org}}{N_{tot}}}{(C/N)_{kerogen}} \tag{6.1}$$

where $(C/N)_{kerogen}$ and C_{org}/N_{tot} are molar ratios, as reported in Table 6.1. The fraction of bulk-rock nitrogen residing in the silicate phase can then be calculated by mass balance using the equation

$$f_{silicate} = 1 - f_{kerogen} \tag{6.2}$$

Kerogen extracts were analyzed for H/C ratios in the Marine Science Institute Analytical Lab at University of California, Santa Barbara. Analyses were conducted on an organic elemental analyzer (CEC 440HA) with high-precision thermal conductivity detectors. The average standard deviation of H/C ratios in replicate analyses was 0.03 ($n = 9$).

6.4 Results

6.4.1 Database analysis

The average C_{org}/N_{tot} value of all marine sediments from Neogene to present is 7.3 ± 4.6 (n = 5928), which closely matches the canonical "Redfield" C/N ratio (6.6; Redfield, 1958). The average C_{org}/N_{tot} value in sediments deposited under the oxygen-deficient waters of the Black Sea, Arabian Sea and Peru Margin is 9.0 ± 2.0 (n = 200). Bootstrap resampling (n = 10,000) of these datasets confirms that the modern oxygen deficient settings indeed exhibit on average higher C_{org}/N_{tot} values than typical marine sediments deposited over the last ∼23 Myrs (Fig. 6.2).

Sediments from the Black Sea, Arabian Sea, and Peru Margin display a positive correlation between C_{org}/N_{tot} and TOC (R^2 = 0.67; Fig. 6.3). Several organic-rich shales in our database also show logarithmic relationships between C_{org}/N_{tot} and TOC, including cores recovered from ODP site 1258 at Demerera Rise that span the Cenomanian-Turonian ocean anoxic event 2 (OAE-2) (Meyers et al., 2006) (R^2 = 0.54), mudrocks from the Kheu River locality that span the Paleocene-Eocene Thermal Maximum (PETM) (Junium et al., 2018) (R^2 = 0.54), the Devonian New Albany Shale of the Illinois Basin (Ingall et al., 1993) (R^2 = 0.95), and the Cambrian Shiyantou Formation of China (Cremonese et al., 2013) (R^2 = 0.88) (Fig. 6.9).

6.4.2 H/C and C/N analyses

The C_{org}/N_{tot} values of samples analyzed in this study range from 8.1 to 237; $(C/N)_{kerogen}$ values range from 38 to 464 (Table 6.1). The H/C molar ratios of kerogen extracts analyzed in this study range from 0.11 to 1.20 (Table 6.1). In all cases where samples have been described in previous studies, the metamorphic grade determined by H/C analysis (following the demarcations in Hayes et al., 1983) is consistent with published estimates of thermal maturity (described in Kipp et al., 2018; Koehler et al., 2018). For the Phosphoria Formation, the H/C values of 0.41 to 0.54 suggest prehnite-pumpellyite facies metamorphism in the

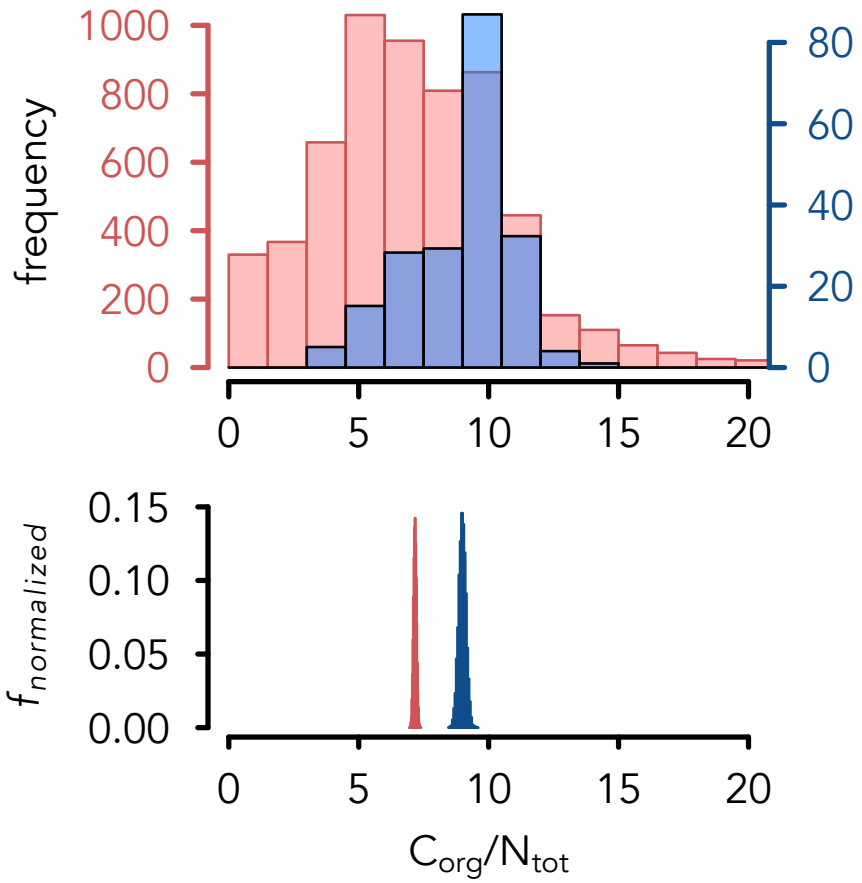

Figure 6.2: **Distribution of C_{org}/N_{tot} in recent marine sediments.** Red denotes all sediments included in the data compilation that were deposited since the beginning of the Neogene (∼23 Ma); blue denotes sediments deposited under modern oxygen-deficient waters (*i.e.*, Black Sea, Arabian Sea, and Peru Margin). Top panel shows distribution of all data; bottom panel shows bootstrap resampled (n = 10,000) means. The mean C_{org}/N_{tot} value of all recent marine sediments (7.3 ± 4.6) is close to the canonical "Redfield" C/N ratio of 6.6, while sediments underlying oxygen-deficient waters on average have higher C_{org}/N_{tot} ratios (9.0 ± 2.0).

studied sections, which is consistent with previous work (Claypool et al., 1978).

6.5 Discussion

6.5.1 The relationship between C/N and TOC in marine sediments

The typically low (<10) C_{org}/N_{tot}ratios in modern marine sediments roughly track the C/N ratio of primary planktonic biomass (Anderson and Sarmiento, 1994). However, notable deviations from this value are observed – particularly in sediments underlying oxygen-deficient waters. Specifically, sediments from the Black Sea, Arabian Sea and Peru Margin show high C_{org}/N_{tot} values (Fig. 6.2) and a positive correlation between C_{org}/N_{tot} and TOC (Fig. 6.3). To a first-order, the occurrence of elevated (>10) C_{org}/N_{tot} ratios in sediments beneath low-oxygen waters is consistent with the trend noted by Twichell et al. (2002), where the prevalence of anaerobic respiration in the water column leads to higher sedimentary C_{org}/N_{tot} ratios due to preferential degradation of nitrogenous biomass (cf. Van Mooy et al., 2002). Moreover, the higher C_{org}/N_{tot} values associated with higher TOC content could conceivably reflect higher productivity, where greater oxygen demand advances anaerobic respiration and enhances organic matter burial. However, higher TOC does not necessarily imply higher export production – for example, sedimentation rates often exert a larger control on organic matter burial (Emerson and Hedges, 1988; Betts and Holland, 1991; Hedges and Keil, 1995) – and therefore this mechanism may not necessarily explain the observed coupling of C_{org}/N_{tot} and TOC. Further insight into the origin of this correlation can be obtained by considering other occurrences of C_{org}/N_{tot}–TOC coupling found in the marine sediment and sedimentary rock database.

For instance, the Devonian New Albany Shale of the Illinois Basin shows a very strong correlation between C_{org}/N_{tot} and TOC (Fig. 6.4). This relationship could similarly derive from elevated productivity and anaerobic remineralization when sediments with high TOC were deposited. However, this mechanism alone cannot explain C_{org}/N_{tot} ratios below ∼5, which are lower than the C/N ratio of marine planktonic biomass (Redfield, 1958). By

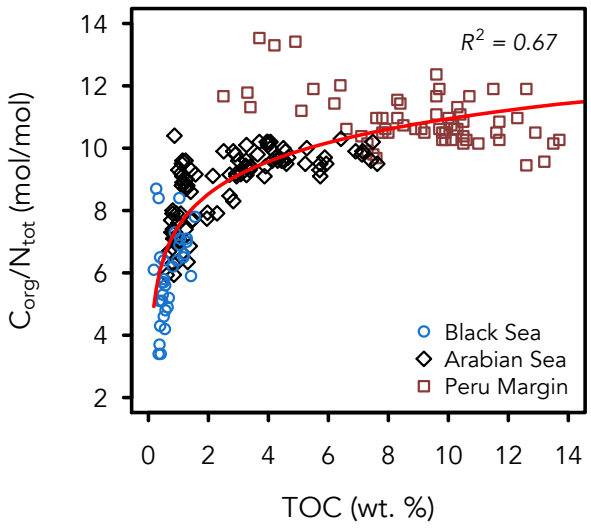

Figure 6.3: **Co-variation of C_{org}/N_{tot} and total organic carbon (TOC) in modern marine sediments deposited under oxygen-deficient waters.** Red trendline denotes logarithmic regression. High C_{org}/N_{tot} ratios in these settings might reflect preferential degradation of nitrogen-rich biomass during anaerobic remineralization.

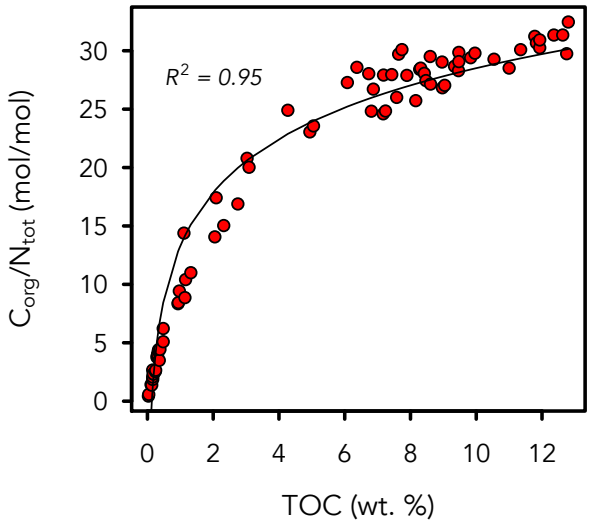

Figure 6.4: **Co-variation of C_{org}/N_{tot} and TOC in the ~375 Ma New Albany Shale.** Black trendline denotes logarithmic regression. High C_{org}/N_{tot} in this setting might reflect a large degree of anaerobic remineralization during deposition and early diagenesis.

analogy to modern settings, it would seem most likely that those samples from the New Albany Shale are proportionally more dominated by mineral-bound nitrogen that was either trapped during the respiration of organic matter in the sediments during diagenesis, or perhaps transported from the continents as detrital silicate-bound nitrogen. Because a continuous relationship between C_{org}/N_{tot} and TOC is observed at values both higher and lower than the C/N ratio of primary biomass, it would be most parsimonious if the same mechanism could explain the deviations toward both high and low values (instead of one process that increases C/N and another that diminishes). We therefore consider one such scenario below.

6.5.2 A two-component mixing model

One way to explain the observed coupling of C_{org}/N_{tot} and TOC (cf. Calvert, 2004) is via two-component mixing between two nitrogen-bearing pools: an organic phase that we

refer to as **kerogen** (which contains both nitrogen and organic carbon, existing primarily as highly polymerized organic compounds, but potentially also including some bitumen in rocks within the oil window) and a clay mineral phase that we refer to as **silicate** (which may contain nitrogen if K-rich, because of NH_4^+ substitution for K^+, but lacks organic carbon). In such a scenario, samples with low C_{org}/N_{tot} would be expected at low TOC contents (*i.e.*, mineral-bound nitrogen being the dominant pool), whereas C_{org}/N_{tot} would increase with higher TOC, as kerogen comes to be the dominant nitrogen pool. We explore this possibility by calculating C_{org}/N_{tot} ratios with a two-component mixing model that is derived from the mass balance equation

$$\frac{C_{org}}{N_{tot}} = (\frac{TOC}{TN_{silicate} + TN_{kerogen}})(\frac{14.01}{12.01}) \tag{6.3}$$

where 14.01 and 12.01 correspond to the molar masses of nitrogen and carbon, respectively, $TN_{silicate}$ and $TN_{kerogen}$are the nitrogen concentrations (in weight percent) of each nitrogen pool, and TOC is the organic carbon concentration (in weight percent) of the bulk rock, which derives from the kerogen phase alone. The nitrogen content of the kerogen phase ($TN_{kerogen}$) can be calculated as a function of TOC using the equation

$$TN_{kerogen} = (\frac{TOC}{\frac{C}{N}_{kerogen}})(\frac{14.01}{12.01}) \tag{6.4}$$

if $(C/N)_{kerogen}$ is known or estimated. Equation 6.4 can be combined with Equation 6.3 to give

$$\frac{C_{org}}{N_{tot}} = (\frac{TOC}{TN_{silicate} + (\frac{(TOC)(14.01)}{\frac{C}{N}_{kerogen}(12.01)})})(\frac{14.01}{12.01}) \tag{6.5}$$

which allows C_{org}/N_{tot} ratios to be calculated for a range of TOC values if the parameters $TN_{silicate}$ and $(C/N)_{kerogen}$ are either known or estimated.

We follow Calvert (2004) in using the New Albany Shale as a case study. The mean TNsilicate value can be determined by computing the y-intercept in a linear regression of N_{tot} vs. TOC (y-intercept = 0.0892, $R^2 = 0.99$). The modeled C_{org}/N_{tot} values of the

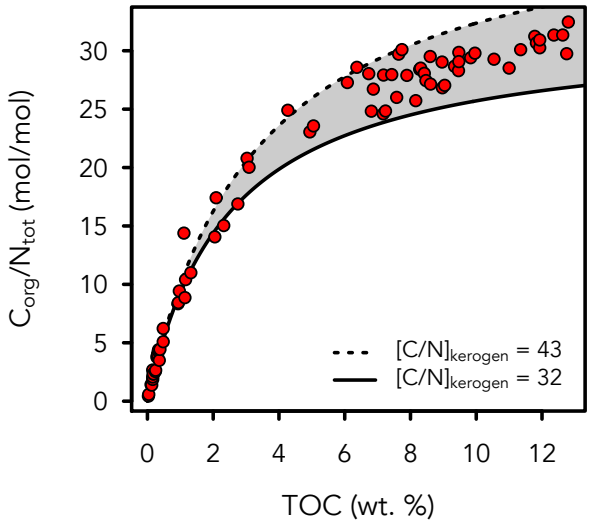

Figure 6.5: **A two-component mixing model reproduces the co-variation of C_{org}/N_{tot} and TOC in the New Albany Shale.** End-member compositions comprise $(C/N)_{kerogen}$ values of 32 and 43, which closely match the measurements of Boudou et al. (2008). Calculations are described in Section 6.5.2.

New Albany Shale can then be computed by using the determined average $TN_{silicate}$ value, estimating the $(C/N)_{kerogen}$ value, and solving the equation for a range of TOC values from 0 to 13% (*i.e.*, the range observed in the data). Using $(C/N)_{kerogen}$ values of 32 and 43 as lower and upper limits, the C_{org}/N_{tot} versus TOC trend observed in the New Albany Shale can be closely reproduced with the mixing model (Fig. 6.5). These $(C/N)_{kerogen}$ values fit well with measurements of six kerogen extracts performed by Boudou et al. (2008), which had $(C/N)_{kerogen}$ values ranging from 32 to 41. This suggests that the C_{org}/N_{tot} variability in the New Albany Shale is in fact due to differing amounts of kerogen relative to a constant silicate-bound nitrogen fraction, as was previously suggested by Calvert (2004).

We can then take this a step further and return to the modern marine sediments deposited under oxygen-deficient waters. While these data are compiled from separate basins, and thus do not have the same sources of kerogen and silicate-bound nitrogen, the same

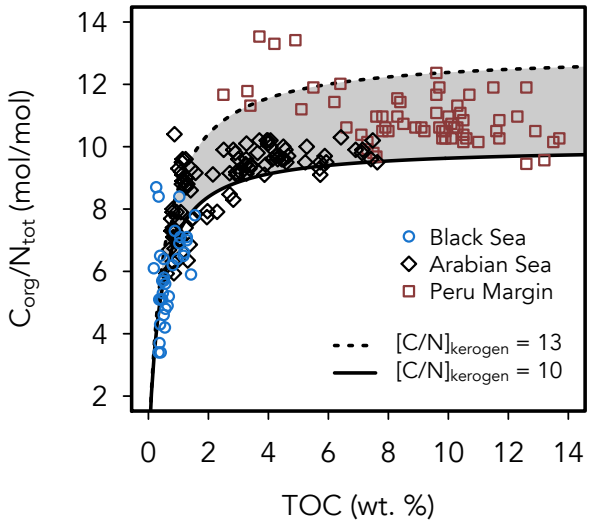

Figure 6.6: **A two-component mixing model also reproduces the co-variation of C_{org}/N_{tot} and TOC in modern oxygen-deficient settings.** In this case, a similarity in the $(C/N)_{kerogen}$ composition of end-members in each setting likely causes the sediments to show similar relationships.

logic might broadly explain the observed trend. For instance, by again computing the average $TN_{silicate}$ value using a linear regression of N_{tot} versus TOC (y-intercept = 0.0448, R^2 = 0.99), C_{org}/N_{tot} ratios can be calculated by estimating the range of $(C/N)_{kerogen}$ values. Using $(C/N)_{kerogen}$ values of 10 to 13 – similar to those observed under the Benguela Current upwelling system (Twichell et al., 2002) – the observed trend of modern oxygen-deficient settings can be reproduced (Fig. 6.6). Again, this would seem to suggest that the coupling between C_{org}/N_{tot} and TOC typically derives from a mixing relationship between the kerogen and silicate nitrogen pools.

It is worth noting that the ability of this mixing model to reproduce trends in C_{org}/N_{tot} and TOC depends on two key assumptions. First, it is assumed that $TN_{silicate}$ is fairly constant in the unit under consideration. The validity of this assumption can either be weighed by directly calculating $TN_{silicate}$ (*i.e.*, by extracting kerogen and observing the difference in

nitrogen content between bulk-rock and kerogen extract) or by assessing the strength of the N_{tot} versus TOC correlation – at higher R^2 values, the assumption is likely to be well founded. Where there is not a strong correlation between total nitrogen and organic carbon, the intercept is likely a poorer indicator of average $TN_{silicate}$ across the section (*i.e.*, there is more variability). In this case, the model can be adapted by including an uncertainty envelope derived from the standard error of the linear regression. Second, the mixing model works best if $(C/N)_{kerogen}$ is also fairly constant across the section of interest. While the calculations can encompass some range of values, the accuracy of the reconstructed trend is highest when $(C/N)_{kerogen}$ is least variable.

The latter point suggests that many units in fact have fairly constant $(C/N)_{kerogen}$ values, reflecting relatively constant depositional, diagenetic, and metamorphic conditions within individual units. To assess the validity of that inference, we closely examined a few units where $(C/N)_{kerogen}$ values have been directly measured. In these instances, a linear correlation between C_{org}/N_{tot} and $f_{kerogen}$ is observed (Fig. 6.7). Moreover, the linear trend fits within a calculated range of C_{org}/N_{tot} values determined by plugging the mean $(C/N)_{kerogen}$ of each unit into Equation 6.1 and solving for C_{org}/N_{tot} as a function of $f_{kerogen}$. This further confirms that the mixing relationship does indeed drive the C_{org}/N_{tot} trends.

The finding that $(C/N)_{kerogen}$ is fairly constant within many units raises the question: what determines variability in $(C/N)_{kerogen}$ between units? In other words, why is there a vertical separation of units in Fig. 6.7? Since C_{org}/N_{tot} equals $(C/N)_{kerogen}$ when $f_{kerogen} = 1$, moving upward along the y-axis in Fig. 7 corresponds to a higher mean $(C/N)_{kerogen}$ value for a given unit. The Twichell et al. (2002) model would seem to suggest that higher $(C/N)_{kerogen}$ should be found under more reducing water-column conditions. This inference does potentially fit the observed trend, where the highest $(C/N)_{kerogen}$ value in Fig. 6.7 corresponds to the Mesoarchean Soanesville Group, which is thought to have been deposited under a strongly anoxic water column (Stüeken et al., 2015). Similarly, the lowest $(C/N)_{kerogen}$ values correspond to the Paleoproterozoic Sengoma Argillite Formation and Francevillian Series, both of which are thought to have been deposited under more oxygen-rich conditions during the

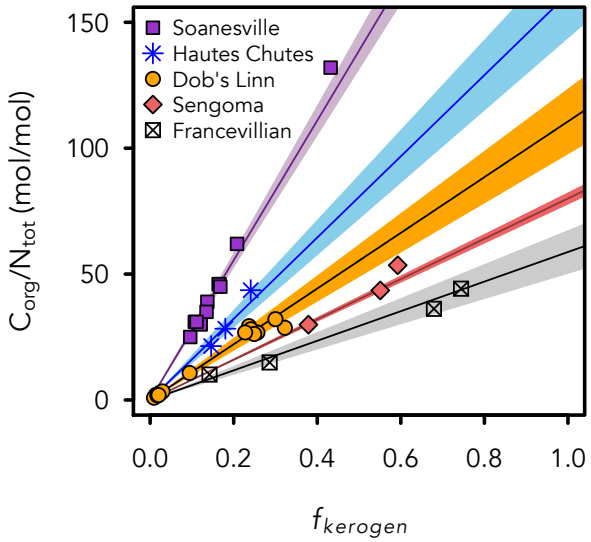

Figure 6.7: **Linear relationships between C_{org}/N_{tot} and $f_{kerogen}$.** Lines denote C_{org}/N_{tot} values calculated using mixing model described in Section 6.5.2 (1σ confidence interval is shown by shaded regions). The fact that analyzed samples plot along mixing model outputs confirms that the mixing of kerogen and silicate nitrogen pools does indeed cause the observed C_{org}/N_{tot} variability in these units. The C_{org}/N_{tot} ratio where $f_{kerogen} = 1$ is equal to the mean $(C/N)_{kerogen}$ value of the unit, meaning that the vertical separation of these units is due to differences in $(C/N)_{kerogen}$.

proposed "oxygen overshoot" event from ∼2.3 to 2.1 Ga (Bekker and Holland, 2012; Kipp et al., 2017). However, an additional consideration that must be weighed is the potential effect of thermal maturation on $(C/N)_{kerogen}$ in these units. Since progressive metamorphism tends to increase $(C/N)_{kerogen}$ values (Bebout and Fogel, 1992; Stüeken et al., 2017), this confounding factor must be assessed before using $(C/N)_{kerogen}$ as a paleo-redox proxy in deep time.

6.5.3 Assessing metamorphic effects on C/N

We used H/C ratios to assess the effect of metamorphism on $(C/N)_{kerogen}$ ratios in ancient marine sedimentary rocks. It is well-established that the H/C ratio of residual organic matter steadily decreases during hydrocarbon generation (catagenesis) and progressive metamorphism (metagenesis) (Baskin, 1997). Therefore, the effect of thermal maturation on $(C/N)_{kerogen}$ should be evident as an inverse correlation with H/C ratios. This can be seen in our $(C/N)_{kerogen}$ versus H/C compilation (Fig. 8a); at higher metamorphic grades, $(C/N)_{kerogen}$ values become extremely elevated (often with C/N > 100) relative to that of primary planktonic biomass. Precisely defining the point at which thermal maturation begins to increase $(C/N)_{kerogen}$ ratios is somewhat difficult. In our data compilation, extremely high $(C/N)_{kerogen}$ values begin around an H/C value of ∼0.35 (Fig. 6.8a). This agrees with previous studies (Ward et al., 2005; Boudou et al., 2008) of organic carbon and nitrogen maturation in Type III kerogen (*i.e.*, terrestrial organic matter), which show an onset of increased $(C/N)_{kerogen}$ values around a vitrinite reflectance (R_{max}) value of ∼3.0%, corresponding to H/C ratios of ∼0.4 or a hydrogen index near zero (Fig. 6.8b). This corresponds to prehnite-pumpellyite facies metamorphism (Hayes et al., 1983), or beyond the end of the "oil window" and catagenesis and after the onset of organic matter metagenesis (Boudou et al., 2008). The shift in $(C/N)_{kerogen}$ at H/C values of ∼0.4 (R_{max} of ∼3%) may result from the transition from the phase of dry gas preservation to that of gas destruction (R_{max} ∼3.2%; Dow, 1977) at which point significant aromatization of heterocycles and aromatic group condensation and enlargement (Huang et al., 2018) should eject non-amine nitrogen

atoms from the residual kerogen.

The ability of even low-grade metamorphism to alter $(C/N)_{kerogen}$ values therefore makes it difficult to use $(C/N)_{kerogen}$ as a paleo-environmental proxy in rocks that have reached upper prehnite-pumpellyite facies metamorphism or above. This unfortunately includes many marine sedimentary rocks of Precambrian age, raising a serious hurdle for the use of C/N as a deep-time paleo-environmental proxy. However, there is still potential for paleo-environmental information to be recorded in $(C/N)_{kerogen}$ values in units that have not been substantially metamorphosed (*i.e.*, have not exceeded the stage of dry gas preservation and gas destruction, corresponding to R_{max} of ∼3 or H/C of ∼0.4). We explore this possibility below.

6.5.4 Case studies: C/N vs. TOC in unmetamorphosed marine sedimentary rocks

Returning to the New Albany Shale, both R_{max} values (0.45-1.45%; Boudou et al., 2008) and organic matter hydrogen content (mean HI = 390 ± 235, approx. H/C = 0.6-1.2; Ingall et al., 1993) indicate that this unit has not reached prehnite-pumpellyite facies metamorphism. Therefore, the effect of thermal maturation on $(C/N)_{kerogen}$ in the New Albany Shale should be minor. The fact that $(C/N)_{kerogen}$ values fall between 32 and 43 may therefore derive from diagenetic effects. In particular, the preferential degradation of nitrogenous biomass during anaerobic remineralization (cf. Twichell et al., 2002; Van Mooy et al., 2002) seems to be a plausible explanation for the New Albany Shale data. This unit frequently displays laminations, indicative of anoxic bottom waters that inhibited bioturbation (Ingall et al., 1993; Calvert et al., 1996). Additionally, near-zero $\delta^{15}N$ values (Calvert et al., 1996) suggest that the system was dominated by nitrogen fixation, or in other words lacks the isotopic signal of non-quantitative denitrification that is typically expressed under oxic-to-suboxic surface waters (cf. Ader et al., 2016; Stüeken et al., 2016). This setting may therefore have comprised a productive environment where high rates of export production generated a significant oxygen demand in the water column, depleting oxygen, and perhaps initiating anaerobic organic matter respiration.

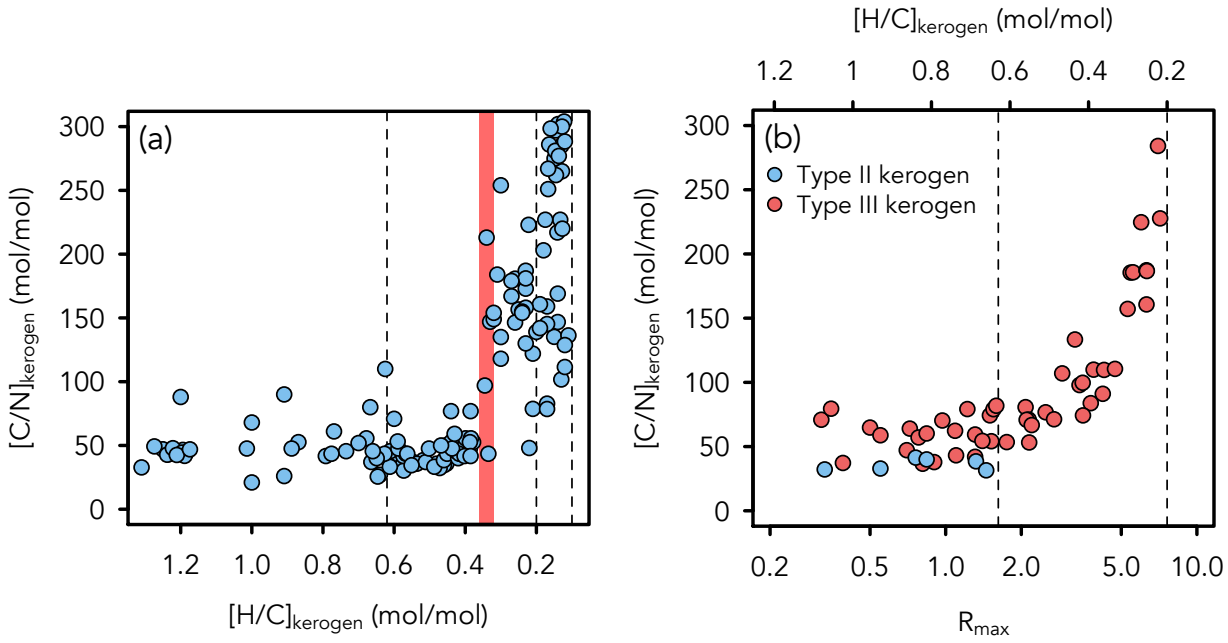

Figure 6.8: **The relationship between $(C/N)_{kerogen}$ and $(H/C)_{kerogen}$ in (a) marine sedimentary rocks analyzed in this study and compiled from the literature, and (b) the studies of Ward et al. (2005) and Boudou et al. (2008).** Dashed lines mark transitions between metamorphic facies (cf. Hayes et al., 1983), with prehnite-pumpellyite facies starting at H/C = 0.63, greenschist facies at 0.2, and amphibolite facies at 0.1. Note that the Ward et al. (2005) and Boudou et al. (2008) studies primarily focused on Type III kerogen (*i.e.*, terrestrial organic matter) and measured vitrinite reflectance (R_{max}), which has been translated to H/C ratios following Burnham and Sweeney (1989). A sharp increase in $(C/N)_{kerogen}$ ratios is seen at H/C values <0.35 (red shaded band) in the left plot, or around ∼0.4 in the right plot. This transition falls within prehnite-pumpellyite facies metamorphism, and may correspond to the end of dry gas preservation and the onset of dry gas destruction (discussed in Section 6.5.3).

If this is indeed the cause of the elevated $(C/N)_{kerogen}$ values in the New Albany Shale, then the fact that the observed $(C/N)_{kerogen}$ values (32-43) are substantially higher than those in sediments deposited beneath the Benguela Current upwelling system (10-15; Twichell et al., 2002) suggests that the degree of water-column anoxia was greater in the former setting. This is plausible, but should be supported by additional instances of elevated $(C/N)_{kerogen}$ values from other oxygen-deficient paleo-environments.

One interval that likely featured such conditions is OAE-2 (∼94 Ma), during which time widespread deposition of organic-rich shales occurred (Arthur et al., 1987), perhaps related to a global expansion of anoxic waters (Clarkson et al., 2018). ODP 1257-1261 cores drilled on the Demerera Rise capture the transition into and out of this event in one marine setting. Meyers et al. (2006) analyzed the organic carbon and total nitrogen contents of these cores, in addition to other geochemical data. While $(C/N)_{kerogen}$ values were not measured for these samples, the mixing model discussed in Section 6.5.2 suggests that C_{org}/N_{tot} versus TOC plots can illustrate differences in $(C/N)_{kerogen}$ between siliciclastic units (when $TN_{silicate}$ is approximated as the y-intercept in an N_{tot} vs. TOC linear regression, cf. Section 6.4.2). Using this approach, the C_{org}/N_{tot} data from core 1258, which spans the Cenomanian-Turonian boundary, show a trend similar to that of the New Albany Shale (Fig. 6.9). Furthermore, nitrogen isotope analyses of sediments from these cores also showed near-zero $\delta^{15}N$ values that are indicative of an anaerobic nitrogen cycle dominated by nitrogen-fixation and quantitative denitrification (Junium and Arthur, 2007) as opposed to oxic-suboxic nitrogen cycling (including non-quantitative denitrification) that occurs on modern continental margins. These data would therefore seem to support the inference that elevated $(C/N)_{kerogen}$ ratios in these settings are derived from anaerobic recycling of organic matter in the water column and/or sediment porewaters.

Junium & Arthur (2007) noted that anaerobic remineralization could have contributed to the elevated C_{org}/N_{tot} ratios at the Demerera Rise across OAE-2. However, using a simple stoichiometric calculation, they argued that this effect could not fully explain the observed C_{org}/N_{tot} values of >40. Moreover, they surmised that due to a nitrogen isotopic offset of

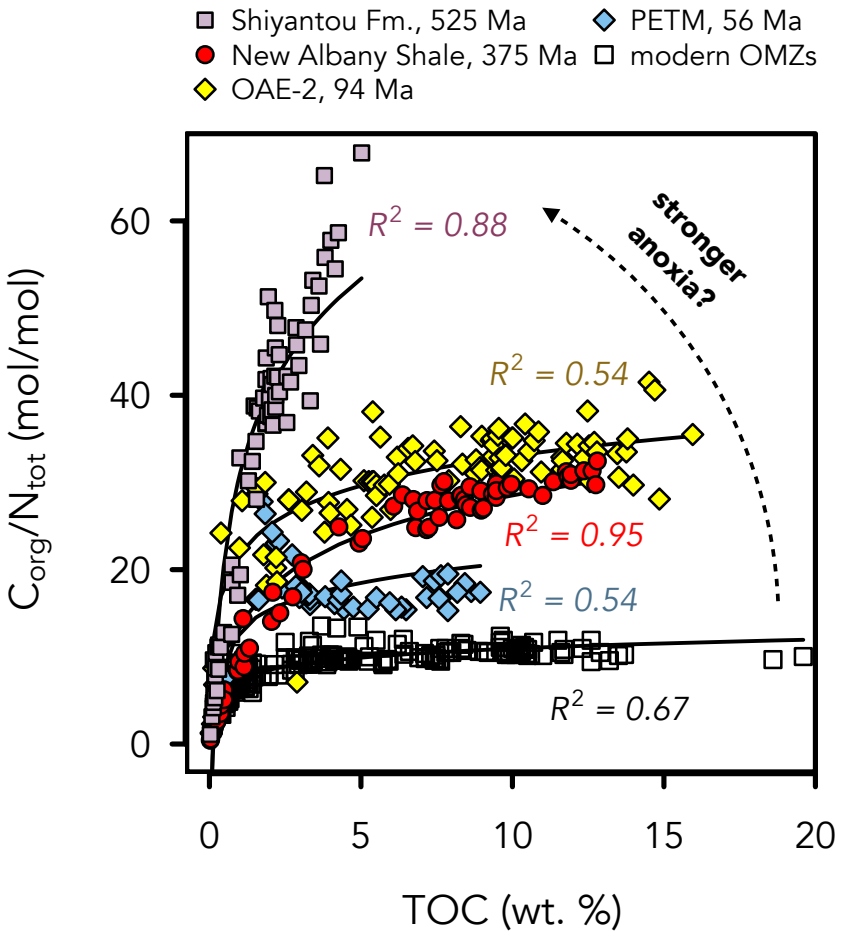

Figure 6.9: **Vertical separation in C_{org}/N_{tot} versus TOC space of modern and ancient oxygen-deficient settings.** All trendlines denote logarithmic regression. In siliciclastic sediments that are well-described by the mixing model, spatial separation in C_{org}/N_{tot} versus TOC space corresponds to differences in $(C/N)_{kerogen}$, with minor contributions from differences in $TN_{silicate}$. Thus, units showing steeper curves in this plot may have undergone a greater degree of anaerobic remineralization during deposition and early diagenesis.

protein relative to bulk cellular biomass – where amino acids are enriched on average by ∼3‰ relative to bulk biomass (Macko et al., 1987) – enhanced protein degradation would give rise to an anti-correlation between $\delta^{15}N$ and C_{org}/N_{tot}, which is in fact observed in multiple cores at the Demerera Rise (Junium and Arthur, 2007). Their stoichiometric calculation suggested that the observed isotopic deviations could be explained with an increase in C_{org}/N_{tot} up to values of no more than ∼20. However, there are two additional issues to consider with respect to this interpretation. The first is that the two-component cellular composition model is an over-simplification for the purpose intended here. For instance, in such a model with a protein C/N ratio of 3.8 and a bulk cellular C/N value of 6.6, complete degradation of all protein leaves a residual $(C/N)_{kerogen}$ ratio of 17.8 if protein comprises 80% of cellular biomass. However, there are several components that comprise the non-protein portion of cellular biomass – including nucleic acids, chlorophyll, carotenoids, lipids and carbohydrates – each with different C/N ratios. By slightly expanding this stoichiometric calculation, we show (detailed description of calculations in Appendix D) that preferential degradation of labile, nitrogen-rich biomass (amino acids and nucleic acids) can conceivably generate C/N ratios in residual biomass in excess of 100 (Fig. 6.10). While this model is also only an approximation of average phytoplankton stoichiometry, it illustrates the plausibility of very high C/N ratios in buried biomass deriving from anaerobic remineralization alone.

As for the nitrogen isotopic effect of this preferential degradation, this more detailed model also shows that the simple ∼3‰ $\delta^{15}N$ offset between protein and bulk cellular biomass does not capture the $\delta^{15}N$ offsets of other cellular components. Moreover, even if an isotopic offset between nitrogen-rich and nitrogen-poor biomass is manifest, the preservation of such a signal during diagenesis might be unlikely since the degradation of nitrogen-rich biomass tends to have an opposite effect, removing isotopically light nitrogen during deamination and leaving residual biomass isotopically heavier (Macko and Estep, 1984). Disentangling these two competing effects is therefore difficult.

To evaluate these effects, we begin with the published data discussed above. Returning to the New Albany Shale, we find a similar anti-correlation of $\delta^{15}N$ and C_{org}/N_{tot} ($R^2 = 0.81$),

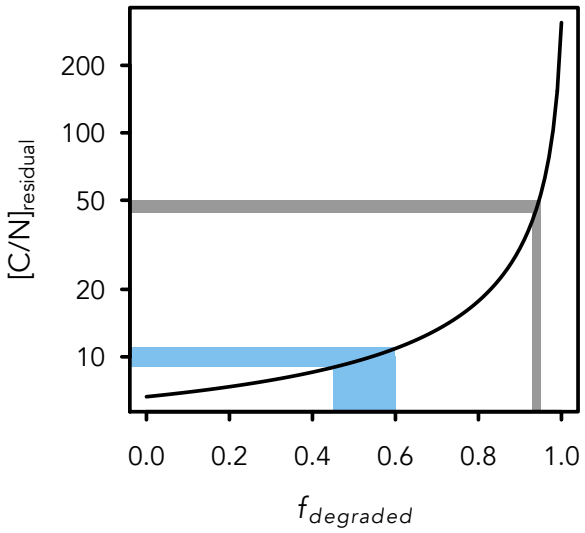

Figure 6.10: **Stoichiometric model calculation of increasing $(C/N)_{kerogen}$ ratios due to preferential degradation of nitrogen-rich biomass.** As anaerobic remineralization preferentially oxidizes amino acids and nucleic acids relative to lipids, substantial increases in the $(C/N)_{kerogen}$ ratio of residual biomass (*i.e.*, $(C/N)_{residual}$) can be obtained at high degrees of completeness (dark grey band). Lesser degrees of anaerobic remineralization may have a smaller effect, such as in modern oxygen-deficient settings (light blue band). A detailed description of calculations can be found in Appendix D.

possibly indicative of enhanced degradation of protein. However, if we use $\delta^{13}C_{org}$ and $\delta^{15}N$ values to guide our interpretation, and amend the mixing model described in Section 6.5.2 to include a minor contribution of recalcitrant, detrital organic matter (detailed description of calculations in Appendix D), we find that this anticorrelation could perhaps be explained by mixing alone (Fig. 6.11). Using this mixing model set-up, we can calculate a predicted $\delta^{13}C_{org}$, $\delta^{15}N$ and C_{org}/N_{tot} chemostratigraphy across the New Albany Shale as a function of TOC. Doing so very closely reproduces the observed data (Fig. 6.12), suggesting that the $\delta^{15}N$-C_{org}/N_{tot} anticorrelation in the New Albany Shale (and in other similar units) could conceivably arise from three-component mixing between a planktonic organic matter phase, a silicate-bound nitrogen phase and a detrital phase comprised of recalcitrant terrestrial organic matter. However, the fit of a mixing model alone does not prove that this mechanism is indeed the underlying cause of the observed co-variation. For instance, primary changes in the isotopic compositions of end-members (*i.e.*, the "kerogen" and "silicate" phases) could give rise to the same trend. The only way to distinguish between these two scenarios (constant end-member composition and mixing versus changing end-member compositions) is to directly measure end-member compositions via kerogen extraction and analysis. This was in fact undertaken for the New Albany Shale (Calvert et al., 1996) and the data reveal that the nitrogen isotopic composition of the kerogen endmember is indeed higher (+2 to +3‰) in the low-TOC (bioturbated) layers than in the high-TOC (laminated) layers (-1 to 0‰). The cause for this primary isotopic change cannot be readily proven – it could be that preferential degradation of nitrogen-rich and isotopically-enriched biomass occurred in the high-TOC layers (cf. Junium & Arthur 2007), or that the planktonic community was more dominated by nitrogen-fixation during deposition of the high-TOC layers. In either case, we use the mixing model here to outline a protocol for distinguishing primary isotopic changes from mixing artifacts that is closely tied to the interrogation of C_{org}/N_{tot} and $(C/N)_{kerogen}$ trends.

As for the $\delta^{13}C_{org}$ trends (Fig. 6.12) – the existence of small amounts of detrital, refractory organic carbon in the New Albany Shale is potentially consistent with the observation

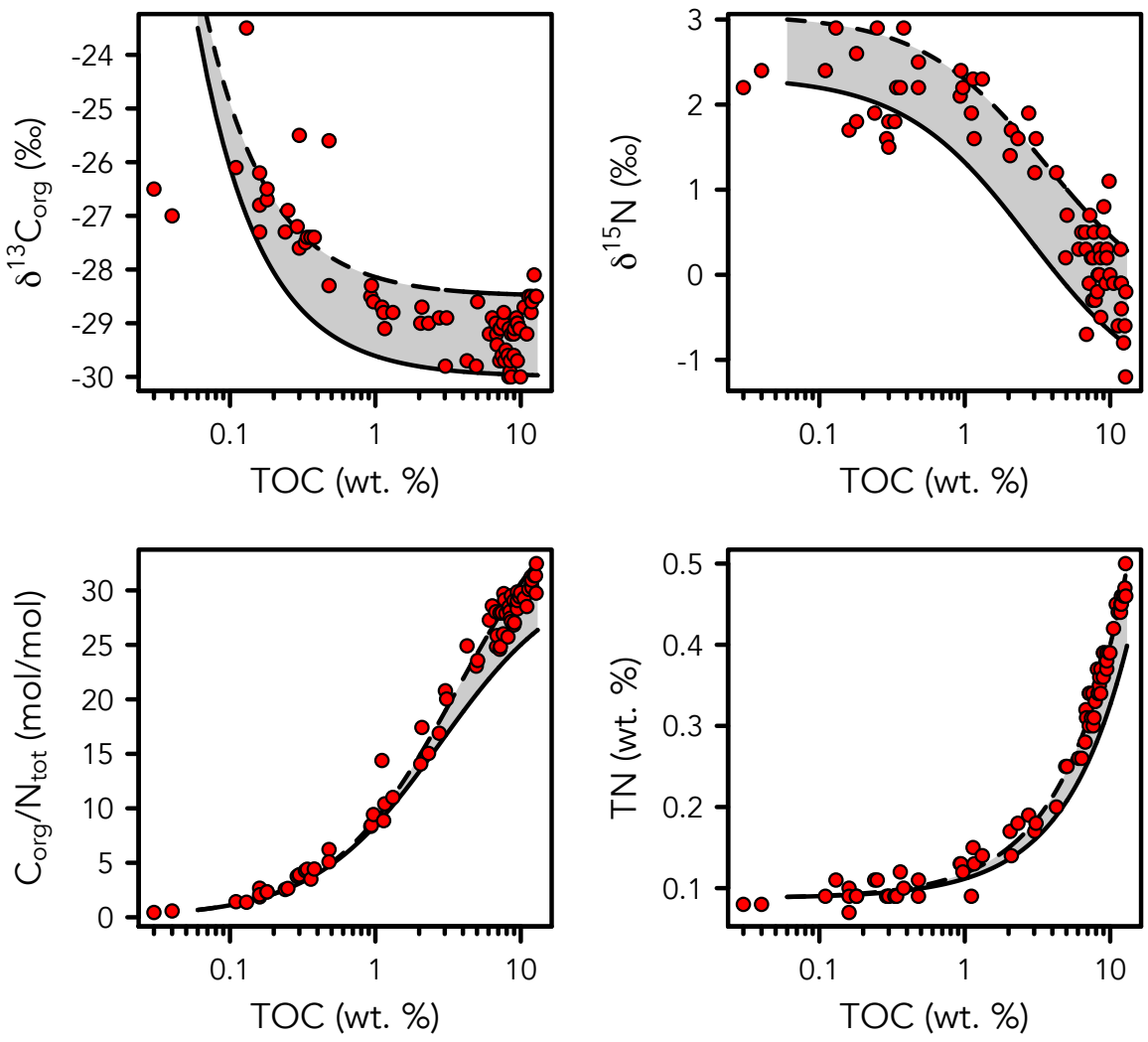

Figure 6.11: **Three-component mixing model for $\delta^{15}N$, $\delta^{13}C_{org}$, C_{org}/N_{tot}, and TN versus TOC in the New Albany Shale.** By including a trace amount of detrital organic carbon, and ascribing isotopic compositions to the end-members, the trends in all above parameters can be closely reproduced by the mixing model. A detailed description of the calculations can be found in Appendix D.

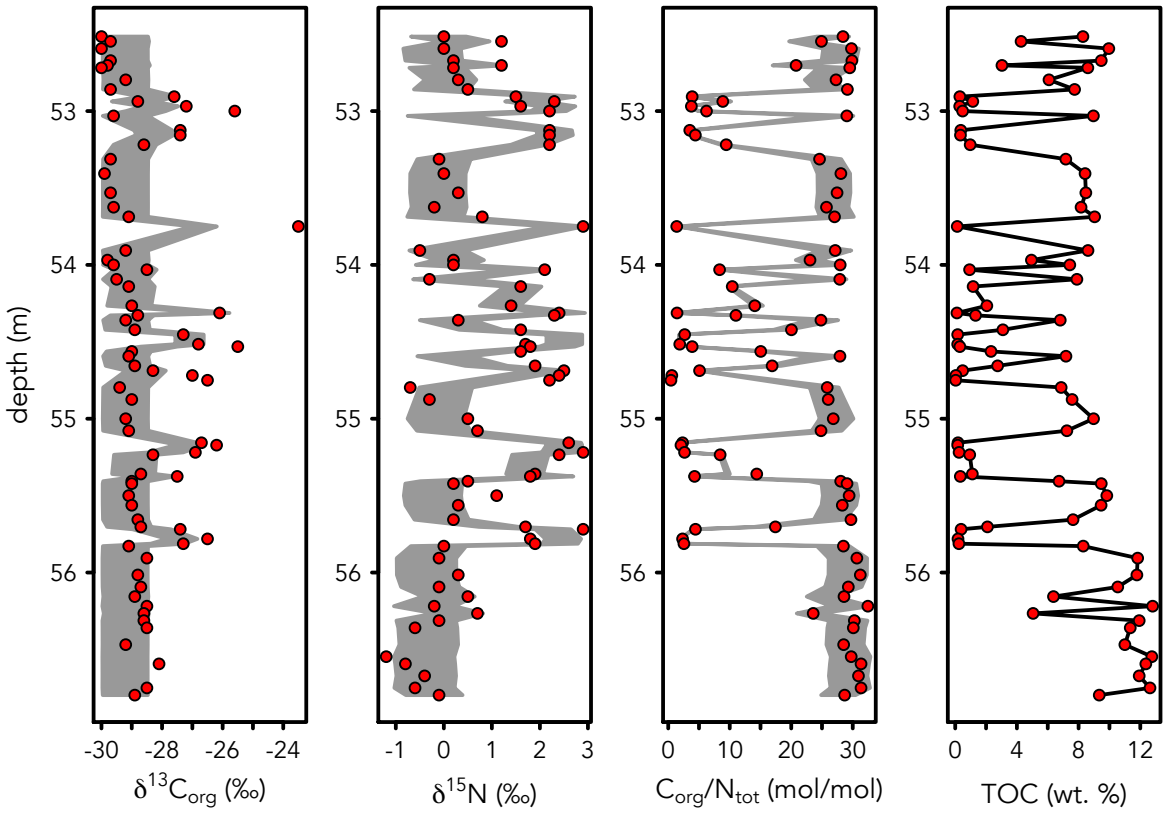

Figure 6.12: **Chemostratigraphy of the New Albany Shale.** The grey shaded region represents values calculated as a function of TOC using the mixing model described in Section 6.5.2. The strong anti-correlation of $\delta^{15}N$ and $\delta^{13}C_{org}$ with C_{org}/N_{tot} are thus shown to potentially arise from mixing of two components with different isotopic compositions.

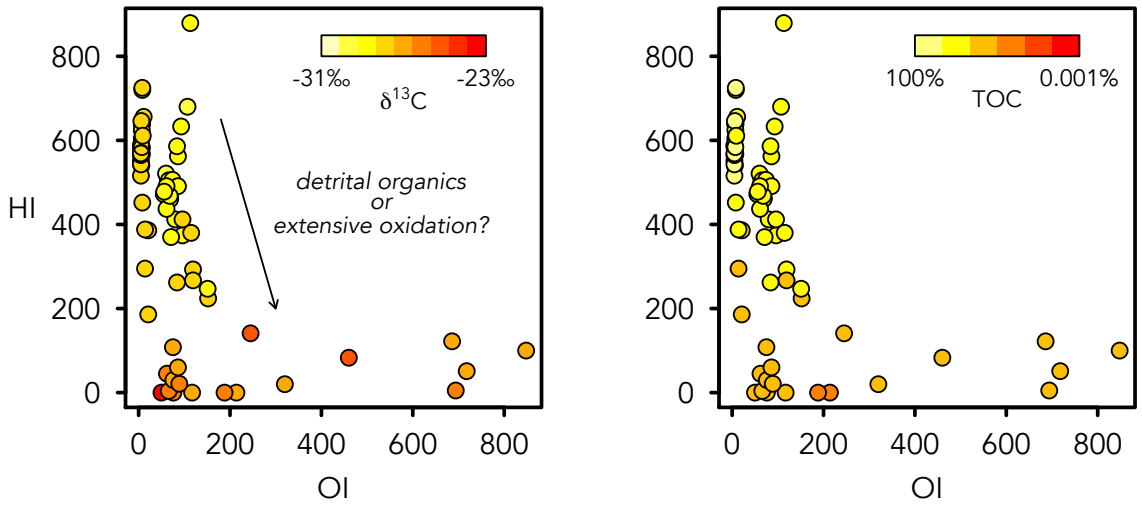

Figure 6.13: **Comparison of $\delta^{13}C_{org}$ and TOC with RockEval parameters.** HI = hydrogen index, OI = oxygen index. The occurrence of more positive $\delta^{13}C_{org}$ and lower TOC in samples with low HI and high OI values is consistent with either dominance of terrestrial material in samples with low TOC or extensive oxidative degradation of organic matter during deposition of the low-TOC horizons. Data are from Ingall et al., (1993) and Calvert et al., (1996).

of high O/C and low H/C ratios in the organic-lean horizons (Ingall et al., 1993; Fig. 6.13), typical of a terrestrial organic matter component. However, a similar trend could conceivably arise from extensive oxidative degradation of organic matter during deposition of the organic-lean horizons (Fig. 6.13). Analysis of $\delta^{13}C_{org}$ in kerogen extracts would not resolve this issue, because (i) $\delta^{13}C_{org}$ enrichment of residual biomass arising from extensive oxidation could mimic the composition of a terrestrial end-member, and (ii) the extracted kerogen would contain both the "kerogen" and "detrital" organic carbon phases as defined in our mixing model. Compound-specific isotopic analyses could perhaps present one avenue for distinguishing between these scenarios.

Given all of the above considerations, we conclude that:

- Anti-correlation of $\delta^{15}N$ and $\delta^{13}C_{org}$ with C_{org}/N_{tot} in the New Albany Shale and the

black shales at the Demerera Rise – as well as in other units – can arise from mixing relationships and/or primary changes in end-member isotopic composition. Careful scrutiny can distinguish between these scenarios, at least for $\delta^{15}N$.

- Enrichment of $(C/N)_{kerogen}$ to values >40 is plausible via selective degradation of nitrogen-rich biomass, potentially with a minor nitrogen isotopic effect on the residual organic matter.

With this in mind, we further explore the potential of elevated C/N values as paleo-redox indicators by considering units that were deposited under different water-column redox conditions than the two units discussed above.

One such example is a black shale sequence near the Kheu River in Russia that has recently been studied (Junium et al., 2018) to reconstruct changes in nitrogen cycling during an expansion of water-column anoxia across the Paleocene-Eocene Thermal Maximum (PETM). These analyses revealed a negative $\delta^{15}N$ excursion (Junium et al., 2018) – reminiscent of values seen during OAE-2 at the Demerera Rise (Junium and Arthur, 2007) – which, together with the observation of elevated TOC, suggests that the water column became more anoxic at that locality during an episode of rapid global warming. The C_{org}/N_{tot} data from the Kheu River site plot at higher values relative to TOC than sediments underlying modern oxygen-deficient waters, but below the New Albany Shale and the OAE-2 black shales from the Demerera Rise (Fig. 6.9). Organic geochemical analyses have been used to suggest that the Kheu River shales are fairly immature (Kodina et al., 1995), meaning that thermal maturation is unlikely to explain the slight increase in C_{org}/N_{tot} values. Under the preferential degradation model, this would suggest that the degree of water-column oxygen depletion (or, more specifically, of anaerobic relative to aerobic remineralization) in this environment was less pronounced than during OAE-2, but greater than in modern oxygen-deficient waters under upwelling zones (*e.g.*, the Peru Margin), generating moderately high C/N values in buried organic matter. To a qualitative degree, this is consistent with the paleo-redox interpretation of Junium et al. (2018).

For an example of potentially stronger anoxia, we consider the mid-Cambrian Shiyantou Formation of South China (Cambrian Stage 2, ∼521-529 Ma; Cremonese et al., 2013). Organic-rich shales of the Shiyantou Formation have $\delta^{15}N$ values ranging from 0 to 3‰ (mean +1.6 ± 0.8‰), consistent with water-column anoxia as in the aforementioned units (Cremonese et al., 2013). However, the C_{org}/N_{tot} values of the Shiyantou Formation samples plot much higher relative to TOC than the previously discussed units, reaching a maximum of 68 (Fig. 6.9). These rocks are thought to be unmetamorphosed, meaning that thermal maturation should not be responsible for the high C/N ratios. These high C_{org}/N_{tot} ratios are therefore likely to derive from organic matter remineralization. While it is difficult to exclude late diagenetic nitrogen loss, the preferential degradation calculations (Fig. 6.10) show that such high values could plausibly derive from a redox-mediated preferential degradation of nitrogen-rich cellular components. Since continental shelf environments are thought to have been more strongly anoxic in the Cambrian than in the later Paleozoic (Dahl et al., 2010; Gill et al., 2011; Sperling et al., 2015; Lenton et al., 2016; Wallace et al., 2017), the Shiyantou Formation may therefore represent a more anoxic end-member, with higher C_{org}/N_{tot} values than the New Albany Shale and Demerera Rise shales.

6.5.5 The utility of C/N as a paleo-redox proxy

As outlined above, the preferential degradation of nitrogen-rich biomass during anaerobic remineralization may cause sediments underlying anoxic waters to display higher C_{org}/N_{tot} and $(C/N)_{kerogen}$ values than those in sediments deposited under more oxygen-rich conditions. This proxy could potentially be of great utility in paleoenvironmental studies that aim to characterize water-column redox conditions and nutrient cycling dynamics. However, as has been stressed throughout this discussion, there are several limitations to this proxy that must be acknowledged and further studied before this geochemical tool can be widely applied. We briefly summarize these below:

- The organic matter must be predominantly marine in origin, with only a negligible

contribution of terrestrial material. A terrestrial component can potentially be identified using three-component mixing calculations, or ideally using organic geochemical indicators (*e.g.*, H/C and O/C ratios, compound-specific isotopes).

- The rocks in consideration must not have experienced thermal alteration beyond the window of dry gas preservation – *i.e.* well into prehnite-pumpellyite facies metamorphism. While extremely high C/N values were not observed in our dataset until an H/C value of ∼0.35, which is past the early stages of the prehnite-pumpellyite facies metamorphism, the potential for minor thermal alteration to mimic small environmental signals renders any interpretations near this level fairly uncertain. Thus, we recommend that an H/C value of 0.4 be used as an upper limit on thermal maturity when considering C/N ratios as a paleo-redox proxy, while H/C values >0.6 (*i.e.*, unmetamorphosed rocks) provide a very conservative limit that should be entirely safe from thermal enrichment.

- The rocks should also have moderate to high TOC levels. Our amended three-component mixing model (Section 6.5.2, Appendix D) suggests that detrital organic matter can potentially dominate the signal at very low TOC levels. Since this material can have variable $\delta^{15}N$, $\delta^{13}C_{org}$, and C/N compositions – and moreover, because the material is by definition allogenic and thus not representative of conditions at the locus of deposition – such samples should be avoided when using C_{org}/N_{tot} or $(C/N)_{kerogen}$ as a paleo-redox proxy.

With these caveats in mind, one interval of Earth's history that is particularly amenable to investigation using this new paleo-redox proxy is also one of the most interesting and poorly constrained: the transition from a low-oxygen world to a fully-oxygenated world in the latest Proterozoic and early Paleozoic (Lyons et al., 2014). During this interval terrestrial vegetation was negligible, many sedimentary successions have undergone only mild metamorphism, and marine oxygen levels were lower than at present, facilitating accumula-

tion of organic-rich marine sediments. Moreover, evolving marine oxygen levels could have caused substantial fluctuations in diagenetic redox conditions, which should be recorded in C_{org}/N_{tot} or $(C/N)_{kerogen}$ in marine sedimentary rocks spanning the late Precambrian pulses of ocean oxygenation (*e.g.*, Sahoo et al., 2012; von Strandmann et al., 2015; Thomson et al., 2015; Kendall et al., 2015; Sahoo et al., 2016; Turner and Bekker, 2016) or the delayed oxygenation of the deep ocean in the Paleozoic (*e.g.*, Dahl et al., 2010; Sperling et al., 2015). Lastly, this proxy may also prove informative in some instances before and after the interval described above, for example in post-Devonian offshore marine settings with minimal terrestrial input, in more ancient metamorphic lacunae with well-preserved organic material, and in more recent high-productivity regions of the ocean. Thus, though currently only qualitative or semi-quantitative, this new paleo-redox proxy could potentially illuminate some of the uncertain aspects of our planet's oxygenation history and should provide a useful supplement to other existing geochemical tools.

6.6 Conclusion

We have presented here a new framework for interpreting C_{org}/N_{tot} and $(C/N)_{kerogen}$ ratios in ancient marine sedimentary rocks. Within individual lithostratigraphic units, variations in C_{org}/N_{tot} can often be attributed to mixing between an authigenic kerogen component, a "silicate" phase containing some nitrogen, and in some cases traces of recalcitrant detrital organic carbon. By assessing the relationship between C_{org}/N_{tot} and TOC in a given unit, the uniformity of $(C/N)_{kerogen}$ and the amount of nitrogen in the silicate phase can be assessed. Furthermore, the average $(C/N)_{kerogen}$ value can be estimated using C_{org}/N_{tot} and TOC data. Since lithological variability can give rise to large C_{org}/N_{tot} fluctuations within a single unit, $(C/N)_{kerogen}$ is the datum that informs paleo-redox evaluation. We find that $(C/N)_{kerogen}$ is often fairly uniform within individual units, and that differences between units are consistent with previously determined qualitative water-column redox constraints. To develop C/N into a more precise – and ultimately, quantitative – paleo-redox proxy, future studies should seek to couple C/N measurements, organic geochemical indicators of diagenetic and metamorphic

conditions, and independent paleo-redox proxies.

6.7 References

Ader M., Thomazo C., Sansjofre P., Busigny V., Papineau D., Laffont R., Cartigny P. and Halverson G. P. (2016) Interpretation of the nitrogen isotopic composition of Precambrian sedimentary rocks: Assumptions and perspectives. *Chemical Geology* 429, 93–110.

Anderson L. A. and Sarmiento J. L. (1994) Redfield ratios of remineralization determined by nutrient data analysis. *Global Biogeochemical Cycles* 8, 65–80.

Arthur M. A., Schlanger S.T. and Jenkyns H. C. (1987) The Cenomanian-Turonian Oceanic Anoxic Event, II. Palaeoceanographic controls on organic-matter production and preservation. *Geological Society, London, Special Publications* 26, 401–420.

Baskin D. K. (1997) Atomic H/C ratio of kerogen as an estimate of thermal maturity and organic matter conversion. *AAPG Bulletin* 81, 1437–1450.

Bebout G. E. and Fogel M. L. (1992) Nitrogen-isotope compositions of metasedimentary rocks in the Catalina Schist, California: implications for metamorphic devolatilization history. *Geochimica et Cosmochimica Acta* 56, 2839–2849.

Bekker A. and Holland H. D. (2012) Oxygen overshoot and recovery during the early Paleoproterozoic. *Earth Planet. Sci. Lett.* 317, 295–304.

Betts J. N. and Holland H. D. (1991) The oxygen content of ocean bottom waters, the burial efficiency of organic carbon, and the regulation of atmospheric oxygen. *Global and Planetary Change* 5, 5–18.

Boudou J.-P., Schimmelmann A., Ader M., Mastalerz M., Sebilo M. and Gengembre L. (2008) Organic nitrogen chemistry during low-grade metamorphism. *Geochimica et Cosmochimica Acta* 72, 1199–1221.

Burnham A. K. and Sweeney J. J. (1989) A chemical kinetic model of vitrinite maturation and reflectance. *Geochimica et Cosmochimica Acta* 53, 2649–2657.

Calvert S. E. (2004) Beware intercepts: interpreting compositional ratios in multi-component sediments and sedimentary rocks. *Organic Geochemistry* 35, 981–987.

Calvert S. E., Bustin R. M. and Ingall E. D. (1996) Influence of water column anoxia and sediment supply on the burial and preservation of organic carbon in marine shales. *Geochimica et Cosmochimica Acta* 60, 1577–1593.

Clarkson M. O., Stirling C. H., Jenkyns H. C., Dickson A. J., Porcelli D., Moy C. M., von Strandmann P. A. P., Cooke I. R. and Lenton T. M. (2018) Uranium isotope evidence for two episodes of deoxygenation during Oceanic Anoxic Event 2. *Proceedings of the National Academy of Sciences*, 201715278.

Claypool G. E., Love A. H. and Maughan E. K. (1978) Organic geochemistry, incipient metamorphism, and oil generation in black shale members of Phosphoria Formation, western interior United States. *AAPG Bulletin* 62, 98–120.

Cremonese L., Shields-Zhou G., Struck U., Ling H.-F., Och L., Chen X. and Li D. (2013) Marine biogeochemical cycling during the early Cambrian constrained by a nitrogen and organic carbon isotope study of the Xiaotan section, South China. *Precambrian Research* 225, 148–165.

Dahl T. W., Hammarlund E. U., Anbar A. D., Bond D. P. G., Gill B. C., Gordon G. W., Knoll A. H., Nielsen A. T., Schovsbo N. H. and Canfield D. E. (2010) Devonian rise in atmospheric oxygen correlated to the radiations of terrestrial plants and large predatory fish. *Proceedings of the National Academy of Sciences* 107, 17911–17915.

Dow W. G. (1977) Kerogen studies and geological interpretations. *Journal of Geochemical Exploration* 7, 79–99.

Emerson S. and Hedges J. I. (1988) Processes controlling the organic carbon content of open ocean sediments. *Paleoceanography* 3, 621–634.

Fagerbakke K. M., Heldal M. and Norland S. (1996) Content of carbon, nitrogen, oxygen, sulfur and phosphorus in native aquatic and cultured bacteria. *Aquatic Microbial Ecology* 10, 15–27.

French K. L., Hallmann C., Hope J. M., Schoon P. L., Zumberge J. A., Hoshino Y., Peters C. A., George S. C., Love G. D., Brocks J. J. and others (2015) Reappraisal of hydrocarbon biomarkers in Archean rocks. *Proceedings of the National Academy of Sciences* 112,

5915–5920.

Geider R. J. and La Roche J. (2002) Redfield revisited: variability of C [ratio] N [ratio] P in marine microalgae and its biochemical basis. *European Journal of Phycology* 37, 1–17.

Gill B. C., Lyons T. W., Young S. A., Kump L. R., Knoll A. H. and Saltzman M. R. (2011) Geochemical evidence for widespread euxinia in the Later Cambrian ocean. *Nature* 469, 80.

Hayes J. M., Wedeking K. W. and Kaplan I. R. (1983) Precambrian organic geochemistry-Preservation of the record.

Hedges J. I. and Keil R. G. (1995) Sedimentary organic matter preservation: An assessment and speculative synthesis. *Marine Chemistry* 49, 81–115.

Huang Z., Liang T., Zhan Z.-W., Zou Y.-R., Li M. and Peng P. (2018) Chemical structure evolution of kerogen during oil generation. *Marine and Petroleum Geology* 98, 422–436.

Ingall E. D., Bustin R. M. and Van Cappellen P. (1993) Influence of water column anoxia on the burial and preservation of carbon and phosphorus in marine shales. *Geochimica et Cosmochimica Acta* 57, 303–316.

Joosu L., Lepland A., Kirsimäe K., Romashkin A. E., Roberts N. M., Martin A. P. and Črne A. E. (2015) The REE-composition and petrography of apatite in 2Ga Zaonega Formation, Russia: The environmental setting for phosphogenesis. *Chemical Geology* 395, 88–107.

Junium C. K. and Arthur M. A. (2007) Nitrogen cycling during the Cretaceous, Cenomanian-Turonian oceanic anoxic event II. *Geochemistry, Geophysics, Geosystems* 8.

Junium C. K., Dickson A. J. and Uveges B. T. (2018) Perturbation to the nitrogen cycle during rapid Early Eocene global warming. *Nature Communications* 9, 3186.

Kendall B., Komiya T., Lyons T. W., Bates S. M., Gordon G. W., Romaniello S. J., Jiang G., Creaser R. A., Xiao S., McFadden K., Sawaki Y., Tahata M., Shu D., Han J., Li Y., Chu X. and Anbar A. D. (2015) Uranium and molybdenum isotope evidence for an episode of widespread ocean oxygenation during the late Ediacaran Period. *Geochimica et Cosmochimica Acta* 156, 173–193.

Kipp M. A. and Stüeken E. E. (2017) Biomass recycling and Earth's early phosphorus cycle. *Science Advances* 3, eaao4795.

Kipp M. A., Stüeken E. E., Bekker A. and Buick R. (2017) Selenium isotopes record extensive marine suboxia during the Great Oxidation Event. *Proceedings of the National Academy of Sciences* 114, 875–880.

Kipp M. A., Stüeken E. E., Yun M., Bekker A. and Buick R. (2018) Pervasive aerobic nitrogen cycling in the surface ocean across the Paleoproterozoic Era. *Earth and Planetary Science Letters* 500, 117–126.

Knoll A. H., Bergmann K. D. and Strauss J. V. (2016) Life: the first two billion years. *Phil. Trans. R. Soc. B* 371, 20150493.

Kodina L. A., Huang Y., Gavrilov Y. O., Jones M. and Eglington G. (1995) Environment of Upper Paleocene black shale deposition in Southern Russia and adjacent regions as revealed by isotope and biomarker study. 17th International Meeting on Organic Geochemistry.

Koehler M. C., Buick R. and Barley M. E. (2018) Nitrogen isotope evidence for anoxic deep marine environments from the Mesoarchean Mosquito Creek Formation, Australia. *Precambrian Research.*

Koehler M. C., Buick R., Kipp M. A., Stüeken E. E. and Zaloumis J. (2018) Transient surface ocean oxygenation recorded in the 2.66 Ga Jeerinah Formation, Australia. *Proceedings of the National Academy of Sciences* 115, 7711–7716.

Koehler M.C., Stüeken E. E., Hillier S., Prave A.R. (submitted) Nitrogen and carbon biogeochemistry across the Ordovician-Silurian boundary at Dob's Linn, Scotland. *Palaeogeography, Palaeoclimatology, Palaeoecology.*

Lenton T. M., Dahl T. W., Daines S. J., Mills B. J., Ozaki K., Saltzman M. R. and Porada P. (2016) Earliest land plants created modern levels of atmospheric oxygen. *Proceedings of the National Academy of Sciences* 113, 9704–9709.

Lyons T. W., Reinhard C. T. and Planavsky N. J. (2014) The rise of oxygen in Earth's early ocean and atmosphere. *Nature* 506, 307–315.

Macko S. A. and Estep M. L. (1984) Microbial alteration of stable nitrogen and carbon isotopic compositions of organic matter. *Organic Geochemistry* 6, 787–790.

Macko S. A., Fogel M. L., Hare P. E. and Hoering T. C. (1987) Isotopic fractionation of nitrogen and carbon in the synthesis of amino acids by microorganisms. *Chemical Geology* 65, 79–92.

Meyers P. A. (1994) Preservation of elemental and isotopic source identification of sedimentary organic matter. *Chemical Geology* 114, 289–302.

Meyers P. A., Bernasconi S. M. and Forster A. (2006) Origins and accumulation of organic matter in expanded Albian to Santonian black shale sequences on the Demerara Rise, South American margin. *Organic Geochemistry* 37, 1816–1830.

Meyers P. A., Silliman J. E. and Shaw T. J. (1996) Effects of turbidity flows on organic matter accumulation, sulfate reduction, and methane generation in deep-sea sediments on the Iberia Abyssal Plain. *Organic Geochemistry* 25, 69–78.

Müller P. J. (1977) CN ratios in Pacific deep-sea sediments: Effect of inorganic ammonium and organic nitrogen compounds sorbed by clays. *Geochimica et Cosmochimica Acta* 41, 765–776.

Papineau D., She Z. and Dodd M. S. (2017) Chemically-oscillating reactions during the diagenetic oxidation of organic matter and in the formation of granules in late Palaeoproterozoic chert from Lake Superior. *Chemical Geology* 470, 33–54.

Parsons T. R., Stephens K. and Strickland J. D. H. (1961) On the chemical composition of eleven species of marine phytoplankters. *Journal of the Fisheries Board of Canada* 18, 1001–1016.

Perkins R. B., McIntyre B., Hein J. R. and Piper D. Z. (2003) Geochemistry of Permian rocks from the margins of the Phosphoria Basin: Lakeridge core, western Wyoming. US Geol. Survey Open-File Rept 3, 21.

Prahl F. G., Cowie G. L., De Lange G. J. and Sparrow M. A. (2003) Selective organic matter preservation in "burn-down" turbidites on the Madeira Abyssal Plain. *Paleoceanography* 18.

Premuzic E. T., Benkovitz C. M., Gaffney J. S. and Walsh J. J. (1982) The nature and distribution of organic matter in the surface sediments of world oceans and seas. *Organic Geochemistry* 4, 63–77.

Redfield A. C. (1934) On the proportions of organic derivatives in sea water and their relation to the composition of plankton. *James Johnstone Memorial Volume*, 176–192.

Redfield A. C. (1958) The biological control of chemical factors in the environment. *American Scientist* 46, 230A–221.

Sahoo S. K., Planavsky N. J., Jiang G., Kendall B., Owens J. D., Wang X., Shi X., Anbar A. D. and Lyons T. W. (2016) Oceanic oxygenation events in the anoxic Ediacaran ocean. *Geobiology* 14, 457–468.

Sahoo S. K., Planavsky N. J., Kendall B., Wang X., Shi X., Scott C., Anbar A. D., Lyons T. W. and Jiang G. (2012) Ocean oxygenation in the wake of the Marinoan glaciation. *Nature* 489, 546–549.

Sheldon R. P. (1963) Physical stratigraphy and mineral resources of Permian rocks in western Wyoming., US Geological Survey.

Sperling E. A., Wolock C. J., Morgan A. S., Gill B. C., Kunzmann M., Halverson G. P., Macdonald F. A., Knoll A. H. and Johnston D. T. (2015) Statistical analysis of iron geochemical data suggests limited late Proterozoic oxygenation. *Nature* 523, 451–454.

Stüeken E. E., Buick R., Guy B. M. and Koehler M. C. (2015) Isotopic evidence for biological nitrogen fixation by molybdenum-nitrogenase from 3.2 Gyr. *Nature* 520, 666–669.

Stüeken E. E., Kipp M. A., Koehler M. C. and Buick R. (2016) The evolution of Earth's biogeochemical nitrogen cycle. *Earth-Science Reviews* 160, 220–239.

Stüeken E. E., Zaloumis J., Meixnerová J. and Buick R. (2017) Differential metamorphic effects on nitrogen isotopes in kerogen extracts and bulk rocks. *Geochimica et Cosmochimica Acta* 217, 80–94.

Thomson D., Rainbird R. H., Planavsky N., Lyons T. W. and Bekker A. (2015) Chemostratigraphy of the Shaler Supergroup, Victoria Island, NW Canada: A record of ocean composition prior to the Cryogenian glaciations. *Precambrian Research* 263, 232–245.

Turner E. C. and Bekker A. (2016) Thick sulfate evaporite accumulations marking a mid-Neoproterozoic oxygenation event (Ten Stone Formation, Northwest Territories, Canada). *GSA Bulletin* 128, 203–222.

Twichell S. C., Meyers P. A. and Diester-Haass L. (2002) Significance of high C/N ratios in organic-carbon-rich Neogene sediments under the Benguela Current upwelling system. *Organic Geochemistry* 33, 715–722.

Van Mooy B. A., Keil R. G. and Devol A. H. (2002) Impact of suboxia on sinking particulate organic carbon: Enhanced carbon flux and preferential degradation of amino acids via denitrification. *Geochimica et Cosmochimica Acta* 66, 457–465.

von Strandmann P. A. P., Stüeken E. E., Elliott T., Poulton S. W., Dehler C. M., Canfield D. E. and Catling D. C. (2015) Selenium isotope evidence for progressive oxidation of the Neoproterozoic biosphere. *Nature Communications* 6.

Wallace M. W., Shuster A., Greig A., Planavsky N. J. and Reed C. P. (2017) Oxygenation history of the Neoproterozoic to early Phanerozoic and the rise of land plants. *Earth and Planetary Science Letters* 466, 12–19.

Walsh J. J., Premuzic E. T. and Whitledge T. E. (1981) Fate of nutrient enrichment on continental shelves as indicated by the C/N content of bottom sediments. In: *Elsevier Oceanography Series* Elsevier. pp. 13–49.

Wang X., Zhao W., Zhang S., Wang H., Su J., Canfield D. E. and Hammarlund E. U. (2018) The aerobic diagenesis of Mesoproterozoic organic matter. *Scientific Reports* 8, 13324.

Ward C. R., Li Z. and Gurba L. W. (2005) Variations in coal maceral chemistry with rank advance in the German Creek and Moranbah Coal Measures of the Bowen Basin, Australia, using electron microprobe techniques. *International Journal of Coal Geology* 63, 117–129.

Zhang S., Wang X., Wang H., Hammarlund E. U., Su J., Wang Y. and Canfield D. E. (2017) The oxic degradation of sedimentary organic matter 1400 Ma constrains atmospheric oxygen levels. *Biogeosciences* 14, 2133–2149.

Chapter 7

EXPLORING CYCAD FOLIAGE AS AN ARCHIVE OF THE ISOTOPIC COMPOSITION OF ATMOSPHERIC NITROGEN

This manuscript is under review at *Geobiology*. Co-authors are Eva Stüeken, Michelle Gehringer, Kim Sterelny, John Scott, Paul Forster, Caroline Strömberg and Roger Buick.

7.1 Abstract

Molecular nitrogen (N_2) constitutes the majority of Earth's modern atmosphere, contributing ~0.79 bar of partial pressure (pN_2). However, fluctuations in pN_2 may have occurred on 10^7-10^9 year timescales in Earth's past, perhaps altering the isotopic composition of atmospheric nitrogen. While modeling work has outlined various plausible trajectories for the evolution of pN_2, empirical constraints are difficult to derive due to the paucity of geological materials that record precise information about atmospheric pressure or N_2 abundance. Here we target an archive that may record the isotopic composition of atmospheric N_2 in deep time: the foliage of cycads. Cycads are ancient gymnosperms that host symbiotic N_2-fixing cyanobacteria in modified root structures known as coralloid roots. All extant species of cycads are known to host symbionts, suggesting that this N_2-fixing capacity is perhaps ancestral, reaching back to the early history of cycads in the late Paleozoic. Therefore, if the process of microbial N_2 fixation records the $\delta^{15}N$ value of atmospheric N_2 in cycad foliage, the fossil record of cycads may provide an archive of atmospheric $\delta^{15}N$ values, which could help constrain changes in pN_2 over the last 200-300 Myrs. To explore this potential proxy we conducted a survey of wild cycads growing in a range of modern environments to determine whether cycad foliage reliably records the isotopic composition of atmospheric N_2. We find that neither biological nor environmental factors significantly influence the $\delta^{15}N$ values of cycad foliage, suggesting

that they provide a reasonably robust record of the $\delta^{15}N$ of atmospheric N_2. Application of this proxy to the record of carbonaceous cycad fossils may not only help to constrain changes in pN_2 since the late Paleozoic, but also could shed light on the antiquity of the N_2-fixing symbiosis between cycads and cyanobacteria.

7.2 Introduction

Molecular nitrogen (N_2) is the most abundant gas in Earth's modern atmosphere, with a partial pressure of ∼0.79 bar. However, little is known about whether the partial pressure of N_2 (pN_2) has fluctuated over the course of Earth's ∼4.5 billion-year history. Modeling work has demonstrated that large pN_2 fluctuations are plausible on $>10^7$ year timescales under reasonable estimates of biogeochemical fluxes (Goldblatt et al., 2009; Busigny et al., 2011; Stüeken et al., 2016b; Johnson & Goldblatt, 2018; Mallik et al., 2018); however, these models have so far been unable to agree on a pN_2 trajectory across Earth's history (Zerkle & Mikhail, 2017). What is clear, though, is that any large change in pN_2 would carry important implications for global climate due to the effect of pressure broadening on the absorption of infrared radiation by greenhouse gases in the troposphere (Goldblatt et al., 2009; Stüeken et al., 2016b). Hence the development of proxies that can record changes in total atmospheric pressure and/or pN_2 has become a topic of interest in paleobiogeochemistry.

To date, many of the best-studied archives of information about ancient atmospheric pressure are geological materials with pressure-dependent characteristics. For instance, the size distribution of fossilized raindrop imprints in ∼2.7 Ga volcanic ash has been used to place an upper limit on atmospheric pressure of ∼1.1 bar (Som et al., 2012) and the size distribution of basalt vesicles in similarly ancient lava flows has been used to derive an estimate of ∼0.25 bar of total atmospheric pressure (Som et al., 2016). More recently, the distribution of grain sizes in ancient aeolian deposits has been explored as a quantitative paleo-barometry proxy (Goosmann et al., 2018), with models suggesting that the average grain size of aeolianites should decrease at lower atmospheric pressure. However, each of these proxies faces shortcomings: the precision of constraints derived from fossilized rain-

drops has been questioned (Kavanagh & Goldblatt, 2015; but see Goosmann et al., 2018 for an alternative view), grain size distributions in Precambrian aeolianites can be difficult to quantify due to recrystallization and deformation (Goosmann et al., 2018) and none of these records has yet been able to produce a consistent time-series dataset of atmospheric pressure – in large part due to the sparse availability and generally poor preservation of the ancient rock record. While further development on these fronts is surely worth pursuit, geochemical records may also prove useful in contributing information about changes in pN_2 in deep time.

Geochemical proxies have an advantage in that they can potentially be measured in a broader range of materials than those required in the special cases for geological paleobarometric work (*e.g.*, fossilized raindrop imprints, basaltic lava flows erupted at sea level). Additionally, individual geochemical measurements can potentially be more quantitatively informative about pN_2, for example by using isotopic ratios to "invert" for a budget in a mass balance model. For instance, if changes in pN_2 are driven by substantial burial of biological nitrogen – which models suggest is a likely mechanism (Stüeken et al., 2016b; Johnson & Goldblatt, 2018) – then the isotopic composition of atmospheric N_2 will be shifted proportionally to the amount and isotopic composition of buried nitrogen to maintain mass balance (similar to what is observed during glacial-interglacial changes in pCO_2; Leuenberger et al., 1992; Marino et al., 1992). If a suitable archive were to exist of the $\delta^{15}N$ of atmospheric N_2, then it could be equated to changes in pN_2 if assumptions are made about the $\delta^{15}N$ of the buried or released nitrogen. Furthermore, such an archive would also provide a critical test of the constancy of atmospheric $\delta^{15}N$ values on geological timescales, which is a foundational premise in deep-time studies of nitrogen isotope systematics (Ader et al., 2016; Stüeken et al., 2016a).

There has been limited work constraining the $\delta^{15}N$ of atmospheric N_2 in deep time. Marty et al. (2013) used N_2/Ar ratios and $\delta^{15}N$ values of fluid inclusions in ∼3.5 Ga hydrothermal quartz to calculate that pN_2 was between 0.5 and 1.1 bar and that the $\delta^{15}N$ of atmospheric N_2 was within ∼3‰ of the modern value. They used these data to speculate that pN_2 has not markedly changed across Earth's history. However, fluid inclusions con-

taining trapped air are scarce in the geologic record and present a considerable analytical and interpretative challenge, making it difficult to extend this technique to large sample sets on broader timescales. More recently, Silverman et al. (2019) showed that the nitrogen isotopic fractionation during N_2 fixation changes as a function of pN_2 in some species of cyanobacteria. As microbial N_2 fixation is thought to have arisen early in Earth's history (Stüeken et al., 2015; Weiss et al., 2016) and cyanobacteria may have dominated primary productivity through much of the Precambrian (Brocks et al., 2017; Gueneli et al., 2018), they could perhaps provide a long-term record of both pN_2 and the $\delta^{15}N$ of atmospheric N_2. However, because $\delta^{15}N$ values of bulk marine sediments can be altered by a few permil during diagenesis (Robinson et al., 2012) and represent a mixture of biomass from N_2-fixing and non-N_2-fixing organisms, this would require the nitrogen isotopic analysis of discrete cyanobacterial fossils instead of bulk marine sediments. While such fossilized remains have been reported throughout much of the Proterozoic (Awramik & Barghoorn, 1977; Golubic et al., 1995; Pang et al., 2018), the preservation of sufficient organic material in these minute fossils would make analysis extremely challenging, and again temporally-limited.

Here we investigate a possible macroscopic archive of the $\delta^{15}N$ value of atmospheric N_2: the foliage of plants with N_2-fixing cyanobacteria. Several plant lineages are known to form symbioses with bacteria that fix atmospheric N_2 into a bioavailable form and supply it to their host (Vessey et al., 2005); most notable are the legumes, which host N_2-fixing bacteria (rhizobia) in their root nodules. The use of foliar $\delta^{15}N$ values for recognizing N_2 fixation in these plant-microbial symbioses has long been established (*e.g.*, Shearer & Kohl, 1986; Handley & Raven, 1992) and in many cases $\delta^{15}N$ values in the foliage of plants with N_2-fixing symbioses have been shown to closely approximate that of atmospheric N_2 (Shearer et al., 1983; Yoneyama et al., 1993; Pate & Unkovich, 1999). This suggests that the measurement of $\delta^{15}N$ in fossilized leaves of such plants could perhaps provide an archive of atmospheric $\delta^{15}N$ values. However, most plants with N_2-fixing symbionts do not have a long enough fossil record to encompass a sufficient stretch of geologic time to detect possible fluctuations in pN_2 (and therefore in $\delta^{15}N$ of atmospheric N_2).

The cycads (Division: *Cycadophyta*) are an exceptional case: these gymnosperms have been deemed "living fossils" due to their morphological similarity to their ancestors, which originated in the late Paleozoic (Zhifeng & Thomas, 1989) and reached substantial diversity by the Mesozoic (Taylor et al., 2009). All extant species of cycads are known to host symbiotic, N_2-fixing cyanobacteria (primarily of the genera *Nostoc* and *Calothrix*; Rasmussen & Nilsson, 2002) in modified, subaerial to shallow subterranean, apogeotrophic roots known as coralloid roots (Costa & Lindblad, 2002). The occurrence of active symbionts in all extant cycad species is consistent with an ancestral nature of N_2 fixation in this lineage (Raven, 2002), meaning that fossilized cycad foliage may indeed provide an archive of atmospheric $\delta^{15}N$ values. As cycads were quite abundant in the past – particularly during the Mesozoic – it may be possible to leverage their organic remains as a comprehensive record of foliar $\delta^{15}N$ values across the last 200-300 Myrs.

While all of these factors make cycads compelling study organisms for recording atmospheric $\delta^{15}N$ values in deep time, a validation of this proxy is first needed in modern ecosystems. This is particularly important because there are multiple confounding factors that can interfere with a plant's ability to record the $\delta^{15}N$ value of atmospheric N_2, even in the presence of active symbiotic N_2-fixing bacteria. These include isotopic fractionation during microbial N_2 fixation, isotopic fractionation during nitrogen transport within plant tissues, and facultative uptake of soil nitrogen pools with variable $\delta^{15}N$ (Handley & Raven, 1992; Boddey et al., 2000; Unkovich & Pate, 2000; Chalk et al., 2016). Furthermore, while such processes have been studied in detail in other plants with N_2-fixing symbioses, such as legumes, nitrogen isotopic studies of the cycad-cyanobacterial symbiosis are comparatively rare and often restricted to individual sites (*e.g.*, Pate & Unkovich, 1999; Álvarez-Yépiz et al., 2014).

Here we explore the nitrogen isotope systematics of the cycad-cyanobacterial symbiosis on a larger geographic scale. We present new data from a nitrogen isotopic survey of cycad foliage growing in three different environments across Australia. We further compile published data from the literature in order to evaluate the significance of the observed trends in a global

context. Using this combined dataset, we consider whether factors such as mean annual temperature (MAT), mean annual precipitation (MAP), leaf age, plant sex, micro-habitat and taxonomic affinity correlate with nitrogen isotopic variability in cycads. We also investigate the nitrogen isotopic composition of cyanobacteria isolated from the coralloid roots of wild cycads and isotopic variability across individual cycad fronds in order to quantify the isotopic effect of N_2 fixation and its preservation at multiple levels within this symbiosis. We use organic carbon concentrations and isotope ratios alongside nitrogen in order to aid in interpretations of isotopic variability, since these parameters can help track changes in leaf stoichiometry. We consider all of these datasets together to determine whether cycad foliage reliably records atmospheric $\delta^{15}N$ values on the modern Earth, and whether cycads present a suitable archive for exploration as a deep-time proxy.

7.2.1 Nitrogen isotope systematics: Global N cycling to intra-plant fractionation

The use of nitrogen isotopes as a biogeochemical proxy in modern and ancient systems has been extensively reviewed elsewhere (*e.g.*, Högberg, 1997; Ader et al., 2016; Stüeken et al., 2016a); a brief summary is given here as it relates to the development of this proxy. The isotopic composition of atmospheric N_2 on the modern Earth is globally homogenous, and has come to be used as the international reference material for nitrogen isotopic analyses (Mariotti, 1983). Modern atmospheric N_2 therefore has a defined $\delta^{15}N$ value of 0‰.

The dominant flux of nitrogen into the biosphere is the fixation of atmospheric N_2 into biomass (shorthand: R-NH_2) by specialized groups of prokaryotes (Dos Santos et al., 2012). This process is typically characterized by a small isotopic fractionation (-2 to +1‰) when the most common nitrogenase enzyme (which contains molybdenum in the catalytic site) is utilized (Minagawa & Wada, 1986; Carpenter et al., 1997; Zerkle et al., 2008). The release of this organic-bound nitrogen during remineralization of biomass accounts for the dominant flux of nitrogen to the rest of the biosphere. This nitrogen is liberated as ammonium (NH_4^+), but in the presence of oxygen this ammonium is typically rapidly converted to nitrate (NO_3^-) in the microbially-mediated process of nitrification. In both the marine and

terrestrial biosphere, the uptake of these dissolved, bioavailable nitrogen pools (ammonium and nitrate) constitutes the dominant influx of nitrogen into biomass (with nitrate dominating over ammonium in typical marine and terrestrial environments on the well-oxygenated modern Earth). The process of remineralization is typically associated with small nitrogen isotopic effects (Freudenthal et al., 2001), and nitrification – although capable of generating large kinetic isotopic effects in culture (Casciotti, 2009) – is known to proceed rapidly even at very low dissolved oxygen levels (Kalvelage et al., 2011) and therefore is thought to be essentially complete in most natural environments, causing no expressed isotopic fractionation (Brandes & Devol, 2002; Devol, 2015). Thus, the initial supply of bioavailable nitrogen to the biosphere has an isotopic composition similar to that of atmospheric N_2.

In both the marine and terrestrial biospheres, the process that exerts the dominant control on the isotopic composition of the dissolved nitrogen pool is the removal of isotopically light nitrogen in the gas phase in low oxygen environments (Amundson et al., 2003; Devol, 2015). This can occur either through the process of "canonical" denitrification, wherein nitrate is progressively reduced to N_2 gas through a series of microbially-mediated reactions, or through anaerobic ammonium oxidation (anammox) by planctomycete bacteria where ammonium is reacted with nitrite to form N_2 gas. In both cases, kinetic isotopic effects cause preferential removal of ^{14}N in the gas phase (Kritee et al., 2012; Brunner et al., 2013; Devol, 2015), leaving the residual pool of dissolved nitrogen enriched in ^{15}N (*i.e.*, with positive $\delta^{15}N$ values). In the modern ocean, this gives dissolved nitrate an average $\delta^{15}N$ value of $+5‰$ (Sigman et al., 2000; Brandes & Devol, 2002); on land, this causes bulk soil $\delta^{15}N$ values in most regions to be more positive than atmospheric N_2 (Amundson et al., 2003; Craine et al., 2015) – though ammonia volatilization can also contribute to ^{15}N enrichment in some soils (Evans, 2007).

Importantly, plants with N_2-fixing symbioses are able to circumvent the soil nitrogen pool and obtain nitrogen directly from atmospheric N_2 via their microbial symbionts. This means that even in the presence of ^{15}N-enriched soil nitrogen, plants with N_2-fixing symbioses can have foliar $\delta^{15}N$ values that fall near $0‰$ (Shearer & Kohl, 1986), thereby making them

faithful recorders of atmospheric nitrogen isotope ratios. However, several processes can obscure this signature.

First, it is known that the isotopic effect of microbial N_2 fixation can vary under certain conditions. Culture work has shown that even molybdenum-nitrogenase is capable of generating more ^{15}N-depleted biomass (down to -4‰; Zerkle et al., 2008) under iron-replete conditions. Moreover, "alternative" nitrogenases that utilize vanadium or iron co-factors are known to yield biomass that is ^{15}N-depleted by several permil *in vitro* (Zhang et al., 2014), and this is thought to be relevant in some terrestrial environments (Bellenger et al., 2014). Thus, for a plant-microbial symbiosis to make a good archive of the δ^{15}N of atmospheric N_2, it must be known whether alternative nitrogenases are significantly expressed in the symbionts.

Second, the transport of nitrogen within plants can cause certain tissues to become enriched or depleted in ^{15}N relative to bulk biomass (Werner & Schmidt, 2002). For instance, it has been shown that actively N_2-fixing legume root nodules tend to become enriched in ^{15}N, causing an isotopic offset to develop between roots and shoots (Wanek & Arndt, 2002). It is therefore imperative that sub-sampling of a plant be conducted to determine which tissues yield suitable estimates of the whole-plant nitrogen isotopic composition.

Lastly, it is known that many N_2-fixing symbioses are opportunistic and only persist when nitrogen is not readily available in the soil (Vessey et al., 2005). This means that the simple identification of N_2-fixing potential in a plant-microbial symbiosis is not sufficient to demonstrate that N_2 fixation is indeed accounting for the plant's entire nitrogen demand; rather, plants may obtain their nitrogen through a mixture of soil and atmospheric sources. The balance between these supply pathways can be influenced by local environmental conditions (*e.g.*, soil moisture, temperature, nutrient availability) or potentially even biological factors (*e.g.*, leaf or plant age, sex). With this being the case, studies that aim to generate robust, quantitative estimates of a plant's reliance on microbial N_2-fixation typically measure the δ^{15}N of foliage in non-N_2-fixing "reference plants" growing in the same habitat (Shearer & Kohl, 1986). These plants serve as integrators of the δ^{15}N of bioavailable nitrogen in

soil and can provide added assurance that an N_2-fixing plant is indeed receiving most of its nitrogen through symbiotic N_2 fixation rather than from the soil.

We consider each of these potential complications below. To address the isotopic effect of microbial N_2 fixation, we cultured isolated cyanobacteria from the coralloid roots of wild cycad populations and observed their isotopic fractionation *in vitro*. We also conducted a sampling transect of a single frond in order to observe the intra-plant isotopic partitioning of nitrogen in cycad foliage. We then turn to our larger dataset and consider whether any environmental or biological factors influence the nitrogen isotopic composition of cycad foliage. We close by considering cycad foliage in comparison to non-N_2-fixing reference plants, and we discuss problems and prospects for employing this proxy in deep time through the isotopic study of carbonaceous cycad fossils.

7.3 Materials and Methods

7.3.1 Collection of plant samples

Cycad leaves were collected in spring and early summer (late October – January) from natural populations growing at three different localities in Australia: University of Western Australia Jandakot Reserve (32.17°S, 115.83°E), Tilba Tilba, New South Wales (36.32°S, 150.04°E), and D'Aguilar National Park, Queensland (27.44°S, 152.83°E; 27.44°S, 152.82°E; 27.28°S, 152.76°E). Samples from New South Wales and Western Australia were classified as "young," "old," or "dead" according to their maturity, where "young" leaves were fronds recently sprouted from the shoot apical meristem on mature plants, "old" leaves were the larger fronds at the periphery on their respective plants, and "dead" leaves were found on the ground beneath living plants. The Western Australia samples were further subdivided into male and female specimens to look for sex-specific isotopic differences. Non-cycad leaves were also collected at the New South Wales and Queensland sample sites to assess the nitrogen isotopic composition of non-N_2-fixing plants. All plant samples were freeze-dried for two days to ensure that all biomass was entirely devoid of water. Leaf samples were then

ground to a homogenous powder in a metal ball mill (WIG-L-BUG) that was cleaned with methanol between samples. The resulting powders were analyzed for carbon and nitrogen concentrations and isotopic ratios.

Climate data for each site were obtained from stations operated by the Australian Bureau of Meteorology (Table 7.1). For each locality, the mean annual precipitation (mm) and mean annual temperature (°C) were compiled from the stations nearest to the sample site.

Table 7.1: **Location and climate data of each sample site.**

Site	Species	Latitude	MAT (°C)	MAP (mm)
D'Aguilar National Park, QLD	*L. peroffskyana* ($n = 3$), *M. lucida* ($n = 6$), *M. macleayi* ($n = 3$)	27°S	19.8	1130
UWA Jandakot Reserve, WA	*M. riedlei* ($n = 41$)	32°S	18.2	791
Tilba Tilba, NSW	*M. communis* ($n = 47$)	36°S	15.7	997

7.3.2 Collection of cyanobacterial samples

Studies of cycads and their symbionts have often focused on plant specimens from greenhouses and botanical gardens, which may reflect a mixture of endogenous and locally-acquired symbionts. Additionally, isotopic studies based on such samples may be unintentionally affected by increased external fixed nitrogen availability. The cyanobacterial cycad symbionts analyzed in this study were previously isolated and characterized from coralloid roots of cycads growing in their natural habitats, without influence of agricultural fertilization (Gehringer et al., 2010). The eight isolates used in this study (Table 7.2) were kept in a nitrogen-free medium from isolation onwards to ensure the maintenance of their N_2-fixing

abilities. Stationary-phase liquid cultures were inoculated in duplicate into 120 mL N-free, BG110 medium in T175 (Sarstedt, Germany) culture flasks (Gehringer et al., 2010). Cultures were grown at 24°C with a 16:8 hour day:night cycle at 60 µmols photons m^{-2} s^{-1} under a daylight plant fluorescent growth lamp. One-month old cultures in late stationary phase were harvested by centrifugation in weighed, sterile 50 mL reagent tubes (Sarstedt, Germany) and washed twice with sterile distilled water. The pellets were freeze-dried and the dry weight was determined prior to isotopic analysis of the biomass.

Table 7.2: **Diazotrophic cyanobacterial symbiont strains isolated from coralloid roots of their respective host cycad species, taken from Gehringer et al., (2010).**

Symbiont	# of cultures	Cycad	Location	Voucher no.
Nostoc sp. 40.5	2	*M. communis*	Currambene	MZ40
Calothrix sp. 61.4	2	*M. parcifolia*	Seaview Range	PIF3107
Nostoc sp. 62.1	2	*M. mountperiensis*	Brooweena	PIF9343
Nostoc sp. 65.1	2	*M. riedlei*	NW Narrogin	PIF30395
Nostoc sp. 73.1	3	*M. serpentina*	Mt. Slopeway	PIF12273A
Nostoc sp. 74.5	1	*M. macleayi*	Mt. Colosseum	PIF12248
Nostoc sp. B1.3	2	*B. serrulata*	Byfield	PIF32324
Nostoc sp. C1.8	1	*C. media*	Botanic Gardens	C1

7.3.3 Isotopic analyses

Isotopic analyses ($\delta^{15}N$, $\delta^{13}C$) of plant material were carried out following published protocols (*e.g.*, Stüeken et al., 2015; Kipp et al., 2018) in IsoLab at the Department of Earth & Space Sciences, University of Washington with a Costech ECS 4010 Elemental Analyzer (EA) coupled with a Conflo III to a ThermoFinnigan MAT253 isotope-ratio mass spectrometer (IRMS). Combustion was carried out with 10 mL O_2 at 1000°C and the resulting gases were then passed through a reduced copper column to consume excess O_2 and to reduce NO_x species to N_2. A magnesium perchlorate trap was used to remove water from the

gas stream. Isotopic measurements were calibrated against three in-house standards (two glutamic acids "GA1" and "GA2," and dried salmon "SA") that have been calibrated to international reference materials USGS-40 and USGS-41. An aliquot of the Neoarchean Mt. McRae shale ("UW-McRae") was also analyzed as a test for long-term precision. All isotopic data are reported in delta notation relative to air for nitrogen and Vienna Pee Dee Belemnite (V-PDB) for carbon.

Analytical blanks were monitored and subtracted from nitrogen data; blanks were negligible for carbon measurements. Average analytical accuracy of $\delta^{15}N$ among individual runs based on in-house standard "GA1" was -0.02 ± 0.04‰. Accuracy of $\delta^{13}C$ measurements based on in-house standard "SA" was -0.02 ± 0.10‰. The average analytical precision (1σ) among all runs based on in-house standard "UW-McRae" was 0.3‰ for $\delta^{15}N$ and 0.4‰ for $\delta^{13}C$. Most cycad samples were analyzed at least twice, with an average standard deviation between sample replicates of 0.2‰ for $\delta^{15}N$ and 0.1‰ for $\delta^{13}C$.

Isotopic analyses of cultured cyanobacteria were carried out at the University of St Andrews, Scotland. Dry biomass was weighed into 8×5 mm tin capsules (ThermoFisher) and analyzed by flash combustion with an Isolink EA coupled with a Conflo IV to a MAT253 IRMS (ThermoFinnigan). The combustion reactor was packed with tungstic oxide as an additional combustion aid, followed by copper wire to consume excess O_2 and to convert NO_x species to N_2. The temperature was set to 1020°C and pure O_2 gas was injected at a flow rate of 250 mL/min for 5 seconds from the drop of the sample. Water generated during the combustion was trapped with magnesium perchlorate at room temperature. The measured isotopic ratios were calibrated to the air scale with USGS-40 and USGS-41, which were analyzed four times during the run. Analytical accuracy was monitored with the international reference material SGR-1 (untreated), for which a value of 17.4 ± 0.3‰ was obtained for $\delta^{15}N$ in good agreement with previous studies (Dennen et al., 2006).

7.3.4 Statistical analyses

Paired comparisons between sample groups were performed using either t-tests (when data adhered to a normal distribution as determined by $p > 0.05$ in a Shapiro-Wilk normality test) or the Mann-Whitney test. Levene's test was used to assess the difference in variance of $\delta^{15}N$ between cycads and non-cycads growing in the same habitats. Linear and logarithmic regression were used to explore correlations between variables. All statistical analyses were conducted in the R Statistical Computing Environment (R Core Team, 2013).

7.4 Results

We considered leaves individually for statistical analyses instead of averaging $\delta^{15}N$ values for whole plants (except where noted otherwise) because this captures more isotopic variability, and therefore should be more conservative in our attempt to demonstrate the isotopic consistency of cycad foliage. Furthermore, this approach is a more directly applicable calibration for analysis of fossilized cycad foliage, which will rely on sub-sampling of disarticulated fronds (which may be sparsely preserved) and where whole-plant averages are unlikely to be obtainable. In any case, we found that this treatment does not influence the observed statistical relationships; all statistical tests yield the same inference when binning data per-plant versus per-leaf.

The average $\delta^{15}N$ value of all cycad leaves analyzed in this study is -0.9 ± 0.8‰ (n = 128; here and throughout the text mean values are reported at ±1σ). The mean $\delta^{15}N$ value of all living cycad foliage (*i.e.*, excluding dead leaves) is -0.8 ± 0.8‰ ($n = 105$), with a range from -2.2‰ to +0.9‰. The mean $\delta^{15}N$ value of living foliage from New South Wales (-1.1 ± 0.7‰, $n = 34$) is statistically indistinguishable from that of Queensland specimens (-1.0 ± 0.8‰, $n = 30$), but both localities are slightly lighter than the specimens from Western Australia (-0.5 ± 0.8‰, $n = 51$) ($p = 0.01$, p = 6e-5, two-tailed t-tests). The average $\delta^{15}N$ values of all foliage from individual species are as follows: *Macrozamia communis* (-1.1 ± 0.7‰, $n = 47$), *M. riedlei* (-0.5 ± 0.8‰, $n = 51$), *M. macleayi* (-0.4 ± 0.4‰, $n = 10$),

M. lucida (-2.0 ± 0.3‰, $n = 10$), *Lepidozamia peroffskyana* (-0.7 ± 0.5‰, $n = 10$). In the Western Australia samples, male plants have an average δ^{15}N value of -0.6 ± 0.7‰ ($n = 35$), which is statistically indistinguishable ($p = 0.2$, two-tailed t-test) from female counterparts with a mean of -0.3 ± 0.9‰ ($n = 16$).

Intra-plant δ^{15}N values from a single sub-sampled frond range from -2.2‰ to 0.1‰ ($n = 19$; Fig. 7.1). Nitrogen isotope ratios within this frond inversely correlate with δ^{13}C values ($p = 8e\text{-}6$, $R^2 = 0.69$, linear regression) and C/N ratios ($p = 5e\text{-}7$, $R^2 = 0.77$, linear regression). A sampling transect of a single leaf on the same frond revealed a strong correlation between distance from the stem and δ^{15}N ($p = 9e\text{-}6$, $R^2 = 0.86$, logarithmic regression), δ^{13}C ($p = 5e\text{-}9$, $R^2 = 0.97$, logarithmic regression), C/N ($p = 9e\text{-}7$, $R^2 = 0.91$, logarithmic regression) and TN ($p = 7e\text{-}7$, $R^2 = 0.92$, logarithmic regression) (Fig. 7.2).

Across the Western Australia and New South Wales samples, young leaves have an average δ^{15}N value of -0.5 ± 0.8‰ ($n = 30$), which is slightly heavier than old leaves (-0.9 ± 0.6‰, $n = 45$) and dead leaves (-1.0 ± 0.9‰, $n = 23$) ($p = 0.03$, two-tailed t-test and Mann-Whitney test, respectively). In young leaves, δ^{15}N values do not correlate with C/N ratios ($p = 0.1$, $R^2 = 0.05$) whereas old leaves ($p = 2e\text{-}6$, $R^2 = 0.42$) and dead leaves ($p = 0.03$, $R^2 = 0.19$) show weak, negative correlations (Fig. 7.3). Among the Australian sites, foliar δ^{15}N values do not correlate with mean annual temperature (MAT) ($p = 0.2$) or mean annual precipitation (MAP) ($p = 0.6$).

The average δ^{13}C value of all cycad leaves analyzed in this study is -26.3 ± 1.8‰ ($n = 128$). The mean δ^{13}C values of living foliage at each site are -25.2 ± 1.1‰, -26.0 ± 0.9‰, and -28.6 ± 1.6‰ for New South Wales, Western Australia, and Queensland, respectively. Among individual species, δ^{13}C values are: *Macrozamia communis* (-25.2 ± 1.1‰, $n = 47$), *M. riedlei* (-26.0 ± 0.9‰, $n = 51$), *M. macleayi* (-28.9 ± 1.7‰, $n = 10$), *M. lucida* (-29.2 ± 1.8‰, $n = 10$), *Lepidozamia peroffskyana* (-27.9 ± 1.0‰, $n = 10$). Male (-26.1 ± 0.9‰, $n = 35$) and female (-25.9 ± 0.8‰, $n = 16$) plants from Western Australia (*M. riedlei*) do not significantly differ in δ^{13}C values ($p = 0.2$, Mann-Whitney test). The mean δ^{13}C value of old leaves from Western Australia and New South Wales (-26.1 ± 0.9‰; $n = 45$) is slightly

lighter than that of young leaves (-25.2 ± 1.1‰, n = 30) and dead leaves (-25.3 ± 1.0‰, n = 23) (p = 0.003, Mann-Whitney test). C/N ratios do not correlate with leaf maturity, with young (C/N = 38.0 ± 6.6, n = 30), old (C/N = 38.6 ± 9.5, n = 45) and dead (C/N = 37.8 ± 8.3, n = 23) leaves all statistically indistinguishable from each other (p = 0.5, Mann-Whitney test).

The average δ^{15}N value of all cultures of isolated cyanobacteria in this study is -0.8 ± 1.5‰ (n = 15), with no significant difference (p = 0.6) between *Nostoc* (-0.8 ± 1.6‰, n = 13) and *Calothrix* (-0.5 ± 0.5‰, n = 2) symbionts. The mean δ^{15}N values of reference plant leaves at individual sites are -0.9 ± 2.6‰ (n = 40, range -4.9‰ to +5.3‰) in New South Wales and -0.8 ± 1.8‰ (n = 63, range -4.3‰ to +3.3‰) in Queensland. At both sites, the mean δ^{15}N value of cycads does not significantly differ from non-cycads (p = 0.4, p = 0.5, Mann-Whitney tests). However, the δ^{15}N values of non-cycads show a larger variance than those of cycads at both New South Wales (p = 2e-7; Levene's test) and Queensland (p = 0.002, Levene's test).

7.5 Discussion

7.5.1 Isotopic effect of N_2 fixation by symbiotic cyanobacteria

We analyzed isolated cyanobacteria from various species of natural cycad populations (Table 7.2). These isolated cyanobionts were cultured in nitrogen-free media to observe the isotopic fractionation during N_2 fixation. The cultures had a mean δ^{15}N value of -0.8 ± 1.5‰ (n = 15), with no statistical difference (p = 0.6) between *Nostoc* (-0.8 ± 1.6‰, n = 13) and *Calothrix* (-0.5 ± 0.5‰, n = 2) cyanobionts. This range of δ^{15}N values is best explained by reliance on molybdenum-nitrogenase for N_2 fixation by the cyanobionts (Zhang et al., 2014); growth in nitrogen-free media should have enabled the expression of alternative nitrogenases as N_2 fixation proceeded.

We take these data to indicate that alternative nitrogenases do not play a significant role in N_2 fixation by cyanobionts in cycads. While a more detailed characterization of

the molecular mechanism of N_2 fixation by cyanobionts in coralloid roots in the field would support this inference, for the purposes of this investigation we are mainly concerned with the net isotopic effect of symbiotic N_2 fixation. By measuring this value *in vitro* and observing a similar range of $\delta^{15}N$ values to that seen in other laboratory studies of N_2-fixing cyanobacteria using molybdenum-nitrogenase (*e.g.*, Carpenter et al., 1997; Zerkle et al., 2008; Zhang et al., 2014), we show that the supply of nitrogen from symbiont to host is likely within 1-2‰ of the atmospheric $\delta^{15}N$ value. This range thus imposes a limit on the precision of reconstructions of atmospheric $\delta^{15}N$ in deep time using cycad foliage, as changes of <1‰ in the $\delta^{15}N$ value of atmospheric N_2 would be difficult to resolve.

7.5.2 Isotopic fractionation during intra-plant nitrogen transport

Next we consider the detailed sub-sampling of a mature frond on a *M. riedlei* specimen from the WA sample site (Fig. 7.1) to determine whether point-sampling of foliage provides a reasonable estimate of the bulk-frond $\delta^{15}N$ value. We found moderate variation (∼2‰) in $\delta^{15}N$ across the entire frond, which followed coherent trends when plotted alongside $\delta^{13}C$, C/N and total nitrogen (TN) as a function of distance from attachment to the stem (Fig. 7.2). Since the $\delta^{15}N$ variability closely follows a change in C/N ratio, we hypothesize that the isotopic offset is due to different stoichiometry in foliage distal to versus adjacent to stems. Namely, a higher protein content in leaves (which is expected due to the high concentration of photosynthetic enzymes; Sterner & Elser, 2002) than in stems (which are relatively more enriched in structural compounds, namely cellulose and lignin) would explain lower C/N ratios and higher TN in the distal portions of the leaves, as we observed (Fig. 7.2). Furthermore, protein is typically slightly enriched in ^{15}N relative to bulk biomass (Macko et al., 1987), meaning that this increase in protein abundance could also explain the $\delta^{15}N$ trend.

Regardless of the precise mechanisms underlying the isotopic variability, the relevant question for our proxy calibration is whether sampling of foliage generates a reliable estimate of whole-plant $\delta^{15}N$. We addressed this question by calculating a weighted-mean $\delta^{15}N$, $\delta^{13}C$ and C/N value for the sub-sampled frond and evaluating whether each point-sample fell

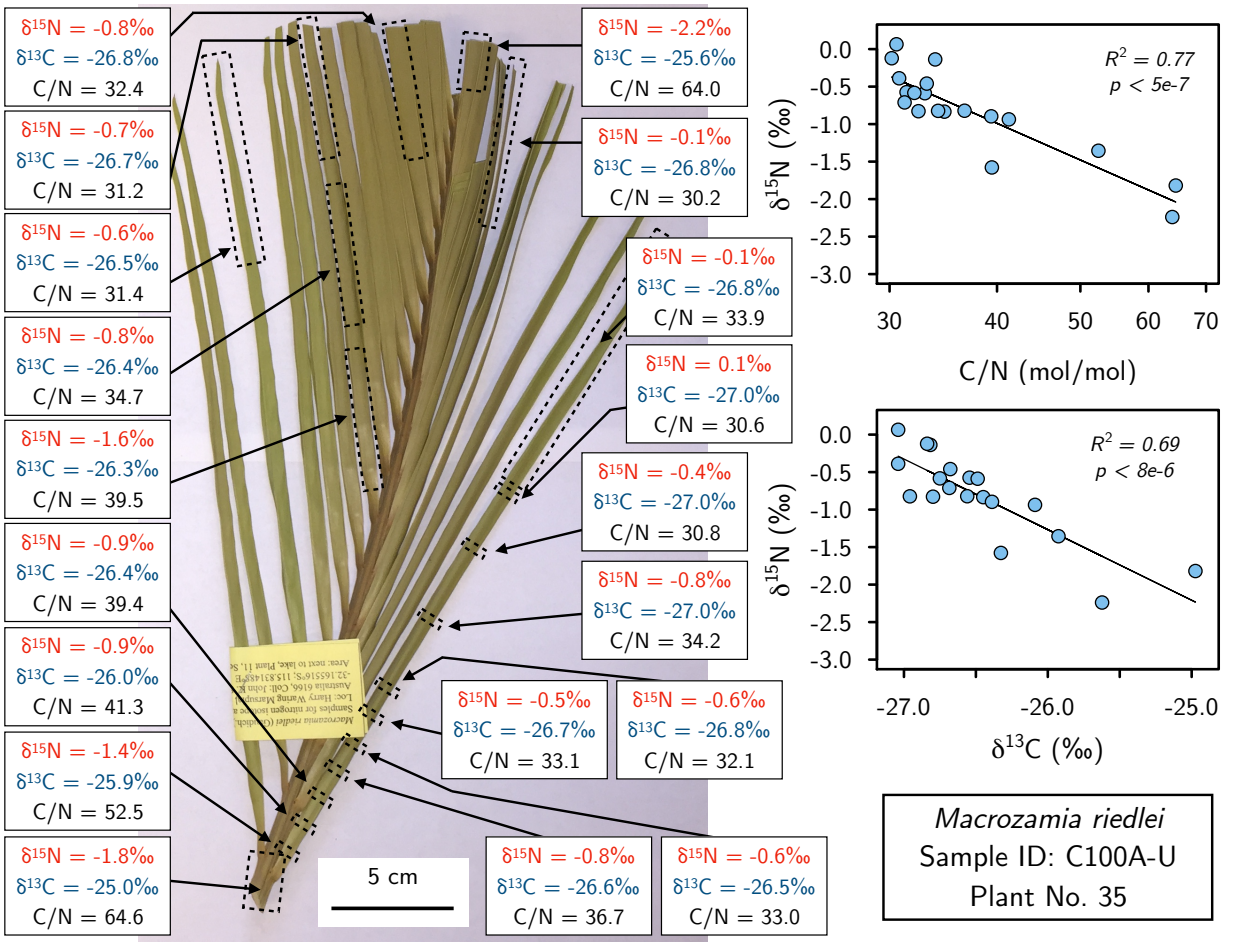

Figure 7.1: **Intra-plant variability in $\delta^{15}N$, $\delta^{13}C$ and C/N ratios.** Relative to leaves, stems are slightly isotopically depleted in carbon and nitrogen and have higher C/N ratios. However, all point-samples on the frond have $\delta^{15}N$ values within the range observed during N_2 fixation by isolated cyanobionts, suggesting minor isotopic fractionation during transport of nitrogen within the plant.

within the 1σ uncertainty interval of the weighted-mean value. We found that while sampling directly at the stem, or potentially at the very distal terminus of the leaf, could yield $\delta^{15}N$ values that are not representative of the bulk-frond (Fig. 7.2), it is easily achievable to collect foliage samples that have representative $\delta^{15}N$ values. This can be done by either targeting the middle of the leaves, or more thoroughly, by homogenizing 5-10 cm of leaf material (as was done for the rest of our dataset). We favor the latter option, and conclude that homogenization of leaf material provides an accurate assessment of the $\delta^{15}N$ value of cycad fronds. With regard to nitrogen isotopic measurements on fossilized cycad foliage, sampling of multiple discrete leaves should provide a fairly accurate assessment of the bulk-frond $\delta^{15}N$ value.

The last component of intra-plant isotopic fractionation is the offset due to transport from symbiont to host. We did not directly constrain this value in our study, since we conducted a separate microbial incubation and intra-plant sampling regime. However, given that the isotopic fractionation during N_2 fixation in vitro by the isolated cyanobacteria (-0.8 ± 1.5‰) entirely overlaps with the observed data for whole-frond $\delta^{15}N$ values, we estimate that there is minimal isotopic fractionation during transport of nitrogen from symbiont to host.

A possible reason for this lack of fractionation is that the cyanobionts in coralloid roots have glutamine synthetase (GS) activity similar to free-living cyanobacteria (Lindblad & Bergman, 1986). This marks the cycads as unique among plants with microbial N_2-fixing symbioses (Vessey et al., 2005), as others suppress the GS activity of their symbionts, causing nitrogen to be transported from symbiont to host as NH_3. Loss of NH_3 from root nodules could potentially explain the observed isotopic enrichment of legume roots relative to shoots (*e.g.*, Wanek & Arndt, 2002). In contrast, since cycads receive nitrogen in the form of glutamine or citrulline (Pate et al., 1988), the transmission of nitrogen from symbiont to host may be more efficient, or less prone to isotopic fractionation. Additionally, the persistence of cyanobionts in the interstitial tissue of the coralloid root structures could enable efficient nitrogen transport to neighboring cycad tissue, perhaps also leading to a smaller isotopic

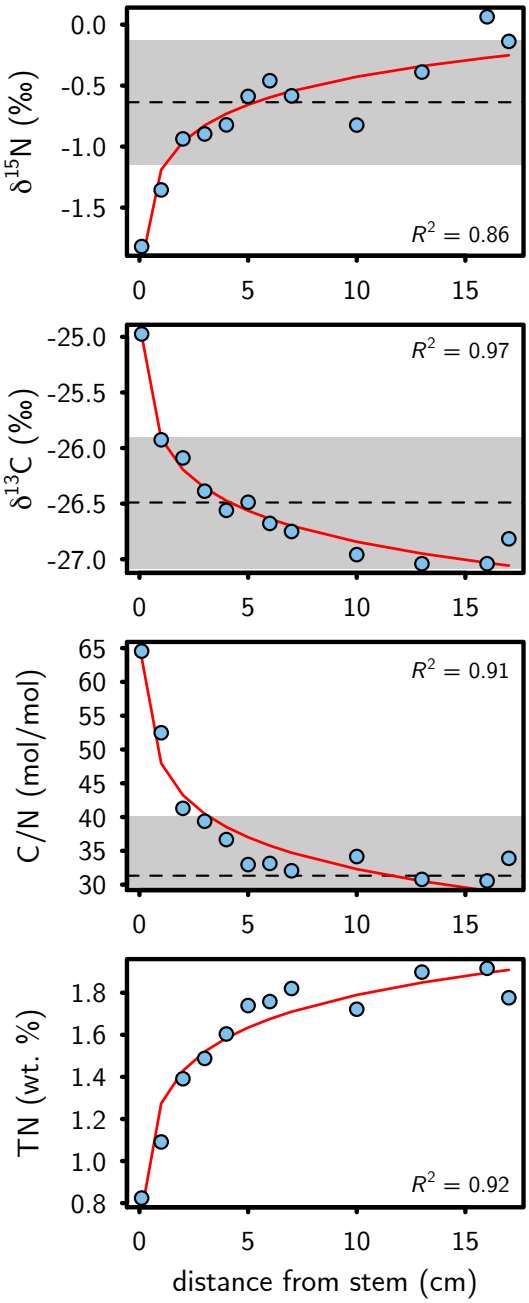

Figure 7.2: **Trends in (a) δ^{15}N, (b) δ^{13}C, (c) C/N and (d) TN along a transect of a single leaf.** Leaf sampling transect is pictured on the bottom right of the frond in Fig. 7.1. Fitted curves denote logarithmic regression. Dotted lines denote the leaf-averaged value for the parameter being plotted; grey shaded region denotes 1σconfidence interval. The higher nitrogen content and isotopic depletion away from stems may reflect an increasing proportion of protein relative to structural material.

fractionation than that observed between root nodules and shoots in legumes.

In any case, we take the cyanobacterial culture data and intra-plant data as evidence that nitrogen isotopic fractionation within the cycad-cyanobacteria symbiosis is fairly small. If accounted for by proper sampling of foliage, intra-plant isotopic variability should introduce less uncertainty into reconstructions of atmospheric $\delta^{15}N$ than the small isotopic fractionation imparted during microbial N_2 fixation.

7.5.3 Effects of life stage, sex and environment on foliar $\delta^{15}N$

We considered leaves of different ages (young vs. old vs. dead) to determine whether ontogeny or early degradational processes could influence $\delta^{15}N$ in cycad foliage. We found that $\delta^{15}N$ values were slightly higher in young leaves than in old and dead leaves. This would be consistent with the stoichiometric control on intra-plant $\delta^{15}N$ variability if young leaves have proportionally more protein than structural material, with a greater investment in vascular tissue coming with leaf maturation. This inference is further supported by the relationship between $\delta^{15}N$ and C/N, where young leaves show no correlation but old and dead leaves show negative correlations between foliar $\delta^{15}N$ values and C/N ratios (Fig. 7.3). Regardless of the precise mechanism, the isotopic offsets across these groups are small (<1‰) and all fall within the range of $\delta^{15}N$ values observed during N_2 fixation by the cyanobionts in vitro, suggesting that these effects should not interfere with cycads' ability to record the $\delta^{15}N$ of atmospheric N_2 in their foliage, even after early decomposition of leaf material.

Next, we considered whether sex-specific differences in nutrient utilization could influence foliar $\delta^{15}N$ values. This was motivated by the findings of Krieg et al. (2017), who studied cycads grown in a botanical garden to investigate differences in nutrient acquisition between male and female plants. Across their entire dataset, they found that males on average had slightly higher $\delta^{15}N$ values (+0.9‰) than females (+0.4‰) (Krieg et al., 2017). This difference was attributed to a greater reliance on cyanobacterial N_2 fixation in female cycads than in males. However, the trend was only found to be significant within the species *Cycas micronesica*; no other species (from the genera *Cycas* and *Zamia*) differed in foliar

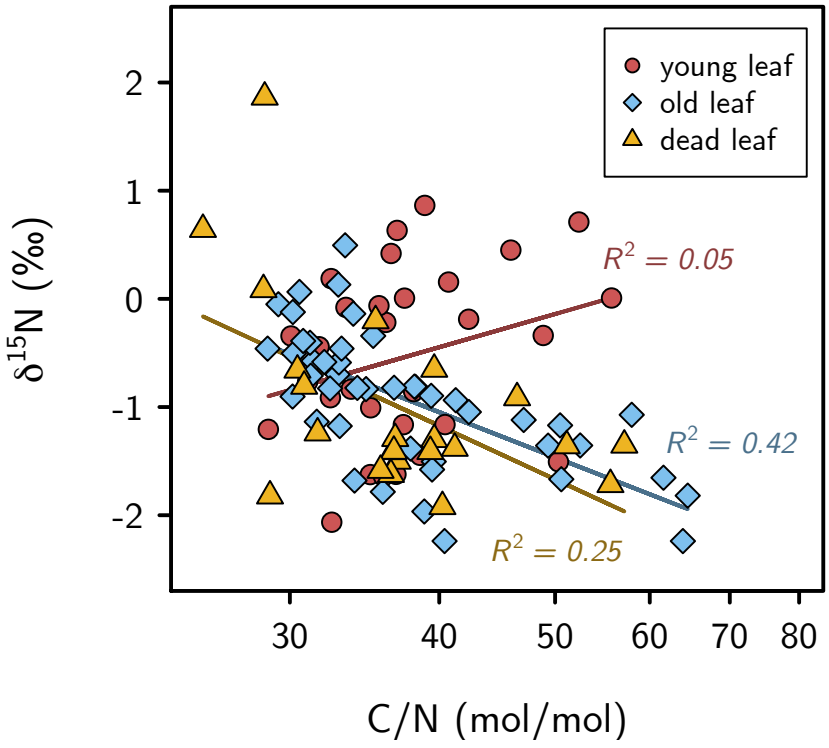

Figure 7.3: **Relationship between δ^{15}N and C/N ratios in modern cycad leaves.** Note log scale on x-axis. Includes samples from New South Wales and Western Australia from this study. Young leaves show no significant correlation between log(C/N) and δ^{15}N values ($p > 0.1$). Old and dead leaves show weak, negative correlations ($p < 10^{-5}$; $p < 0.01$). The grey band marks the typical range of δ^{15}N values generated via N_2-fixation in free-living cyanobacteria (Zhang et al., 2014).

$\delta^{15}N$ values between sexes. The *M. riedlei* samples in this study did not differ in foliar $\delta^{15}N$ values between sexes, similar to most of the species previously explored for sex-specific differences. This suggests that sex-specific differences in nutrient acquisition are not prevalent in wild populations of Macrozamia, and the similarity to many botanical garden specimens might indicate that this is a broader trend among cycads. Furthermore, even in the botanical garden specimens, the observed $\delta^{15}N$ values of both males and females fall within the range expected for N_2 fixation by cyanobionts. We therefore conclude that sex does not interfere with the ability of cycads to record the $\delta^{15}N$ of atmospheric N_2 in their foliage.

Beyond biological factors, we considered whether environmental conditions could influence cycad $\delta^{15}N$ values. For instance, environmental parameters such as MAT and MAP correlate with foliar $\delta^{15}N$ values in recent global compilations of broad plant populations (Amundson et al., 2003; Craine et al., 2009), with foliar $\delta^{15}N$ values increasing at higher MAT and lower MAP (Craine et al., 2009). These trends are thought to be related to changes in the isotopic composition of nitrogen in soils and therefore should not be observed in plants that always rely on a supply of nitrogen from symbiotic $_2$-fixing bacteria. Thus, to a first order it is notable that cycads display no correlation between foliar $\delta^{15}N$ values and MAT ($p = 0.2$) or MAP ($p = 0.6$). However, with only three sample sites this inference is necessarily based on limited climatic coverage. More importantly, while slight isotopic differences are observed among sites (Western Australia is slightly heavier than New South Wales and Queensland), foliar $\delta^{15}N$ values of cycads at all sites are tightly clustered within the range seen during N_2 fixation by the isolated cyanobionts. Interestingly, the global foliar $\delta^{15}N$ compilation by Craine et al. (2009) showed that N_2-fixing plants have a larger range in $\delta^{15}N$ values at higher MAT. This was not observed in our dataset, although our sites only spanned a limited range of MAT (15-20°C). Put most simply, our initial survey suggests that climatic gradients (as manifest in the observed differences in MAT and MAP) do not seem to influence the foliar $\delta^{15}N$ values of these wild cycad populations.

7.5.4 Foliar $\delta^{15}N$ values of cycads and non-N_2-fixing plants

Taking into account the findings described above, we then consider the foliar $\delta^{15}N$ values of cycads and non-N_2-fixing reference plants from our different sites. The early work of Yoneyama et al. (1993) and Pate & Unkovich (1999) demonstrated that foliar $\delta^{15}N$ values can effectively identify N_2 fixation in wild cycads at field sites in Thailand and Western Australia, respectively, through comparison of cycad foliage with non-N_2-fixing reference plants. They found that cycads consistently had near-zero foliar $\delta^{15}N$ values while other plants had more elevated $\delta^{15}N$ values. More recently, Álvarez-Yépiz et al. (2014) showed that cycads (Dioon sonorense) in the Sonora region of Mexico also have foliar $\delta^{15}N$ values that are consistent with N_2 fixation; however, they did not measure $\delta^{15}N$ values in non-N_2-fixing reference plants. We sought to extend these findings to other sites and with larger datasets. First considering our cycad data from the UWA Jandakot Reserve in Western Australia, the $\delta^{15}N$ values obtained in this study (-0.5 ± 0.8‰) agree well with previous work in the region (Pate & Unkovich, 1999) and are thus consistent with a substantial reliance of these cycads on N_2 fixation.

We then consider the Queensland and New South Wales sites, which differ in that they have more nutrient-rich soils (∼10% organic carbon by dry weight instead of 1-2% typical of Banksia woodland and <1% typical of sandplain heath in Western Australia; Foulds, 1993; Bui & Henderson, 2013). At both of these localities, foliar $\delta^{15}N$ values in cycads (-1.3 ± 0.7‰ QLD; -1.1 ± 0.7‰ NSW) also fall near-zero and within the range seen in pure cultures of the isolated cyanobionts, suggesting a consistent reliance on microbial N_2 fixation across these different habitats. However, a survey of a wide variety of non-N_2-fixing reference plants at each site showed similar mean foliar $\delta^{15}N$ values (-0.8 ± 1.8‰ QLD; -0.9 ± 2.6‰ NSW) albeit with a significantly larger variance in both cases (Fig. 7.4). In contrast to field studies of legumes, which can target non-N_2-fixing reference plants of close taxonomic affinity (occasionally even non-nodulating legume species), the paucity of gymnosperms makes selection of reference plants for cycads a bit more difficult. Two

coniferous gymnosperms (*Araucaria cunninghamii* and *Podocarpus elatus*) present at the Queensland site had foliar $\delta^{15}N$ values of +1.4‰ and +2.3‰, respectively, which are >2‰ heavier than co-occurring cycads. With only two specimens, though, a statistical comparison to the cycad population is not feasible. We therefore considered a wide variety of non-N_2-fixing plants, within which we did not observe any systematic bias in foliar $\delta^{15}N$ values. At both sites, monocots and dicots had statistically indistinguishable $\delta^{15}N$values ($p = 0.5$ QLD; $p = 0.9$ NSW) and many of the sampled leaves had $\delta^{15}N$ values that overlapped with the range seen in cycads.

The similarity in mean $\delta^{15}N$ values between cycads and non-N_2-fixing reference plants precludes a quantitative assessment of N_2 fixation by cycads at these sites. However, this does not mean that cycads are not strongly reliant on symbiotic N_2 fixation in these settings. If anything, the greater variance in foliar $\delta^{15}N$ values of reference plants seems indicative of isotopically variable soil pools, which cycads are not accessing. Furthermore, the narrow range of foliar $\delta^{15}N$ values in cycads at all of our sites – as well as all other sites studied to date (*e.g.*, Yoneyama et al., 1993; Pate & Unkovich, 1999; Álvarez-Yépiz et al., 2014) – is suggestive of a consistently high reliance on symbiotic N_2 fixation for their nitrogen demand. The occurrence of similar $\delta^{15}N$ values in non-N_2-fixing plants at these sites could even be related to N_2 fixation in the cycad-cyanobacterial symbiosis, since it has been determined that cycads can constitute a substantial input of nitrogen to their habitat (*e.g.*, Halliday & Pate, 1976). Additionally, surveys of cyanobacterial diversity in the rhizosphere in cycad habitats have found that N_2-fixing cyanobacteria are often present and active (Cuddy et al., 2012), suggesting that plants without explicit N_2-fixing symbioses could receive some nitrogen with an atmospheric $\delta^{15}N$ value. The relative impact of these mechanisms could be assessed with further study of $\delta^{15}N$ values in the roots, symbionts and leaves of cycads and non-N_2-fixing plants in a broader range of sites and species worldwide.

In any case, our results highlight a limitation of foliar $\delta^{15}N$ values as an N_2 fixation proxy. Distinct distributions of foliar $\delta^{15}N$ values in N_2-fixing versus non-N_2-fixing plants can provide strong evidence of microbial N_2 fixation, but absence of a difference does not

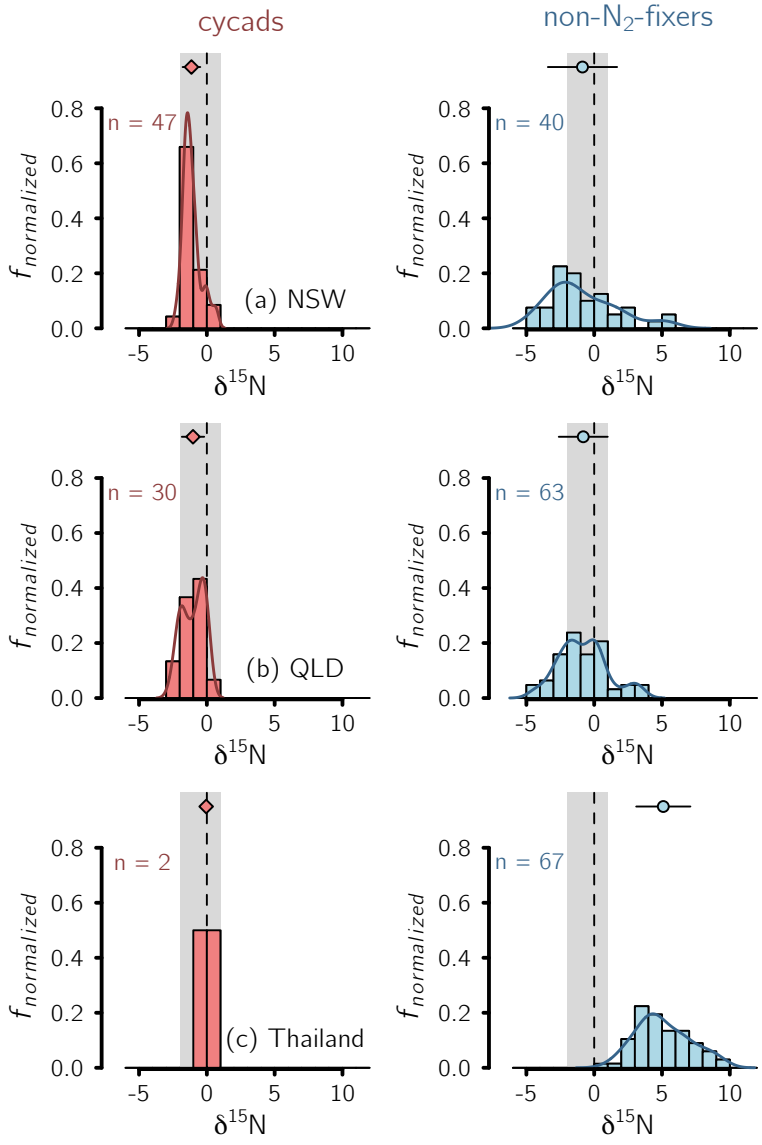

Figure 7.4: **Density distribution of δ^{15}N values in cycads and non-cycads from (a) New South Wales and (b) Queensland sampling sites, and (c) from Thailand (Yoneyama et al., 1993).** Grey shaded regions denote the typical range of δ^{15}N values generated via N_2 fixation in free-living cyanobacteria (Zhang et al., 2014). Dotted line denotes atmospheric δ^{15}N value. Circles mark mean δ^{15}N values $\pm 1\sigma$. Cycad foliage in all three settings has δ^{15}N values consistent with reliance on N_2 fixation. The similarity in mean δ^{15}N values between cycads and non-N_2-fixing reference plants in the Australian sites highlights a potential difficulty in unambiguously inferring N_2 fixation in ancient cycads; however, the larger variance in non-N_2-fixers is perhaps suggestive of assimilation of isotopically variable soil nitrogen.

provide evidence for absence of symbiosis. This limitation must be held in mind when applying the cycad $\delta^{15}N$ proxy to fossil assemblages in deep time.

7.5.5 Outlook for foliar $\delta^{15}N$ values as a proxy for $\delta^{15}N$ of atmospheric N_2 in deep time

Based on the data presented here, we consider that cycad foliage provides a reasonably robust archive of the nitrogen isotopic composition of atmospheric N_2 in modern environments. The isotopic fractionation associated with cyanobacterial N_2 fixation is small and the isotopic effect of nitrogen transport within cycads seems to even smaller. Sampling of homogenized leaf material provides adequate assessments of whole-frond $\delta^{15}N$, and foliar $\delta^{15}N$ values do not appear to vary across biological or environmental gradients.

This suggests that the nitrogen isotopic composition of carbonaceous cycad fossils – which are quite abundant through the Mesozoic and into the late Paleozoic (Taylor et al., 2009) – could provide a record of the $\delta^{15}N$ of atmospheric N_2 over the last 200-300 Myrs (Fig. 7.5). Some have proposed that pN_2 has remained quite constant throughout the last ∼600 Myrs (Berner, 2006), and so under such a model we would expect the $\delta^{15}N$ of atmospheric N_2 to be fairly stable (Fig. 7.5). However, if the atmosphere has been steadily losing nitrogen through the Phanerozoic (Johnson & Goldblatt, 2018), a monotonic trend would be expected (Fig. 7.5).

In addition to providing insight into these differing models of pN_2 through time, the application of this proxy to the fossil record would ground future deep-time applications of the $\delta^{15}N$ proxy by constraining the $\delta^{15}N$ of atmospheric N_2. Fixation of atmospheric N_2 is the initial input to the biogeochemical nitrogen cycle and widely assumed in isotope mass balance models (*e.g.*, Algeo et al., 2014; Kipp et al., 2018) to have maintained a constant isotopic ratio through geologic time.

Lastly, in addition to answering questions about the evolution of atmospheric N_2, the application of this proxy to the fossil record could provide insight into the longevity of the cycad-cyanobacterial symbiosis. Many N_2-fixing symbioses are thought to have fairly ancient origins (Sprent & Raven, 1992), but empirical evidence for their establishment in

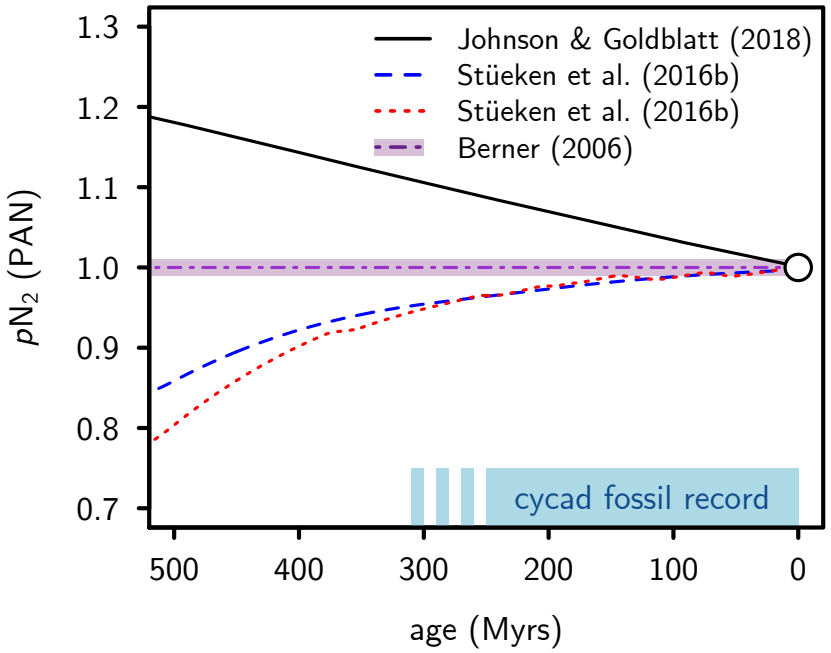

Figure 7.5: **Modeled evolution of pN_2 over the last 500 Myrs.** PAN = present atmospheric nitrogen, which is 0.79 bar. The model output of Johnson and Goldblatt (2018) has been increased by 0.02 PAN so that all models finish at exactly 1 PAN. Blue dotted line denotes base model of Stüeken et al. (2016b); red dotted line denotes model including variable mantle outgassing. Models disagree on whether pN_2 has increased, decreased, or remained constant over the Phanerozoic. Reconstructing the isotopic composition of N_2 over the last ~300 Myrs with fossilized cycad foliage could perhaps constrain the magnitude of changes during that interval.

antiquity is typically difficult to derive. While the occurrence of cyanobacterial symbiosis in all extant species of cycads is consistent with an ancestral origin, the current diversity of cycad species (within already existing genera) may have been largely generated in the last ∼12 Myrs (Nagalingum et al., 2011). Thus, it is perhaps the case that N_2 fixation has become an obligatory feature of cycad physiology only recently and was not prevalent early in cycad evolution. This would be evident if fossilized cycad leaves showed highly variable $\delta^{15}N$ values, in contrast to the narrow range observed in all modern environments studied to date. Therefore, in many ways, the nitrogen isotopic study of carbonaceous cycad fossils holds promise as a means to learn about nitrogen cycling in ancient environments.

7.6 Conclusions

We have conducted a survey of cycads in three environments across Australia to determine whether symbiotic N_2 fixation allows their foliage to accurately and consistently record the isotopic composition of atmospheric N_2. Cultured isolates of cyanobionts show fairly small and consistent isotopic offsets during N_2 fixation *in vitro* (-0.8 ± 1.5‰), and isotopic fractionations during transport within cycad tissues appear to be of smaller magnitude, with homogenized leaves providing accurate assessments of whole-frond $\delta^{15}N$. Furthermore, no biological or environmental factors caused foliar $\delta^{15}N$ values to fall outside of the range expected for cyanobacterial N_2 fixation. Therefore, cycad foliage seems to provide a robust archive of atmospheric $\delta^{15}N$ values. Application of this proxy to the fossil record should note that the measurement of $\delta^{15}N$ values in non-N_2-fixing reference plants can potentially corroborate the inference of N_2 fixation, but is unable to refute it. Thus, assembly of large datasets from various units will likely prove critical in generating a robust record of atmospheric $\delta^{15}N$ values over the last 200-300 Myrs.

7.7 References

Ader, M., Thomazo, C., Sansjofre, P., Busigny, V., Papineau, D., Laffont, R., Cartigny, P., Halverson, G.P., 2016. Interpretation of the nitrogen isotopic composition of Precam-

brian sedimentary rocks: Assumptions and perspectives. *Chem. Geol.* 429, 93–110.

Algeo, T.J., Meyers, P.A., Robinson, R.S., Rowe, H., Jiang, G.Q., 2014. Icehouse-greenhouse variations in marine denitrification. *Biogeosciences* 11, 1273–1295.

Álvarez-Yépiz, J.C., Cueva, A., Dovčiak, M., Teece, M., Yepez, E.A., 2014. Ontogenetic resource-use strategies in a rare long-lived cycad along environmental gradients. *Conserv. Physiol.* 2, 1–12.

Amundson, R., Austin, A.T., Schuur, E.A., Yoo, K., Matzek, V., Kendall, C., Uebersax, A., Brenner, D., Baisden, W.T., 2003. Global patterns of the isotopic composition of soil and plant nitrogen. *Glob. Biogeochem. Cycles* 17, 1031.

Awramik, S.M., Barghoorn, E.S., 1977. The Gunflint microbiota. *Precambrian Res.* 5, 121–142.

Bellenger, J.P., Xu, Y., Zhang, X., Morel, F.M.M., Kraepiel, A.M.L., 2014. Possible contribution of alternative nitrogenases to nitrogen fixation by asymbiotic N_2-fixing bacteria in soils. *Soil Biol. Biochem.* 69, 413–420.

Berner, R.A., 2006. Geological nitrogen cycle and atmospheric N_2 over Phanerozoic time. *Geology* 34, 413–415.

Boddey, R.M., Peoples, M.B., Palmer, B., Dart, P.J., 2000. Use of the ^{15}N natural abundance technique to quantify biological nitrogen fixation by woody perennials. *Nutr. Cycl. Agroecosystems* 57, 235–270.

Brandes, J.A., Devol, A.H., 2002. A global marine-fixed nitrogen isotopic budget: Implications for Holocene nitrogen cycling. *Glob. Biogeochem. Cycles* 16.

Brocks, J.J., Jarrett, A.J., Sirantoine, E., Hallmann, C., Hoshino, Y., Liyanage, T., 2017. The rise of algae in Cryogenian oceans and the emergence of animals. *Nature* 548, 578.

Brunner, B., Contreras, S., Lehmann, M.F., Matantseva, O., Rollog, M., Kalvelage, T., Klockgether, G., Lavik, G., Jetten, M.S., Kartal, B., others, 2013. Nitrogen isotope effects induced by anammox bacteria. *Proc. Natl. Acad. Sci.* 110, 18994–18999.

Bui, E.N., Henderson, B.L., 2013. C:N:P stoichiometry in Australian soils with respect to vegetation and environmental factors. *Plant Soil* 373, 553–568.

Busigny, V., Cartigny, P., Philippot, P., 2011. Nitrogen isotopes in ophiolitic metagabbros: A re-evaluation of modern nitrogen fluxes in subduction zones and implication for the early Earth atmosphere. *Geochim. Cosmochim. Acta* 75, 7502–7521.

Carpenter, E.J., Harvey, H.R., Fry, B., Capone, D.G., 1997. Biogeochemical tracers of the marine cyanobacterium Trichodesmium. *Deep Sea Res. Part Oceanogr. Res. Pap.* 44, 27–38.

Casciotti, K.L., 2009. Inverse kinetic isotope fractionation during bacterial nitrite oxidation. *Geochim. Cosmochim. Acta* 73, 2061–2076.

Chalk, P.M., Inácio, C.T., Balieiro, F.C., Rouws, J.R., 2016. Do techniques based on ^{15}N enrichment and ^{15}N natural abundance give consistent estimates of the symbiotic dependence of N_2-fixing plants? *Plant Soil* 399, 415–426.

Costa, J.-L., Lindblad, P., 2002. Cyanobacteria in symbiosis with cycads, in: *Cyanobacteria in Symbiosis*. Springer, pp. 195–205.

Craine, J.M., Elmore, A.J., Aidar, M.P.M., Bustamante, M., Dawson, T.E., Hobbie, E.A., Kahmen, A., Mack, M.C., McLauchlan, K.K., Michelsen, A., Nardoto, G.B., Pardo, L.H., Peñuelas, J., Reich, P.B., Schuur, E.A.G., Stock, W.D., Templer, P.H., Virginia, R.A., Welker, J.M., Wright, I.J., 2009. Global patterns of foliar nitrogen isotopes and their relationships with climate, mycorrhizal fungi, foliar nutrient concentrations, and nitrogen availability. *New Phytol.* 183, 980–992.

Craine, J.M., Elmore, A.J., Wang, L., Augusto, L., Baisden, W.T., Brookshire, E.N.J., Cramer, M.D., Hasselquist, N.J., Hobbie, E.A., Kahmen, A., 2015. Convergence of soil nitrogen isotopes across global climate gradients. *Sci. Rep.* 5, 8280.

Cuddy, W.S., Neilan, B.A., Gehringer, M.M., 2012. Comparative analysis of cyanobacteria in the rhizosphere and as endosymbionts of cycads in drought-affected soils. *FEMS Microbiol. Ecol.* 80, 204–215.

Dennen, K.O., Johnson, C.A., Otter, M.L., Silva, S.R., Wandless, G.A., 2006. $\delta^{15}N$ and non-carbonate $\delta^{13}C$ values for two petroleum source rock reference materials and a marine sediment reference material (Open File Report No. 2006–1071). USGS.

Devol, A.H., 2015. Denitrification, anammox, and N_2 production in marine sediments. Annu. Rev. Mar. Sci. 7, 403–423.

Dos Santos, P.C., Fang, Z., Mason, S.W., Setubal, J.C., Dixon, R., 2012. Distribution of nitrogen fixation and nitrogenase-like sequences amongst microbial genomes. *BMC Genomics* 13, 162.

Evans, R.D., 2007. Soil nitrogen isotope composition. *Stable Isot. Ecol. Environ. Sci.* 2, 83–98.

Foulds, W., 1993. Nutrient concentrations of foliage and soil in south-western Australia. *New Phytol.* 125, 529–546.

Freudenthal, T., Wagner, T., Wenzhöfer, F., Zabel, M., Wefer, G., 2001. Early diagenesis of organic matter from sediments of the eastern subtropical Atlantic: evidence from stable nitrogen and carbon isotopes. *Geochim. Cosmochim. Acta* 65, 1795–1808.

Gehringer, M.M., Pengelly, J.J., Cuddy, W.S., Fieker, C., Forster, P.I., Neilan, B.A., 2010. Host selection of symbiotic cyanobacteria in 31 species of the Australian cycad genus: *Macrozamia* (*Zamiaceae*). *Mol. Plant. Microbe Interact.* 23, 811–822.

Goldblatt, C., Claire, M.W., Lenton, T.M., Matthews, A.J., Watson, A.J., Zahnle, K.J., 2009. Nitrogen-enhanced greenhouse warming on early Earth. *Nat. Geosci.* 2, 891–896.

Golubic, S., Sergeev, V.N., Knoll, A.H., 1995. Mesoproterozoic *Archaeoellipsoides*: akinetes of heterocystous cyanobacteria. *Lethaia* 28, 285–298.

Goosmann, E.A., Catling, D.C., Som, S.M., Altermann, W., Buick, R., 2018. Eolianite Grain Size Distributions as a Proxy for Large Changes in Planetary Atmospheric Density. *J. Geophys. Res. Planets* 123, 2506–2526.

Gueneli, N., McKenna, A.M., Ohkouchi, N., Boreham, C.J., Beghin, J., Javaux, E.J., Brocks, J.J., 2018. 1.1-billion-year-old porphyrins establish a marine ecosystem dominated by bacterial primary producers. *Proc. Natl. Acad. Sci.* 115, E6978–E6986.

Halliday, J., Pate, J.S., 1976. Symbiotic nitrogen fixation by coralloid roots of the cycad *Macrozamia riedlei*: physiological characteristics and ecological significance. *Funct. Plant Biol.* 3, 349–358.

Handley, L.L., Raven, J.A., 1992. The use of natural abundance of nitrogen isotopes in plant physiology and ecology. *Plant Cell Environ.* 15, 965–985.

Hogberg, P., 1997. Tansley Review No. 95: ^{15}N natural abundance in soil–plant systems. *New Phytol.* 137, 179–203.

Johnson, B.W., Goldblatt, C., 2018. EarthN: A new Earth system nitrogen model. *Geochem. Geophys. Geosystems* 19, 2516–2542.

Kalvelage, T., Jensen, M.M., Contreras, S., Revsbech, N.P., Lam, P., Günter, M., LaRoche, J., Lavik, G., Kuypers, M.M.M., 2011. Oxygen Sensitivity of Anammox and Coupled N-Cycle Processes in Oxygen Minimum Zones. *PLOS ONE* 6, e29299.

Kavanagh, L., Goldblatt, C., 2015. Using raindrops to constrain past atmospheric density. *Earth Planet. Sci. Lett.* 413, 51–58.

Kipp, M.A., Stüeken, E.E., Yun, M., Bekker, A., Buick, R., 2018. Pervasive aerobic nitrogen cycling in the surface ocean across the Paleoproterozoic Era. *Earth Planet. Sci. Lett.* 500, 117–126.

Krieg, C., Watkins Jr, J.E., Chambers, S., Husby, C.E., 2017. Sex-specific differences in functional traits and resource acquisition in five cycad species. *AoB Plants* 9, plx013.

Kritee, K., Sigman, D.M., Granger, J., Ward, B.B., Jayakumar, A., Deutsch, C., 2012. Reduced isotope fractionation by denitrification under conditions relevant to the ocean. *Geochim. Cosmochim. Acta* 92, 243–259.

Leuenberger, M., Siegenthaler, U., Langway, C., 1992. Carbon isotope composition of atmospheric CO_2 during the last ice age from an Antarctic ice core. *Nature* 357, 488.

Lindblad, P., Bergman, B., 1986. Glutamine synthetase: Activity and localization in cyanobacteria of the cycads *Cycas revoluta* and *Zamia skinneri*. *Planta* 169, 1–7.

Macko, S.A., Fogel, M.L., Hare, P.E., Hoering, T.C., 1987. Isotopic fractionation of nitrogen and carbon in the synthesis of amino acids by microorganisms. *Chem. Geol. Isot. Geosci. Sect.* 65, 79–92.

Mallik, A., Li, Y., Wiedenbeck, M., 2018. Nitrogen evolution within the Earth's atmosphere–mantle system assessed by recycling in subduction zones. *Earth Planet. Sci.*

Lett. 482, 556–566.

Marino, B.D., McElroy, M.B., Salawitch, R.J., Spaulding, W.G., 1992. Glacial-to-interglacial variations in the carbon isotopic composition of atmospheric CO_2. *Nature* 357, 461.

Mariotti, A., 1983. Atmospheric nitrogen is a reliable standard for natural ^{15}N abundance measurements. *Nature* 303, 685–687.

Marty, B., Zimmermann, L., Pujol, M., Burgess, R., Philippot, P., 2013. Nitrogen isotopic composition and density of the Archean atmosphere. *Science* 342, 101–104.

Minagawa, M., Wada, E., 1986. Nitrogen isotope ratios of red tide organisms in the East China Sea: A characterization of biological nitrogen fixation. *Mar. Chem.* 19, 245–259.

Nagalingum, N.S., Marshall, C.R., Quental, T.B., Rai, H.S., Little, D.P., Mathews, S., 2011. Recent synchronous radiation of a living fossil. *Science* 334, 796–799.

Pang, K., Tang, Q., Chen, L., Wan, B., Niu, C., Yuan, X., Xiao, S., 2018. Nitrogen-fixing heterocystous cyanobacteria in the Tonian Period. *Curr. Biol.* 28, 616–622.

Pate, J.S., Lindblad, P., Atkins, C.A., 1988. Pathways of assimilation and transfer of fixed nitrogen in coralloid roots of cycad-*Nostoc* symbioses. *Planta* 176, 461–471.

Pate, J.S., Unkovich, M.J., 1999. Measuring symbiotic nitrogen fixation: case studies of natural and agricultural ecosystems in a Western Australian setting, in: Scholes, J.D., Barker, M.G. (Eds.), *Physiological Plant Ecology.* Blackwell Science, Oxford, pp. 153–173.

R Core Team, 2013. R: A language and environment for statistical computing. R Foundation for Statistical Computing.

Rasmussen, U., Nilsson, M., 2002. Cyanobacterial diversity and specificity in plant symbioses, in: Rai, A.N., Bergman, B., Rasmussen, U. (Eds.), *Cyanobacteria in Symbiosis.* Springer, Dordrecht, pp. 313–328.

Raven, J.A., 2002. Evolution of cyanobacterial symbioses, in: Rai, A.N., Bergman, B., Rasmussen, U. (Eds.),*Cyanobacteria in Symbiosis.* Springer, Dordrecht, pp. 329–346.

Robinson, R.S., Kienast, M., Luiza Albuquerque, A., Altabet, M., Contreras, S., De Pol Holz, R., Dubois, N., Francois, R., Galbraith, E., Hsu, T.-C., others, 2012. A review of

nitrogen isotopic alteration in marine sediments. *Paleoceanography* 27.

Shearer, G., Kohl, D.H., 1986. N2-fixation in field settings: Estimations based on natural ^{15}N abundance. *Funct. Plant Biol.* 13, 699–756.

Shearer, G., Kohl, D.H., Virginia, Ra., Bryan, B.A., Skeeters, J.L., Nilsen, E.T., Sharifi, M.R., Rundel, P.W., 1983. Estimates of N_2-fixation from variation in the natural abundance of ^{15}N in Sonoran Desert ecosystems. *Oecologia* 56, 365–373.

Sigman, D.M., Altabet, M.A., McCorkle, D.C., Francois, R., Fischer, G., 2000. The $\delta^{15}N$ of nitrate in the Southern Ocean: Nitrogen cycling and circulation in the ocean interior. *J. Geophys. Res. Oceans* 105, 19599–19614.

Silverman, S.N., Kopf, S.H., Bebout, B.M., Gordon, R., Som, S.M., 2019. Morphological and isotopic changes of heterocystous cyanobacteria in response to N_2 partial pressure. *Geobiology* 17, 60–75.

Som, S.M., Buick, R., Hagadorn, J.W., Blake, T.S., Perreault, J.M., Harnmeijer, J.P., Catling, D.C., 2016. Earth's air pressure 2.7 billion years ago constrained to less than half of modern levels. *Nat. Geosci.*

Som, S.M., Catling, D.C., Harnmeijer, J.P., Polivka, P.M., Buick, R., 2012. Air density 2.7 billion years ago limited to less than twice modern levels by fossil raindrop imprints. *Nature* 484, 359–362.

Sprent, J.I., Raven, J.A., 1992. Evolution of nitrogen-fixing symbioses. *Biol. Nitrogen Fixat.* 461–496.

Sterner, R.W., Elser, J.J., 2002. Ecological stoichiometry: The biology of elements from molecules to the biosphere. Princeton University Press.

Stüeken, E.E., Buick, R., Guy, B.M., Koehler, M.C., 2015. Isotopic evidence for biological nitrogen fixation by molybdenum-nitrogenase from 3.2 Gyr. *Nature* 520, 666–669.

Stüeken, Eva E., Kipp, M.A., Koehler, M.C., Buick, R., 2016. The evolution of Earth's biogeochemical nitrogen cycle. *Earth-Sci. Rev.* 160, 220–239.

Stüeken, E. E., Kipp, M.A., Koehler, M.C., Schwieterman, E.W., Johnson, B., Buick, R., 2016. Modeling pN_2 through Geological Time: Implications for Planetary Climates and

Atmospheric Biosignatures. *Astrobiology* 16, 949–963.

Taylor, E.L., Taylor, T.N., Krings, M., 2009. Paleobotany: The biology and evolution of fossil plants. Academic Press, Burlington, MA.

Unkovich, M.J., Pate, J.S., 2000. An appraisal of recent field measurements of symbiotic N_2 fixation by annual legumes. *Field Crops Res.* 65, 211–228.

Vessey, J.K., Pawlowski, K., Bergman, B., 2005. Root-based N_2-fixing symbioses: Legumes, actinorhizal plants, *Parasponia* sp. and cycads. *Plant Soil* 274, 51–78.

Wanek, W., Arndt, S.K., 2002. Difference in $\delta^{15}N$ signatures between nodulated roots and shoots of soybean is indicative of the contribution of symbiotic N_2 fixation to plant N. *J. Exp. Bot.* 53, 1109–1118.

Weiss, M.C., Sousa, F.L., Mrnjavac, N., Neukirchen, S., Roettger, M., Nelson-Sathi, S., Martin, W.F., 2016. The physiology and habitat of the last universal common ancestor. *Nat. Microbiol.* 1, 16116.

Werner, R.A., Schmidt, H.-L., 2002. The in vivo nitrogen isotope discrimination among organic plant compounds. *Phytochemistry* 61, 465–484.

Yoneyama, T., Muraoka, T., Murakami, T., Boonkerd, N., 1993. Natural abundance of ^{15}N in tropical plants with emphasis on tree legumes. *Plant Soil* 153, 295–304.

Zerkle, A.L., Junium, C.K., Canfield, D.E., House, C.H., 2008. Production of ^{15}N-depleted biomass during cyanobacterial N_2-fixation at high Fe concentrations. *J. Geophys. Res. Biogeosciences* 113, G03014.

Zerkle, A.L., Mikhail, S., 2017. The geobiological nitrogen cycle: from microbes to the mantle. *Geobiology* 15, 343–352.

Zhang, X., Sigman, D.M., Morel, F.M., Kraepiel, A.M., 2014. Nitrogen isotope fractionation by alternative nitrogenases and past ocean anoxia. *Proc. Natl. Acad. Sci.* 111, 4782–4787.

Zhifeng, G., Thomas, B.A., 1989. A review of fossil cycad megasporophylls, with new evidence of *Crossozamia* Pomel and its associated leaves from the Lower Permian of Taiyuan, China. *Rev. Palaeobot. Palynol.* 60, 205–223.

Chapter 8

NITROGEN ISOTOPES IN FOSSIL CYCADS RECORD A LATE ONSET OF NITROGEN-FIXING SYMBIOSIS

This manuscript is in preparation for submission to *Nature Ecology and Evolution*. Co-authors are Eva Stüeken, Caroline Strömberg and Roger Buick.

8.1 Introductory text

The cycads are an ancient clade of gymnosperms, sometimes referred to as "living fossils" due to their morphological similarity to their Mesozoic ancestors. While the cycads were dominant understory flora in the Mesozoic (Taylor et al., 2009), their abundance declined drastically in the Cenozoic, with extant cycads relegated to a narrow range of tropical and subtropical habitats. In addition to a decline in abundance, the cycads are also thought to have undergone rapid speciation in the later Cenozoic (Nagalingum et al., 2011). Many questions plague our understanding of this transition, including the role of a hallmark of cycad physiology: N_2 fixation. All extant cycads exist in symbiosis with N_2-fixing cyanobacteria, which reside in modified root structures and supply nitrogen to the cycads (Costa and Lindblad, 2002; Lindblad and Bergman, 1990). The universal occurrence of this symbiosis across the cycads is consistent with an ancient origin in the clade (Raven, 2002); however, the recognition of recent speciation (Nagalingum et al., 2011) and habitat contraction in the cycads may point instead to a recent population bottleneck as the explanation for this distribution of N_2-fixing capacity. Here we use nitrogen isotope ratios – a well-established proxy for studying N_2 fixation in modern plant systems (Robinson, 2001; Shearer and Kohl, 1986) – to probe the antiquity of the cycad-cyanobacterial symbiosis. We find that the organic leaf residues from ∼50 million-year-old cycads in the Eocene Chuckanut Formation show a nar-

row distribution of nitrogen isotope ratios that is consistent with cyanobacterial N_2 fixation, in contrast to other plants growing in the same habitat. However, older cycad assemblages show more positive and variable nitrogen isotope ratios, similar to other plants growing in their midst, suggesting that cycads did not obtain nitrogen via cyanobacterial symbionts in those settings. These results suggest that N_2-fixing symbiosis was not prevalent in cycads during the Mesozoic, but perhaps arose later due to their diminishing ecological role as angiosperms came to dominate understory settings and cycads were ousted to nutrient-poor habitats.

8.2 Main text

Nitrogen is an essential nutrient for all organisms. It can therefore play an important role in regulating the productivity of both marine and terrestrial ecosystems (Gruber and Galloway, 2008). However, despite its abundance at Earth's surface as atmospheric N_2, nitrogen is scarce in many habitats. This is because only relatively few prokaryotes (∼15% of phyla; Dos Santos et al., 2012) – and no eukaryotes – possess the metabolic capacity for splitting the N_2 molecule and forming bioavailable nitrogen (*i.e.*, "N_2 fixation"). Thus, nearly the entire supply of bioavailable nitrogen to the biosphere flows through these N_2-fixing prokaryotes.

Most plants obtain their nitrogen as nitrate (NO_3^-) or ammonium (NH_4^+) that is available for uptake from soil via roots due to the activity of prokaryotes that either fixed atmospheric N_2 into bioavailable form or liberated biomass-bound nitrogen for re-use. However, certain plants have forged direct symbiotic associations with bacteria that are capable of N_2 fixation. These include the nodulating legumes, actinorhizal plants, liverworts and hornworts, and the cycads, among others (Rai et al., 2000; Vessey et al., 2005). The ability of these plants to obtain nitrogen from atmospheric N_2 allows them to persist in low-nutrient soils (Halliday and Pate, 1976) or in the midst of other species that out-compete them for nitrogen in soil (Bond, 1989).

Given the ability of nitrogen to regulate biological productivity and set the ecological balance of terrestrial ecosystems, it follows that access to bioavailable nitrogen may have

played an important role in major evolutionary or ecological events in Earth's history. A case study of such a dynamic may be found in the cycads (Division: *Cycadophyta*), which are a far more ancient lineage than other plants with N_2-fixing symbioses and physiologically distinct in many respects.

First, cycads harbor cyanobacteria (primarily of the genera *Nostoc* and *Calothrix*; Rasmussen and Nilsson, 2002) as their symbionts, as opposed to the rhizobia hosted by legumes or *Frankia* hosted by actinorhizal plants (Vessey et al., 2005). Additionally, the symbiotic cyanobacteria reside directly within the cycads' modified subaerial to shallow subterranean root structures, known as coralloid roots (Costa and Lindblad, 2002), in contrast to the root nodules present in other symbioses (Vessey et al., 2005). Further, nitrogen is transported from cyanobacterial symbionts to cycad hosts in the form of amino acids (glutamine and citrulline; Pate et al., 1988), in contrast to ammonia (NH_3) that is the nitrogen transport substrate in other symbioses (Vessey et al., 2005). Lastly, active symbiosis with N_2-fixing cyanobacteria is observed in all extant cycad species (Costa and Lindblad, 2002; Lindblad and Bergman, 1990; Raven, 2002), unlike the patchy distributions in other clades, such as the legumes (Vessey et al., 2005).

For all of these reasons, it seems that N_2 fixation played an important role in the evolutionary ecology of the cycad lineage. Specifically, the occurrence of extant cycads in nutrient-poor soils, where their capacity for N_2 fixation enables their persistence (Halliday and Pate, 1976), stands in stark contrast to their dominance as understory flora in rich fossil assemblages from the Mesozoic (Taylor et al., 2009). This begs the question: did the cycad-cyanobacterial N_2-fixing symbiosis exist during the Mesozoic? The universal occurrence of N_2-fixing symbioses in extant cycads may imply such a scenario (Raven, 2002); however, this would contradict the observation in modern systems that N_2-fixation is a costly process only undertaken when necessary for survival in nutrient-scarce habitats (Rai et al., 2000; Vessey et al., 2005). On the other hand, if cycads did not forge symbioses with cyanobacteria in the Mesozoic, when did the symbiosis arise? Further, what environmental or ecological changes could have promoted such a strategy to be first adopted by cycads, and eventually become

universally distributed across the clade?

We set out to investigate the role of N_2 fixation in cycad evolution by utilizing a proxy that is well-studied in the modern environment: foliar nitrogen isotope ratios ($\delta^{15}N$). This proxy is derived from the observation that the foliage of plants obtaining nitrogen directly from N_2-fixing symbionts tends to be distinct from that of plants assimilating nitrogen from soil (Shearer and Kohl, 1986). Specifically, plants with N_2-fixing symbionts tend to have foliar $\delta^{15}N$ values near 0‰, which is the value of atmospheric N_2. Since the process of microbial N_2 fixation only slightly fractionates nitrogen isotopes (typically <2‰ relative to the N_2 source; Wada, 1980; Minagawa and Wada, 1986; Carpenter et al., 1997), plants with N_2-fixing symbionts tend to have foliar $\delta^{15}N$ values close to the atmospheric value (0‰). In contrast, bioavailable nitrogen (NO_3^- and NH_4^+) in soils tends to be isotopically variable, and often enriched relative to atmospheric N_2 by several permil (Craine et al., 2015; Shearer and Kohl, 1986) ($\delta^{15}N >> 0$‰). Thus, in a given habitat, N_2-fixing plants can be distinguished from non-N_2-fixing plants if the former have foliar $\delta^{15}N$ values near 0‰, while the latter have $\delta^{15}N$ values >> 0‰ (Shearer and Kohl, 1986).

While built on straightforward and sound logic, this proxy faces some limitations. First, isotopic fractionation during transport of nitrogen from symbiont to host can lead to elevated foliar $\delta^{15}N$ values in spite of active N_2 fixation (Evans, 2001). However, such a process has not been observed in cycads (Kipp et al., in review), perhaps due to the transport of nitrogen as amino acids instead of ammonia, the latter of which is more volatile and prone to leakage from the system with an accompanying isotopic fractionation.

Second, the facultative nature of microbial N_2 fixation means that plants may only periodically receive nitrogen from their symbionts, whereas at other times they assimilate nitrogen from the soil (Rai et al., 2000). Such oscillations would cause foliar $\delta^{15}N$ values to integrate the isotopic composition of the two pools (soil and atmospheric N_2), perhaps leading to elevated $\delta^{15}N$ values in spite of active N_2 fixation. All modern cycads studied to-date have $\delta^{15}N$ values that fall firmly within the range generated by microbial N_2 fixation (Kipp et al., in review; Álvarez-Yépiz et al., 2014; Pate and Unkovich, 1999; Yoneyama et al.,

1993), consistent with cycads in fact receiving most of their nitrogen from their symbionts. However, if aiming to identify N_2 fixation in deep time (as in the present study), it must be borne in mind that the $\delta^{15}N$ proxy is specifically tracking the physiological and ecological significance of N_2 fixation, not merely the capacity for N_2 fixation.

Lastly, in habitats with soil $\delta^{15}N$ values that are close to the atmospheric value (0‰), plants assimilating nitrogen from the soil will tend to have similar $\delta^{15}N$ values to plants that are receiving nitrogen from N_2-fixing symbionts (Shearer et al., 1983). Such data does not preclude the possibility that N_2 fixation is active, but rather makes the $\delta^{15}N$ proxy inconclusive in those cases (Kipp et al., in review).

With these limitations in mind, we applied this proxy to a large compilation ($n = 121$) of carbonaceous cycad fossils from a variety of localities worldwide spanning the late Paleozoic through Cenozoic. At four sites where specimens were available, we also analyzed fossilized foliage from other plants to constrain the integrated $\delta^{15}N$ value of plants receiving nitrogen from the soil.

The data reveal a large range of $\delta^{15}N$ values in ancient cycads (Fig. 8.1), often reaching higher values than are observed in modern cycads (-2.6 to +1.2‰; Álvarez-Yépiz et al., 2014; Kipp et al., in review; Pate and Unkovich, 1999; Yoneyama et al., 1993). To a first order, this suggests that cycads were not obtaining appreciable nitrogen from cyanobacterial symbionts in these settings, particularly throughout the Mesozoic, when they attained their maximum abundance and diversity. Furthermore, $\delta^{15}N$ values in fossilized cycads and other non-N_2-fixing plants from the same Mesozoic units are statistically unresolvable (Fig. 8.2A-C). This likely reflects the fact that cycads were obtaining nitrogen from the same soil pool(s) as other plants growing in their midst.

In contrast to the Mesozoic data, cycads (genus: *Dioon*) from the ∼50 Ma Chuckanut Formation have foliar $\delta^{15}N$ values (mean +0.3 ± 0.7, $n = 20$; Fig. 8.2D) similar to that of modern cycads. Moreover, non-N_2-fixing plants growing in the same habitat have significantly higher ($p < 10^{-10}$) foliar $\delta^{15}N$ values (mean +2.7 ± 1.9‰, $n = 18$; Fig. 8.2D) that are reminiscent of nitrogen assimilation from isotopically-enriched soil nitrogen pools. Im-

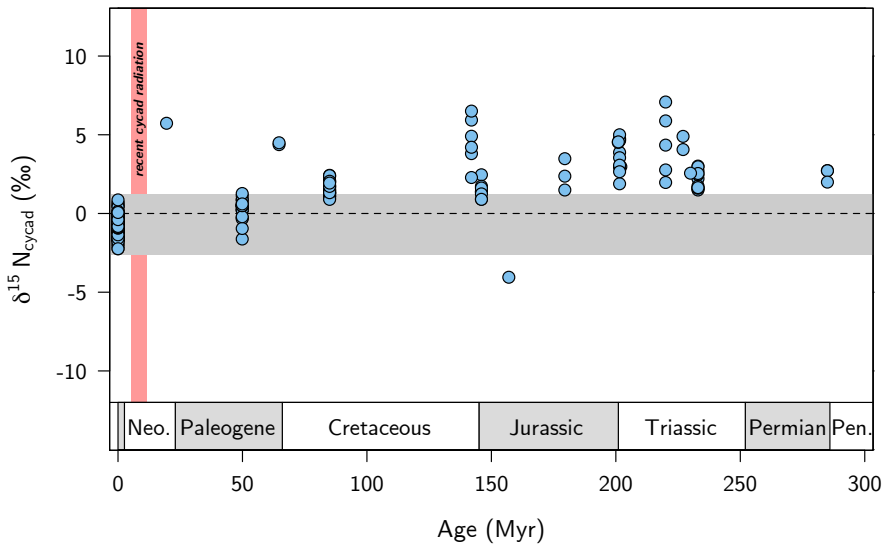

Figure 8.1: **δ^{15}N values in modern cycads and fossilized cycad leaves over the last ~300 Myrs.** Grey band denotes range of values observed in modern cycad leaves. Red band denotes proposed timing of recent cycad speciation.

portantly, the two populations do not have significantly different foliar C/N ratios ($p = 0.74$; Fig. 8.2D), suggesting that the isotopic trend is not an artifact of differential preservation, but rather is likely primary. This suggests that the cycads in this habitat were receiving a significant portion of their nitrogen from N_2-fixing symbionts.

The near-zero δ^{15}N values in the foliage of cycads from the Chuckanut Formation suggest that an N_2-fixing symbiosis was active by ~50 Ma in at least some cycad lineages. Whether the onset of the symbiosis significantly pre-dates the Chuckanut Formation cannot be determined using δ^{15}N data, but notably the fact that most Mesozoic cycad foliage has elevated δ^{15}N values suggests that the symbiosis – even if in existence in some cycad linages – was not widespread at that time. The fact that nitrogen isotopic evidence for N_2-fixing symbiosis first appears in cycads in the early Cenozoic may therefore reflect the shift from the gymnosperm-dominated understory of the Mesozoic (Taylor et al., 2009) to the angiosperm-dominated world in which gymnosperms were driven into subdued ecological roles (Bond,

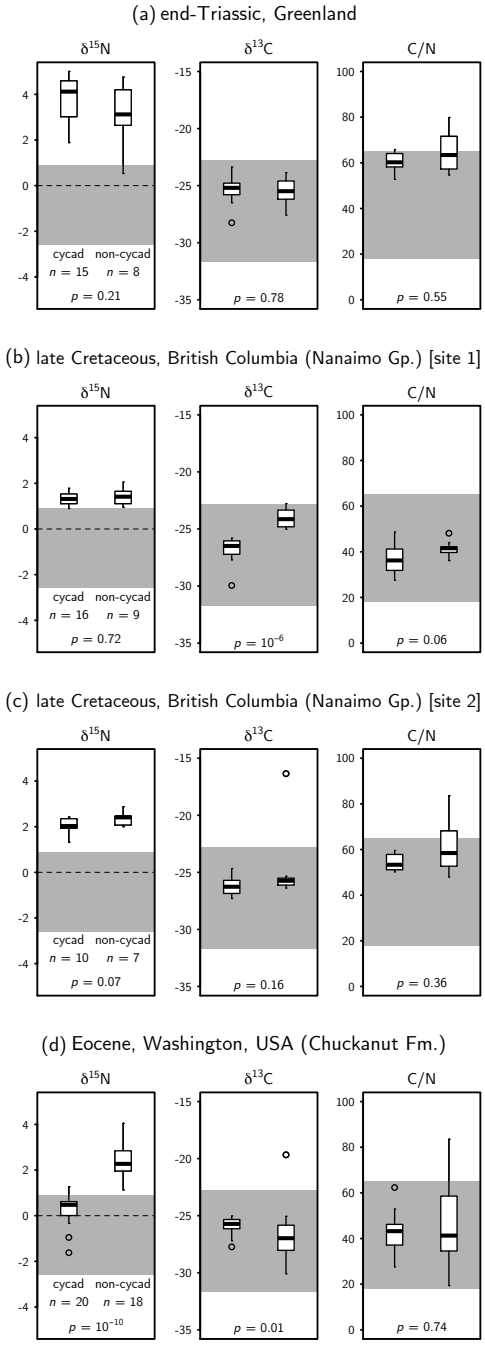

Figure 8.2: **δ^{15}N, δ^{13}C and C/N data from cycad and non-cycad foliage in (A) the end-Triassic Kap Stewart Fm., (B-C) the late Cretaceous Comox Fm., and (D) the Eocene Chuckanut Fm.** Grey bands denote range of values observed in modern cycad for each parameter. The disparity in δ^{15}N values between cycad and non-cycad foliage in the Chuckaunt Fm. is best explained by significant N_2-fixing symbiosis in the cycads at that time.

1989), if not to extinction (Knoll, 1986).

The paucity of Cenozoic cycad fossils renders it difficult to assess the timescale on which N_2-fixing symbiosis became a universal feature of the clade. However, our limited data from early Miocene cycads show elevated $\delta^{15}N$ values (Fig. 8.1), suggesting a lack of symbiosis in at least one lineage (genus: *Pseudodioon*) at that time. The data presented here are therefore consistent with recent cycad speciation since the late Miocene (Nagalingum et al., 2011) acting as a bottleneck that gave rise to the universal occurrence of N_2-fixing symbiosis in extant cycads. It thus appears that as modern biomes and seasonality became established, cycads were relegated to semi-arid, nutrient-poor settings where their capacity for N_2-fixation has become critical for their survival. This marks a profound ecological shift since the Mesozoic "Age of Cycads" when they once flourished across Earth's surface.

8.3 Methods

8.3.1 Sample collection and preparation

Carbonaceous compressions of cycads and, in some cases, non-cycads growing in their midst, were obtained from museum collections. All cycad specimens utilized in the study were previously characterized to the genus level; non-cycads were identified to varying taxonomic levels as allowed by specimen morphology.

Organic residues were removed from the background rock matrix using one of two methods. In the majority of cases, the carbonaceous film was separated from the matrix via abrasion with a razor blade. The blades were wiped with methanol between all samples and air-dried to avoid cross-contamination. In some samples that were not amenable to handling with a razor blade, an ultra-fine drill was used to remove a thin layer of organic matter from the fossil.

Under both protocols, the same method was applied to a portion of the rock matrix adjacent to the fossil in which no carbonaceous fossil remains were evident. This allowed a quantification of the background signal that could have potentially be contaminating the

signal obtained from the isolated fossil material. The concentration of nitrogen (TN, total nitrogen) in the isolated fossil material was higher than in the background matrix for all measurements, on average by a factor of 8.6. Similarly, carbon concentrations (TC, total carbon) were higher in isolated fossil material than the matrix by a factor of 16.8 on average. These observations lead us to conclude that the methods used for isolating fossilized organic matter were indeed predominantly capturing the signature of the discrete fossilized specimens and not disseminated organic matter in the matrix or nitrogen bound in clay minerals.

8.3.2 Analytical protocols

The concentration and isotopic composition of carbon and nitrogen in powders isolated from fossil and matrix material were measured on a Costech™ ECS 4010 Elemental Analyzer coupled to a Thermo Finnigan™ MAT253 continuous flow isotope ratio mass spectrometer in IsoLab at University of Washington following published protocols (Kipp et al., 2018). Combustion was carried out at 1000°C with a 20 mL pulse of O_2. The resulting gases were then passed through a reduced copper column held at 700°C to reduce NO_x species to N_2 and scrub excess O_2 from the gas stream. A magnesium perchlorate trap was then used to remove water from the gas stream, after which the gases were separated via gas chromatography and fed into the mass spectrometer via a Thermo Finnigan Conflo III. Raw isotopic data were corrected using a two-point calibration (Coplen et al., 2006) with three in-house standards: two glutamic acids (GA1, TC = 40.8%, TN = 9.5%, $\delta^{13}C$ = -28.3‰, $\delta^{15}N$ = -4.6‰; GA2, TC = 40.8%, TN = 9.5%, $\delta^{13}C$ = -13.7‰, $\delta^{15}N$ = -5.7‰) and dried salmon (SA, TC = 45.7%, TN = 11.8%, $\delta^{13}C$ = -21.3‰, $\delta^{15}N$ = +11.3‰), which are calibrated against international reference materials USGS-40 and USGS-41. Each in-house standard was analyzed four times per analytical session. Analytical blanks resulting from combustion were measured and subtracted from nitrogen data; analytical blanks were below detection limits for carbon. All isotopic data are reported in delta notation relative to air for nitrogen and Vienna Pee Dee Belemnite (V-PDB) for carbon. The average analytical precision (1σ) of isotopic measurements across all runs, as determined by replicate analyses of in-house

standard UW-McRae ($\delta^{15}N$ = +5.6‰, $\delta^{13}C$ = -37.4‰), was ±0.2‰ for $\delta^{15}N$ and ±0.1‰ for $\delta^{13}C$. Average precision (relative error) of concentration measurements was ±1.7% for TN and ±1.4% for TC.

8.4 References

Álvarez-Yépiz, J.C., Cueva, A., Dovčiak, M., Teece, M., Yepez, E.A., 2014. Ontogenetic resource-use strategies in a rare long-lived cycad along environmental gradients. *Conserv. Physiol.* 2, 1–12.

Bond, W.J., 1989. The tortoise and the hare: ecology of angiosperm dominance and gymnosperm persistence. *Biol. J. Linn. Soc.* 36, 227–249.

Carpenter, E.J., Harvey, H.R., Fry, B., Capone, D.G., 1997. Biogeochemical tracers of the marine cyanobacterium Trichodesmium. *Deep Sea Res. Part Oceanogr. Res. Pap.* 44, 27–38.

Costa, J.-L., Lindblad, P., 2002. Cyanobacteria in symbiosis with cycads, in: *Cyanobacteria in Symbiosis*. Springer, pp. 195–205.

Craine, J.M., Elmore, A.J., Wang, L., Augusto, L., Baisden, W.T., Brookshire, E.N.J., Cramer, M.D., Hasselquist, N.J., Hobbie, E.A., Kahmen, A., 2015. Convergence of soil nitrogen isotopes across global climate gradients. *Sci. Rep.* 5, 8280.

Dos Santos, P.C., Fang, Z., Mason, S.W., Setubal, J.C., Dixon, R., 2012. Distribution of nitrogen fixation and nitrogenase-like sequences amongst microbial genomes. *BMC Genomics* 13, 162.

Evans, R.D., 2001. Physiological mechanisms influencing plant nitrogen isotope composition. *Trends Plant Sci.* 6, 121–126.

Gruber, N., Galloway, J.N., 2008. An Earth-system perspective of the global nitrogen cycle. *Nature* 451, 293–296.

Halliday, J., Pate, J.S., 1976. Symbiotic nitrogen fixation by coralloid roots of the cycad Macrozamia riedlei: physiological characteristics and ecological significance. *Funct. Plant Biol.* 3, 349–358.

Kipp, M.A., Stüeken, E.E., Gehringer, M.M., Sterelny, K., Scott, J.K., Forster, P.I., Stromberg, C.A.E., Buick, R., in review. Exploring cycad foliage as an archive of the isotopic composition of atmospheric nitrogen. *Geobiology*.

Knoll, A.H., 1986. Patterns of change in plant communities through geological time, in: Diamond, J., Case, T. (Eds.), Community Ecology. Harper & Row, New York, pp. 126–141.

Lindblad, P., Bergman, B., 1990. The cycad-cyanobacterial symbiosis. *Handb. Symbiotic Cyanobacteria* 137–159.

Minagawa, M., Wada, E., 1986. Nitrogen isotope ratios of red tide organisms in the East China Sea: a characterization of biological nitrogen fixation. *Mar. Chem.* 19, 245–259.

Nagalingum, N.S., Marshall, C.R., Quental, T.B., Rai, H.S., Little, D.P., Mathews, S., 2011. Recent synchronous radiation of a living fossil. *Science* 334, 796–799.

Pate, J.S., Lindblad, P., Atkins, C.A., 1988. Pathways of assimilation and transfer of fixed nitrogen in coralloid roots of cycad-Nostoc symbioses. *Planta* 176, 461–471.

Pate, J.S., Unkovich, M.J., 1999. Measuring symbiotic nitrogen fixation: case studies of natural and agricultural ecosystems in a Western Australian setting, in: Scholes, J.D., Barker, M.G. (Eds.), *Physiological Plant Ecology*. Blackwell Science, Oxford, pp. 153–173.

Rai, A.N., Söderbäck, E., Bergman, B., 2000. Tansley Review No. 116: Cyanobacterium-plant symbioses. *New Phytol.* 147, 449–481.

Rasmussen, U., Nilsson, M., 2002. Cyanobacterial diversity and specificity in plant symbioses, in: Rai, A.N., Bergman, B., Rasmussen, U. (Eds.), *Cyanobacteria in Symbiosis*. Springer, Dordrecht, pp. 313–328.

Raven, J.A., 2002. Evolution of cyanobacterial symbioses, in: *Cyanobacteria in Symbiosis*. Springer, pp. 329–346.

Robinson, D., 2001. δ15N as an integrator of the nitrogen cycle. *Trends Ecol. Evol.* 16, 153–162.

Shearer, G., Kohl, D.H., 1986. N_2-fixation in field settings: Estimations based on natural

^{15}N abundance. *Funct. Plant Biol.* 13, 699–756.

Shearer, G., Kohl, D.H., Virginia, Ra., Bryan, B.A., Skeeters, J.L., Nilsen, E.T., Sharifi, M.R., Rundel, P.W., 1983. Estimates of N_2-fixation from variation in the natural abundance of ^{15}N in Sonoran Desert ecosystems. *Oecologia* 56, 365–373.

Taylor, E.L., Taylor, T.N., Krings, M., 2009. Paleobotany: The biology and evolution of fossil plants. Academic Press, Burlington, MA.

Vessey, J.K., Pawlowski, K., Bergman, B., 2005. Root-based N_2-fixing symbioses: Legumes, actinorhizal plants, Parasponia sp. and cycads. *Plant Soil* 274, 51–78.

Wada, E., 1980. Nitrogen isotope fractionation and its significance in biogeochemical processes occurring in marine environments. *Isot. Mar. Chem.* 375–398.

Yoneyama, T., Muraoka, T., Murakami, T., Boonkerd, N., 1993. Natural abundance of ^{15}N in tropical plants with emphasis on tree legumes. *Plant Soil* 153, 295–304.

8.5 Methods references

Coplen, T.B., Brand, W.A., Gehre, M., Gröning, M., Meijer, H.A., Toman, B., Verkouteren, R.M., 2006. New guidelines for δ^{13}C measurements. *Anal. Chem.* 78, 2439–2441.

Kipp, M.A., Stüeken, E.E., Yun, M., Bekker, A., Buick, R., 2018. Pervasive aerobic nitrogen cycling in the surface ocean across the Paleoproterozoic Era. *Earth Planet. Sci. Lett.* 500, 117–126.

CONCLUSIONS

The projects contained in this thesis have each contributed a small piece to our broader understanding of the co-evolution of life and its environment across Earth's history. The studies in Part I all used the selenium paleo-redox proxy in a slightly different context to understand aspects of Earth's oxygenation. Chapter 1 showed that selenium was mobile in surface environments during the GOE, implicating dissolved oxygen levels above critical eukaryotic thresholds. Chapter 2 showed that selenium mobility was limited in the aftermath of the GOE, at least in one semi-restricted basin. Intervals of selenium enrichment coincided with episodes of phosphogenesis, demonstrating a link between redox conditions and the cycling of macronutrients. Chapter 3 showed that intense basinal restriction can lead to selenium enrichment and isotopic fractionation patterns that are not representative of global conditions; such processes can be identified by using supporting major and trace element datasets along with selenium.

Chapters 4 and 5 each demonstrated how the cycling of major nutrients changed in tandem with the oxygenation of Earth's surface environment. Chapter 4 presented a new model for Precambrian phosphorus limitation that can be tested in future studies of organic-rich shales. Chapter 5 corroborated inferences drawn from selenium geochemsitry in Chapter 1, and further demonstrated that the surface ocean could have been hospitable to eukaryotes long before their appearance in the fossil record.

Chapter 6 highlighted a potentially novel way of reconstructing redox conditions in deep time using C/N ratios; future work to generate coupled datasets with C/N and other redox proxies will help to determine its sensitivity and utility in various paleoceanographic settings.

Chapters 7 and 8 highlighted a new use of nitrogen isotope ratios to identify nitrogen-fixing symbiosis in deep time. This not only led to a novel inference about the evolutionary

ecology of the cycad lineage, but also has opened the door for future work to employ nitrogen isotope ratios as a tool in the study of fossil plants.

In sum, these projects outline various ways of studying the co-evolution of life and its environment across a range of temporal and spatial scales. The continued development of geochemical tools for such invesitgations will surely lead to a richer understanding of this complex narrative, particularly when multiple approaches are employed in a complementary fashion. Ultimately, these studies will have served their purpose if they can shed light on our place in the Cosmos, inform our inferences about the distribution of life on other planets, and provide examples of past environmental change that both educate us and stir us to action to carefully manage our species' impact on its own habitat.

Appendix A

CHAPTER 1 - SUPPLEMENTARY MATERIALS

A.1 Geologic Context

A.1.1 Menihek Formation, Upper Labrador Trough (ca. 1.85 Ga)

The Menihek Formation of the Labrador Trough in eastern Canada is the youngest division of the Knob Lake Group and overlies the ca. 1.88 Ga Sokoman Iron Formation (Findlay et al., 1995; Machado et al., 1997). It was deposited in a deep-water setting along the eastern margin of the Superior craton. Hoffman (Hoffman, 1987) regarded this unit as foreland basin fill; however, correlative units along the southern margin of the Superior craton in the Animikie basin are considered to have been deposited in a back-arc basin (Schulz and Cannon, 2007). Regardless of the exact tectonic setting, this formation was deposited in a deep-water, open-marine environment. The Menihek Formation consists of organic-rich, sulfidic, thinly laminated, fissile shales, slates and siltstones more than 300 m in thickness (Dimroth, 1972, 1970; Zajac, 1974). The contact with the underlying granular iron formation is sharp with locally developed conglomerates. The sampled drill-core, 12-HR-1322D, is from the Howse River area. The age of ca. 1.85 Ga places deposition of the Menihek Formation >200 Myrs after the end of the Lomagundi carbon isotope excursion (Bekker, 2014).

A.1.2 Union Island Group, Canada (ca. 2.1-2.0 Ga)

The Union Island Group in the southwestern region of the East Arm basin in the Great Slave Lake area is now considered to be the lowermost unit of the Paleoproterozoic cover succession deposited on the margin of the Slave craton (Sheen et al., 2016), in contrast to previous interpretations (Hoffman, 1988, 1968; Hoffman et al., 1977; Kjarsgaard et al., 2013).

The age of the group is poorly constrained, but is younger than the 2217 ± 4 Ma Simpson Islands dikes that intrude the Archean basement but not the Union Island Group (Hoffman, 1988; Thorstad, 1976; Mumford et al., 2012), and older than the unconformably overlying ca. 1.86 Ga Sosan Group (Hoffman, 1988; Kjarsgaard et al., 2013). The group has been subdivided (Goff, 1984; Hoffman et al., 1977; Thorstad, 1976) into the following from the base to the top: 1) a lower massive dolostone, locally underlain by quartzite and/or quartz pebble conglomerate, which rests on Archean granitic basement and a well-developed regolith; 2) organic-rich and sulfidic mudstone with decimeter-thick carbonate beds; 3) alkaline to sub-alkaline, asthenosphere-derived and crustally uncontaminated basalts with flows, flow breccia, pillows, and pillow breccia; 4) well-bedded and laminated upper dolostone with thin red mudstone beds at the top and locally developed, sub-alkaline pillow basalts; and 5) red and green laminated mudstone with soft-sediment deformation structures. Deposition was below the wave- and storm-base and possibly the photic zone for the most of the succession with the exception of the upper part of the unit 4 and unit 5. Carbonates of the first and second units have highly positive carbon isotope values, comparable to carbonates deposited during the Lomagundi carbon isotope excursion, whereas carbonates of the fourth unit have carbon isotope values close to 0‰ V-PDB. We therefore consider that the black shales analyzed in this study – collected from the second unit – were deposited in the aftermath of the Lomagundi carbon isotope excursion, after ca. 2.11-2.06 Ga (Karhu and Holland, 1996). Samples were collected from outcrops on Union Island.

A.1.3 Zaonega Formation, Karelia, Russia (ca. 2.1-2.0 Ga)

The Zaonega Formation of Karelia, Russia comprises a 1500 m thick sequence of basaltic tuffs, siltstones, mudstones, and cherts. The Upper Zaonega sub-formation contains the majority of the organic-rich shales in the Zaonega Formation (Medvedev et al., 2001). It is from these horizons that samples were selected for Se analysis.

The minimum age of the Zaonega Formation is constrained by dolerite sills that are thought to be co-magmatic with volcanics of the overlying Suisar Formation, and yield U-Pb

ages of 1983 ± 6.5 and 1984 ± 8 Ma (Filippov et al., 2007). In the Onega Basin, the Zaonega Formation lies disconformably above the Tulomozero Formation, which contains isotopically heavy carbonates (>+10‰ δ13C) – consistent with deposition during the Lomagundi carbon isotope excursion (Bekker, 2014). A carbonate Pb-Pb age of 2090 ± 70 Ma for the Tulomozero Formation (Ovchinnikova et al., 2007) suggests that the Zaonega Formation was deposited during the latest stages of the GOE/LE (ca. 2.11-2.06 Ga(Karhu and Holland, 1996). This is further supported by smaller carbon isotope enrichments seen in carbonates of the Lower Zaonega sub-formation than in the Tulomozero Formation (up to +7.9‰ $\delta^{13}C$; refs. 4, 5).

Samples analyzed in this study come from three drill cores: 13A, 5190 and 175. Core 13A was drilled in the Onega Basin as part of the Fennoscandia Arctic Russia-Drilling Early Earth Program (FAR-DEEP). These cores have been studied for C, N, Mo and U isotopes as well as Fe speciation (Asael et al., 2013; Kump et al., 2011). The C isotope trends were used to identify the Shunga-Francevillian anomaly (Kump et al., 2011), and were argued to reflect a widespread decrease in environmental oxygen levels in the wake of the GOE. While post-depositional alteration rendered the Fe speciation data difficult to interpret, Mo isotopes corroborated the story of deoxygenation (Asael et al., 2013), suggesting deposition in a euxinic environment connected to a largely anoxic global ocean.

Cores 5190 and 175 have been studied for C, S and Mo isotopes, as well as Fe speciation. Multiple S isotope systematics have been interpreted as reflecting a smaller marine sulfate reservoir during deposition of the Zaonega Formation than during the Lomagundi excursion (Scott et al., 2014). Fe speciation data suggest that these units were deposited in an environment that was transiently euxinic (Scott et al., 2014).

A.1.4 FC Member, Francevillian Series, Gabon (ca. 2.1 Ga)

The unmetamorphosed Paleoproterozoic Francevillian Basin developed on the Archean Chaillu Block (Congo craton). Its tectonic setting is still debated with interpretations ranging from intracratonic basin (Weber, 1968) to foreland basin (Thieblemont et al., 2009).

Regardless of the tectonic setting, the basin was open to the global ocean. The Francevillian Series hosts carbonates recording the Lomagundi carbon isotope excursion and organic-rich shales with highly negative carbon isotope values linked to the Shunga-Francevillian anomaly (Gauthier-Lafaye and Weber, 2003; Préat et al., 2011). The age of the Francevillian Series is best constrained by a U-Pb SHRIMP age for the welded tuff at the top of the FD member of 2083 ± 6 Ma (Gauthier-Lafaye, 2006; Horie et al., 2005). Black shales suggest deposition under anoxic and even euxinic conditions based on Fe speciation and Mo concentrations and isotope ratios (Canfield et al., 2013; El Albani et al., 2010; Scott et al., 2008); whereas sulfur and iron isotope values of diagenetic pyrites indicate access to large sulfate and dissolved Fe reservoirs (El Albani et al., 2014, 2010). The sampled interval in the drillcore LST-12 collared in the Lastoursville sub-basin belongs to the FC Member and straddles the end of the Lomagundi carbon isotope excursion. The FC Member in this drillcore contains organic-rich and sulfidic shales, grey massive carbonates, and cherts. Deposition was likely below wave-base and the photic zone. Sediments passed through the oil and gas windows and migrated, solidified pyrobitumen is present in the drillcore.

A.1.5 Hautes Chutes Formation, Lower Labrador Trough (ca. 2.1 Ga)

The Hautes Chutes Formation is the lowermost unit of the Swampy Bay Subgroup, and immediately overlies carbonates of the Pistolet Subgroup (Uve and Alder formations) that have highly positive carbon isotope values recording the Lomagundi carbon isotope excursion (Melezhik et al., 1997). The age of this unit is between 2169 ± 2 Ma, an age of the granophyre dike that intrudes the underlying Seward Subgroup but not the Swampy Bay Subgroup (Rohon et al., 1993), and ca. 1.88 Ga, the age of the overlying Sokoman Iron Formation (Findlay et al., 1995; Machado et al., 1997). It was deposited on the passive margin along the eastern boundary of the Superior craton and consists of up to 100 m of graphitic, pyritiferous, thinly laminated slate (Dimroth, 1978). The samples were collected from the drillcore 12-LR-1036D that was collared in 2012 in the Lake Raitche area.

A.1.6 Sengoma Argillite Formation, Bushveld Basin, S.E. Botswana (ca. 2.2-2.1 Ga)

The Sengoma Argillite Formation (SAF) was deposited in an offshore, open-marine environment on the Kaapvaal craton (Rouxel et al., 2005). Deposition evidently occurred during the Lomagundi carbon isotope excursion (Bekker, 2014), as evidenced by highly ^{13}C-enriched carbonates occurring above and below the SAF (Bekker et al., 2008; Schidlowski et al., 1976). While there are no direct geochronologic constraints on the timing of SAF deposition, the 2.05-2.06 Ga age of the unconformably overlying Rooiberg Group and intruding Bushveld Complex confirm the inference that deposition occurred before the termination of the LE (Olsson et al., 2010; Walraven, 1997). Thus, a depositional age of 2.2-2.1 Ga has previously been inferred for the SAF (Bekker et al., 2008; Scott et al., 2014). Studies of organic carbon isotopes in the SAF have shown a large offset between δ^{13}Ccarb and δ^{13}Corg, implying a redox-stratified ocean that supported vigorous secondary production below the chemocline (Bekker et al., 2008). Fe speciation data suggest that the SAF was deposited under mostly euxinic conditions (Scott et al., 2014), but S isotope systematics indicate that the marine sulfate reservoir had expanded considerably (Scott et al., 2014), consistent with studies of S isotopes in carbonate-associated sulfate (Planavsky et al., 2012).

A.1.7 Wewe Slate, Chocolay Group, Marquette Range Supergroup (ca. 2.2-2.1 Ga)

The Wewe Slate is in the uppermost Chocolay Group, and is unconformably overlain by the 1874 ± 9 Ma Menominee Group (Fralick et al., 2002). The Kona Dolomite conformably underlies the Wewe Slate, and contains isotopically enriched carbonates (up to +9.5‰ δ^{13}C) associated with the Lomagundi carbon isotope excursion (Bekker, 2014; Bekker et al., 2006). In the Marquette Range of Michigan, the Kona Dolomite lies in unconformable contact with the Menominee Group, indicating the limited geographic extent of the Wewe Slate and suggesting that it was deposited during an episode of basin-deepening (Bekker et al., 2006). A maximum age is derived from detrital zircon U-Pb ages of 2288 ± 15 Ma for the Enchantment Lake Formation in the lowermost Chocolay Group (Vallini et al., 2006). The

lack of tight chronological constraints allows for a wide range of possible ages for the Wewe Slate; however, conformable contact with the underlying Kona Dolomite and cross-basinal correlations with other portions of the Marquette Range Supergroup suggest that an age of ca. 2.2-2.1 Ga seems most likely (Bekker et al., 2006). The Bear Creek Hole 35, drilled by Cleveland Cliffs Iron Co., was sampled for this study.

The Wewe Slate was predominantly deposited below normal wave base, but starved ripples suggest occasional sediment delivery by strong currents resulting in erosion overwhelming sediment supply. Additionally, the conformably underlying stromatolitic Kona Dolomite and mature Mesnard Quartzite indicate their deposition in a tidally-influenced shallow-marine environment (Larue, 1981). Thus, it seems possible that the Wewe Slate was deposited in a nearer-shore environment than the other shales analyzed in this study. This interpretation is supported by the lower TOC and TSe contents of the Wewe Slate compared to the other formations studied here (Table A.1). Deposition in a near-shore environment could have allowed the Wewe Slate to capture a different Se isotope signal than the outer shelf environments that were sampled in the other formations studied here. Accordingly, both extremely negative and extremely positive $\delta^{82/78}$Se values are seen in a relatively short section of the Wewe Slate core profile (Fig. A.1). The lack of a trend across the core profile suggests that these different values do not reflect secular evolution of the depositional environment (see main text for discussion).

A.2 Mass-dependent fractionation of selenium isotopes

Due to the geochemical similarity of selenium and sulfur, it was once hypothesized that selenium compounds might have been subject to significant mass-independent fractionation early in Earth's history (Stüeken, 2017; Stüeken et al., 2015). Subsequent work has found no evidence for significant mass-independent fractionation of selenium isotopes (Stüeken et al., 2015). This dataset also displays no mass independent fractionation (Fig. A.2). All deviations from the mass-dependent fractionation lines can likely be explained via residual isobaric interferences (Stüeken et al., 2013).

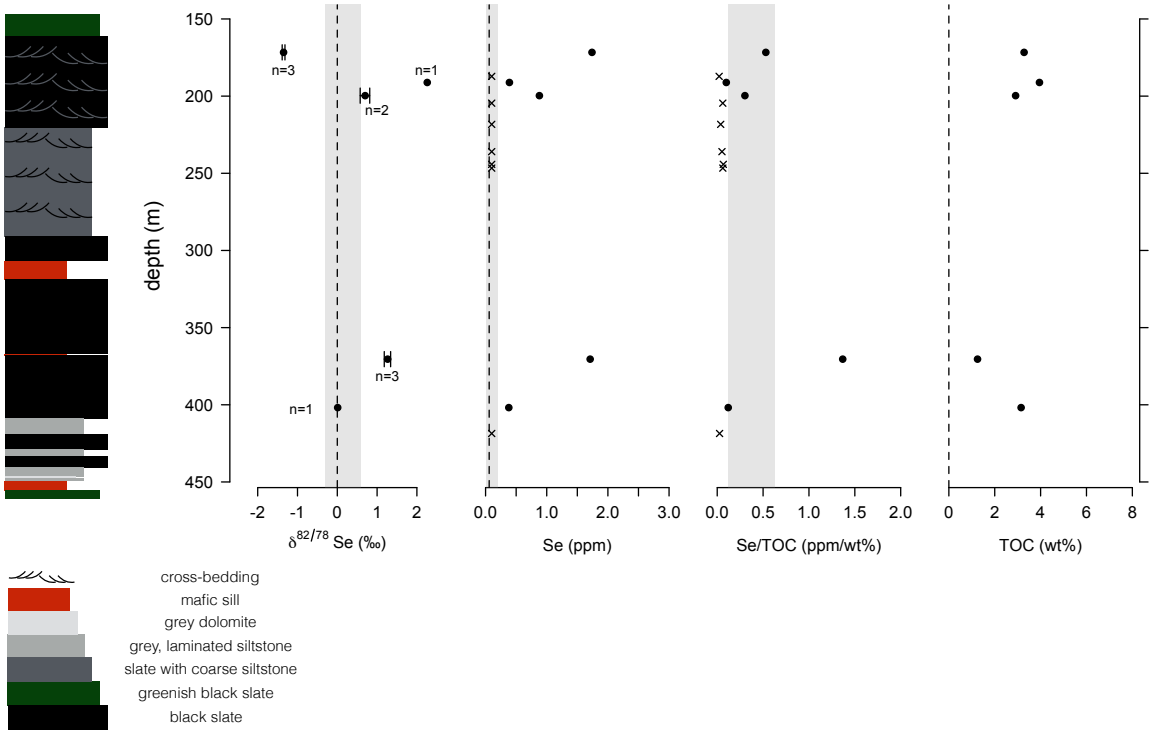

Figure A.1: **Core profile of Wewe slate.** Solid points represent averages of multiple measurements on a single sample; crosses are samples that had insufficient Se for isotopic analysis. Error bars in Se, Se/TOC and TOC plots are omitted because they are smaller than points. No trend is seen in either $\delta^{82/78}$Se or TSe, suggesting that no secular change in redox or depositional environment caused the spread of values. Rather, a depositional environment that straddled a chemocline with fluctuating depth could have experienced both non-quantitative and quantitative Se oxyanion reduction, causing the occurrence of very negative and very positive $\delta^{82/78}$Se values in <100 m of core. See text for discussion.

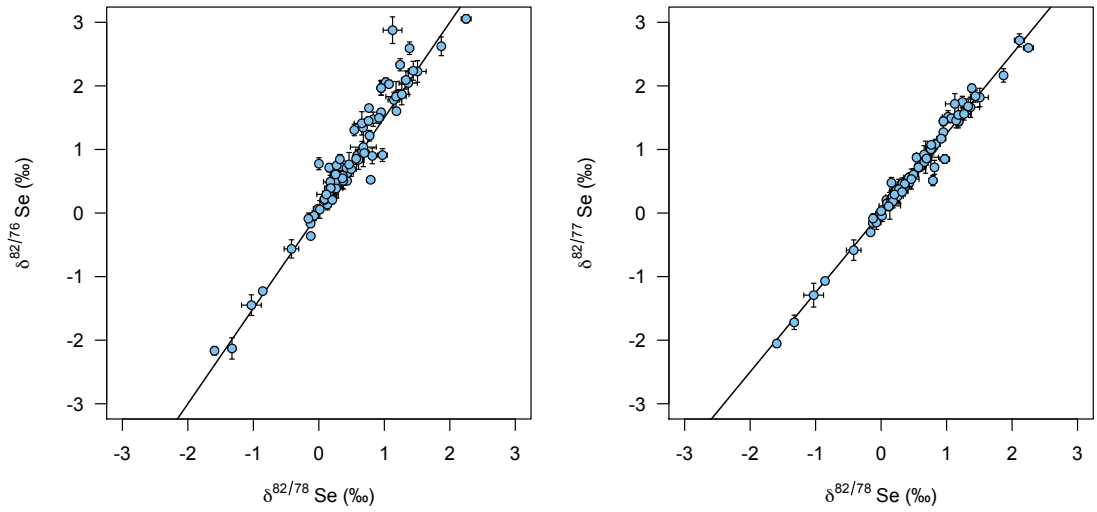

Figure A.2: **Three-isotope diagrams of $\delta^{82/76}$Se vs. $\delta^{82/78}$Se (left) and $\delta^{82/77}$Se vs. $\delta^{82/78}$Se (right).** Error bars are 1σ; trend lines are plotted for mass-dependent fractionation (MDF). All samples display mass-dependent fractionation, with any deviations from the MDF lines likely deriving from residual interferences (see Stüeken et al., 2013 for discussion of method and corrections for isobaric interferences).

A.3 References

Asael, D., Tissot, F.L., Reinhard, C.T., Rouxel, O., Dauphas, N., Lyons, T.W., Ponzevera, E., Liorzou, C., Chéron, S., 2013. Coupled molybdenum, iron and uranium stable isotopes as oceanic paleoredox proxies during the Paleoproterozoic Shunga Event. *Chem. Geol.* 362, 193–210.

Bekker, A., 2014. Lomagundi Carbon Isotope Excursion. *Encycl. Astrobiol.*

Bekker, A., Holmden, C., Beukes, N.J., Kenig, F., Eglinton, B., Patterson, W.P., 2008. Fractionation between inorganic and organic carbon during the Lomagundi (2.22–2.1 Ga) carbon isotope excursion. *Earth Planet. Sci. Lett.* 271, 278–291.

Bekker, A., Karhu, J.A., Kaufman, A.J., 2006. Carbon isotope record for the onset of the Lomagundi carbon isotope excursion in the Great Lakes area, North America. *Precambrian Res.* 148, 145–180.

Canfield, D.E., Ngombi-Pemba, L., Hammarlund, E.U., Bengtson, S., Chaussidon, M., Gauthier-Lafaye, F., Meunier, A., Riboulleau, A., Rollion-Bard, C., Rouxel, O., Asael, D., Pierson-Wickmann, A.-C., Albani, A.E., 2013. Oxygen dynamics in the aftermath of the Great Oxidation of Earth's atmosphere. *Proc. Natl. Acad. Sci.* 110, 16736–16741.

Dimroth, E., 1978. Labrador trough area. *Geol Rep* 193.

Dimroth, E., 1972. Stratigraphy of part of the Central Labrador Trough (between Latitude 5630' and the Height of Land), DP-154 (GM-28691).

Dimroth, E., 1970. The filling of the circum-Ungava geosyncline, in: Symposium on Basins and Geosynclines of the Canadian Shield. Geological Survey of Canada, pp. 45–142.

El Albani, A., Bengtson, S., Canfield, D.E., Bekker, A., Macchiarelli, R., Mazurier, A., Hammarlund, E.U., Boulvais, P., Dupuy, J.-J., Fontaine, C., Fürsich, F.T., Gauthier-Lafaye, F., Janvier, P., Javaux, E., Ossa, F.O., Pierson-Wickmann, A.-C., Riboulleau, A., Sardini, P., Vachard, D., Whitehouse, M., Meunier, A., 2010. Large colonial organisms with coordinated growth in oxygenated environments 2.1Gyr ago. *Nature* 466, 100–104.

El Albani, A., Bengtson, S., Canfield, D.E., Riboulleau, A., Bard, C.R., Macchiarelli, R.,

Pemba, L.N., Hammarlund, E., Meunier, A., Mouele, I.M., Benzerara, K., Bernard, S., Boulvais, P., Chaussidon, M., Cesari, C., Fontaine, C., Chi-Fru, E., Ruiz, J.M.G., Gauthier-Lafaye, F., Mazurier, A., Pierson-Wickmann, A.C., Rouxel, O., Trentesaux, A., Vecoli, M., Versteegh, G.J.M., White, L., Whitehouse, M., Bekker, A., 2014. The 2.1 Ga Old Francevillian Biota: Biogenicity, Taphonomy and Biodiversity. *PLOS ONE* 9, e99438.

Filippov, N.B., Trofimov, N.N., Golubev, A.I., Sergeev, S.A., Huhma, H., 2007. Isotopic age data on the Koikary-Svyatnavolok and Pudozhgora sheeted intrusions. *Geol Useful Min. Karelia* 10, 49–68.

Findlay, J.M., Parrish, R.R., Birkett, T.C., Watanabe, D.H., 1995. U-Pb ages from the Nimish Formation and Montagnais glomeroporphyritic gabbro of the central New Québec Orogen, Canada. *Can. J. Earth Sci.* 32, 1208–1220.

Fralick, P., Davis, D.W., Kissin, S.A., 2002. The age of the Gunflint Formation, Ontario, Canada: single zircon U Pb age determinations from reworked volcanic ash. *Can. J. Earth Sci.* 39, 1085–1091.

Gauthier-Lafaye, F., 2006. Time constraint for the occurrence of uranium deposits and natural nuclear fission reactors in the Paleoproterozoic Franceville Basin (Gabon). *Geol. Soc. Am. Mem.* 198, 157–167.

Gauthier-Lafaye, F., Weber, F., 2003. Natural nuclear fission reactors: time constraints for occurrence, and their relation to uranium and manganese deposits and to the evolution of the atmosphere. *Precambrian Res.* 120, 81–100.

Goff, S.P., 1984. The magmatic and metamorphic history of the Earth Arm, Great Slave Lake, N.W.T. [Ph.D. thesis], University of Alberta, Edmonton. Ph.D. thesis, University of Alberta.

Hoffman, P.F., 1988. Geology and tectonics, East Arm of Great Slave Lake, Northwest Territories.

Hoffman, P.F., 1987. Early Proterozoic Foredeeps, Foredeep Magmatism, and Superior-Type Iron-Formations of the Canadian Shield. *Proterozic Lithospheric Evol.* 85–98.

Hoffman, P.F., 1968. Stratigraphy of the Great Slave Lake Supergroup (Aphebian), east arm of Great Slave Lake. Dist. Mackenzie Geol. Surv. Can. Pap. 68–42.

Hoffman, P.F., Bell, I.R., Hildebrand, R.S., Thorstad, L., 1977. Geology of the Athapuscow aulacogen, east arm of Great Slave Lake, District of Mackenzie. Rep. Act.

Horie, K., Hidaka, H., Gauthier-Lafaye, F., 2005. U-Pb geochronolog and geochemistry of zircon from the Franceville series at Bidoudouma, Gabon, in: 15th Annual Goldschmidt Conference.

Karhu, J.A., Holland, H.D., 1996. Carbon isotopes and the rise of atmospheric oxygen. *Geology* 24, 867–870.

Kjarsgaard, B.A., Pearson, D.G., DuFrane, A., Heaman, L.M., 2013. Proterozoic geology of the East Arm Basin with emphasis on Paleoproterozoic magmatic rocks, Thaidene Nene MERA study area, in: Wright, D.F., Ambrose, E.J., Lemkow, D., Bonham-Carter, G.F. (Eds.), Mineral and Energy Resource Assessment for the Proposed Thaidene Nene National Park Reserve in the Area of the East Arm of Great Slave Lake, Northwest Territories. Geological Survey of Canada, pp. 77–117.

Kump, L.R., Junium, C., Arthur, M.A., Brasier, A., Fallick, A., Melezhik, V., Lepland, A., Črne, A.E., Luo, G., 2011. Isotopic Evidence for Massive Oxidation of Organic Matter Following the Great Oxidation Event. *Science* 334, 1694–1696.

Larue, D.K., 1981. The Chocolay Group, Lake Superior region, USA: sedimentologic evidence for deposition in basinal and platform settings on an early Proterozoic craton. *Geol. Soc. Am. Bull.* 92, 417–435.

Machado, N., Clark, T., David, J., Goulet, N., 1997. U-Pb ages for magmatism and deformation in the New Quebec Orogen. *Can. J. Earth Sci.* 34, 716–723.

Medvedev, P.V., Philippov, M., Romashkin, A.E., Vávra, N., 2001. Primary organic matter and lithofacies of siliceous shungite rocks from Karelia. *Neues Jahrb Geol Paläontol Abh* 11, 641–658.

Melezhik, V., Fallick, A., Clark, T., 1997. Two billion year old isotopically heavy carbon: evidence from the Labrador Trough, Canada. *Can. J. Earth Sci.* 34, 271–285.

Mumford, T.R., Ketchum, J., Falck, H., Heaman, L.M., 2012. New geochemical, geochronological, and isotopic data for the Blatchford Lake intrusive suite and the SImpson Island dyke.

Olsson, J.R., Söderlund, U., Klausen, M.B., Ernst, R.E., 2010. U-Pb baddeleyite ages of major Archean dyke swarms and the Bushveld Complex, Kaapvaal Craton (South Africa): correlations to volcanic rift forming events. *Precambrian Res.* 183, 490–500.

Ovchinnikova, G.V., Kuznetsov, A.B., Melezhik, V.A., Gorokhov, I.M., Vasil'eva, I.M., Gorokhovskii, B.M., 2007. Pb-Pb age of Jatulian carbonate rocks: the Tulomozero Formation of southeast Karelia. *Stratigr. Geol. Correl.* 15, 359–372.

Planavsky, N.J., Bekker, A., Hofmann, A., Owens, J.D., Lyons, T.W., 2012. Sulfur record of rising and falling marine oxygen and sulfate levels during the Lomagundi event. *Proc. Natl. Acad. Sci.* 109, 18300–18305.

Préat, A., Bouton, P., Thiéblemont, D., Prian, J.-P., Ndounze, S.S., Delpomdor, F., 2011. Paleoproterozoic high $\delta^{13}C$ dolomites from the Lastoursville and Franceville basins (SE Gabon): stratigraphic and synsedimentary subsidence implications. *Precambrian Res.* 189, 212–228.

Rohon, M.-L., Vialette, Y., Clark, T., Roger, G., Ohnenstetter, D., Vidal, P., 1993. Aphebian mafic-ultramafic magmatism in the Labrador Trough (New Quebec): its age and the nature of its mantle source. *Can. J. Earth Sci.* 30, 1582–1593.

Rouxel, O.J., Bekker, A., Edwards, K.J., 2005. Iron isotope constraints on the Archean and Paleoproterozoic ocean redox state. *Science* 307, 1088–1091.

Schidlowski, M., Eichmann, R., Junge, C.E., 1976. Carbon isotope geochemistry of the Precambrian Lomagundi carbonate province, Rhodesia. *Geochim. Cosmochim. Acta* 40, 449–455.

Schulz, K.J., Cannon, W.F., 2007. The Penokean orogeny in the Lake Superior region. *Precambrian Res.* 157, 4–25.

Scott, C., Lyons, T.W., Bekker, A., Shen, Y., Poulton, S.W., Chu, X., Anbar, A.D., 2008. Tracing the stepwise oxygenation of the Proterozoic ocean. *Nature* 452, 456-U5.

Scott, C., Wing, B.A., Bekker, A., Planavsky, N.J., Medvedev, P., Bates, S.M., Yun, M., Lyons, T.W., 2014. Pyrite multiple-sulfur isotope evidence for rapid expansion and contraction of the early Paleoproterozoic seawater sulfate reservoir. *Earth Planet. Sci. Lett.* 389, 95–104.

Sheen, A., Heaman, L.M., Ootes, L., Kjarsgaard, B., 2016. Union Island Group, East Arm Basin: A Record of Continental Rifting Prior to 1.9 Ga. GAC-MAC Abstr.

Stüeken, E.E., 2017. Selenium isotopes as a biogeochemical proxy. *Rev. Mineral. Geochem.*

Stüeken, E.E., Buick, R., Bekker, A., Catling, D., Foriel, J., Guy, B.M., Kah, L.C., Machel, H.G., Montañez, I.P., Poulton, S.W., 2015. The evolution of the global selenium cycle: Secular trends in Se isotopes and abundances. *Geochim. Cosmochim. Acta* 162, 109–125.

Stüeken, E.E., Foriel, J., Nelson, B.K., Buick, R., Catling, D.C., 2013. Selenium isotope analysis of organic-rich shales: advances in sample preparation and isobaric interference correction. *J. Anal. At. Spectrom.* 28, 1734–1749.

Thieblemont, D., Castaing, C., Billa, M., Bouton, P., Préat, A., 2009. Notice explicative de la Carte géologique et des Ressources minérales de la République gabonaise à 1/1 000 000. Editions DGMG, Ministère des Mines, du Pétrole, des Hydrocarbures. Libreville, 384 p.

Thorstad, L., 1976. Structure, stratigraphy, and petrology of the Union Island Group, East Arm of the Great Slave Lake, N.W.T. [B.Sc. thesis], University of British Columbia, Vancouver. B.Sc. thesis, University of British Columbia.

Tikhomirova, M., Makarikhin, V.V., 1993. Possible reasons for the $\delta^{13}C$ anomaly of lower Proterozoic sedimentary carbonates. Terra Nova 5, 244–248.

Vallini, D.A., Cannon, W.F., Schulz, K.J., 2006. Age constraints for Paleoproterozoic glaciation in the Lake Superior Region: detrital zircon and hydrothermal xenotime ages for the Chocolay Group, Marquette Range Supergroup. *Can. J. Earth Sci.* 43, 571–591.

Walraven, F., 1997. Geochronology of the Rooiberg Group, Transvaal Supergroup, South Africa. Economic Geology Research Unit, University of the Witwatersrand.

Weber, F., 1968. Une série précambrienne du Gabon, le Francevillien: sédimentologie, géochimie, relations avec lkes gîtes minéraux associés. Université de Strasbourg.

Yudovich, Y.E., Makarikhin, V.V., Medvedev, P.V., Sukhanov, N.V., 1991. Carbon isotope anomalies in carbonates of the Karelian Complex. *Geochem Int* 28, 56–62.

Zajac, I.S., 1974. The stratigraphy and mineralogy of the Sokoman Formation in the Knob Lake area, Quebec and Newfoundland. Department of Energy, Mines and Resources.

Appendix B

CHAPTER 4 - SUPPLEMENTARY MATERIALS

B.1 Electron acceptor compilation

B.1.1 Oxygen

Dissolved oxygen levels were constrained either by proxies that are sensitive to particular levels of dissolved oxygen, or by scaling estimates of atmospheric oxygen levels to dissolved oxygen according to Henry's Law (where $pO_2 = 0.21$ bar gives an equilibrium concentration of 325 µM).

Atmospheric oxygen levels prior to the Great Oxidation Event (GOE) are constrained by the record of mass-independent fractionation of sulfur isotopes (MIF-S) (Farquhar et al., 2000). Modeling of this signal imposes an upper limit on pO_2 of less than 10^{-5} PAL (present atmospheric level, *i.e.* ~0.21 bar) (Pavlov and Kasting, 2002), which equates to 3.25 nM dissolved oxygen in the surface ocean. Oxygen oases containing up to 1-10 µM dissolved oxygen have been proposed for the late Archean (Olson et al., 2013), however, these oases are thought to have been limited in spatial extent and thus the persistence of the MIF-S signature through the Archean can be taken as more representative of global oxygen levels. Even if surface ocean oxygen levels were persistently enriched above equilibrium with atmospheric levels, these concentrations would contribute minimally to global P regeneration (see below).

During the proposed "oxygen overshoot" associated with the GOE (Bekker and Holland, 2012), evidence from iodate concentrations in carbonates (Hardisty et al., 2014) and selenium isotope fractionations (Kipp et al., 2017) suggest that surface ocean oxygen concentrations were at least ~1 µM. While it has been suggested that atmospheric oxygen levels perhaps approached modern values during the "oxygen overshoot" (Bekker and Holland, 2012), there

is so far no compelling evidence for such an extreme increase in ambient oxygen. We adopted 5 µM as a conservative estimate of dissolved oxygen from 2.3-2.1 Ga.

After the "oxygen overshoot", pO_2 is thought to have dropped to below 10^{-3} PAL on the basis of unfractionated chromium isotopes in iron formations (Planavsky et al., 2014) and shales (Cole et al., 2016). This estimate has been challenged by a study that found vanadium depletion in organic-rich shales deposited at 1.4 Ga (Zhang et al., 2016), and argued that this reflects suboxic bottom waters under atmospheric oxygen levels of ∼4% PAL. In spite of the disagreement about precisely how much oxygen was in the atmosphere and surface ocean during the mid-Proterozoic, the range of values being proposed (0.1-4% PAL) yields minor phosphorus liberation at both the lowest and highest estimates (0.002-0.075 µM P). We adopted the chromium constraint for our preferred model, but note that new evidence for higher mid-Proterozoic oxygen could slightly shift these values. However, it is unlikely that new constraints would significantly change the model output, which consistently shows a small contribution of aerobic respiration to phosphorus recycling (<0.1 µM) before the latest Proterozoic.

It was not until the late Neoproterozoic that atmospheric oxygen began to approach modern levels, and this transition may have been protracted across the early Paleozoic (Sperling et al., 2015). We estimated Phanerozoic oxygen levels following the GEOCARBSULF model (Berner, 2006). While there remains some dispute as to which model most accurately captures the dynamics of pO_2 over the Phanerozoic, the discrepancies between models do not change our major conclusions.

B.1.2 Nitrate

Marine nitrate concentrations are related to water column redox state, however, the limiting nature of nitrogen as a macronutrient in the marine environment (Tyrrell, 1999) prevents nitrate from building up to substantial levels, even in the oxygen-rich world of the Phanerozoic. Nitrate concentrations in the modern ocean approach ∼30 µM (Levitus et al., 1993) in regions of nutrient regeneration (*i.e.*, nutrient-rich deep waters and upwelling zones), and

we therefore consider this as an upper limit on surface ocean nitrate levels from the onset of persistent aerobic nitrogen cycling during the GOE (Stüeken et al., 2016). Nitrogen isotope data suggest that nitrate did not accumulate in appreciable levels in the oceans during the early- and mid-Archean (Stüeken et al., 2015), and only transiently during the late Archean (Garvin et al., 2009; Godfrey and Falkowski, 2009). We therefore considered nitrate to be absent from the oceans prior to 2.7 Ga, at which point it increased to perhaps ∼1 µM (globally averaged). Our preferred nitrate abundance curve reaches modern levels during the GOE, after which it diminishes to 10 µM during the mid-Proterozoic, when there is isotopic evidence for nitrate limitation in offshore environments (Koehler et al., 2017; Stüeken, 2013), and returns to modern levels in the Neoproterozoic. While these estimates remain only qualitatively constrained, the contribution of nitrate respiration to phosphorus liberation is small compared to aerobic respiration and sulfate reduction, and therefore changing between our upper and lower limits does not impact our ultimate conclusions.

B.1.3 Manganese

Manganese (Mn) has multiple oxidation states, and can serve as a strong oxidizing agent in the natural environment. In aqueous environments, Mn typically occupies the +II or +IV oxidation state, the latter of which is insoluble. As such, the secular increase in oxygen content of Earth's surface environment has likely been accompanied by a decline in the Mn content of the ocean (Saito et al., 2003).

Dissolved Mn^{+II} is present at a concentration of ∼1 nM in modern seawater (Chester and Stoner, 1974; Klinkhammer and Bender, 1980), and the dominant oxidized Mn species (particulate MnO_2) has a correspondingly short residence time in seawater due to its relatively rapid settling out of the water column (Landing and Bruland, 1987). As such, Mn does not significantly impact organic remineralization or P liberation on a global scale [although in local environments it can play a substantial role (Canfield et al., 1993)]. While empirical constraints on Precambrian Mn concentrations are lacking, modeling work (Saito et al., 2003) has estimated that concentrations were slightly higher than modern in the more

reducing oceans of the Archean and Proterozoic. We therefore adopted the estimate of 1-10 nM (Saito et al., 2003) for Precambrian levels, with 10 nM as our preferred value. At these levels, Mn remains a negligible contributor to global P liberation.

B.1.4 Iron

The concentration of dissolved iron and persistence of ferruginous conditions in the Precambrian has long been the subject of geochemical scrutiny; however, precise empirical constraints on iron concentrations remain difficult to obtain. Holland estimated that Archean and early Paleoproterozoic ferrous iron concentrations were 40-120 µM (Holland, 1984, 2003; Canfield, 2005). This range corresponds to the concentration of ferrous iron at saturation with respect to siderite and calcite, assuming a range of calcium concentrations similar to Phanerozoic values. The absence of considerable siderite in Archean carbonates would seem to suggest that ferrous iron concentrations were well below this value. If calcium concentrations were in fact higher in the Archean, as recent models have considered (Jones et al., 2015), and atmospheric CO_2 levels were considerably higher than modern (Haqq-Misra et al., 2008), then the corresponding iron concentrations at siderite and calcite saturation could have been even lower. Still, we adopted the higher end of this range as our preferred value in order to remain conservative in our calculations.

Recent work has introduced additional complexity to the picture of Archean seawater Fe levels. Some have challenged these constraints on the basis that precipitation kinetics are much slower for siderite than for calcite (Derry, 2015); in order to achieve similar precipitation rates for calcite and siderite, some experiments have shown that the saturation state of siderite needed to be ∼3 orders of magnitude higher than calcite (Jimenez-Lopez and Romanek, 2004). The threshold for ferrous iron concentrations imposed by the lack of considerable siderite in Archean carbonates may thus be much higher than estimated above. However, siderite precipitation may still have played a role in determining dissolved iron concentrations. The abiotic precipitation of calcite from seawater tends to occur when the degree of supersaturation exceeds ∼20 (Lee and Morse, 2010), whereas siderite tends to require ∼50

times supersaturation (Bruno et al., 1992). Recent workers have compared the upper limits on ferrous iron concentrations imposed by kinetically-inhibited siderite precipitation to upper limits imposed by reduced iron-silicate minerals (Halevy et al., 2017; Tosca et al., 2016). This work has shown that requiring ∼60 times supersaturation for siderite formation generates approximately the same upper limit as would be imposed by the precipitation of greenalite from seawater, which is ∼1 mM (Tosca et al., 2016). However, more recent modeling has suggested that "green rust" – a metastable, ferrous-ferric mineral – could have been precipitated more efficiently from Archean seawater than greenalite (Halevy et al., 2017), perhaps implying that ferrous iron concentrations could have been well below the 1 mM upper limit proposed based on greenalite solubility. In either case, the reported discovery of primary iron-silicate phases in BIFs would seem to support the notion that ferrous minerals did in fact precipitate from seawater in the Archean and contribute to BIF deposition in at least some environments (Rasmussen et al., 2013, 2015). The emerging view now holds that there may have been differences in primary mineralogy among BIFs deposited in deeper versus shallower environments (Konhauser et al., 2017). In order to allow for all possibilities in our model scenarios, we have generated our Archean model outputs as a function of iron availability ranging up to the 1 mM greenalite constraint.

Assuming that all of this ferrous iron could be upwelled onto continental shelves and quantitatively oxidized to ferric iron, this can be used as an upper limit on ferric iron concentrations (Canfield et al., 2006). It is important to note that phototrophic oxidation of ferrous iron does not add to the net supply of oxidants for P recycling, because phototrophic organisms consume P at first instance. In principle, the same is true for chemotrophic Fe^{2+} oxidation with O_2 or NO_3^-. However, the O_2 and NO_3^- concentrations that we used in our model (Section 4.2.1) are equilibrium values after reaction with Fe^{2+}. The Fe^{3+} generated in those reactions can therefore enter the equation. Our approach of allowing all dissolved Fe^{2+} to convert to Fe^{3+} is highly conservative. Abiotic photochemical Fe^{2+} oxidation is presumably of minor importance (Konhauser et al., 2007a), though again this pathway is accounted for in the equilibrium concentrations used in our calculations. To constrain ferric

iron concentrations after the cessation of substantial BIF deposition at 1.8 Ga, we follow the model of Saito et al. (2003), which estimated ∼100 nM levels for the mid-Proterozoic and ∼1 nM levels for the Phanerozoic, which is consistent with observations in the modern ocean (Chester and Stoner, 1974).

B.1.5 Sulfate

Sulfate is a major ion in modern seawater, with a concentration of ∼28 mM. Paleo-concentrations of sulfate in the surface ocean are estimated primarily using sulfur isotope geochemistry, including multiple sulfur isotope systematics and the rate of change of sulfur isotope values along stratigraphic profiles. These studies have generated a record of Phanerozoic sulfate concentrations that fluctuate in the mM range (Algeo et al., 2015), as well as several constraints from the Precambrian.

Early constraints on Archean sulfate concentrations were derived from the observation of minimal sulfur isotope fractionation during sulfate reduction in cultures with sulfate concentrations <200 µM (Habicht and Canfield, 2001). The muted isotopic variability of sulfur in sedimentary sulfides prior to the GOE is thus compelling evidence for surface ocean sulfate concentrations below this threshold (Habicht et al., 2002). However, new insights into sulfur isotope systematics have successively pushed this limit lower. Data from Neoarchean volcanogenic massive sulfides were used to generate an estimate of ∼80 µM sulfate at this time, with a probability distribution encompassing 0 µM to 175 µM (Jamieson et al., 2013). More recently, studies of modern analog environments and new Neoarchean sulfur isotope stratigraphy have established an upper limit of <10 µM and a maximum likelihood estimate of 2.5 µM (Crowe et al., 2014; Zhelezinskaia et al., 2014) which we adopted for our calculations.

During the GOE, it has been argued that the marine sulfate reservoir expanded coincident with the proposed "oxygen overshoot" event (Planavsky et al., 2012; Schröder et al., 2008; Scott et al., 2014), perhaps reaching near-modern levels (5-20 mM) before contracting in the aftermath of the GOE. In the mid-Proterozoic, estimates range from 100-350 µM

(Luo et al., 2015) to 1-4 mM (Kah et al., 2004). We adopted a value of 10 mM during the GOE, and subsequent return to 350 µM in the mid-Proterozoic. From the mid-Proterozoic onward, sulfate levels steadily increase to ∼2 mM in the later Proterozoic, and higher in the Phanerozoic. While there is not yet a clear consensus regarding a preferred secular trend, we considered the entire range of the most recent estimates to derive our uncertainty interval.

B.2 Soluble vs. insoluble electron acceptors

Unlike the other electron acceptors in our calculation, both Mn and Fe are less soluble in their oxidized states than reduced states (Stumm and Morgan, 1981). For this reason, their cycling within the ocean system is considerably different. Both Mn and Fe are transported to the ocean by fluvial, aeolian, and hydrothermal processes (Landing and Bruland, 1987; Klinkhammer et al., 1977, 1985), with fluvial inputs dominating the modern flux (Canfield, 1998; Landing and Bruland, 1987). Upon reaching the ocean, Mn and Fe oxides have a short residence time. It is estimated that ∼95% of riverine Fe and ∼25-45% of riverine Mn are oxidized into reactive particulates during fluvial transport and estuarine mixing (Sholkovitz, 1976, 1978). Abundance profiles moving offshore show relatively quick removal of Fe and Mn from the water column and settling into sediments (Landing and Bruland, 1987). Thus, while these oxidized particulates are highly reactive toward organic matter, their oxidative capacity is spatially limited to sediments near riverine sources. Furthermore, as the dissolved phases tend to flocculate upon oxidation (Sholkovitz, 1978), the oxidizing potential becomes restricted to particle surfaces, meaning that the net oxidative capacity is lower than would be predicted by bulk concentrations. In the Precambrian, the hydrothermal Fe and Mn sources may have dominated (Kump and Seyfried, 2005), and oxidation may have occurred primarily in upwelling zones, perhaps represented by banded iron formations on continental shelves (Bekker et al., 2010). But in any case, the observations from modern rivers illustrate the short reach of iron oxides as biomass oxidants.

In our calculations, we have treated insoluble and soluble electron acceptors equally for the sake of simplicity and in order to generate a conservative upper limit on potential P

recycling. In reality, an accurate consideration of net organic remineralization achieved by Fe and Mn would require more detailed chemical modeling than is the goal of this calculation. However, because we have operated on the conservative assumption that all dissolved Fe and Mn in the ocean system could be oxidized, and quantitatively used to oxidize organic matter, the net amount of P recycling we are attributed to these electron acceptors is likely an over-estimate of the real amount. Thus, we find this treatment of insoluble electron acceptors to be sufficient for the purposes of our calculations (which is to demonstrate the maximum possible amount of P recycling in the Precambrian oceans), despite being an over-simplification of the operating chemistry.

B.3 Constraining the contribution of organic disproportionation reactions

When the supply of electron acceptors becomes depleted, biomass can continue to be degraded through organic disproportionation reactions that do not utilize dissolved electron acceptors. Instead, these reactions can split organic molecules with no net change in oxidation state. A common example is heterotrophic methanogenesis, with the net reaction:

$$2CH_2O \rightarrow CH_4 + CO_2 \tag{B.1}$$

Additionally, fermentative reactions can split organic matter and produce hydrogen in the process:

$$2CH_2O + 2H_2O \rightarrow 2CO_2 + 4H_2 \tag{B.2}$$

which can then be utilized to fuel autotrophic methanogenesis:

$$CO_2 + 4H_2 \rightarrow CH_4 + 2H_2O \tag{B.3}$$

All of these reactions can contribute to P liberation, and are hereafter referred to simply as "methanogenesis" since the net outcome of the proliferation of these metabolic pathways is the production of biogenic methane.

In the modern ocean, methanogenesis is not thermodynamically favorable in the water column (Reeburgh, 2007), but can become significant at depth in sediments, particularly where settling rates of organic material are high. However, its spatial restriction and limited supply of substrate make methanogenesis a minor player in the recycling of P within the modern ocean. Canfield estimated that the net contribution of methanogenesis to organic remineralization is 5-10 times less than that of sulfate reduction, which itself sustains only 8-14% of total biomass recycling (Canfield, 1993). Scaling this output to modern P recycling rates generates a modern methanogenic P recycling flux of 0.008-0.028 µM, with a mean of 0.018 µM.

In order to scale this value for the Precambrian, we compare modern methanogenesis rates in marine sediments [20 Tmol/yr (Reeburgh, 2007)] to proposed values for the late Archean [96 Tmoly/yr (Izon et al., 2017)], which is thought to have been a time of vigorous methanogenesis on the basis of extreme depletion in the carbon isotopic composition of organic matter in late Archean sedimentary rocks (Fig. 4.1B). Thus, by scaling to this interval, we are making the most conservative assumption regarding the possible impact of methanogenesis on P recycling. Multiplying the modern value (0.018 µM) by a scaling factor of 4.8 (96/20) gives a P regeneration flux of 0.086 µM. This is our upper limit on Precambrian P recycling by methanogenesis, and we conservatively apply this value to the entirety of the Precambrian, even though the late Archean was likely a time of exceptionally vigorous methane production. Furthermore, if the higher biogenic methane flux in the late Archean in fact came predominantly from autotrophic methanogenesis that utilized a higher H_2 flux than is present on the modern Earth, we would be considerably over-estimating the methanogenic contribution since most autotrophic methanogenesis on the modern Earth is fueled by fermentation-derived H_2 (Reaction B.2), which requires biomass degradation for its production. In light of this assessment, it seems that methanogenesis could have had a non-negligible impact on P recycling in the Archean, but likely could not have overcome the inhibition of P recycling at this time.

B.4 Interpreting the proxy record

Testing the limited-recycling model will require careful interrogation of the sedimentary record. To date, most empirical studies of P in ancient marine sedimentary rocks have focused on iron-oxide rich sedimentary rocks (Bjerrum and Canfield, 2002; Jones et al., 2015; Planavsky et al., 2010); more recently siliciclastic sedimentary rocks have been targeted as well (Reinhard et al., 2017). These records have both been used to argue for low P levels in the Precambrian (Bjerrum and Canfield, 2002; Jones et al., 2015; Reinhard et al., 2017), though extracting quantitative estimates of P levels has remained contentious (Konhauser et al., 2007b; Poulton, 2017). Here we consider the Fe-oxide and shale records through the lens of the limited-recycling model.

By carefully considering the environmental chemistry in the depositional sites, P/Fe ratios in iron-rich sedimentary rocks can be used to generate estimates of dissolved P levels at the time of deposition (Feely et al., 1998; Poulton and Canfield, 2006). The first such work in a Precambrian context focused on Archean and late Paleoproterozoic banded iron formations (BIFs), with results implying significantly lower marine P levels (Bjerrum and Canfield, 2002). While this interpretation hinges on several assumptions about paleo-seawater composition (Konhauser et al., 2007b), the latest modeling and experimental work has suggested that the original interpretation of low P remains valid (Jones et al., 2015).

Unfortunately, the record of BIFs is discontinuous, and is tied to the very chemical conditions that are thought to be conducive to low P levels (anoxic oceans with possibly limited biomass recycling, as well as potentially vigorous Fe-scavenging). Thus, it may be unsurprising that these archives persistently generate estimates of low marine P levels. The BIF record compellingly shows that P was fairly low in the late Archean and in the aftermath of the "oxygen overshoot" of the Paleoproterozoic [after ∼2.06 Ga]. Our model is entirely consistent with these observations, and in fact invokes higher P in the gaps of the BIF record, *i.e.* during oxygen overshoot [∼2.32-2.06 Ga (Bekker and Holland, 2012)] and in the later Proterozoic. Thus, the BIF record may not be a suitable place to test the limited-recycling

model.

In search of a more ubiquitous lithology, Reinhard et al. (2017) assembled a database of P abundances in marginal marine siliciclastic sedimentary rocks (Fig. B.3). The record of these sediments is much more continuous, even despite the generally sparse nature of the Precambrian rock record. The interpretation of this dataset favored by Reinhard et al. (Reinhard et al., 2017) was that the significant increase in P concentrations in these sedimentary archives in the latest Proterozoic coincided with the termination of effective Fe-scavenging, which was limiting the size of the P reservoir throughout most of the Precambrian. Alternatively, it is possible that at times, the limited P enrichment in these rocks is a result of limited recycling of biomass-bound P. There is a small, but statistically significant spike in the P content of marine sediments during the GOE (Fig. B.3), as well as a decrease in C:P ratios (Fig. B.3). This could be a result of more oxidizing conditions in the oceans, with greater rates of P recycling, a larger P reservoir, and thus greater contribution of authigenic P to the total P content of marine sedimentary rocks, causing C:P ratios to be lower than "Redfield" values. The return to lower P levels and higher C:P ratios in the aftermath of the GOE may be signal of a return to low-P conditions, although whether this is due to Fe-scavenging or limited recycling is not discernible with these data alone. Given the available data, though, the changes seen across the GOE seem indicative of an over-arching redox control of P cycle behavior.

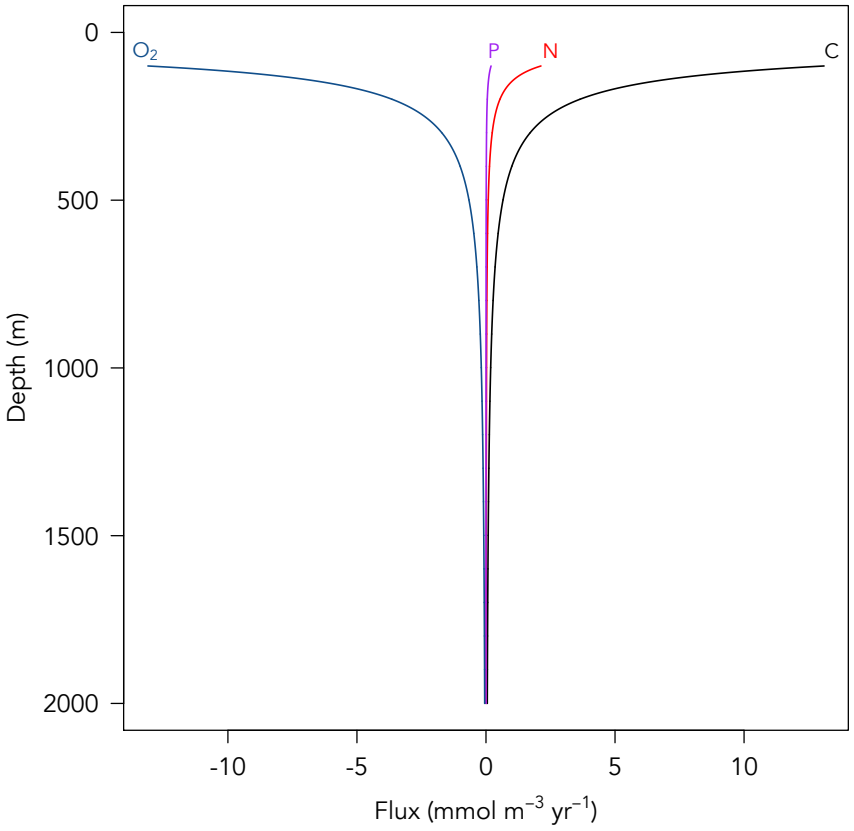

Figure B.1: **Estimated annual fluxes of C, N and P and O_2 consumption as a function of depth.** Modified after Figure 6 in Martin et al. (1987). C and N curves were derived from normalized power functions used to fit data obtained in Martin et al. (1987). P curve was generated by stoichiometrically converting the C curve based on published estimate of preferential release coefficient (Sarmiento et al., 1988). O_2 curve was generated assuming 1:1 O_2:C net stoichiometry of aerobic respiration (Canfield et al., 1993).

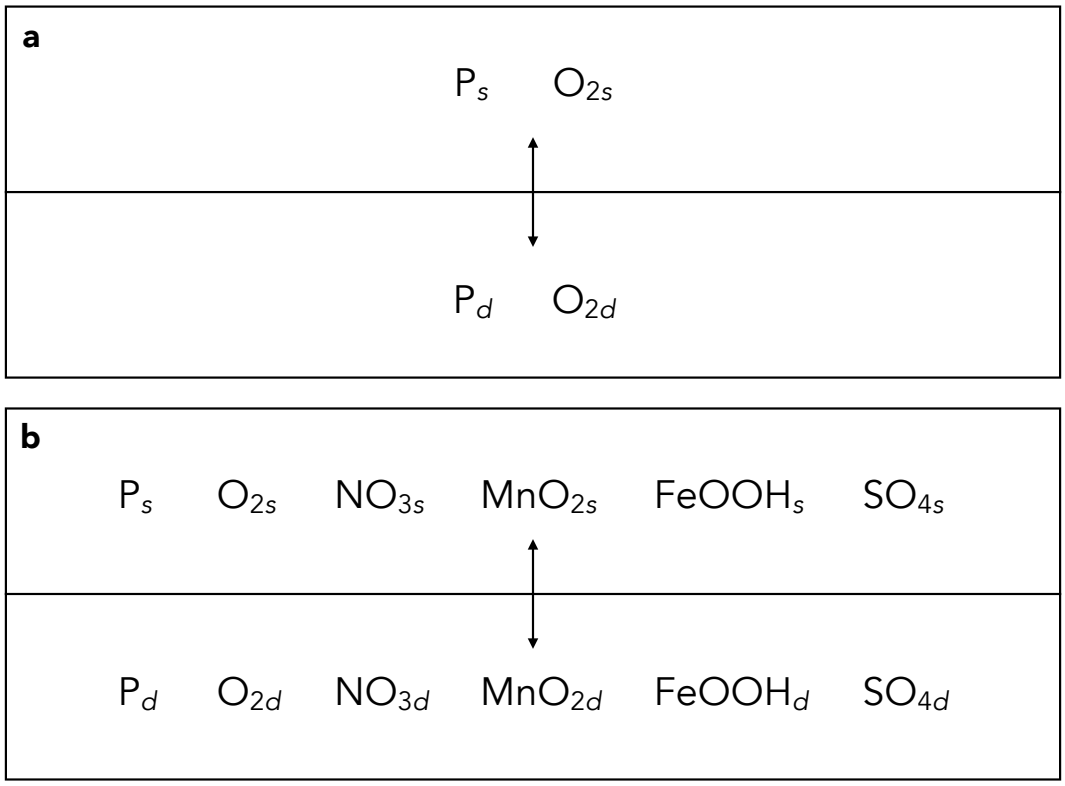

Figure B.2: **Box model schematic.** (A) shows O_2-only model, from (Sarmiento et al., 1988); (B) shows modified Precambrian model including anaerobic oxidation pathways.

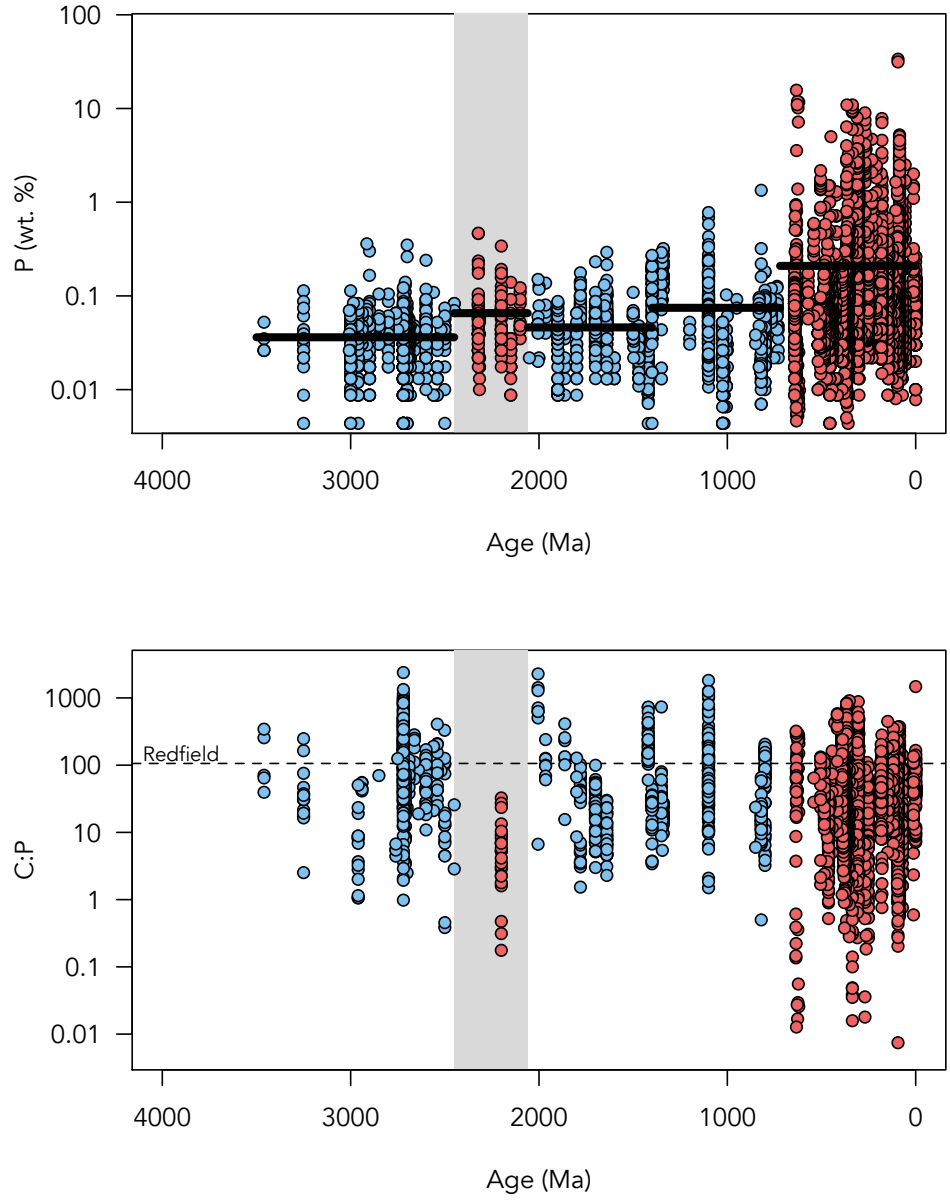

Figure B.3: **Phosphorus concentrations (top) and organic carbon:phosphorus ratios (bottom) in marginal marine siliciclastic sedimentary rocks (Reinhard et al., 2016).** Black bars in top panel show average values within age bins (pre-GOE, >2.45 Ga; GOE, 2.45-2.06 Ga; post-GOE, 2.06-1.4 Ga; late Proterozoic, 1.4-0.72 Ga; modern, <0.72 Ga). Grey shaded regions mark the "oxygen overshoot", where our model predicts higher marine P levels. Dotted line in bottom panel shows modern Redfield C:P ratio.

B.5 References

Baranova, O., et al. 2005. World Ocean Atlas.

Bekker, A., Holland, H.D., Wang, P.-L., Rumble, D., Stein, H.J., Hannah, J.L., Coetzee, L.L., Beukes, N.J., 2004. Dating the rise of atmospheric oxygen. *Nature* 427, 117–120.

Bjerrum, C.J., Canfield, D.E., 2002. Ocean productivity before about 1.9 Gyr ago limited by phosphorus adsorption onto iron oxides. *Nature* 417, 159–162.

Broecker, W.S., Peng, T.-H., 1982. *Tracers in the Sea.* Lamont-Doherty Geological Observatory, Columbia University.

Calvert, S.E., Pedersen, T.F., 1992. Organic Carbon Accumulation and Preservation in Marine Sediments: How Important is Anoxia?, in: Whelan, J., Farrington, J.W. (Eds.), Organic Matter: Productivity, Accumulation, and Preservation in Recent and Ancient Sediments. Columbia University Press, pp. 231–263.

Canfield, D.E., 1998. A new model for Proterozoic ocean chemistry. *Nature* 396, 450–453.

Canfield, D.E., Jørgensen, B.B., Fossing, H., Glud, R., Gundersen, J., Ramsing, N.B., Thamdrup, B., Hansen, J.W., Nielsen, L.P., Hall, P.O.J., 1993. Pathways of organic carbon oxidation in three continental margin sediments. *Mar. Geol.* 113, 27–40.

Clark, L.L., Ingall, E.D., Benner, R., 1998. Marine phosphorus is selectively remineralized. *Nature* 393, 426–426.

Crowe, S.A., Paris, G., Katsev, S., Jones, C., Kim, S.-T., Zerkle, A.L., Nomosatryo, S., Fowle, D.A., Adkins, J.F., Sessions, A.L., Farquhar, J., Canfield, D.E., 2014. Sulfate was a trace constituent of Archean seawater. *Science* 346, 735–739.

Emerson, S., Hedges, J.I., 1988. Processes controlling the organic carbon content of open ocean sediments. *Paleoceanography* 3, 621–634.

Farquhar, J., Bao, H.M., Thiemens, M., 2000. Atmospheric influence of Earth's earliest sulfur cycle. *Science* 289, 756–758.

Froelich, P., Klinkhammer, G.P., Bender, M. a al, Luedtke, N.A., Heath, G.R., Cullen, D., Dauphin, P., Hammond, D., Hartman, B., Maynard, V., 1979. Early oxidation of or-

ganic matter in pelagic sediments of the eastern equatorial Atlantic: suboxic diagenesis. *Geochim. Cosmochim. Acta* 43, 1075–1090.

Hao, J., Sverjensky, D.A., Hazen, R.M., 2017. A model for late Archean chemical weathering and world average river water. *Earth Planet. Sci. Lett.* 457, 191–203.

Hedges, J.I., Keil, R.G., 1995. Sedimentary organic matter preservation: An assessment and speculative synthesis. *Mar. Chem.* 49, 81–115.

Holland, H.D., 2003. The geologic history of seawater, in: *Treatise on Geochemistry*. pp. 583–625.

Holland, H.D., 1984. The chemical evolution of the atmosphere and oceans. Princeton University Press.

Izon, G., Zerkle, A.L., Williford, K.H., Farquhar, J., Poulton, S.W., Claire, M.W., 2017. Biological regulation of atmospheric chemistry en route to planetary oxygenation. *Proc. Natl. Acad. Sci.* 114, E2571–E2579.

Jones, C., Nomosatryo, S., Crowe, S.A., Bjerrum, C.J., Canfield, D.E., 2015. Iron oxides, divalent cations, silica, and the early earth phosphorus crisis. *Geology* 43, 135–138.

Kasting, J.F., 2013. What caused the rise of atmospheric O_2? *Chem. Geol.* 362, 13–25.

Konhauser, K.O., Lalonde, S.V., Amskold, L., Holland, H.D., 2007. Was there really an Archean phosphate crisis? *Science* 315, 1234–1234.

Krissansen-Totton, J., Buick, R., Catling, D.C., 2015. A statistical analysis of the carbon isotope record from the Archean to Phanerozoic and implications for the rise of oxygen. *Am. J. Sci.* 315, 275–316.

Levitus, S., Conkright, M.E., Reid, J.L., Najjar, R.G., Mantyla, A., 1993. Distribution of nitrate, phosphate and silicate in the world oceans. *Prog. Oceanogr.* 31, 245–273.

Martin, J.H., Knauer, G.A., Karl, D.M., Broenkow, W.W., 1987. VERTEX: carbon cycling in the northeast Pacific. *Deep Sea Res. Part Oceanogr. Res. Pap.* 34, 267–285.

Planavsky, N.J., Asael, D., Hofmann, A., Reinhard, C.T., Lalonde, S.V., Knudsen, A., Wang, X., Ossa Ossa, F., Pecoits, E., Smith, A.J.B., Beukes, N.J., Bekker, A., Johnson, T.M., Konhauser, K.O., Lyons, T.W., Rouxel, O.J., 2014. Evidence for oxygenic photosyn-

thesis half a billion years before the Great Oxidation Event. *Nat. Geosci.* 7, 283–286.

Planavsky, N.J., Rouxel, O.J., Bekker, A., Lalonde, S.V., Konhauser, K.O., Reinhard, C.T., Lyons, T.W., 2010. The evolution of the marine phosphate reservoir. *Nature* 467, 1088–1090.

Redfield, A.C., 1963. The influence of organisms on the composition of sea-water. *The Sea* 26–77.

Reeburgh, W.S., 2007. Oceanic methane biogeochemistry. *Chem. Rev.* 107, 486–513.

Reinhard, C.T., Planavsky, N.J., Gill, B.C., Ozaki, K., Robbins, L.J., Lyons, T.W., Fischer, W.W., Wang, C., Cole, D.B., Konhauser, K.O., 2016. Evolution of the global phosphorus cycle. *Nature* 541, 386–389.

Sarmiento, J.L., Herbert, T.D., Toggweiler, J.R., 1988. Causes of anoxia in the world ocean. *Glob. Biogeochem. Cycles* 2, 115–128.

Schlesinger, W.H., Bernhardt, E.S., 2013. Biogeochemistry: An Analysis of Global Change, 3rd ed. Academic Press.

Shaffer, G., 1996. Biogeochemical cycling in the global ocean. 2. New production, Redfield ratios and remineralisation in the organic pump. *J Geophys Res* 101, C2.

Stüeken, E.E., Catling, D.C., Buick, R., 2012. Contributions to late Archaean sulphur cycling by life on land. *Nat. Geosci.* 5, 722–725.

Takahashi, T., Broecker, W.S., Langer, S., 1985. Redfield ratio based on chemical data from isopycnal surfaces. *J. Geophys. Res. Oceans* 90, 6907–6924.

Tosca, N.J., Guggenheim, S., Pufahl, P.K., 2016. An authigenic origin for Precambrian greenalite: Implications for iron formation and the chemistry of ancient seawater. *Geol. Soc. Am. Bull.* 128, 511–530.

Tyrrell, T., 1999. The relative influences of nitrogen and phosphorus on oceanic primary production. *Nature* 400, 525–531.

White, A.E., Spitz, Y.H., Karl, D.M., Letelier, R.M., 2006. Flexible elemental stoichiometry in *Trichodesmium* spp. and its ecological implications. *Limnol. Oceanogr.* 51, 1777–1790.

Zhelezinskaia, I., Kaufman, A.J., Farquhar, J., Cliff, J., 2014. Large sulfur isotope fractionations associated with Neoarchean microbial sulfate reduction. *Science* 346, 742–744.

Appendix C

CHAPTER 5 - SUPPLEMENTARY MATERIALS

C.1 Unit descriptions

C.1.1 Turee Creek Group (ca. 2.45-2.42 Ga)

The Turee Creek Group is located on the Pilbara Craton of Western Australia and formed in a retroarc basin located in front of a magmatic fold-thrust belt on the southwestern margin of the Pilbara craton (Krapež et al., 2017). It is deposited conformably on top of the 2.45 Ga banded iron formations and volcanics of the Hamersley Group and contains the Meteorite Bore Member Diamictite, which is considered to be the second-oldest Paleoproterozoic glacial event (Caquineau et al., 2018). A minimum age of 2.21 Ga is inferred from intruding dolerite sills (Müller et al., 2005). The youngest mode of detrital zircon ages from the Turee Creek Group is ca. 2.442 Ma, which is considered close to the depositional age (Krapež et al., 2017) . The metamorphic grade ranges from prehnite-actinolite to lower greenschist facies (Shibuya et al., 2010; Smith et al., 1982). The samples are from the Rio Tinto drill core DD04 and above the Meteorite Bore Member glacial interval, with an estimated age of around 2.44 Ga.

C.1.2 Timeball Hill Formation (ca. 2.32-2.26 Ga)

The Timeball Hill Formation (THF) sits in the Lower Pretoria Group, which is part of the Transvaal Supergroup in the Kaapvaal Craton of South Africa. The THF consists of four upward-shallowing cycles of organic-rich and pyritiferous siltstones and mudstones, with occasional sandstones, and was deposited in a deltaic setting of the open-marine Transvaal Basin between the second and third glacial events of the early Paleoproterozoic (Bekker, 2014a; Gumsley et al., 2017). The formation experienced lower greenschist facies metamor-

phism (Coetzee, 2001). Recent age constraints for the THF come from a 2316 ± 7 Ma Re-Os isochron pyrite age (Hanh et al., 2004) as well as ages of 2310 ± 9 Ma and 2256 ± 6 Ma for welded tuffs within the unit (Rasmussen et al., 2013). The latter age constraint implies a major hiatus in the middle of the Timeball Hill Formation, across the sequence boundary (cf. Gumsley et al., 2017; Rasmussen et al., 2013).

The Rooihoogte and Timeball Hill formations record the disappearance of the mass-independent fractionation of sulfur isotopes, signaling the onset of the Great Oxidation Event (Bekker et al., 2004; Gumsley et al., 2017). Recent work has documented evidence of aerobic nitrogen cycling in the immediate aftermath of this transition (Zerkle et al., 2017), which was interpreted as the onset of a persistently aerobic nitrogen cycle in the marine environment. We analyzed samples from the drill core EBA-1, collared in the Potchefstroom area through the THF, which predominantly come from the Upper Timeball Hill Formation with an age of ca. 2.26 Ga. Two exceptions are a sample of the ca. 2.32 Ga Lower Timeball Hill Formation from a depth of 1037.6 m and another sample at the boundary of the Upper Timeball Hill Formation and the overlying Boshoek Formation from a depth of 560.5 m. Our data supports the inferences of Zerkle et al. (2017) regarding nitrogen cycling at the early stage of the GOE, which were based on analyses of samples from the basal part of the Lower Timeball Hill Formation in the drill core EBA-2.

C.1.3 Wewe Slate (ca. 2.2 Ga)

The Wewe Slate sits in the uppermost Chocolay Group of the Marquette Range Supergroup. The age is constrained by the unconformably overlying 1874 ± 9 Ma Menominee Group (Fralick et al., 2002) and a 2288 ± 15 Ma U-Pb age on detrital zircon from the underlying glacially influenced Enchantment Lake Formation (Vallini et al., 2006). The Kona Dolomite directly underlies the Wewe Slate, and contains carbonates with highly positive carbon isotope values corresponding to the Lomagundi carbon isotope excursion (Bekker et al., 2006; Bekker, 2014b). In the Marquette Range of Michigan, the Wewe Slate has limited geographic extent due to a protracted period of erosion before deposition of the Menominee Group started.

The Wewe Slate was deposited during an episode of basin-deepening and experienced lower greenschist (chlorite-biotite) metamorphism during the Penokean Orogeny (Bekker et al., 2006; James, 1955). The samples analyzed in this study come from Bear Creek Hole 35, drilled by Cliffs Natural Resources.

The Wewe Slate was deposited below fair-weather wave base, but starved ripples suggest occasional sediment delivery by strong currents resulting in erosion sometimes overwhelming sediment supply (Larue, 1981). In contrast, the conformably underlying stromatolitic Kona Dolomite and mature Mesnard Quartzite indicate deposition in a tidally-influenced shallow-marine environment. Extremely elevated selenium isotope ratios in the Wewe Slate have been used to argue for mildly oxygenated surface waters during deposition (Kipp et al., 2017).

C.1.4 Sengoma Argillite Formation (ca. 2.15 Ga)

The Sengoma Argillite Formation (SAF) belongs to the Paleoproterozoic Pretoria Series in Botswana and was deposited along the northern margin of the Kaapvaal Craton in an offshore, open-marine environment (Bekker et al., 2008). It is likely correlative with the Silverton Formation in the Transvaal basin of South Africa. Carbonates both underlying and overlying the SAF contain highly positive carbon isotope values, suggesting that the SAF was deposited in the midst of the Lomagundi carbon isotope excursion. This inference is supported by age constraints imposed by the underlying ca. 2.22 Ga Hekpoort Lava and overlying 2.05-2.06 Ga Rooiberg Group and intruding Bushveld Complex, which suggest that deposition occurred before the termination of the Lomagundi excursion (Dorland, 2004; Olsson et al., 2010; Walraven, 1997). The unit experienced lower greenschist facies metamorphism (Bekker et al., 2008).

The predominance of organic-rich shales is suggestive of deposition below wave base. Previous studies have shown that on the basis of Fe-speciation (Scott et al., 2014), and organic carbon isotopes (Bekker et al., 2008), the SAF was deposited in a redox-stratified ocean under locally euxinic conditions. Elevated selenium isotope ratios in the SAF suggest oxy-

genated surface waters in the basin at this time (Kipp et al., 2017), while high trace metal enrichments (e.g. Partin et al., 2013) are consistent with a global expansion of oxic shallow sea-water and local deep sea-water anoxia at that time. The samples were collected from the drill core Start 2 that was collared near Lobatse, Botswana (Key, 1983).

C.1.5 Hautes Chutes Formation (ca. 2.1 Ga)

The Hautes Chutes Formation is the lowermost unit of the Swampy Bay Subgroup in the Labrador Trough of Canada, and overlies carbonates of the Pistolet Subgroup that have highly positive carbon isotope values, associated with the Lomagundi carbon isotope excursion (Melezhik et al., 1997). The age is constrained by a 2169 ± 2 Ma granophyre dike that intrudes the underlying Seward Subgroup but not the Swampy Bay Subgroup (Rohon et al., 1993), and by the overlying 1.88 Ga Sokoman Iron Formation (Findlay et al., 1995; Machado et al., 1997). In the western part of the Labrador Trough, from which samples were taken for this study, parautochtonous regions experienced only prehnite-pumpellyite facies metamorphism (Klein, 1978; Klein and Fink, 1976).

The sampled unit was deposited on a passive margin along the eastern boundary of the Superior carton, and consists of ∼100 m of graphitic, sulfidic, thinly laminated slate (Dimroth, 1978). The samples analyzed in this study come from the 12-LR-1036D drill core, which was collared in the Lake Raitche area.

C.1.6 Francevillian Series (ca. 2.08 Ga)

The unmetamorphosed Paleoproterozoic Francevillian Basin developed on the Archean Chaillu Block (Congo Craton). The tectonic setting is debated, with interpretations ranging from intracratonic (Weber, 1968) to foreland or back-arc basin (Bankole et al., in revision; Thieblemont et al., 2009). The Francevillian Series records the Lomagundi carbon isotope excursion, as well the extremely negative carbon isotope excursion known as the Shunga-Francevilian anomaly (Gauthier-Lafaye and Weber, 2003; Kump et al., 2011; Préat et al.,

2011). The age is best constrained by a U-Pb SHRIMP age of 2083 ± 6 Ma for the welded tuff at the top of the FD member (Horie et al., 2005; Gauthier-Lafaye, 2006).

Deposition was evidently below wave base, with organic-rich and sulfidic shales showing Fe-speciation and Mo-isotopic evidence for anoxic and even euxinic conditions (Scott et al., 2008; El Albani et al., 2010; Canfield et al., 2013). Iron and sulfur isotope systematics in diagenetic pyrites suggest access to large dissolved sulfate and Fe reservoirs (El Albani et al., 2010, 2014).

We analyzed samples from the LST-12 drill core, collared in the Lastoursville sub-basin. The samples included in this study come from the FC member, which straddles the end of the Lomagundi carbon isotope excursion. In addition to black shale, the FC member in this core contains grey massive carbonates and cherts. The shale horizons sampled here occur between thick carbonate beds, which could imply a degree a restriction during deposition of the shales. However, sulfur isotope ratios in diagenetic pyrites are inconsistent with severe restriction to the extent that the sulfate supply became limited (Albani et al., 2010, 2014).

C.1.7 Union Island (ca. 2.04 Ga)

The Union Island Group in the East Arm basin of the Great Slave Lake region is the lowermost unit of the Paleoproterozoic cover deposited on the margin of the Slave Craton (Sheen, 2017). The maximum age is constrained by the 2217 ± 4 Ma Simpson Island dikes that intrude Archean basement but not the Union Island Group (Hoffman, 1988; Mumford et al., 2012; Thorstad, 1976) and a lower age limit is provided by the unconformably overlying ∼1.86 Ga Sosan Group (Hoffman, 1988; Kjarsgaard et al., 2013). Sheen (2017) recently dated baddeleyite from a dike that intrudes the upper part of the Union Island Group using the U-Pb ID-TIMS method and considered it to be a feeder for volcanic rocks in this group, thus providing a direct age of deposition.

The group has been divided into 5 units (Hoffman et al., 1977; Goff, 1984; Thorstad, 1976), from bottom to top: (1) massive dolostone, locally underlain by quartzite and/or quartz pebble conglomerate, which rests on Archean granitic basement and a well-developed regolith;

(2) organic-rich and sulfidic mudstone with decimeter-thick carbonate beds; (3) alkaline to sub-alkaline, asthenosphere-derived and crustally uncontaminated basalts with flows, flow breccia, pillows, and pillow breccias; (4) well-bedded and laminated upper dolostone with thin red mudstone beds at the top and locally developed, sub-alkaline pillow basalts; (5) red and green laminated mudstone with soft-sediments deformation structures.

Deposition was below wave- and storm-base and possibly the photic zone for most of the succession, with the exception of the upper part of unit 4 and unit 5. Carbonates of units 1 and 2 have highly positive carbon isotope values, comparable to carbonates deposited during the Lomagundi carbon isotope excursion, whereas carbonates from unit 4 have isotopic values near 0‰. The Union Island Group was metamorphosed to lower-greenschist facies based on actinolite-chlorite-epidote-titanite mineralogy of mafic units and experienced mild hydrothermal alteration recorded by carbonate veins (Sheen, 2017).

We analyzed black shales from unit 2, which is inferred to have been deposited at the end of the Lomagundi carbon isotope excursion, i.e. after 2.11-2.06 Ga (Karhu and Holland, 1996; Kipp et al., 2017). Samples were collected from lake outcrops near Union Island.

C.1.8 Maraloou Formation (ca. 2.0 Ga)

The Maraloou Formation is part of the Mooloogool Subgroup in the Yerrida Group of Western Australia (Olierook et al., 2018; Pirajno et al., 1998). The Yerrida Group was deposited in a back-arc (strike-slip) basin (Krapez and Martin, 1999), with lithologies including basalts, stromatolitic dolostone, sulfate evaporites, graphitic shale, carbonaceous siltstone and sandstone, and conglomerate/breccia. It was deposited in near-shore to offshore depositional environments in a deepening basin, with the stromatolitic and evaporitic horizons suggesting restricted circulation between the basin and open ocean at those times. The Yerrida Group is considered to be unmetamorphosed except near tectonic boundaries where lower greenschist facies metamorphism is developed (Pirajno et al., 2004). The age of the Mooloogool Subgroup is broadly constrained by a 2173 ± 64 Ma Pb-Pb age on stromatolitic carbonate of the Bubble Well Member of the Windplain Subgroup (Woodhead and Hergt, 1997) that also

record the ca. 2.22-2.06 Ga Lomagundi carbon isotope excursion (Bekker, 2014b) and by the 1954 ± 5 Ma U-Pb SHRIMP zircon ages of micro-tuffs in the unconformably overlying Yelma Formation of the Tooloo Group (Sheppard et al., 2016). We use a conservative estimate of ca. 2.0 Ga for the age of the Maraloou Formation.

The Maraloou Formation consists of ∼1000 m of finely lamited, organic-rich and sulfidic argillite, marl, dolostone, and minor chert, and thus marks a trend toward deeper deposition than the underlying intercalated Thadu (arkosic and lithic sandstones, quartz wacke, minor conglomerate, siltstone, mudstone, and laminated quartz sandstone with locally present basaltic scoria) and Killara (tholeitic basalt, lithic sandstone and chert breccia) formations, which comprise mostly shallow-water facies (Pirajno et al., 1998, 2004; Olierook et al., 2018). Monazite from the base of the Maraloou Formation yielded a U-Pb age of 1843 ± 10 Ma (Rasmussen and Fletcher, 2002), but this has recently been re-interpreted as a signature of a low-grade metamorphic overprint (Olierook et al., 2018). The samples analyzed in this study were collected from the drill-core KDD1.

C.1.9 Menihek Formation (ca. 1.85 Ga)

The Menihek Formation is the youngest unit of the Knob Lake Group in eastern Canada, and overlies the 1.88 Ga Sokoman Iron Formation (Findlay et al., 1995; Machado et al., 1997). The tectonic setting is somewhat contentious; Hoffman regarded this unit to be a part of foreland basin fill (Hoffman, 1987), while correlative units along the southern margin of the Superior craton are thought to have been deposited in a back-arc basin (Schulz and Cannon, 2007). In either case, the Menihek Formation was deposited in a deep-water, open-marine environment on the eastern margin of the Superior craton. The Menihek Formation stratigraphy consists of >300 m of organic-rich, sulfidic, thinly laminated, fissile shales, slate, and siltstones (Dimroth, 1970, 1972; Zajac, 1974). The persistence of near-crustal selenium isotope ratios in the Menihek Formation has been interpreted as a sign of deposition in a less-oxygenated ocean than that during the Paleoproterozoic "oxygen overshoot" event (Kipp et al., 2017). The contact with the underlying granular iron formation is sharp, with locally

developed conglomerates. In the western part of the Labrador Trough, parautochtonous regions experienced only metamorphism up to prehnite-pumpellyite facies (Klein, 1978; Klein and Fink, 1976). We analyzed samples from the 12-HR-1322D drill core, which was collared in the Howells River area, in the western part of the Labrador Trough.

C.2 Box model setup

C.2.1 Box model architecture

We assembled a steady-state box model (Fig. 5.1) to track nitrogen isotope mass balance, using previously developed Earth system nitrogen box models as a starting point (Algeo et al., 2014; Stüeken et al., 2016). Unlike previous studies, however, this model separately tracks N_2-fixing (N_{fixers}) and nitrate-assimilating ($N_{assimilators}$) organisms. The only input flux for the N_{fixers} is fixation of atmospheric N_2 ($f_{fixation}$) to ammonium in biomass. The dominant output flux from the N_{fixers} is remineralization of biogenic ammonium and subsequent nitrification of ammonium to nitrate ($f_{remin\text{-}nitrif}$). A minor sink (<1%) is the burial of biogenic ammonium in marine sediments ($f_{fixer\text{-}burial}$), which includes both organic-bound and mineral-bound nitrogen. The $N_{assimilators}$ are assumed to quantitatively assimilate all available nitrate dissolved in the surface ocean (Tyrrell, 1999). The dominant input (>99%) of nitrate is nitrification ($f_{remin\text{-}nitrif}$), with atmospheric deposition ($f_{deposition}$) and riverine inputs (f_{river}) comprising minor contributions (<1%). There are three output fluxes from the dissolved nitrate reservoir: water-column denitrification of nitrate to N_2 gas (f_{wcd}), sedimentary denitrification (f_{sd}), and burial of biomass of nitrate-assimilating organisms ($f_{assimilator\text{-}burial}$). Burial is a negligible output flux (<1%) compared to denitrification, the latter of which roughly balances the input of nitrogen to the ocean system (Devol, 2015).

We began by confirming that this model can reproduce modern isotope mass balance. Reservoir masses (m_i) for the atmosphere (2.87×10^{20} mol N) and continental crust (1.21×10^{20} mol N) were taken from Johnson and Goldblatt (2015). We adopted flux constants (k_i) for $f_{fixation}$ ($k_{fixation} = 1.3 \times 10^{-7}$), $f_{deposition}$ ($k_{deposition} = 3.21 \times 10^{-10}$), and f_{river} ($k_{river} = 1.27 \times$

10^{-9}) based on previous formulations of nitrogen cycle models for the modern Earth system (Canfield et al., 2010; Algeo et al., 2014; Stüeken et al., 2016), and calculated these fluxes as

$$f_i = k_i m_i \tag{C.1}$$

with the mass corresponding to the respective source reservoir. The remaining fluxes were calculated following the assumption of steady state, such that

$$f_{fixation} = f_{remin-nitrif} + f_{fixer-burial} \tag{C.2}$$

where $f_{\text{fixer-burial}}$ is the fraction of nitrogen in N_2-fixing organisms that escapes remineralization to ammonium in the water column and sedimentary pore-waters, and gets buried with marine sediments. Since the timescales we are concerned with are on the order of Myrs, the assumption of a steady-state marine nitrogen cycle is valid (Tyrrell, 1999), despite the fact that on kyr-timescales the oceans can operate at a potentially significant nitrogen deficit (Codispoti et al., 2001). The balance of the nitrate reservoir at steady-state can be represented as

$$f_{remin-nitrif} + f_{deposition} + f_{river} = f_{wcd} + f_{sd} + f_{assimilator-burial} \tag{C.3}$$

which can be simplified as

$$f_{surface-inputs} = f_{wcd} + f_{sd} + f_{assimilator-burial} \tag{C.4}$$

where in the modern ocean $f_{\text{assimilator-burial}}$ is 0.2% of $f_{\text{surface-inputs}}$ (Tyrrell, 1999). The ratio of f_{sd} to f_{wcd} in the modern ocean is presumed to be 2.4, based on isotope mass balance (Brandes and Devol, 2002; DeVries et al., 2012; Devol, 2015). These numbers are likely to have changed over time (see below).

We then assigned isotopic fractionations (ε_i) to each pathway (Section 5.2.2; Table C.2), and calculated the isotopic composition of both N_{fixers} and $N_{\text{assimilators}}$ using both closed

system

$$\delta^{15}N_{reservoir} = \delta^{15}N_{input} + (\epsilon_i ln(1 - f_i)) \tag{C.5}$$

and open system

$$\delta^{15}N_{reservoir} = \delta^{15}N_{input} - (\epsilon_i f_i) \tag{C.6}$$

formulations, where f_i is the fraction of the reservoir removed by a given pathway. Since the residence time of nitrogen in the modern ocean is $\sim$ 3 kyrs (Tyrrell, 1999; Brandes and Devol, 2002) – slightly longer than the ocean mixing time – nitrogen should be moderately well mixed in the global ocean today, and thus isotope mass balance should follow open-system dynamics. However, it is possible for semi-closed system dynamics to apply to modern basins where denitrification rates are high. We have thus presented calculations for both end-members, recognizing that the open-system formulation likely best represents the average value of global marine sediments, while individual basins can follow semi-closed dynamics.

Ultimately, the nitrogen isotopic composition of marine sediments was calculated using the equation

$$\delta^{15}N_{sed} = \frac{(\delta^{15}N_{fixer-burial} f_{fixer-burial}) + (\delta^{15}N_{assimilator-burial} f_{assimilator-burial})}{f_{fixer-burial} + f_{assimilator-burial}} \tag{C.7}$$

which combines the burial fluxes from N_2-fixing and nitrate-assimilating organisms. Solving the equations using parameterizations based on the modern Earth system yields a range of $\delta^{15}N_{sed}$ values (+2.6 to +7.3‰, mean +4.5‰) that is in good agreement with observations from recent marine sediments (mode +4-6‰ ± 2.5‰; Tesdal et al., 2013).

The model was then modified in order to make it applicable to the range of redox conditions that persisted during the Precambrian Era. First, we considered atmospheric deposition and riverine input of nitrate to the surface ocean. We performed a sensitivity test using a range of fluxes for these parameters, spanning modern values to zero. Despite uncertainties surrounding the role of atmospheric deposition and riverine transport as nitrogen

sources in the Precambrian, the contribution of these inputs is negligible (<1%) compared to fixation-remineralization, even at the highest plausible values. Thus, switching between the highest and lowest plausible values for these fluxes does not impact the response of the model to increasing ocean anoxia (<<1‰). In our model for the Precambrian, we removed these minor nitrogen inputs due to uncertainty surrounding their values in deep time.

Next, we considered potential variability in the ratio of water-column to sedimentary denitrification ($f_{\mathrm{wcd}}/f_{\mathrm{sd}}$) as a function of marine redox conditions. In the modern ocean, sedimentary denitrification is a ∼2.4× larger flux than water-column denitrification (Devol, 2015). However, the available volume of suitable environments for sedimentary denitrification (suboxic-to-anoxic sedimentary porewaters; $\mathrm{V_{pore}}$) is greater than the ocean volume in which water-column denitrification occurs (suboxic-to-anoxic cores of oxygen-minimum zones in the modern ocean; $\mathrm{V_{an\text{-}sub}}$) by a factor of ∼200 (Keeling et al., 2009; LaRowe et al., 2017). Thus, denitrification must be much more rapid in the water column than in diffusion-limited sediment pore-waters (this is corroborated by the difference in isotopic effects, which are a result of reaction rates and yields). We defined volumetric flux constants (in units of mol $\mathrm{N/m^3/yr}$) for sedimentary (k_{sd}) and water-column denitrification (k_{wcd}) using the equation

$$f_{total-denit} = f_{wcd} + f_{sd} = (k_{sd}V_{pore}) + (k_{wcd}V_{an-sub}) \tag{C.8}$$

where $f_{\mathrm{total\text{-}denit}}$ is the net rate of denitrification in the ocean system (in mol N/yr). Given that even sediments underlying oxygenated waters often reach the zone of denitrification in the upper <1 cm (Canfield et al., 1993; Wang and Van Cappellen, 1996), we assumed that today the entirety of the global marine sedimentary pore-water volume is thermodynamically conducive to denitrification. Regarding water-column denitrification, we adopted 4.5 µM $\mathrm{O_2}$ as our cutoff for "suboxic-to-anoxic" waters (Keeling et al., 2009), as most water-column denitrification occurs in waters that fall below this threshold of oxygen availability (Codispoti et al., 2001). While both denitrification and anammox have been observed to operate at higher oxygen levels, up to ∼20-25 µM $\mathrm{O_2}$ in some instances, the rates of these processes drop off substantially with increasing oxygen at most sites that have been studied (Kalvelage

et al., 2011), and furthermore in other settings substantial denitrification does not begin until closer to ∼1 µM O_2 (Paulmier and Ruiz-Pino, 2009). Thus, we take the <4.5 µM O_2 cutoff to be representative of waters in the global ocean in which the vast majority of water column denitrification occurs (Keeling et al., 2009; Paulmier and Ruiz-Pino, 2009).

Equation 8 can be manipulated to solve for k_{sd} or k_{wcd} by plugging in literature values for V_{pore}, and $V_{\mathrm{an\text{-}sub}}$ (Keeling et al., 2009; LaRowe et al., 2017) and assuming (following nitrogen isotope mass balance; see above) that today the net sedimentary denitrification flux is 2.4 times that of water-column denitrification (Devol, 2015), such that

$$k_{sd}V_{pore} = 2.4(k_{wcd}V_{an-sub}) \tag{C.9}$$

We then define the term k to be the relative difference in volumetric flux constants of sedimentary and water-column denitrification

$$k = \frac{k_{wcd}}{k_{sd}} \tag{C.10}$$

and find that under the parameterizations listed above, k is approximately 80. In other words, denitrification proceeds ∼80 times faster in open ocean waters than in diffusion-limited porewaters. Expansion of water-column denitrification would therefore lead to faster nitrate loss from the ocean (cf. Fennel et al., 2005). While this ratio could also be determined by *in-situ* rate measurements of sedimentary and water-column denitrification, we find the volumetric approach to be most appropriate for considering long-term changes in the mass of oxic and anoxic waters in the global ocean, since it averages contributions across environments that have variable nutrient supply, temperature, salinity, pH and microbial ecology.

In order to consider the effect of a changing balance of f_{wcd} and f_{sd}, we calculated corresponding changes in the rate of denitrification for a range of $V_{\mathrm{an\text{-}sub}}$ values using the equation

$$R = \frac{f_{total-denit}}{f_{total-denit-mod}} \tag{C.11}$$

where $f_{\text{total-denit-mod}}$ is the net rate of denitrification in the modern ocean, and R represents the relative change in denitrification rate. Conceptually, the value $k = 80$ implies that an increase in water-column denitrification due to an expansion of anoxia in the water column would increase the total denitrification rate. The parameter R captures this change as a function of water-column anoxia. Since the cores of the major OMZ's are confined to the upper 1 km of the ocean (Paulmier and Ruiz-Pino, 2009), we assume that the redox state of this part of the ocean exerts the major control on the rate of denitrification and the isotopic composition of residual nitrate. To explore the effect of increasing anoxia, we varied the volume of suboxic-to-anoxic waters ($V_{\text{an-sub}}$) from 0% to 100% of the upper 1 km of the ocean. We held V_{pore} constant, such that we are effectively exploring changes in the ratio of suboxic-to-anoxic water column volume to suboxic-to-anoxic sediment pore-water volume. While the volume of suboxic-to-anoxic sedimentary pore-waters may have also changed with time, our modeling reflects the influence of a relative increase in importance of water column over sedimentary denitrification. As the net rate of nitrogen removal increases with increasing water-column denitrification, export production from nitrogen-assimilating organisms ($f_{\text{assimilator-burial}}$) decreases as

$$f_{assimilator-burial} \propto \frac{1}{R} \tag{C.12}$$

causing nitrogen-fixing organisms to comprise a larger proportion of export production than nitrogen-assimilators. We maintained a constant total export production across all model outputs (*i.e.*, assuming that phosphorus, not nitrogen, was the limiting nutrient on geologic timescales across all of Earth's history), meaning that N_2-fixers compensate for decreased productivity by nitrate-assimilators. This was achieved by calculating the burial of nitrogen fixing organisms as

$$f_{fixer-burial} = f_{total-burial} - f_{assimilator-burial} \tag{C.13}$$

while $f_{\text{total-burial}}$ was held at a constant value of 0.26 Tmol N/yr.

While it has been proposed that primary productivity was hampered in the Precambrian due to phosphorus scarcity (Kipp and Stüeken, 2017; Reinhard et al., 2017), we did not attempt to scale total productivity as a function of marine redox conditions. The relationship between ocean oxygen content and export production is not precisely understood, and so including this parameterization would add uncertainty to our model outputs. By holding primary productivity and burial efficiency constant, we are isolating the influence of denitrification rates on $\delta^{15}N_{sed}$ values. Furthermore, if limited biomass recycling and resultant phosphorus scarcity in fact limited primary productivity in the Precambrian (cf. Kipp and Stüeken, 2017), the higher burial efficiency would lead to an even greater contribution of nitrogen-fixing biomass in our model outputs, thus strengthening our conclusion that $\delta^{15}N_{sed}$ values would converge toward the "fixation window" in strongly anoxic oceans. Because the exact evolution of burial efficiency through time is quite uncertain, we have left this term constant so as not to obscure the trends being investigated in our modeling, while noting that if anything, the expected changes would only further support the conclusions drawn here. By plugging the results for $f_{\text{assimilator-burial}}$ (Equation C.12) and $f_{\text{fixer-burial}}$ (Equation 13) into Equation C.7, the effect of expanding of water-column anoxia on sedimentary $\delta^{15}N$ could thus be evaluated. The model outputs are presented as a function of water column anoxia-to-suboxia (Fig. 5.6) using the parameter $p_{\text{an-sub}}$, which is defined as the percentage of the upper 1 km of the ocean that is suboxic-to-anoxic, using the equation

$$p_{an-sub} = \frac{V_{an-sub}}{V_{ocean-1km}} \tag{C.14}$$

where $V_{\text{ocean-1km}}$ is the volume of the upper 1 km of the ocean, meaning that a totally anoxic ocean would have a $p_{\text{an-sub}}$ value of 100%. The modern ocean has a $p_{\text{an-sub}}$ value of 0.3% under our parameterizations.

C.2.2 Isotope fractionation in the nitrogen cycle

Extensive reviews of the processes controlling nitrogen isotope fractionation in the ocean and marine sediments have recently been published (*e.g.*, Devol, 2015; Stüeken et al., 2016),

and are discussed in the main text (section 5.2.1). Briefly, the major input of nitrogen to the oceans, nitrogen fixation, exerts a small isotopic fractionation when the most common nitrogenase enzyme is used (average -1‰, range -2‰ to +1‰). This has been shown in laboratory studies (*e.g.*, Zerkle et al., 2008; Zhang et al., 2014) as well as field measurements of nitrogen-fixing cyanobacteria (Wada, 1980; Migawa and Wada, 1984, 1986; Carpenter et al., 1997). On the contrary, the major outgoing flux of nitrogen from the oceans – denitrification (and anammox) – can impart large kinetic isotopic fractionations, with the lighter nitrogen isotope preferentially removed from the ocean (Devol, 2015). However, the expressed isotopic fractionation associated with these nitrogen removal pathways depends on the environment. In the open ocean, where transport of substrates is rapid, observed fractionation factors typically range from -30‰ to -22‰ (Cline and Kaplan, 1975; Brandes et al., 1998; Altabet et al., 1999; Voss et al., 2001), although some recent work has suggested that this effect may in some cases be as small as -15‰ to -10‰ (*e.g.*, Kritee et al., 2012). In marine sediments, where limited resupply of substrates leads to nearly-quantitative reaction yields, isotopic fractionations are typically ∼0‰ (Brandes and Devol, 1997; Lehmann et al., 2007). It is important to note that for both of these estimates, the measurements are a community-scale fractionation, and thus account for the contribution of anammox, which in laboratory settings has been shown to exert a nitrogen isotopic fractionation of a similar magnitude to canonical denitrification (Brunner et al., 2013). In our model runs, we explored a wide range of values for these major fluxes (Table C.1).

Due to the large magnitude of fixation and denitrification fluxes, and the large isotopic fractionation associated with water-column denitrification (and anammox), these processes largely set the isotopic mass balance of the ocean system. Minor inputs and outputs, as well as recycling within the ocean, represent secondary effects that can influence nitrogen isotope ratios in marine sediments, but do not substantially change the overall picture of nitrogen isotope balance. This inference is supported by a strong similarity in outputs generated by simple and complex box models of the nitrogen cycle (Algeo et al., 2014). As noted above, minor inputs of nitrogen to the marine system (atmospheric deposition and riverine flux)

were left out of our final model runs, since they had negligible effects on the model outputs but highly uncertain trajectories across Earth's history.

After fixation, organically-bound nitrogen can be liberated (remineralized) as NH_4^+ in the process of ammonification in both the water column and sedimentary porewaters. Under oxic conditions, this process can enrich residual biomass by 1.4-2.3‰ (Freudenthal et al., 2001; Lehmann et al., 2002; Möbius, 2013), though the effect is smaller in low-O_2 and high-productivity environments (Lehmann et al., 2002; Robinson et al., 2012; Thunell et al., 2004). In our model, we assumed that the net isotopic effect of remineralization was negligible (∼0‰) because (1) in the predominantly anoxic Precambrian oceans, which are the focus of our model, the isotopic effect of remineralization was probably minor, and (2) any small effect of remineralization on the nitrogen isotope composition would be considerably smaller than the spread of values occurring due to the range of isotopic fractionations associated with nitrogen fixation and denitrification (Table C.1). Thus, any real effect of remineralization would be impossible to distinguish from the major processes controlling nitrogen isotope mass balance.

Following remineralization, we assumed that all ammonium was quantitatively oxidized to nitrate during nitrification. This is based on the observation that nitrification is rapid in the modern ocean, even at very low to undetectable levels of dissolved oxygen (Kalvelage et al., 2011; Thamdrup, 2012). This assumption renders our model only applicable to marine nitrogen cycling after the evolution of nitrification, for which there is no clear isotopic evidence until ∼2.7 Ga (Godfrey and Falkowski, 2009). However, our modeling suggests that the isotopic effects of vigorous nitrification-denitrification could be absent from the sedimentary record in strongly anoxic oceans, due to nearly quantitative denitrification. Thus, it remains possible that nitrification was occurring in the surface oceans as soon as oxygenic photosynthesis emerged and began generating free O_2, which may have occurred before 3.0 Ga (*e.g.*, Planavsky et al., 2014).

Table C.1: **Isotopic fractionation factors (ε_i) associated with nitrogen fluxes.**

flux	**fractionation (ε)**	**reference**
$f_{fixation}$	-1‰ (-2‰ to +1‰)	Zhang et al., (2014)
$f_{remin\text{-}nitrif}$	0‰	Robinson et al., (2012)
f_{burial}	0‰	Robinson et al., (2012)
$f_{deposition}$	-4‰	Algeo et al., (2014)
f_{river}	+3‰	Algeo et al., (2014)
f_{wcd}	-26‰ (-30‰ to -22‰)	Devol (2015)
f_{sd}	0‰	Devol (2015)

C.2.3 LOWESS curve

Secular changes in the nitrogen isotope record were described using locally weighted scatterplot smoothing (LOWESS), which is a non-parametric, locally-fitted smoothing algorithm designed for visualization of trends in irregularly-spaced time series data (Cleveland, 1979). For each data point, a polynomial of order d is fitted to all data pairs in a moving window, with each point weighted tricubically as a function of its distance from the center of the reference frame. We utilized a d value of 1, meaning that the local fits were via linear regression. The estimated values are then weighted by their residuals and the procedure is repeated twice, which ensures that outliers (which have low robustness weights) do not play a large role in determining the shape of the smoothing curve (Cleveland, 1979). The width of the moving window (f) is a fraction of the entire data range. We utilized an f value of 0.3 in order to minimize variability in the smoothed points while not distorting the trends in the data (Cleveland, 1979). All LOWESS calculations were performed in the R Statistical Programming Environment using the loess package (Cleveland et al., 1992; R Core Team, 2013).

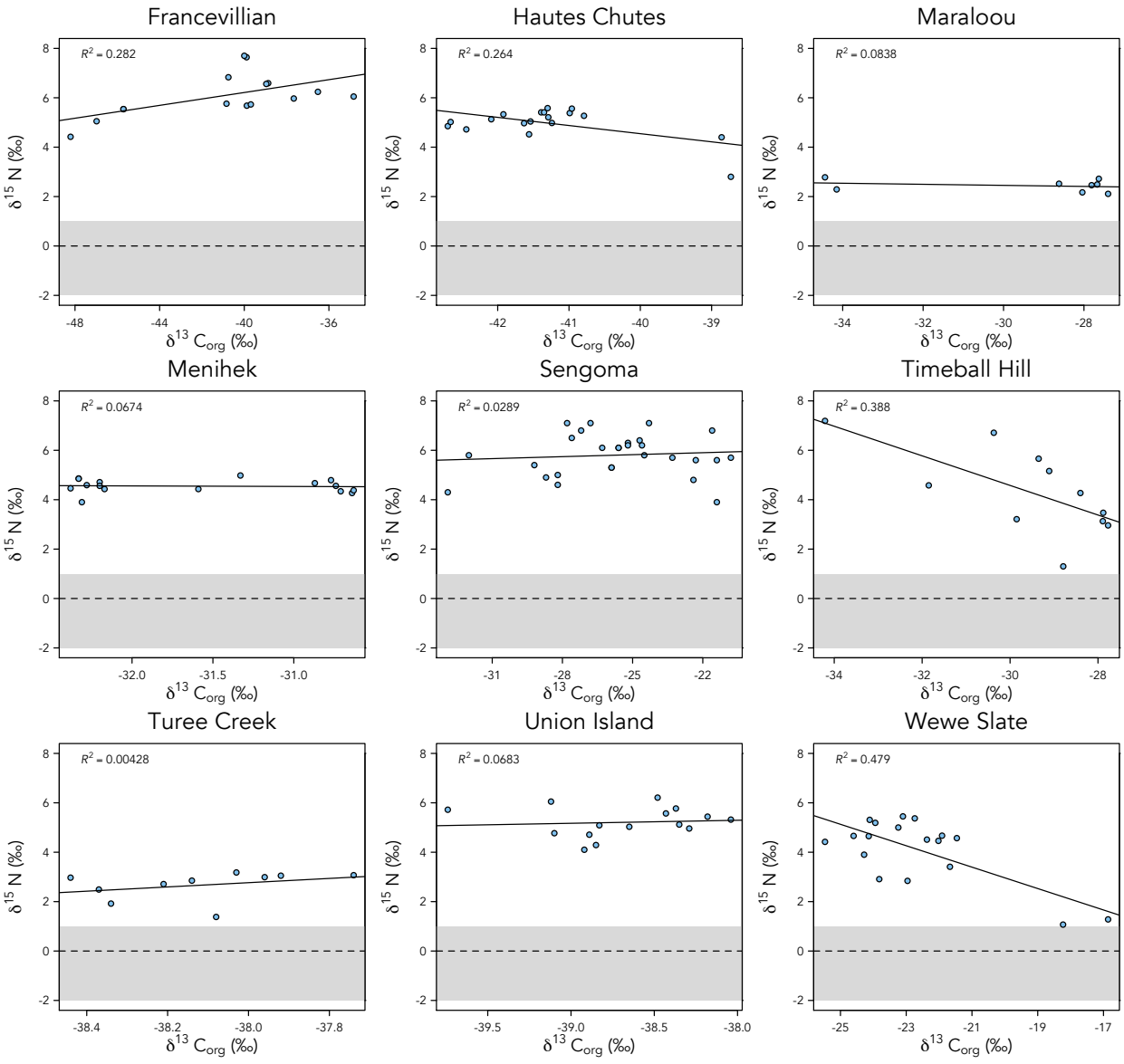

Figure C.1: **Cross-plots of δ^{15}N vs. $\delta^{13}C_{org}$ for individual units.**

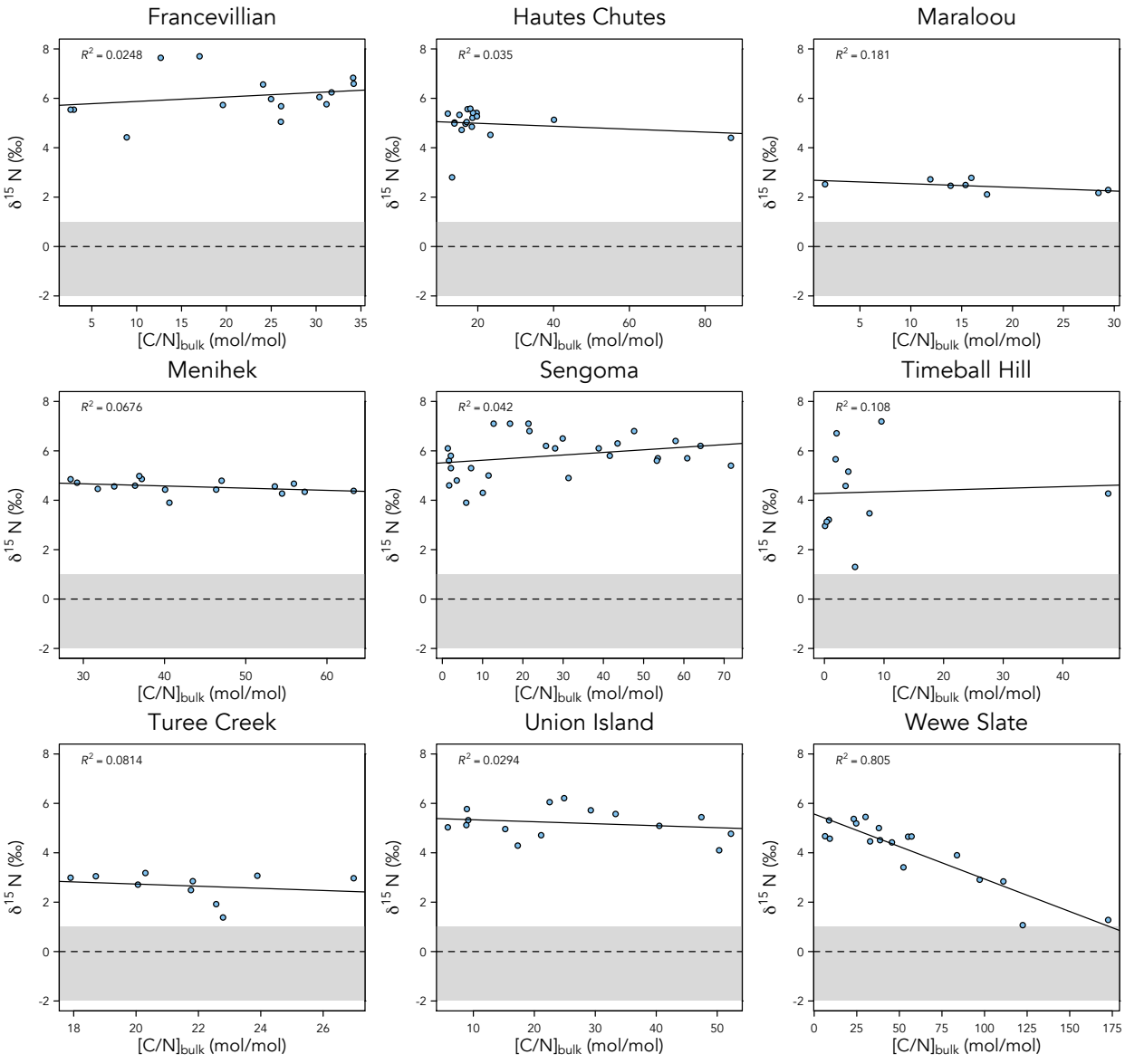

Figure C.2: **Cross-plots of δ^{15}N vs. C/N (atomic) for individual units.**

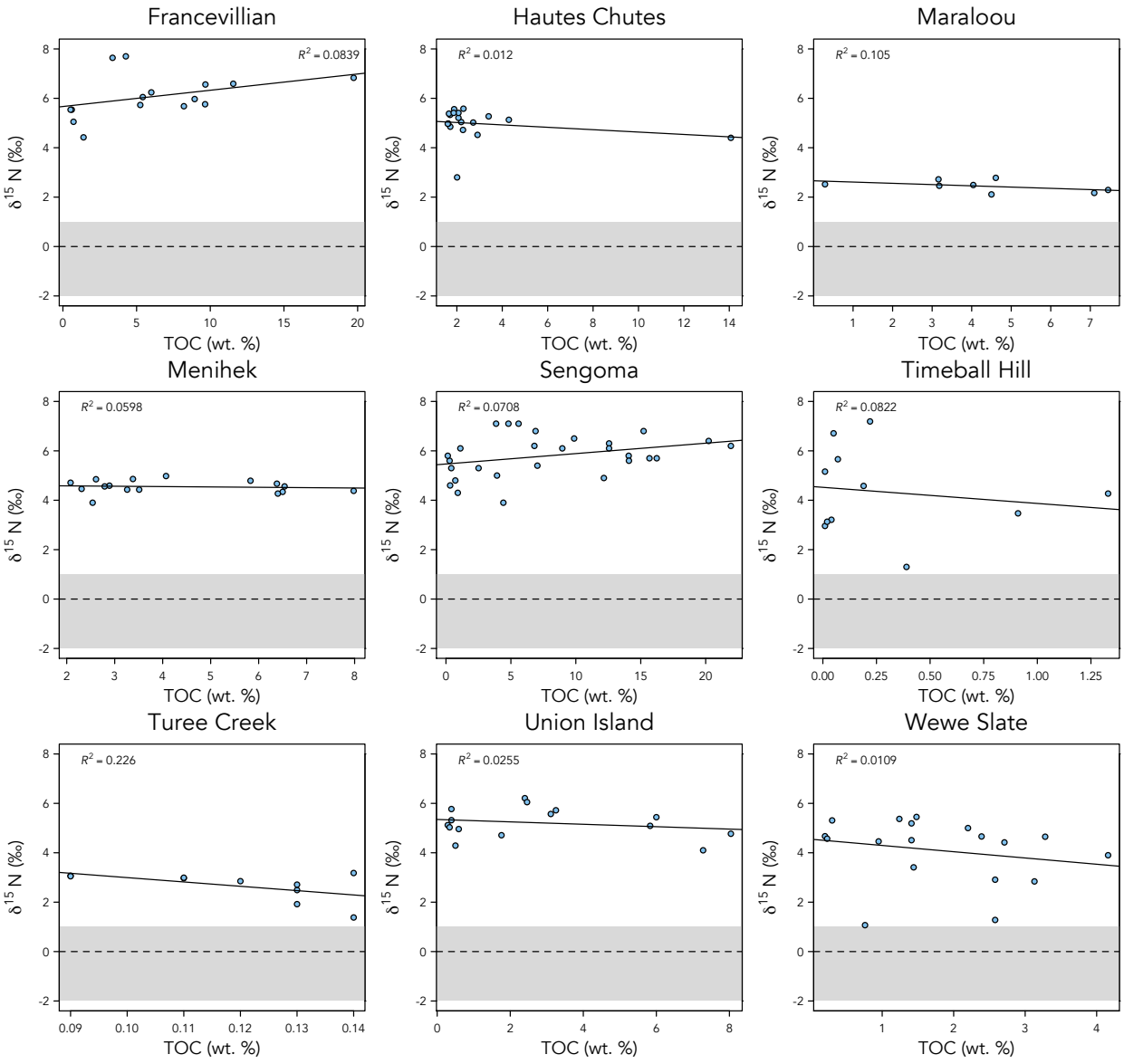

Figure C.3: **Cross-plots of δ^{15}N vs. TOC (wt. %) for individual units.**

C.3 References

Algeo, T.J., Meyers, P.A., Robinson, R.S., Rowe, H., Jiang, G.Q., 2014. Icehouse-greenhouse variations in marine denitrification. *Biogeosciences* 11, 1273–1295.

Altabet, M.A., Pilskaln, C., Thunell, R., Pride, C., Sigman, D., Chavez, F., Francois, R., 1999. The nitrogen isotope biogeochemistry of sinking particles from the margin of the Eastern North Pacific. *Deep Sea Res. Part Oceanogr. Res. Pap.* 46, 655–679.

Bankole, M.O., El Albani, A., Meunier, A., Pambo, F., Paquette, J.-L., Bekker, A., in revision. Earth's oldest preserved K-bentonites in the ca. 2.1 Ga Francevillian Basin, Gabon. *Am. J. Sci.*

Bekker, A., 2014a. Great Oxygenation Event. *Encycl. Astrobiol.*

Bekker, A., 2014b. Lomagundi Carbon Isotope Excursion. *Encycl. Astrobiol.*

Bekker, A., Holland, H.D., Wang, P.-L., Rumble, D., Stein, H.J., Hannah, J.L., Coetzee, L.L., Beukes, N.J., 2004. Dating the rise of atmospheric oxygen. *Nature* 427, 117–120.

Bekker, A., Holmden, C., Beukes, N.J., Kenig, F., Eglinton, B., Patterson, W.P., 2008. Fractionation between inorganic and organic carbon during the Lomagundi (2.22–2.1 Ga) carbon isotope excursion. *Earth Planet. Sci. Lett.* 271, 278–291.

Bekker, A., Karhu, J.A., Kaufman, A.J., 2006. Carbon isotope record for the onset of the Lomagundi carbon isotope excursion in the Great Lakes area, North America. *Precambrian Res.* 148, 145–180.

Brandes, J.A., Devol, A.H., 2002. A global marine-fixed nitrogen isotopic budget: Implications for Holocene nitrogen cycling. *Glob. Biogeochem. Cycles* 16.

Brandes, J.A., Devol, A.H., 1997. Isotopic fractionation of oxygen and nitrogen in coastal marine sediments. *Geochim. Cosmochim. Acta* 61, 1793–1801.

Brandes, J.A., Devol, A.H., Yoshinari, T., Jayakumar, D.A., Naqvi, S.W.A., 1998. Isotopic composition of nitrate in the central Arabian Sea and eastern tropical North Pacific: A tracer for mixing and nitrogen cycles. *Limnol. Oceanogr.* 43, 1680–1689.

Brunner, B., Contreras, S., Lehmann, M.F., Matantseva, O., Rollog, M., Kalvelage, T.,

Klockgether, G., Lavik, G., Jetten, M.S., Kartal, B., others, 2013. Nitrogen isotope effects induced by anammox bacteria. *Proc. Natl. Acad. Sci.* 110, 18994–18999.

Canfield, D.E., Glazer, A.N., Falkowski, P.G., 2010. The Evolution and Future of Earth's Nitrogen Cycle. *Science* 330, 192–196.

Canfield, D.E., Jørgensen, B.B., Fossing, H., Glud, R., Gundersen, J., Ramsing, N.B., Thamdrup, B., Hansen, J.W., Nielsen, L.P., Hall, P.O.J., 1993. Pathways of organic carbon oxidation in three continental margin sediments. *Mar. Geol.* 113, 27–40.

Canfield, D.E., Ngombi-Pemba, L., Hammarlund, E.U., Bengtson, S., Chaussidon, M., Gauthier-Lafaye, F., Meunier, A., Riboulleau, A., Rollion-Bard, C., Rouxel, O., Asael, D., Pierson-Wickmann, A.-C., Albani, A.E., 2013. Oxygen dynamics in the aftermath of the Great Oxidation of Earth's atmosphere. *Proc. Natl. Acad. Sci.* 110, 16736–16741.

Caquineau, T., Paquette, J.-L., Philippot, P., 2018. U-Pb detrital zircon geochronology of the Turee Creek Group, Hamersley Basin, Western Australia: timing and correlation of the Paleoproterozoic glaciations. *Precambrian Res.*

Carpenter, E.J., Harvey, H.R., Fry, B., Capone, D.G., 1997. Biogeochemical tracers of the marine cyanobacterium Trichodesmium. *Deep Sea Res. Part Oceanogr. Res. Pap.* 44, 27–38.

Cleveland, W.S., 1979. Robust locally weighted regression and smoothing scatterplots. *J. Am. Stat. Assoc.* 74, 829–836.

Cleveland, W.S., Grosse, E., Shyu, W.M., 1992. Local regression models. *Stat. Models* S 2, 309–376.

Cline, J.D., Kaplan, I.R., 1975. Isotopic fractionation of dissolved nitrate during denitrification in the eastern tropical North Pacific Ocean. *Mar. Chem.* 3, 271–299.

Codispoti, L.A., Brandes, J.A., Christensen, J.P., Devol, A.H., Naqvi, S.W.A., Paerl, H.W., Yoshinari, T., 2001. The oceanic fixed nitrogen and nitrous oxide budgets: Moving targets as we enter the anthropocene? *Sci. Mar.* 65, 85–105.

Coetzee, L.L., 2001. Genetic stratigraphy of the Paleoproterozoic Pretoria Group in the Western Transvaal [Ph.D. thesis]: Johannesburg, Rand Afrikaans University, 212 p.

Devol, A.H., 2015. Denitrification, anammox, and N2 production in marine sediments. *Annu. Rev. Mar. Sci.* 7, 403–423.

DeVries, T., Deutsch, C., Primeau, F., Chang, B., Devol, A., 2012. Global rates of water-column denitrification derived from nitrogen gas measurements. *Nat. Geosci.* 5, 547.

Dimroth, E., 1978. Labrador trough area. *Geol Rep* 193.

Dimroth, E., 1972. Stratigraphy of part of the Central Labrador Trough (between Latitude 5630' and the Height of Land), DP-154 (GM-28691).

Dimroth, E., 1970. The filling of the circum-Ungava geosyncline, in: Symposium on Basins and Geosynclines of the Canadian Shield. Geological Survey of Canada, pp. 45–142.

Dorland, H.C., 2004. Provenance ages and timing of sedimentation of selected Neoarchean and Paleoproterozoic successions on the Kaapvaal Craton [Ph.D. thesis], Rand Afrikaans University, Johannesburg, 326 p.

El Albani, A., Bengtson, S., Canfield, D.E., Bekker, A., Macchiarelli, R., Mazurier, A., Hammarlund, E.U., Boulvais, P., Dupuy, J.-J., Fontaine, C., Fürsich, F.T., Gauthier-Lafaye, F., Janvier, P., Javaux, E., Ossa, F.O., Pierson-Wickmann, A.-C., Riboulleau, A., Sardini, P., Vachard, D., Whitehouse, M., Meunier, A., 2010. Large colonial organisms with coordinated growth in oxygenated environments 2.1Gyr ago. *Nature* 466, 100–104.

El Albani, A., Bengtson, S., Canfield, D.E., Riboulleau, A., Bard, C.R., Macchiarelli, R., Pemba, L.N., Hammarlund, E., Meunier, A., Mouele, I.M., Benzerara, K., Bernard, S., Boulvais, P., Chaussidon, M., Cesari, C., Fontaine, C., Chi-Fru, E., Ruiz, J.M.G., Gauthier-Lafaye, F., Mazurier, A., Pierson-Wickmann, A.C., Rouxel, O., Trentesaux, A., Vecoli, M., Versteegh, G.J.M., White, L., Whitehouse, M., Bekker, A., 2014. The 2.1 Ga Old Francevillian Biota: Biogenicity, Taphonomy and Biodiversity. *PLOS ONE* 9, e99438.

Fennel, K., Follows, M., Falkowski, P.G., 2005. The co-evolution of the nitrogen, carbon and oxygen cycles in the Proterozoic ocean. *Am. J. Sci.* 305, 526–545.

Findlay, J.M., Parrish, R.R., Birkett, T.C., Watanabe, D.H., 1995. U-Pb ages from the Nimish Formation and Montagnais glomeroporphyritic gabbro of the central New

Québec Orogen, Canada. *Can. J. Earth Sci.* 32, 1208–1220.

Fralick, P., Davis, D.W., Kissin, S.A., 2002. The age of the Gunflint Formation, Ontario, Canada: single zircon U Pb age determinations from reworked volcanic ash. *Can. J. Earth Sci.* 39, 1085–1091.

Freudenthal, T., Wagner, T., Wenzhöfer, F., Zabel, M., Wefer, G., 2001. Early diagenesis of organic matter from sediments of the eastern subtropical Atlantic: evidence from stable nitrogen and carbon isotopes. *Geochim. Cosmochim. Acta* 65, 1795–1808.

Gauthier-Lafaye, F., 2006. Time constraint for the occurrence of uranium deposits and natural nuclear fission reactors in the Paleoproterozoic Franceville Basin (Gabon). *Geol. Soc. Am. Mem.* 198, 157–167.

Gauthier-Lafaye, F., Weber, F., 2003. Natural nuclear fission reactors: time constraints for occurrence, and their relation to uranium and manganese deposits and to the evolution of the atmosphere. *Precambrian Res.* 120, 81–100.

Godfrey, L.V., Falkowski, P.G., 2009. The cycling and redox state of nitrogen in the Archaean ocean. *Nat. Geosci.* 2, 725–729.

Goff, S.P., 1984. The magmatic and metamorphic history of the Earth Arm, Great Slave Lake, N.W.T. [Ph.D. thesis], University of Alberta, Edmonton. Ph.D. thesis, University of Alberta.

Gumsley, A.P., Chamberlain, K.R., Bleeker, W., Söderlund, U., Kock, M.O. de, Larsson, E.R., Bekker, A., 2017. Timing and tempo of the Great Oxidation Event. *Proc. Natl. Acad. Sci.* 114, 1811–1816.

Hannah, J.L., Bekker, A., Stein, H.J., Markey, R.J., Holland, H.D., 2004. Primitive Os and 2316 Ma age for marine shale: implications for Paleoproterozoic glacial events and the rise of atmospheric oxygen. *Earth Planet. Sci. Lett.* 225, 43–52.

Hoffman, P.F., 1988. Geology and tectonics, East Arm of Great Slave Lake, Northwest Territories.

Hoffman, P.F., 1987. Early Proterozoic Foredeeps, Foredeep Magmatism, and Superior-Type Iron-Formations of the Canadian Shield. *Proterozic Lithospheric Evol.* 85–98.

Hoffman, P.F., Bell, I.R., Hildebrand, R.S., Thorstad, L., 1977. Geology of the Athapuscow aulacogen, east arm of Great Slave Lake, District of Mackenzie. Rep. Act.

Horie, K., Hidaka, H., Gauthier-Lafaye, F., 2005. U-Pb geochronolog and geochemistry of zircon from the Franceville series at Bidoudouma, Gabon, in: 15th Annual Goldschmidt Conference.

James, H.L., 1955. Zones of regional metamorphism in the Precambrian of northern Michigan. *Geol. Soc. Am. Bull.* 66, 1455–1488.

Johnson, B., Goldblatt, C., 2015. The nitrogen budget of Earth. Earth-Sci. Rev. 148, 150–173.

Kalvelage, T., Jensen, M.M., Contreras, S., Revsbech, N.P., Lam, P., Günter, M., LaRoche, J., Lavik, G., Kuypers, M.M.M., 2011. Oxygen Sensitivity of Anammox and Coupled N-Cycle Processes in Oxygen Minimum Zones. *PLOS ONE* 6, e29299.

Karhu, J.A., Holland, H.D., 1996. Carbon isotopes and the rise of atmospheric oxygen. *Geology* 24, 867–870.

Keeling, R.F., Körtzinger, A., Gruber, N., 2009. Ocean deoxygenation in a warming world. *Ann. Rev. Earth Planet. Sci.*

Key, R.M., 1983. The geology of the area around Gaborone and Lobatse, Kweneng, Kgatleng, Souther and South East Districts, District Memoir 5, 230 p.

Kipp, M.A., Stüeken, E.E., 2017. Biomass recycling and Earth's early phosphorus cycle. *Sci. Adv.* 3, eaao4795.

Kipp, M.A., Stüeken, E.E., Bekker, A., Buick, R., 2017. Selenium isotopes record extensive marine suboxia during the Great Oxidation Event. *Proc. Natl. Acad. Sci.* 114, 875–880.

Kjarsgaard, B.A., Pearson, D.G., DuFrane, A., Heaman, L.M., 2013. Proterozoic geology of the East Arm Basin with emphasis on Paleoproterozoic magmatic rocks, Thaidene Nene MERA study area, in: Wright, D.F., Ambrose, E.J., Lemkow, D., Bonham-Carter, G.F. (Eds.), Mineral and Energy Resource Assessment for the Proposed Thaidene Nene National Park Reserve in the Area of the East Arm of Great Slave Lake, Northwest Territories. Geological Survey of Canada, pp. 77–117.

Klein, C., 1978. Regional metamorphism of Proterozoic iron-formation, Labrador Trough, Canada. *Am. Mineral.* 63, 898–912.

Klein, C., Fink, R.P., 1976. Petrology of the Sokoman Iron Formation in the Howells River area, at the western edge of the Labrador Trough. *Econ. Geol.* 71, 453–487.

Krapez, B., Martin, D.M., 1999. Sequence stratigraphy of the Palaeoproterozoic Nabberu Province of Western Australia. *Aust. J. Earth Sci.* 46, 89–103.

Krapež, B., Müller, S.G., Fletcher, I.R., Rasmussen, B., 2017. A tale of two basins? Stratigraphy and detrital zircon provenance of the Palaeoproterozoic Turee Creek and Horseshoe basins of Western Australia. *Precambrian Res.* 294, 67–90.

Kritee, K., Sigman, D.M., Granger, J., Ward, B.B., Jayakumar, A., Deutsch, C., 2012. Reduced isotope fractionation by denitrification under conditions relevant to the ocean. *Geochim. Cosmochim. Acta* 92, 243–259.

Kump, L.R., Junium, C., Arthur, M.A., Brasier, A., Fallick, A., Melezhik, V., Lepland, A., Črne, A.E., Luo, G., 2011. Isotopic Evidence for Massive Oxidation of Organic Matter Following the Great Oxidation Event. *Science* 334, 1694–1696.

LaRowe, D.E., Burwicz, E., Arndt, S., Dale, A.W., Amend, J.P., 2017. Temperature and volume of global marine sediments. *Geology* 45, 275–278.

Larue, D.K., 1981. The Chocolay Group, Lake Superior region, USA: sedimentologic evidence for deposition in basinal and platform settings on an early Proterozoic craton. *Geol. Soc. Am. Bull.* 92, 417–435.

Lehmann, M.F., Bernasconi, S.M., Barbieri, A., McKenzie, J.A., 2002. Preservation of organic matter and alteration of its carbon and nitrogen isotope composition during simulated and in situ early sedimentary diagenesis. *Geochim. Cosmochim. Acta* 66, 3573–3584.

Lehmann, M.F., Sigman, D.M., McCorkle, D.C., Granger, J., Hoffmann, S., Cane, G., Brunelle, B.G., 2007. The distribution of nitrate $^{15}N/^{14}N$ in marine sediments and the impact of benthic nitrogen loss on the isotopic composition of oceanic nitrate. *Geochim. Cosmochim. Acta* 71, 5384–5404.

Machado, N., Clark, T., David, J., Goulet, N., 1997. U-Pb ages for magmatism and deformation in the New Quebec Orogen. *Can. J. Earth Sci.* 34, 716–723.

Melezhik, V., Fallick, A., Clark, T., 1997. Two billion year old isotopically heavy carbon: evidence from the Labrador Trough, Canada. *Can. J. Earth Sci.* 34, 271–285.

Minagawa, M., Wada, E., 1986. Nitrogen isotope ratios of red tide organisms in the East China Sea: a characterization of biological nitrogen fixation. *Mar. Chem.* 19, 245–259.

Minagawa, M., Wada, E., 1984. Stepwise enrichment of 15 N along food chains: further evidence and the relation between δ 15 N and animal age. *Geochim. Cosmochim. Acta* 48, 1135–1140.

Möbius, J., 2013. Isotope fractionation during nitrogen remineralization (ammonification): Implications for nitrogen isotope biogeochemistry. *Geochim. Cosmochim. Acta* 105, 422–432.

Müller, S.G., Krapež, B., Barley, M.E., Fletcher, I.R., 2005. Giant iron-ore deposits of the Hamersley province related to the breakup of Paleoproterozoic Australia: New insights from in situ SHRIMP dating of baddeleyite from mafic intrusions. *Geology* 33, 577–580.

Mumford, T.R., Ketchum, J., Falck, H., Heaman, L.M., 2012. New geochemical, geochronological, and isotopic data for the Blatchford Lake intrusive suite and the Simpson Island dyke.

Olierook, H.K., Sheppard, S., Johnson, S.P., Occhipinti, S.A., Reddy, S.M., Clark, C., Fletcher, I.R., Rasmussen, B., Zi, J.-W., Pirajno, F., 2018. Extensional episodes in the Paleoproterozoic Capricorn Orogen, Western Australia, revealed by petrogenesis and geochronology of mafic–ultramafic rocks. *Precambrian Res.* 306, 22–40.

Olsson, J.R., Söderlund, U., Klausen, M.B., Ernst, R.E., 2010. U-Pb baddeleyite ages of major Archean dyke swarms and the Bushveld Complex, Kaapvaal Craton (South Africa): correlations to volcanic rift forming events. *Precambrian Res.* 183, 490–500.

Partin, C.A., Bekker, A., Planavsky, N.J., Scott, C.T., Gill, B.C., Li, C., Podkovyrov, V., Maslov, A., Konhauser, K.O., Lalonde, S.V., Love, G.D., Poulton, S.W., Lyons, T.W., 2013. Large-scale fluctuations in Precambrian atmospheric and oceanic oxygen levels

from the record of U in shales. *Earth Planet. Sci. Lett.* 369, 284–293.

Paulmier, A., Ruiz-Pino, D., 2009. Oxygen minimum zones (OMZs) in the modern ocean. *Prog. Oceanogr.* 80, 113–128.

Pirajno, F., Jones, J.A., Hocking, R.M., Halilovic, J., 2004. Geology and tectonic evolution of Palaeoproterozoic basins of the eastern Capricorn Orogen, Western Australia. *Precambrian Res.* 128, 315–342.

Pirajno, F., Occhipinti, S.A., Swager, C.P., 1998. Geology and tectonic evolution of the Palaeoproterozoic Bryah, Padbury and Yerrida Basins (formerly Glengarry Basin), Western Australia: implications for the history of the south-central Capricorn Orogen. *Precambrian Res.* 90, 119–140.

Planavsky, N.J., Asael, D., Hofmann, A., Reinhard, C.T., Lalonde, S.V., Knudsen, A., Wang, X., Ossa Ossa, F., Pecoits, E., Smith, A.J.B., Beukes, N.J., Bekker, A., Johnson, T.M., Konhauser, K.O., Lyons, T.W., Rouxel, O.J., 2014. Evidence for oxygenic photosynthesis half a billion years before the Great Oxidation Event. *Nat. Geosci.* 7, 283–286.

Préat, A., Bouton, P., Thiéblemont, D., Prian, J.-P., Ndounze, S.S., Delpomdor, F., 2011. Paleoproterozoic high δ 13 C dolomites from the Lastoursville and Franceville basins (SE Gabon): stratigraphic and synsedimentary subsidence implications. *Precambrian Res.* 189, 212–228.

R Core Team, 2013. R: A language and environment for statistical computing. R Foundation for Statistical Computing.

Rasmussen, B., Bekker, A., Fletcher, I.R., 2013. Correlation of Paleoproterozoic glaciations based on U–Pb zircon ages for tuff beds in the Transvaal and Huronian Supergroups. *Earth Planet. Sci. Lett.* 382, 173–180.

Rasmussen, B., Fletcher, I.R., 2002. Indirect dating of mafic intrusions by SHRIMP U–Pb analysis of monazite in contact metamorphosed shale: an example from the Palaeoproterozoic Capricorn Orogen, Western Australia. *Earth Planet. Sci. Lett.* 197, 287–299.

Reinhard, C.T., Planavsky, N.J., Gill, B.C., Ozaki, K., Robbins, L.J., Lyons, T.W., Fischer, W.W., Wang, C., Cole, D.B., Konhauser, K.O., 2016. Evolution of the global

phosphorus cycle. *Nature* 541, 386–389.

Robinson, R.S., Kienast, M., Luiza Albuquerque, A., Altabet, M., Contreras, S., De Pol Holz, R., Dubois, N., Francois, R., Galbraith, E., Hsu, T.-C., others, 2012. A review of nitrogen isotopic alteration in marine sediments. *Paleoceanography* 27.

Rohon, M.-L., Vialette, Y., Clark, T., Roger, G., Ohnenstetter, D., Vidal, P., 1993. Aphebian mafic-ultramafic magmatism in the Labrador Trough (New Quebec): its age and the nature of its mantle source. Can. J. Earth Sci. 30, 1582–1593.

Schulz, K.J., Cannon, W.F., 2007. The Penokean orogeny in the Lake Superior region. *Precambrian Res.* 157, 4–25.

Scott, C., Lyons, T.W., Bekker, A., Shen, Y., Poulton, S.W., Chu, X., Anbar, A.D., 2008. Tracing the stepwise oxygenation of the Proterozoic ocean. *Nature* 452, 456-U5.

Scott, C., Wing, B.A., Bekker, A., Planavsky, N.J., Medvedev, P., Bates, S.M., Yun, M., Lyons, T.W., 2014. Pyrite multiple-sulfur isotope evidence for rapid expansion and contraction of the early Paleoproterozoic seawater sulfate reservoir. *Earth Planet. Sci. Lett.* 389, 95–104.

Sheen, A.I.-F., 2017. Geochronological and geochemical constraints on the origin of the Paleoproterozoic Union Island Group mafic magmatism, East Arm Basin, N.W.T. University of Alberta, Edmonton.

Sheppard, S., Fletcher, I.R., Rasmussen, B., Zi, J.-W., Muhling, J.R., Occhipinti, S.A., Wingate, M.T., Johnson, S.P., 2016. A new Paleoproterozoic tectonic history of the eastern Capricorn Orogen, Western Australia, revealed by U–Pb zircon dating of microtuffs. *Precambrian Res.* 286, 1–19.

Shibuya, T., Aoki, K., Komiya, T., Maruyama, S., 2010. Stratigraphy-related, low-pressure metamorphism in the Hardey Syncline, Hamersley Province, Western Australia. *Gondwana Res.* 18, 213–221.

Smith, R.E., Perdrix, J.L., Parks, T.C., 1982. Burial metamorphism in the Hamersley basin, Western Australia. *J. Petrol.* 23, 75–102.

Stüeken, Eva E., Kipp, M.A., Koehler, M.C., Buick, R., 2016. The evolution of Earth's

biogeochemical nitrogen cycle. *Earth-Sci. Rev.* 160, 220–239.

Stüeken, E. E., Kipp, M.A., Koehler, M.C., Schwieterman, E.W., Johnson, B., Buick, R., 2016. Modeling p N2 through Geological Time: Implications for Planetary Climates and Atmospheric Biosignatures. *Astrobiology* 16, 949–963.

Tesdal, J.-E., Galbraith, E.D., Kienast, M., 2013. Nitrogen isotopes in bulk marine sediment: linking seafloor observations with subseafloor records. *Biogeosciences* 10, 101–118.

Thamdrup, B., 2012. New pathways and processes in the global nitrogen cycle. *Annu. Rev. Ecol. Evol. Syst.* 43, 407–428.

Thieblemont, D., Castaing, C., Billa, M., Bouton, P., Préat, A., 2009. Notice explicative de la Carte géologique et des Ressources minérales de la République gabonaise à 1/1 000 000. Editions DGMG, Ministère des Mines, du Pétrole, des Hydrocarbures. Libreville, 384 p.

Thorstad, L., 1976. Structure, stratigraphy, and petrology of the Union Island Group, East Arm of the Great Slave Lake, N.W.T. [B.Sc. thesis], University of British Columbia, Vancouver. B.Sc. thesis, University of British Columbia.

Thunell, R.C., Sigman, D.M., Muller-Karger, F., Astor, Y., Varela, R., 2004. Nitrogen isotope dynamics of the Cariaco Basin, Venezuela. *Glob. Biogeochem. Cycles* 18.

Tyrrell, T., 1999. The relative influences of nitrogen and phosphorus on oceanic primary production. *Nature* 400, 525–531.

Vallini, D.A., Cannon, W.F., Schulz, K.J., 2006. Age constraints for Paleoproterozoic glaciation in the Lake Superior Region: detrital zircon and hydrothermal xenotime ages for the Chocolay Group, Marquette Range Supergroup. Can. J. Earth Sci. 43, 571–591.

Voss, M., Dippner, J.W., Montoya, J.P., 2001. Nitrogen isotope patterns in the oxygen-deficient waters of the Eastern Tropical North Pacific Ocean. *Deep Sea Res. Part Oceanogr. Res. Pap.* 48, 1905–1921.

Wada, E., 1980. Nitrogen isotope fractionation and its significance in biogeochemical processes occurring in marine environments. *Isot. Mar. Chem.* 375–398.

Walraven, F., 1997. Geochronology of the Rooiberg Group, Transvaal Supergroup, South

Africa. Economic Geology Research Unit, University of the Witwatersrand.

Wang, Y., Van Cappellen, P., 1996. A multicomponent reactive transport model of early diagenesis: Application to redox cycling in coastal marine sediments. *Geochim. Cosmochim. Acta* 60, 2993–3014.

Weber, F., 1968. Une série précambrienne du Gabon, le Francevillien: sédimentologie, géochimie, relations avec lkes gîtes minéraux associés. Université de Strasbourg.

Woodhead, J.D., Hergt, J.M., 1997. Application of thedouble spike'technique to Pb-isotope geochronology. *Chem. Geol.* 138, 311–321.

Zajac, I.S., 1974. The stratigraphy and mineralogy of the Sokoman Formation in the Knob Lake area, Quebec and Newfoundland. Department of Energy, Mines and Resources.

Zerkle, A.L., Junium, C.K., Canfield, D.E., House, C.H., 2008. Production of ^{15}N-depleted biomass during cyanobacterial N2-fixation at high Fe concentrations. *J. Geophys. Res. Biogeosciences* 113, G03014.

Zerkle, A.L., Poulton, S.W., Newton, R.J., Mettam, C., Claire, M.W., Bekker, A., Junium, C.K., 2017. Onset of the aerobic nitrogen cycle during the Great Oxidation Event. *Nature* 543, 465–467.

Zhang, X., Sigman, D.M., Morel, F.M., Kraepiel, A.M., 2014. Nitrogen isotope fractionation by alternative nitrogenases and past ocean anoxia. *Proc. Natl. Acad. Sci.* 111, 4782–4787.

Appendix D

CHAPTER 6 - SUPPLEMENTARY MATERIALS

D.1 Stoichiometric model of phytoplankton degradation

Here we describe the stoichiometric model of phytoplankton composition and the effect of selective degradation on C/N ratios. All calculations conducted using these equations, which were used to generate Fig. 6.10 in the main text, are available in an R script that is included as part of the Supplementary Materials.

We used a published compilation of the C/N stoichiometry of cellular components in phytoplankton (Geider and La Roche, 2002; see Table D.1 for cellular components and their chemical compositions) to determine whether it is plausible to generate C/N ratios of >50 in residual biomass that has been degraded via anaerobic remineralization. The bulk C/N ratio (*i.e.*, $(C/N)_{bulk}$) of cellular biomass was determined as:

$$(C/N)_{bulk} = \frac{C_{protein} + C_{RNA} + C_{DNA} + C_{lipid} + C_{phos} + C_{chlor} + C_{carot} + C_{ATP} + C_{carb}}{N_{protein} + N_{RNA} + N_{DNA} + N_{phos} + N_{chlor} + N_{ATP}} \tag{D.1}$$

where C_i and N_i are the carbon and nitrogen content (in mol) of each cellular component, which were calculated as:

$$C_i = (\frac{M_C}{M_C + M_H + M_O + M_N + M_S + M_P + M_{Mg}})(\frac{1}{12.01})f_i \tag{D.2}$$

$$C_i = (\frac{M_C}{M_C + M_H + M_O + M_N + M_S + M_P + M_{Mg}})(\frac{1}{12.01})f_i \tag{D.3}$$

where M_i is the mass (in grams) of each respective element in the component of interest (determined as the stoichiometric coefficient [Table D.1, column 2] multiplied by the molar

mass), fi is the fraction of cellular biomass comprised by the component of interest [Table D.1, column 4], and 12.01 and 14.01 are the molar masses of carbon and nitrogen, respectively. The baseline composition shown in Table D.1 gives a $(C/N)_{bulk}$ ratio of 6.64, which closely matches the canonical Redfield C/N ratio (Redfield, 1934; Redfield, 1958).

We then determined the C/N ratio of residual biomass (*i.e.*, $(C/N)_{residual}$) that has experienced selective degradation of nitrogen-rich components during anaerobic remineralization (cf. Van Mooy et al., 2002). This was modeled assuming that the degradational process only removes protein, RNA and DNA, and does so in a fashion that does not change the C/N stoichiometry of each pool during degradation, but rather removes each component with its respective C/N ratio. We thus calculated $(C/N)_{residual}$ as:

$$(C/N)_{residual} = \frac{(1 - f_{degraded})(C_{protein} + C_{RNA} + C_{DNA}) + C_{lipid} + C_{phos} + C_{chlor} + C_{carot} + C_{ATP} + C_{carb}}{(1 - f_{degraded})(N_{protein} + N_{RNA} + N_{DNA}) + N_{phos} + N_{chlor} + N_{ATP}} \quad \text{(D.4)}$$

where $f_{degraded}$ denotes the proportion of the nitrogen-rich components that have been degraded, ranging 0 (no degradation) to 1 (complete degradation). Under the baseline composition in Table D.1, $(C/N)_{residual}$ is ∼11 when fdegraded is 0.6 and ∼53 when $f_{degraded}$ is 0.95 (Figs. 6/9, D.1). To demonstrate the robustness of this calculation, we also explored two end-member scenarios that correspond to disproportionately high and low $(C/N)_{bulk}$ values resulting from different proportions of cellular components (Table D.2). Even in these cases, $(C/N)_{residual}$ can exceed 50 at near-complete degradation of nitrogen-rich components (dotted curves in Fig. D.1). It is therefore plausible that selective degradation of nitrogen-rich cellular components in strongly anoxic marine environments can generate very high C/N ratios in residual biomass if the degradation is near-complete. This seems plausible given that burial efficiency of organic matter in the modern ocean is thought to be much less than 1% (*e.g.*, Hedges and Keil, 1995). While most of the remineralization that keeps burial efficiency so low is done aerobically in the modern ocean, in ancient low-oxygen water columns the contribution of anaerobic metabolisms may have been much higher, such that selective degradation of nitrogen-rich biomass was more pronounced (*i.e.*, $f_{degraded} > 0.9$).

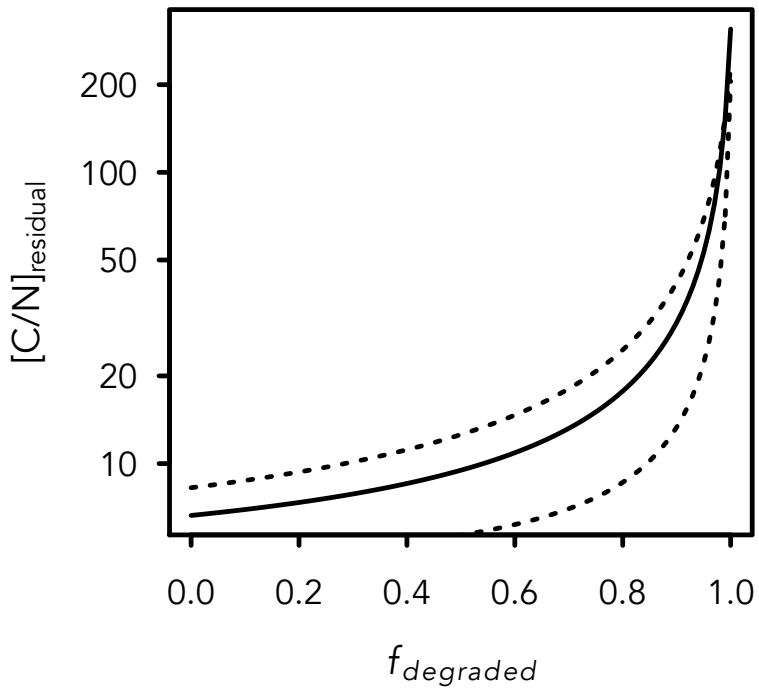

Figure D.1: **Enrichment of C/N ratios in residual biomass due to selective degradation of nitrogen-rich components.** Solid curve denotes standard phytoplankton stoichiometry (*i.e.*, $(C/N)_{biomass} = 6.6$); dotted curves correspond to higher and lower $(C/N)_{biomass}$ endmembers with different proportions of cellular components (see Table D.2).

Table D.1: **C/N ratios of cellular components in phytoplankton.** Data are from Table 1 in Geider & La Roche (2002).

component	composition	C/N (molar)	fraction of mass (f_i)
protein	$C_{4.43}H_7N_{1.16}S_{0.019}$	3.82	0.5 [0.45-0.85]
RNA	$C_{9.5}H_{13.75}O_8N_{3.75}P$	3.52	0.05 [0.03-0.15]
DNA	$C_{9.5}H_{14.25}O_8N_{3.75}P$	2.6	0.01 [0.005-0.03]
lipids	$C_{40}H_{74}O_5$	N/A	0.1 [0.1-0.5]
phosphoglycerides	$C_{37.9}H_{72.5}O_{9.4}N_{0.43}P$	88.14	0.05 [0.05-0.15]
chlorophyll	$C_{35}H_{29}O_5N_4Mg$	8.75	0.005 [0.002-0.05]
carotenoids	$C_{39\text{-}48}H_{52\text{-}68}O_{0\text{-}8}$	N/A	0.005 [0.002-0.05]
ATP	$C_{10}H_{16}O_{13}N_5P_3$	2	0.001
carbohydrates	$C_6H_{12}O_6$	N/A	0.279 [0.05-0.45]
TOTAL		**6.64**	**1**

Table D.2: **Sensitivity test parameters.**

component	f_i - high C/N case	f_i - low C/N case
protein	0.45	0.7
RNA	0.03	0.1
DNA	0.005	0.03
lipids	0.2	0.1
phosphoglycerides	0.1	0.05
chlorophyll	0.01	0.002
carotenoids	0.01	0.002
ATP	0.001	0.001
carbohydrates	0.194	0.015
TOTAL	**1**	**1**

D.2 Amended mixing model calcualtions

Below is a description of an amended mixing model that tracks three components of marine sedimentary carbon and nitrogen, as well as their isotopic compositions. All calculations conducted using these equations, which were used to generate Figs. 6.11 and 6.12 in the main text, are available in an R script that is included as part of the Supplementary Materials.

D.2.1 A three-component mixing model

We amended the two-component mixing model described in Section 6.5.2 to account for the contribution of detrital organic matter to marine sediments. While the goal of the discussion in this paper is to deduce redox effects on the C/N ratio of marine organic matter, minor contributions of "detrital" organic matter (here defined as allogenic organic carbon transported from the continents to marine sediments, which may be derived from either terrestrial plant / fungal / microbial material, and/or organic matter in exposed sedimentary rocks) may be present in these settings. Thus, recognizing and accounting for this contribution in our mixing model calculations can be critical.

We begin by operationally defining three components that comprise the total organic carbon and total nitrogen content of a marine sediment:

1. The **kerogen** phase is here defined as marine organic matter that is exported from the water column to the sediment. This phase contains both carbon and nitrogen. We opt to use the term "kerogen" in spite of the fact that this phase (as it is here defined) can also contain bitumen when sediments containing appreciable kerogen are subjected to thermal maturation within the oil window. However, because kerogen (organic solvent-insoluble organic matter) is the dominant organic pool in most marine sedimentary rocks that have either remained below the oil window or exceeded the oil window (*e.g.*, Durand, 1980), and perhaps even dominant in oil shales, where conversion yields of kerogen to bitumen can be quite low (Durand, 1980), we simply refer to this phase as "kerogen."

2. The **silicate** phase is here defined as clay minerals in the marine sediment that contain nitrogen that derives from either (a) diagenetic release of nitrogen (as ammonium, NH_4^+) from the kerogen phase, which can be trapped in clay minerals, or (b) "detrital" clay-bound nitrogen that has been transported from the continents. It is thought that the former contribution is dominant in most marine settings (*e.g.*, Müller, 1977). As defined, this phase contains no carbon.

3. The **detrital** phase is here defined as organic matter that has been transported from the continents to marine sediments. This material is typically recalcitrant, as it has escaped oxidation during transport to the ocean, and is therefore assumed here to contain no nitrogen. As noted above, this material can derive from either extant organisms living on land or from organic matter in exposed sedimentary rocks.

Under this framework, the total organic carbon content (TOC_{bulk}) of a marine sediment can be calculated as:

$$TOC_{bulk} = TOC_{kerogen} + TOC_{detrital} \tag{D.5}$$

where $TOC_{kerogen}$ and $TOC_{detrital}$ are the respective contributions of carbon from the kerogen and detrital phases. Similarly, the total nitrogen content (TN_{bulk}) of a marine sediment can be calculated as:

$$TN_{bulk} = TN_{kerogen} + TN_{silicate} \tag{D.6}$$

where $TN_{kerogen}$ and $TN_{silicate}$ represent the respective contributions of nitrogen from the kerogen and silicate phases. The carbon/nitrogen ratio of the bulk sediment (C_{org}/N_{tot}) can then be calculated as:

$$\frac{C_{org}}{N_{tot}} = \frac{TOC_{bulk}}{TN_{bulk}} \tag{D.7}$$

These calculations thus enable a detrital carbon phase to be tracked; if $\mathrm{TOC_{detrital}} = 0$ then the outputs of these calculations will be the same as those described in Section 6.5.2 of the main text.

D.2.2 Tracking $\delta^{15}N$, $\delta^{13}C_{org}$, and C_{org}/N_{tot} with the three-component mixing model

This model can be used to assess mixing controls on $\delta^{15}\mathrm{N}$ and $\delta^{13}\mathrm{C_{org}}$ values in a sedimentary section if the isotopic compositions of individual components are known or estimated. The organic carbon isotope composition of the bulk sediment ($\delta^{13}\mathrm{C_{org\text{-}bulk}}$) can be calculated as:

$$\delta^{13}C_{org-bulk} = \frac{(\delta^{13}C_{org-kerogen} \times TOC_{kerogen}) + (\delta^{13}C_{org-detrital} \times TOC_{detrital})}{TOC_{kerogen} + TOC_{detrital}} \tag{D.8}$$

where $\delta^{13}\mathrm{C_{org\text{-}kerogen}}$ and $\delta^{13}\mathrm{C_{org\text{-}detrital}}$ are the organic carbon isotope compositions of the kerogen and detrital phases, respectively. Similarly, the nitrogen isotope composition of the bulk sediment ($\delta^{15}\mathrm{N_{bulk}}$) can be calculated as:

$$\delta^{15}N_{bulk} = \frac{(\delta^{15}N_{kerogen} \times TN_{kerogen}) + (\delta^{15}N_{silicate} \times TN_{silicate})}{TN_{kerogen} + TN_{silicate}} \tag{D.9}$$

where $\delta^{15}\mathrm{N_{kerogen}}$ and $\delta^{15}\mathrm{N_{silicate}}$ are the nitrogen isotope compositions of the kerogen and silicate phases, respectively.